UNIVERSITÉ DE NANTES

university of
groningen

THESE DE DOCTORAT DE

L'UNIVERSITE DE NANTES

ECOLE DOCTORALE N° 602
Sciences pour l'Ingénieur
Spécialité : Génie des procédés

Par

Li HE

Catalytic Methane Combustion in Microreactors

Thèse présentée et soutenue à Groningen, le 04 Septembre 2020
Unité de recherche : Laboratoire de Thermique et Energie de Nantes (LTEN), UMR CNRS 6607

Rapporteurs avant soutenance :

Jean-Marc COMMENGE   Professeur, Université de Lorraine
Francesco PICCHIONI   Professeur, Université de Groningen

Composition du Jury :

Président :   Jean-Marc Commenge Professeur, University of Lorraine
Examinateurs : Jack LEGRAND   Professeur, Université de Nantes
               Jun YUE   Professeur, Université de Groningen
               Patrizio MASSOLI   Directeur de Recherche, Istituto Motori CNR

Dir. de thèse :   Lingai LUO   Directeur de Recherche, CNRS, LTEN

Invité(s)
Jérôme BELLETTRE   Professeur, Université de Nantes
Yilin FAN   Chargé de Recherche, CNRS, LTEN

Titre : Combustion catalytique du méthane dans les microréacteurs

Mots clés : Combustion catalytique du méthane; Catalyseur Pt/γ-Al$_2$O$_3$; microréacteur; enrobage; transfert de masse

Résumé : La thèse actuelle traite de la combustion catalytique du méthane dans des microréacteurs à catalyseur Pt/γ-Al$_2$O$_3$ à revêtement mural. La préparation de la couche de lavage Pt/γ-Al$_2$O$_3$, les systèmes de revêtement catalytique monocouche et multicouche et les différentes conceptions de géométries des microréacteurs ont été particulièrement étudiés. Divers aspects ont ainsi été abordés, y compris les procédures de préparation du revêtement de catalyseur (par exemple, les propriétés du liant, la valeur de pH, la taille de particule initiale d' Al$_2$O$_3$), l'optimisation de différentes conditions de réaction avec des systèmes de revêtement monocouche et multicouche (par exemple, température, débit, rapport molaire O$_2$/CH$_4$, charge de Pt et épaisseur de revêtement), l'effet des configurations de canaux internes dans le microréacteur (c'est-à-dire impliquant des canaux parallèles droits, une cavité, des canaux doubles serpentins, des canaux parallèles obstrués, un circuit maillé et un réseau vasculaire) sur les performances de réaction.

Title : Catalytic Methane Combustion in Microreactors

Keywords : Catalytic methane combustion; Pt/γ-Al$_2$O$_3$ catalyst; reactor; coating; mass transfer

Abstract : The current thesis deals with the catalytic methane combustion in microreactors with wall-coated Pt/γ-Al$_2$O$_3$ catalyst. The Pt/γ-Al$_2$O$_3$ washcoat preparation, the single- and multi-layer catalytic coating systems, and the different designs of microreactor geometries were particularly investigated. Various aspects were thus addressed, including the preparation procedures of the catalyst coating (e.g., the binder properties, pH value, initial Al$_2$O$_3$ particle size), the optimization of different reaction conditions with single- and multi-layer coating systems (e.g., temperature, flow rate, O$_2$/CH$_4$ molar ratio, Pt loading and coating thickness), the effect of internal channel configurations in the microreactor (i.e., involving straight parallel channels, cavity, double serpentine channels, obstacled parallel channels, meshed circuit and vascular network) on the reaction performance.

Catalytic Methane Combustion in Microreactors

Li He

Cover design: Li He, background picture is downloaded from www.shutterstock.com

Print: ProefschriftMaken

Catalytic Methane Combustion in Microreactors

PhD thesis

to obtain the degree of PhD at the
University of Groningen
on the authority of the
Rector Magnificus Prof. C. Wijmenga
and in accordance with
the decision by the College of Deans

and

to obtain the degree of PhD of
Université de Nantes
on the authority of the
President Prof. Carine Bernault
and in accordance with
the decision by the College of Deans.

Double PhD degree

This thesis will be defended in public on

04 September 2020 at 11:00 hours

by

Li He

born on 19 June 1986
in Liaoning, China

Supervisors

Prof. J. Yue
Prof. H.J. Heeres
Prof. L. Luo
Prof. J. Bellettre

Assessment Committee
Prof. F. Picchioni
Prof. W. de Jong
Prof. J.M. Commenge
Prof. J. Legrand

Dedicated to my beloved family.

谨以此书献给我亲爱的家人

Table of contents

Abstract

The current thesis deals with the catalytic methane combustion in microreactors with wall-coated $Pt/\gamma\text{-}Al_2O_3$ catalyst. The $Pt/\gamma\text{-}Al_2O_3$ washcoat preparation, the single- and multi-layer catalytic coating systems, and the different designs of microreactor geometries were particularly investigated. Various aspects were thus addressed, including the preparation procedures of the catalyst coating (e.g., the binder properties, pH value, initial Al_2O_3 particle size), the optimization of different reaction conditions with single- and multi-layer coating systems (e.g., temperature, flow rate, O_2/CH_4 molar ratio, Pt loading and coating thickness), the effect of internal channel configurations in the microreactor (i.e., involving straight parallel channels, cavity, double serpentine channels, obstacled parallel channels, meshed circuit and vascular network) on the reaction performance.

The thesis starts with a comprehensive literature review on the catalytic methane combustion at low temperatures, including catalyst, mechanisms, reaction conditions and reactor designs. Then, the preparation procedures of $Pt/\gamma\text{-}Al_2O_3$ washcoat catalyst have been studied in details, in order to improve its adhesion and uniformity on FeCrAlloy and stainless steel microreactors. A good adhesion could be obtained by using the slurry with 20 wt% $\gamma\text{-}Al_2O_3$ (particle size: 3 μm), pH = 3.5, and 3 to 5 wt% polyvinyl alcohol (molecular weight of 57,000 - 186,000). Based on the above-mentioned optimized preparation, $Pt/\gamma\text{-}Al_2O_3$ washcoat catalysts of various loadings were deposited inside the stainless-steel capillary microreactors and studied both in the single- and multi-layer catalytic coating systems. The influence of different operating conditions including the reaction temperature, total flow rate, molar ratio of $O_2:CH_4$, and the reproducibility of catalyst were tested. The results demonstrate that in general the methane conversion was improved

with the temperature rise, and presented the highest at an oxygen to methane molar ratio of ca.1.5. An obvious decrease in the methane conversion could be found over the multi-layer systems compared to their respective single-layer counterparts (if the Pt mass in the catalyst was kept equal), due to the more significant internal diffusion limitation in thicker coatings. Among all the tested microreactor geometries washcoated with Pt/γ-Al$_2$O$_3$ catalyst, the highest methane conversion could be obtained in the double serpentine channel microreactor and the lowest presented in the mesh circuit microreactor, which can be explained based on the available coating surface area, flow distribution and residence time property. In order to achieve a desirable methane conversion in microreactors, a proper tuning of the catalytic coating properties (e.g., surface area, Pt loading and thickness), the residence time, the fluid distribution uniformity and other reaction parameters (e.g., temperature and oxygen to methane molar ratio) are required.

Chapter 1

Aim and scope of the thesis

Methane combustion has been a focus research topic for decades. The large volumetric flow rate of methane and a relatively high concentration in practice present a major challenge for the combustion technology development in order to abate the associated pollutant emission. Many researches on the catalytic methane combustion at low temperatures (typically < 600 °C) have been investigated towards achieving a lower light-off/working temperature, and with that less exhaust emission and more stable combustion. The ideal catalysts for the methane combustion endowed with high temperature stability, low activation energy and excellent resistance to poison still need to be further developed. Apart from the catalyst development, there is a quest for efficient reactor engineering concepts. Microreactors offer a great promise and can be broadly employed for intensifying (catalytic) reaction processes, especially for strongly exothermic reactions (such as the methane combustion). This is mainly due to the enhanced heat and mass transfer in microreactors, allowing the suppression of hot spot formation and a better catalyst usage for the improved reaction rate. The washcoat catalyst immobilized onto the walls of microreactors avoids high pressure drop and temperature gradient likely present in microreactors with packed catalyst bed. Thus, the catalytic combustion of methane over the washcoat catalyst (particularly of the promising noble metal based one) in microreactors represents an attractive research field, and is thus dealt with in this thesis. In this respect, a good adhesion and dispersion of the catalytic coating layer onto the microreactor wall is essential, and the influence of the coating properties, fluid flow, mass transfer and reaction parameters in various microreactor geometries should be thus well addressed towards obtaining an optimal performance of the catalytic methane combustion.

1.1. Research objective

The main aims of this thesis are to first develop the washcoating method of $Pt/\gamma-Al_2O_3$ catalyst in FeCrAlloy and stainless steel microreactors. The optimized coating method was then applied in single- and multi-channel microreactors to investigate the mass transfer behaviour and performance of the catalytic methane combustion, over both the single- and multi-layer coating systems. Typical tested operating conditions include the reaction temperature, total flow rate, O_2/CH_4 molar ratio, Pt loading and weight. Moreover, different internal channel configurations of microreactors have been experimentally studied for the catalytic methane combustion, where the preliminary results on the optimized reaction conditions and configurations were presented. The present thesis may serve as a useful reference for the catalytic methane combustion, by providing valuable insights into the microreactor design and operation, as well as the wall-coated catalyst for the potential upscaling in the industrial applications.

1.2. Thesis outline

The main structure and contents of this thesis are as follows:

Chapter 2

This chapter provides a comprehensive literature review on the catalytic methane combustion at low temperatures regarding catalysts, mechanisms, reaction conditions and reactor designs. A detailed description of the current understanding into the influence of various operational conditions and reactor types on the reaction performance have been well addressed. This chapter may offer an essential and comprehensive reference for developing the optimal strategies by selection of the active/stable catalyst equipped with appropriate reactors under different operating conditions.

Chapter 3

This chapter deals with the development of the methods for coating $Pt/\gamma-Al_2O_3$ catalyst onto microreactor walls in order to form a stable, homogeneous and well-adhesive coating layer. The influence of binder properties, pH value, $\gamma-Al_2O_3$ concentration, initial particle size and slurry viscosity has been particularly studied and discussed in details. The influence of substrate material and channel shape on the coating adhesion has also been evaluated. The different operational conditions and temperature distribution (along the microchannel) were briefly investigated in the microreactor for the catalytic methane combustion. The main aim of this chapter is to shed light on the preparation and characterization of the washcoat slurry preparation in the microreactor.

Chapter 4

This chapter presents the catalytic performance of single- and multi-layer $Pt/\gamma-Al_2O_3$ catalytic coatings inside the capillary microreactor, with regard to the effect of the reaction temperature, total flow rate, molar ratio of O_2 to CH_4, Pt loading or mass. The results provide a good understanding of mass transfer limitations that could be present during the catalytic methane combustion in microreactors. Additionally, the stability of catalyst have been examined. This chapter may serve as a good reference for the qualitative discussion about the effect of the (external and internal) mass transfer over the single-and multi-layer systems on the reaction performance in microreactors.

Chapter 5

Based on the findings of Chapter 3, this chapter firstly investigated mainly the influence of

different operational conditions (e.g., working temperature, total flow rate), Pt/γ-Al$_2$O$_3$ coating properties (e.g., specific catalyst loading) on the catalytic combustion of methane in the straight parallel channel microreactor. In order to optimize the microreactor geometry, five other types of microreactors with different internal channel configurations have been coated with Pt/γ-Al$_2$O$_3$ catalyst, and tested regarding their performance in the catalytic methane combustion, which is experimentally rarely reported according to our best knowledge. The main aim of this chapter is to provide a useful reference on the optimization of microreactor designs that can ensure a good coating surface area, residence time and fluid uniformity towards achieving a favourable methane conversion.

Chapter 6

This chapter summarizes the main conclusions of this thesis, and provides an outlook with main focuses on the trends, challenges and future perspectives relevant to the catalytic methane combustion in microreactors. It is categorized into a short-term investigation that is required as a continuation of the current thesis work, and a long-term research for future investigation. The contents include the improvement of the noble metal catalyst activity, coating preparation, catalyst deactivation, reaction kinetics and mechanism, and different microreactor systems for coupling exothermic and endothermic reactions. These are deemed to provide a useful reference for the future research and application of microreactor systems in this upcoming field.

Chapter 2

A review on catalytic methane combustion at low temperatures: catalyst, mechanisms, reaction conditions and reactor designs

ABSTRACT: Natural gas (with methane as its main component) provides an attractive energy source because of its large abundance and its high heat of combustion per mole of carbon dioxide generated. However, the emissions released from the conventional flame combustion (essentially NO_x) have harmful impacts on the environment and the human health. Within the scope of rational and clean use of fossil energies, the catalytic combustion of natural gas appears as one of the most promising alternatives to flammable combustion. The presence of catalysts enables complete oxidation of methane at much lower temperatures (typically 500 °C), so that the formation of pollutants can be largely avoided. This work presents a literature review on the catalytic methane combustion. Various aspects are discussed including the catalyst types, the reaction mechanisms and kinetic characteristics, effects of various influencing operational factors and different reactor types proposed and tested. This paper may serve as an essential reference that contributes to the development of well-designed reactors, equipped with appropriate catalysts, and under well-handled operating conditions to realize the favorable (kinetic) performance, for their future applications and propagation in different industrial sectors.

Abbreviations

3DOM: Three-dimensionally ordered microporous

$AB_xAl_{(12-x)}O_{19}$ (x = 1, 3, 6, 9, 12): Hexaaluminate formula

ABO_3 (or $A^IB^VO_3$, $A^{II}B^{IV}O_3$, or $A^{III}B^{III}O_3$): Perovskites formula

BET: Brunauer, Emmett and Teller method, specific surface area of catalyst, unit: $m^2 \cdot g^{-1}$

BHA: Barium hexaaluminate

CMC: Catalytic methane combustion

DP: Deposition precipitation

DRIFT: Diffuse reflectance infrared spectroscopy

HDP: Homogeneous deposition precipitation

HTF: Heat transfer fluid

ITM: Ion transport membrane reactor

NGVs: Natural gas vehicles

SEM: Scanning electron microscope

SOFCs: Solid oxide fuel cells

SNG: Synthetic natural gas

2.1. Introduction

One of the major concerns over economic growth and social development nowadays is the constantly increasing energy demand [1]. The study of U.S. Energy Information Administration has forecasted an increase of 28 % in the world's energy consumption from 2015 to 2040 [2]. While there is a constant progress year by year for the development of renewable energies, the use of fossil sources (petroleum, coal and natural gas) is still dominant, and remains indispensable in the near future [3].

Among the fossil energy resources, the natural gas presents a particular interest because of its higher energy content (55.7 kJ g^{-1} if fully based on methane as its main component) than coal (39.3 kJ g^{-1}) and petroleum (43.6 kJ g^{-1}) as well as its reduced CO_2 emission (50 % less than coal and 30 % less than petroleum). Moreover, the proven natural gas reserves worldwide are abundant, reaching about 193.5 trillion cubic meters at the end of 2017 [4]. As a result, natural gas has accounted for the largest increment (24 %) in the main energy consumption in the past decade until 2017, and has been suggested as a substitute for oil and coal as a future leading energy source for the next 20 years [5]. In response to this, there is a rapidly growing number of research & development efforts yearly on the deployment of natural gas for their use in various sectors including industrial, residential, power, transport and many others [6].
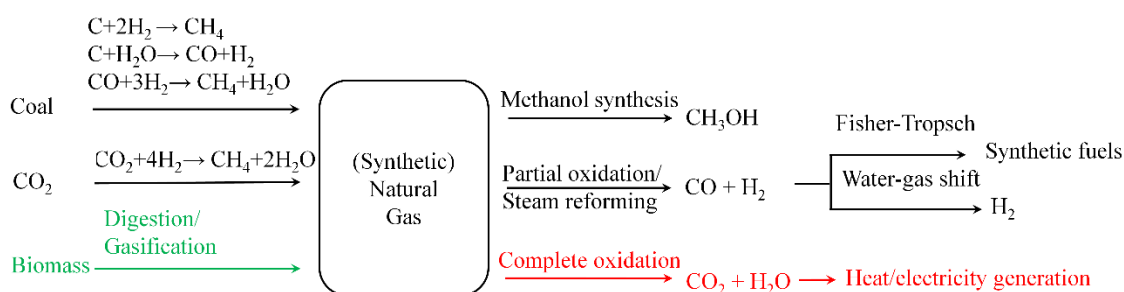
Fig. 2.1. Main reaction network of synthetic natural gas.

Besides the natural gas fields, the synthetic natural gas (SNG) can also be derived from coal gasification, CO_2 methanation and biomass gasification/digestion [7,8]. Fig. 2.1 shows the main reaction network of SNG in the industry. Biomass is particularly promising as a substitute for fossil resources owing to its benefits of energy security and environmental friendliness. On one hand, the SNG can be obtained from upgrading biogas that is generated from biomass digestion (e.g., manure) and/or from carbohydrate fermentation by bacteria in an anaerobic environment [9-11]. On the other hand, the SNG can be produced via gasification of biomass (e.g., wood, straw and crops) followed by the process of methanation [12,13]. The syngas and methanol can be

synthesized by partial oxidation and steam reforming reaction, producing consequently synthetic fuels and hydrogen. Meanwhile, the combustion of methane can provide the heat and electricity due to the strongly exothermic nature of the reaction.

The conventional flame combustion of (synthetic) natural gas occurs typically at above 1400 °C and releases harmful pollutants (such as NO_x, CO and hydrocarbon). The impact of NO_x on human health (respiratory diseases) has been widely recognized [14]. Its emission also has harmful environmental impacts including the formation of photochemical smog and acid rain [15]. More and more stringent regulations are thus applicable over European countries. For example, in September, 2018, the maximum NO_x emission level has been reduced from 70 mg kWh^{-1} (class 5) to 56 mg kWh^{-1} for all domestic boilers sold in Europe [16]. As a result, the complete oxidation of natural gas in the presence of catalysts (i.e. the catalytic combustion) appears as one of the most promising alternative solutions for the rational and clean use of fossil energies. The activation energy is reduced from 100-200 kJ mol^{-1} (conventional combustion) to 40-80 kJ mol^{-1} (catalytic combustion), leading to a lower working temperature (< 600 °C). In this regard, less pollutant emissions could be reached (~5 ppm compared with 150-200 ppm for conventional combustion). Hence, the catalytic combustion of methane or natural gas as a clean technology has received increasing research attention [17], indicated by the significantly increasing number of yearly publications over the past two decades (Fig. 2.2).
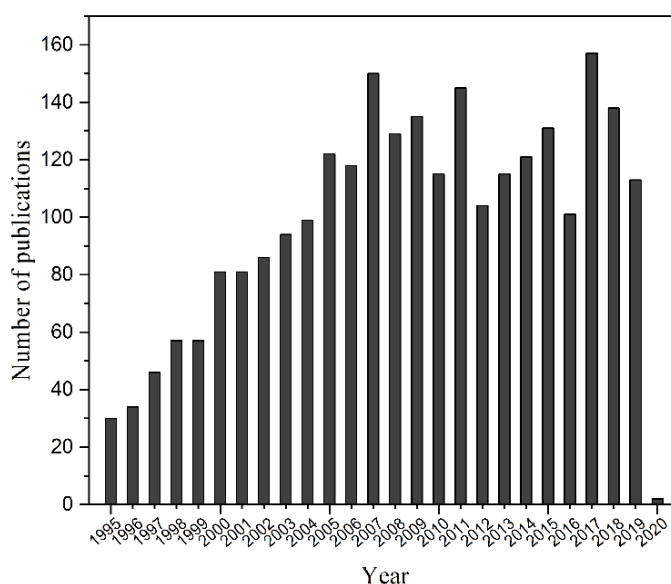
Fig. 2.2. Number of publications on the catalytic methane combustion (source: Scopus; keyword: catalytic methane combustion; date: 17 October, 2019).

Various application areas of methane catalytic combustion (CMC) have been proposed and attempted, as illustrated in Fig. 2.3 and briefly described below.

(i) Natural gas vehicles (NGVs) [18-21] (ca. 300 - 700 ^{o}C): NGVs have the advantages in the abatement of greenhouse gas emissions and smog emissions compared to gasoline or diesel-driven vehicles. Three-way catalysts are applied on NGVs mainly for exhaust purification in practice.

(ii) Gas turbine [22-27] (ca. 700 - 1400 ^{o}C): Methane combustion is widely used as the fuel on the gas turbine. The combusted gas is used to drive a turbine for power generation. For example, 25 kW electricity output can be obtained with 0.8 vol.% methane in the air [24].

(iii) Solid oxide fuel cells (SOFCs) [28] (ca. 500 - 1000 ^{o}C): The preheated compressed air passes into the cathode of the battery while the compressed methane mixed with the overheated steam enters into the anode of the fuel cell. The methane electrochemical conversion in SOFCs, if properly controlled, could obtain a high conversion efficiency and an environmental benefit due to a significant decrease in pollutant emissions.

(iv) Domestic heating systems [29-32] (ca. 300 - 700 ^{o}C): the heat released from the exothermic CMC reaction is utilized to drive the domestic heating systems, such as the central boilers or gas stoves. A high energy conversion efficiency and eco-friendly water boiler prototype with a hot water yield of 11.5 kg min^{-1} has been reported [33].

(v) Coupling with endothermic reaction (ca. 300 - 700 ^{o}C): the reaction heat from CMC is commonly used to drive an endothermic reaction so as to maintain the continuous autothermal operation [34]. Novel reactor designs have been proposed for coupling the CMC with an endothermic reaction (methane steam reforming [35,36], dehydrogenation of propane to propylene [37], dehydrogenation of ethane to ethylene [38,39], etc.), owing to the optimized energy integration and the process intensification.
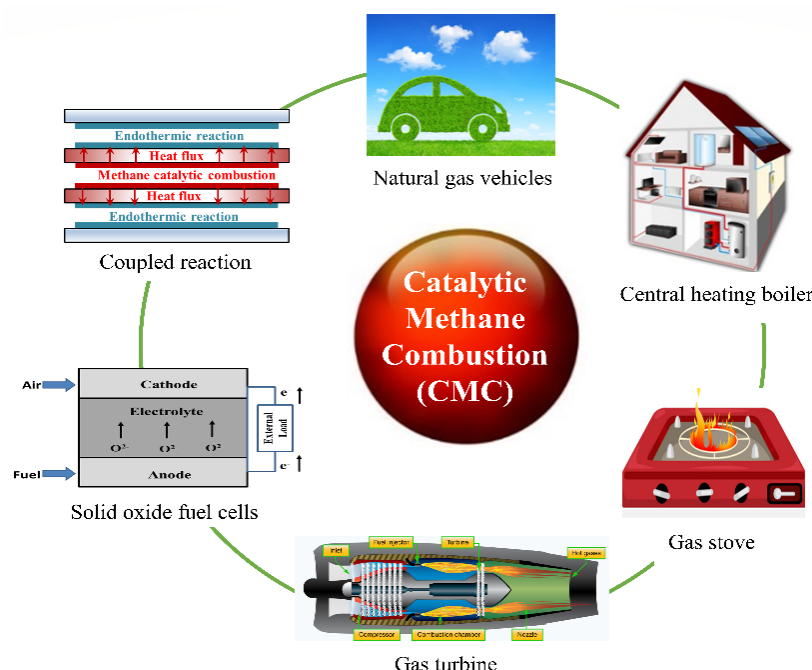
Fig. 2.3. Main applications of CMC.

It may be discovered that compared to the conventional flame combustion, the presence of catalysts enables a decrease of the working temperature (<1400 °C). Depending on the target application, the operational temperature for CMC can be further divided into a relatively lower range (about 300 - 700 °C) and a relatively higher one (about 700 - 1400 °C). The low-temperature CMC becomes more attractive due to the remarkable abatement of pollutant emissions and the prolonged catalyst lifetime. For instance, the reusability and the reproducibility of catalysts, especially for noble metal catalysts, are shortened at high temperatures. In this field, developing catalysts with high catalytic activity, low light-off temperature and good thermal stability even for such low temperature operations is still a challenging issue.

A great number of researches have been devoted to catalyst development [18,40,41] and reactor design [42-44] for CMC. Noble metal catalysts (e.g., Pt, Pd and Rh) have been widely investigated owing to their high catalytic activity. Hexaaluminate and perovskite catalysts, due to their relatively lower catalytic activity and high thermal stability, are commonly used for high temperature applications (600 - 1400 °C). Optimization of reaction conditions over various catalysts has been broadly investigated [19], such as the effect of light-off temperature, reactant concentration, oxygen to methane molar ratio, residence time, etc. Moreover, the mechanistic studies mainly focusing on kinetic models for various catalysts have been well elaborated in earlier literatures [45-48]. The reactor designs (e.g., micro/mini-structured reactor) with

coupled endothermic reaction have become a hotspot direction in recent decade [49-51]. Reviews papers related to CMC have also been published, as summarized in Table 2.1. Nevertheless, most of them primarily focus on the improvement of catalytic activity (e.g., noble metal-based catalysts [17,18,40,41], hexaaluminates/perovskite catalysts [52,53]). Other review papers may involve the CMC in one or several sub-sections, but they are mainly devoted to a specific topic, e.g., heating system [54,55], SOFCs [28], coupling exothermic/endothermic reactions [34], SNGs [9,56], etc.

The present review on CMC aims at filling the literature gap by providing a comprehensive and combined understanding of catalysts, mechanisms, reaction conditions and reactor designs. In particular, the present paper has the following objectives:

A brief introduction of the catalyst types, their advantages/disadvantages, associated reaction mechanisms and kinetic characteristics.

A complete survey on the effects of various operational factors on the performance of CMC, including temperature, space velocity, O_2/CH_4 ratio, natural gas composition and pressure.

A review on different reactor types used for CMC, with a special focus on microchannel reactor-heat exchangers.

This paper may serve as an essential reference that contributes to the development of well-designed reactors, equipped with appropriate catalysts and under well-handled operating conditions, towards realizing their favorable (kinetic) performance and for their future application and propagation in different industrial sectors.

Table 2.1 Summary of some published reviews related to CMC.

Reference	Main contents
Gélin & Primet 2002 [18]	Noble metal catalysts for methane complete oxidation at low temperatures (1) Pd, Pt-based catalysts with silica and alumina support (2) Kinetics, active sites nature (Pd, Pt), mechanism (3) Particle size effect (4) Sulphur poisoning effect (5) Improved support: ZrO_2, SnO_2, CeO_2, Co_3O_4, etc. (6) Bimetallic system: Pd-Pt catalyst

Choudhary et al. 2002 [40]	Catalysts for oxidation of methane and lower alkanes
	(1) Noble metal based catalysts: Pd, Pt, Rh, Au
	(2) Metal oxide catalysts
	  Single metal oxides: CuO, MgO, Co_3O_4, etc.
	  Mixed metal oxides: perovskites, hexaaluminate, doped metal oxides

Ciuparu et al. 2002 [57]	CMC over Pd-based catalysts
	(1) Catalyst characterization, deactivation, reaction conditions, etc.
	(2) Transformation of Pd and PdO phases
	(3) Catalytic mechanism
Li & Hoflund 2003 [41]	Complete oxidation of methane at low temperatures over noble/non-noble metal catalysts
	(1) Kinetics and mechanism over Pd/Al_2O_3
	(2) Effect of Ce additives on the activity
	(3) Effect of CO_2 and H_2O on the activity
	(4) Perovskite-type oxides
Rahimpou et al. 2012 [34]	Coupling exothermic and endothermic catalytic reactions
	(1) Reactor type: fixed bed, fluidized bed, etc.
	(2) Various alternatives for thermal coupling
	(3) Various coupling catalytic reactions, including:
	CMC reaction coupled with:
	methane steam reforming (with H_2O or CO_2) or
	dehydrogenation of propane to propylene or
	dehydrogenation of ethane to ethylene or
	methane partial oxidation coupled with methane steam reforming, etc.
Zhu et al. 2014 [53]	Perovskite preparation and application in heterogeneous catalysis
	(1) Structure and properties, characterizations
	(2) Synthesis with morphologies: bulk, nanosized, porous, nanospheres, etc.
	(3) Applications: NO decomposition; NO reduction; NO oxidation; N_2O decomposition CH_4 combustion; CO oxidation; oxidative reforming of hydrocarbon; volatile organic compound combustion
Chen et al. 2015 [17]	Catalysts for methane combustion
	(1) Noble metal catalyst:
	Pd-based catalyst: active nature, support effect, additive effect, sulphur poisoning
	Pt-based catalyst: chlorine effect, particle size, SO_2, H_2/propane addition
	Au-based catalyst: Au state, different preparation methods effects
	Bimetallic system: Pt-Pd, Pd-Rh, Pd-Au, etc.
	(2) Metal oxide catalyst:
	Single metal oxide-based catalysts: CuO, Co_3O_4, MnO_x, CeO_2
	Perovskite catalysts: substitution effect, sulfur poisoning, and preparation methods
	Spine catalysts: catalytic activity, cation substitution, etc.
	Hexaaluminate catalyst: preparation methods, cation substitution, etc.
	Kinetics and reaction mechanism over metal oxide catalysts
Tian et al. 2016 [52]	Hexaaluminate structure and catalytic performance
	(1) Structure: β-Al_2O_3 and magnetoplumbite structures, prosperities
	(2) Synthesis: sol-gel, co-precipitation, reverse microemulsion, etc.
	(3) Catalytic performances: methane combustion, methane partial oxidation, N_2O decomposition
Gür 2016 [28]	Methane conversion in SOFCs:
	(1) Catalytic methane oxidation
	(2) Electrochemical conversion of methane
	(3) Major challenges for methane conversion on catalytic anodes

Cruellas et al. 2017 [58]	Advanced reactor concepts for oxidative coupling of methane
	    (1) Concept and type of reactors for methane oxidative coupling
	    (2) Heat management system
	    (3) Applications

Yang & Guo 2018 [59]	Nanostructured perovskite oxides
	    (1) CMC reaction mechanism
	    (2) Properties and structure design of perovskite
	    (3) Recent advances of perovskite for CMC

Current review	*Various aspects on CMC*
	    (1) Catalysts: hexaaluminates, perovskite, noble metal
	    (2) Reaction mechanism and kinetics
	    (3) Reaction operational conditions: effect of temperature, ratio of oxygen to methane, space velocity, natural gas composition, pressure
	    (4) Reactor types: fixed-bed reactor, wall-coated reactor (folded plate-type, tube-coated type, monolithic, microchannel plate-type), membrane bed, fluidized bed

2.2. Catalysts for methane combustion

2.2.1 Catalyst category

Catalysts play an important role in terms of catalytic activity and reaction rate on the CMC, and are mainly categorized into metal oxide catalysts (e.g., hexaaluminate, perovskites, and single-metal oxides) and noble metal-based catalysts. The research interests on perovskites and noble metal catalysts are remarkably increasing over the years, with the latter being the most popular. The main advantages and disadvantages of catalysts are summarized in Table 2.2.

2.2.1.1 Mixed oxide catalysts

(1) Hexaaluminate [52,60-63] possesses a typical lamellar structure consisting of alternatively packed spinel blocks and conduction layers (mirror symmetry plane), as shown in Fig. 2.4a. It can be represented by the formula $ABxAl_{(12-x)}O_{19}$ (x = 1, 3, 6, 9, 12), wherein A is a large cation (e.g., of Na, K, Ba, La) residing in the conduction layer and B is the transition metal ion (e.g., of Mn, Fe, Co, Cu or Ni) or noble metal ion (e.g., of Ir, Ru, Pd or Rh) which substitutes A cation in both the spinel block and the conduction layer. Magnetoplumbite and β-alumina are two common structures for hexaaluminate in terms of the different arrangement, charge and radius of ions in the conduction layer [64]. Magnetoplumbite structure consists of A cation, O, Al in the conduction layers, while β-alumina consists of A cation and O. Importantly, the cation-substituted hexaaluminate with high sintering resistance greatly improves the catalytic activity in methane combustion due to the availability of the valent variation of transition metals (e.g., Mn, Ba, La, etc.) in the crystal lattice [65-67].
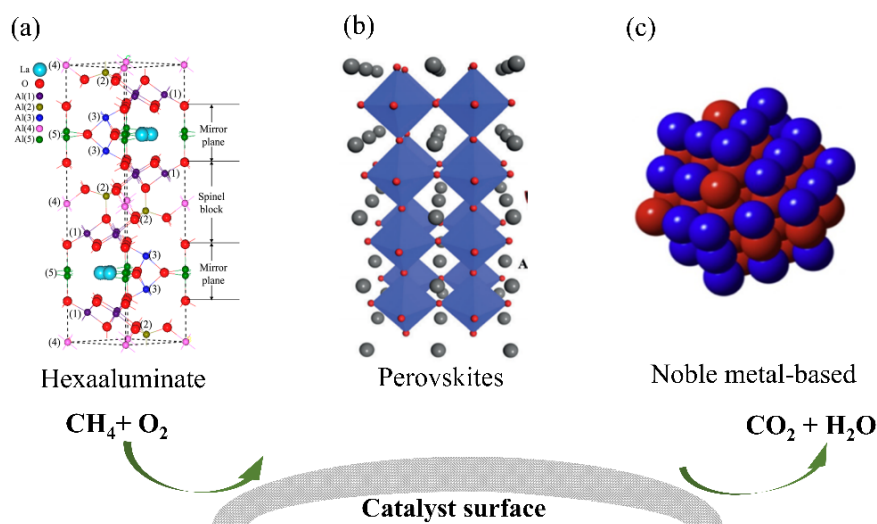
Fig. 2.4. Schematic structure of catalysts for CMC. (a) hexaaluminate (LaFeAl$_{11}$O$_{19}$) [68]; (b) perovskites (La$_{0.5}$Sr$_{0.5}$CoO$_{3-\delta}$) [69]; (c) noble metal-based (Pd-Ru) catalyst [70].

Hexaaluminate has been applied for CMC since 1987, owing to its exceptionally high thermal stability and strong resistance to thermal shock [71]. Thus, hexaaluminate is considered as the most suitable catalyst for high temperature applications (e.g., for gas turbines). Other main applications include the methane partial oxidation, the dry reforming of methane and the decomposition of N$_2$O. Although a great improvement of specific surface has been achieved, efforts are still required so as to synthesize hexaaluminate with simple procedures, as well as an excellent catalytic activity.

(2) Perovskites [72-74] are represented by a standard formula as ABO$_3$ (or more complicated as A^{I}B^{V}O$_3$, A^{II}B^{IV}O$_3$ or A^{III}B^{III}O$_3$). A as a larger cation is commonly composed of alkaline/rare earth elements (e.g., of La, Sr, Bi, etc.), residing on the edge of the structure for its stabilization with less effect on the catalytic activity. B as a smaller cation consists of transition metal that is surrounded by octahedral of oxygen anions, functioning as the main catalytic active centers. Their structure is schematically shown in Fig. 2.4b. The microstructure of mixed oxide catalyst is beneficial for their oxygen mobility and catalytic activity [75]. The presence of defect structure in oxygen vacancies, the existence of unusual valence and the availability of reversibly released oxygen have been considered relevant to the enhanced catalytic activity, even comparable to that of noble metal catalysts [76,77]. It can be explained by the fact that the oxygen vacancies are directly relevant to the adsorbed oxygen species over the catalyst surface. The more oxygen vacancies, the more adsorbed oxygen formed over the surface, leading to the higher catalytic activities in methane oxidation. A recent work reported by Miao et al. [78] reveals that more active oxygen species could be obtained using La(Mn, Fe)O$_{3+\lambda}$ perovskite

catalyst, and the catalytic activity of CMC thereby was significantly improved. The cation-substitution of perovskites effectively increases the oxygen vacancies by varying the distribution of B oxidation state [79,80]. Different aspects of perovskites have been addressed in several review papers, including the structure, synthesis and applications [53,59,81], the acid-base catalytic properties of perovskites [82], and the lanthanum-based perovskites [83]. The mechanism and kinetics may be found in the book of Granger et al. [84].

A lower calcination temperature is required for the perovskite phase than the hexaaluminate phase [85]. Perovskite catalysts are featured by their high thermal stability as well as the improved specific surface area, displaying a better catalytic activity in CMC. The higher catalytic performance is mainly ascribed to the foreign-cation substitution, the produced oxygen lattice and the deficiency over catalyst surface. A promising direction of improvement is designing perovskite catalysts with featured morphologies (e.g., nano-sized, porous, hollow), favoring their potential industrial applications.

2.2.1.2 Noble metal catalysts

Noble metal catalysts have been most intensively investigated for CMC, owing to their high catalytic activity at low temperatures [57,86-88]. Their basic structure is shown in Fig. 2.4c. Pd, Pt, Rh, Au and Co as the active component have been widely studied in the literature. Among them, Pd and Pt-based catalysts were reported as the most active one by far. Various support materials, such as ZrO_2, CeO_2, Al_2O_3, SnO_2, TiO_2, were considered. The base/acid properties of the support affect the catalytic activity by interacting with the oxidized/metallized state of noble metals. It was reported that the decreased acidity strength of Al_2O_3 support (with Pd as the active component) could enhance the performance of CMC [89]. Moreover, the introduction of additives (e.g., of La, Mn, Ce, Mg, V) could stabilize the catalyst support and active sites, and prolong the catalyst life. It has been reported by Farrauto et al. [90,91] that the CeO_2 addition is favorable to prevent the catalyst deactivation. The PdO species on the catalyst surface thereby are stabilized due to the increased temperature of PdO decomposition. Moreover, the improved storage and exchange of oxygen species in the presence of CeO_2 effectively promote the Pd reoxidation, resulting in a higher catalytic performance [92]. The recent study by Toso et al [93] illustrated that the stability of $Pd/Ce_{0.75}Zr_{0.25}O_2$ catalyst exposure to the water was improved by well-dispersed small Pd nanoparticles. More detailed reviews can be found in the literature [17,18,41].

The formation of active sites is mainly dependent on the support composition, properties, and

the preparation method. With respect to Pd and Pt-based catalysts, Pd is supposed to be superior to Pt, not only for the CMC but also for the oxidation of higher alkanes and olefins [94]. It is commonly considered that Pd in the oxidized state (PdO) is the most active and stable (up to 800 °C) [95]. Farrauto et al. [90] proposed that at least two different PdO species were present on the Al_2O_3 support. Dispersed PdO decomposed in a temperature range between 750 and 800 °C, whereas crystalline PdO decomposed from 800 to 850 °C. Hicks et al. [96] identified at least two different phases by infrared spectra. The crystalline palladium with a smaller size presented 10 to 100 higher catalytic activity than dispersed PdO phase. Similarly, the Pt crystalline phase has a higher catalytic activity than that in the dispersed PtO_2 phase due to the formation of chemisorbed oxygen in the crystalline phase [96].

Moreover, bi- or trimetallic catalysts have been reported to have higher catalytic activity and stability compared to monometallic ones [97-101]. For example, $Pd-Pt/Al_2O_3$ catalyst is more active and stable than Pd/Al_2O_3 [102,103]. It has been reported that Pt-Pd catalysts showed a higher activity even than Pd-Ag, Pd-Co, Pd-Ni and Pd-Rh over the Al_2O_3 support [97]. A better synergetic effect and the formation of bi-metal structure have proved to improve the catalyst activity and life-time. Other factors such as the support structure, the particle size and the surface morphology also have significant influence on the catalytic performance. More details on the influence of these factors can be found in the references [19,104-106].

The electrochemical field-assisted CMC is a relatively novel direction in recent years owing to the synergetic effect. Electrocatalysis process commonly involves the oxidation and reduction reactions via direct electrons transformation (i.e., the produced electrical current). Electrolytes as promoting species can modify the electronic properties of the catalyst surface via the formation of favorable bonds between reactants and the electrodes. The decrease of the activation energy through the synergetic effect between electric field and catalysis results in the enhancement of reaction rate for CMC [107-109]. Li et al. [109] reported that the reaction rate of CMC over the Mn_xCo_y catalyst was remarkably accelerated by the improved reducibility of Co^{3+} in the electric field, promoting the methane activation at low temperature. The light-off temperature ($T_{50} = 255$ °C) over $PdCe_{0.75}Zr_{0.25}O_x$ catalyst can be significantly reduced because of the enhanced reducibility of PdO_x species in electric field (e.g., 3 mA current) [110]. More details on the electrochemical-assisted CMC may be found in a recent reference [111].

Although noble metal catalysts present advantages such as high specific surface area, high dispersion of active component and mild reaction conditions, the catalyst deactivation (due to sintering, particle size growth, poisoning, etc.) and the high cost are the main limitations for

their large-scale application in the industry.

2.2.2 Shaping of catalyst

The shaping of catalysts could significantly affect the pressure drop and the reactant-catalyst mass transfer in the reactor. Fig. 2.5 shows a variety of catalyst shapes used for CMC. Fine powders are more suitable for being incorporated into minireactors or microreactors with higher catalyst surface area. However, powder catalysts (Fig. 2.5a) could lead to a high pressure drop if packed in a long (e.g., several meters) fixed-bed reactor, or possibly be blown out when used in a fluidized-bed reactor. To decrease the pressure drop, the catalyst is commonly shaped into larger bodies, e.g., pellet, round ball, cylindrical shape (Fig. 2.5b-d). Moreover, a sufficient mechanical strength of the catalyst support is essential for the catalyst's long-term structural durability.

Washcoated catalysts have received an increasing attention owing to its high surface area, low pressure drop and better usage of catalyst. This type of catalyst is usually used in monolithic reactors (Fig. 2.5e) [112,113], foam reactors (Fig. 2.5f) [114,115], multichannel microreactors (Fig. 2.5g) [116-118] and tube reactors (Fig. 2.5h) [32,119]. The recent progress of washcoated and packed-bed microreactors is reviewed in the reference [50]. The washcoated catalyst is commonly deposited as a thin layer on structured surfaces using typically a dip-coating method [120]. Other methods, such as suspension method [118,121-123], sol-gel technique [124,125], chemical vapor deposition [126,127], physical vapor deposition [128,129] are also widely used. In our previous work [118], the preparation of a well-adhered $Pt/\gamma\text{-}Al_2O_3$ catalytic coating in microreactors has been elaborated by applying various binders, particle size, pH conditions, etc. The preparation of the suspension and the pretreatment of the substrate hosting the catalytic layer have to be adapted to obtain a high thermal stability and a well dispersion of the coating [116,118,130].
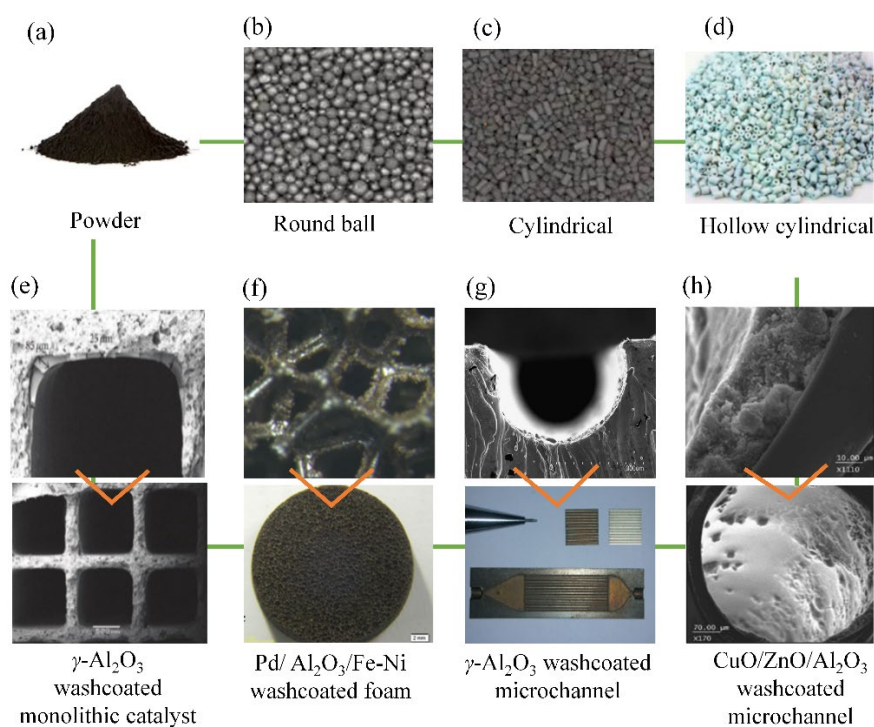
Fig. 2.5. Various shaping of catalysts. (a) Powder catalyst; (b) Pellet catalyst; (c) Round ball catalyst; (d) Ring shape catalyst; (e) SEM images of γ-Al$_2$O$_3$ washcoated layer on cordierite monolith [112]; (f) Microscopic image of Pd/Al$_2$O$_3$/Fe-Ni foam [114]; (g) SEM (scanning electron microscope) images of γ-Al$_2$O$_3$ washcoated microchannel [131]; (h) SEM images of CuO/ZnO/Al$_2$O$_3$ washcoated capillary microreactor [132].

Table 2.2 Comparison of main catalysts used for methane combustion.

Reference	Catalyst type	BET surface area (m^2 g^{-1}) [a]	Calcination temperature (°C)	Reaction temperature (°C)	Advantages	Disadvantages	Applications
[52]	Hexaaluminate	0-30	900-1300	< 1000	- High thermal stability - Doped cation substitution (improved catalytic activity) - Different oxygen species - Relatively low cost	- Low surface area - High light-off temperature	High temperature reaction (e.g., partial/complete oxidation of methane, N$_2$O decomposition)

[53,73]	Perovskite	0-30	700-1100	< 1000	- High thermal stability - Doped cation substitution - higher oxygen mobility and species - Relatively low cost	Ditto	Ditto
[18,40,41]	Noble metal (e.g., Pt, Pd, Rh)	> 100	450-600	< 600	- High catalytic activity - High surface area - Low light-off temperature	- Catalyst sintering - Relatively high cost	Low temperature reaction (e.g., partial/complete oxidation, methane steam reforming)

[a] Average specific surface area measured by BET (Brunauer, Emmett and Teller) method is shown here, but may vary depending on the preparation method.

2.3. Mechanism and kinetic study of CMC

Compared to other higher alkanes, methane is the most stable alkane molecule with high ionization potential (12.5 eV), low electron affinity (4.4 eV) and high C-H bond energy (434 kJ mol^{-1}), rendering it extremely difficult to be activated under mild conditions. A high reaction temperature (> 1400 ^{o}C) is often required for carrying out conventional methane flame combustion. Hence, mechanistic and kinetic studies are important for guiding the catalyst design and the process optimization in order to achieve an efficient combustion at relative low temperature levels (< 600 ^{o}C) [133-135]. The reaction has been reported to be zero order in oxygen and first order in methane [136]. The kinetic model and the elementary steps were elaborated in the literature [137-143], and the main kinetics parameters are summarized in Table 2.3.

Regarding the noble metal catalyst, a great number of studies have been devoted to revealing the mechanism of catalytic methane oxidation [48,144-146]. The classic reaction routes over noble metal catalysts are shown in Fig. 2.6 [147]. CH_4 molecules are first adsorbed on the catalyst and dissociated to the adsorbed methyl ($CH_3\cdot$) or methylene ($CH_2\cdot$) species, which further interact with the adsorbed oxygen, either to directly produce CO_2 and H_2O, or to form the adsorbed CO and H_2 via formaldehyde (HCHO) as the intermediate [148,149]. The adsorbed CO and H_2 further interact with the adsorbed oxygen to form the final product (CO_2 and H_2O) based on the reactant ratios (theoretically, partial oxidation occurs at O_2/CH_4 molar ratio < 2). The adsorbed CO is predominant with the increasing methane coverage, whereas CO_2 formation

is more favorable at high oxygen coverages. However, due to the swift dissociation of CO, the variation of the surface concentrations of methane and oxygen is negligible. Experimental measurements over Pt/Al$_2$O$_3$ catalysts have indicated that the reaction rate determining step was shifted from the oxygen desorption to the methane adsorption with the increasing catalyst surface temperature [141]. Given the higher methane adsorption energy than oxygen [150-152], at the beginning the oxygen adsorption reaction (O$_2$ + 2Pt(*) → 2O(*) + 2Pt; * is the molecule adsorbed on the surface), this rate determining step may be additionally due to the competitive adsorption of oxygen that inhibits the methane oxidation by excluding the weakly adsorbed methane on the active sites [147]. At high oxygen atom coverages, methane is converted through the proposed reaction (CH$_4$ + O(*) + Pt(*) → CH$_3$(*) + OH(*) + Pt). As a result, the surface temperature increases due to the release of the reaction heat. The number of the adsorbed oxygen atoms is generally decreased with the increasing temperature and the reaction of the methane adsorption (CH$_4$ + 2Pt(*) → CH$_3$(*) + H(*) + 2Pt) becomes more prominent. The light-off phenomenon thus happens once the favorable coverage of methane and oxygen on the catalyst surface is reached [133,153].
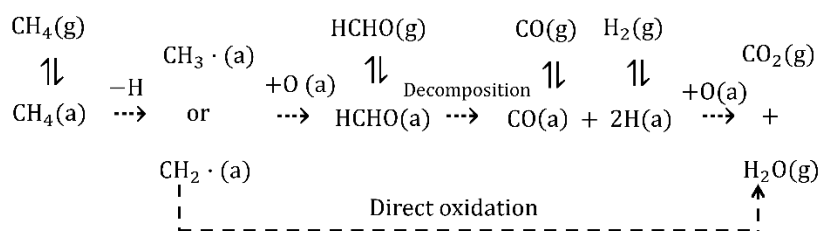
Fig. 2.6. Reaction routes of methane catalytic oxidation over noble metal catalysts. The bracket (a) indicates the adsorbed state and (g) the gas phase [147].

Three types of mechanism and the corresponding kinetic models have been proposed for CMC in the literature, including the Langmuir-Hinselwood mechanism [154-156], the Eley-Rideal mechanism [157] and the Mars-van Krevelen mechanism [158-161]. The rate-determining step for both the Langmuir-Hinselwood and Eley-Rideal mechanisms is commonly considered as the superficial reaction. The reaction rate is associated to the electronic properties of transition ions over the catalyst surface. On the contrary, the CMC is considered as the interfacial reaction by the Mars-van Krevelen mechanism; the reaction rate is mainly correlated to the lattice oxygen vacancies.

Regarding the Langmuir-Hinselwood mechanism, the molecules of both gas phase reactants are adsorbed on the catalyst surface and react via surface diffusion. The formed products are then desorbed from the catalyst surface to complete the reaction. The kinetic models of CMC

proposed by Trimm and Lam [162] over Pt/Al_2O_3 catalyst well fit the Langmuir-Hinselwood mechanism, indicating that both the adsorbed methane and oxygen were involved in the reaction. Their study confirmed that the temperature increase was mainly to change the reaction path from the oxygen adsorption to methane adsorption [162]. However, Jodłowski et al. [163] observed that methane over $Co-Pd/\gamma-Al_2O_3$ catalyst was only adsorbed with pre-adsorbed oxygen over the surface (under oxygen-rich conditions) by using the DRIFT (diffuse reflectance infrared spectroscopy), suggesting that the Langmuir-Hinshelwood mechanism should not be recommended.

The Eley-Rideal mechanism suggests that only one gas phase reactant has to be adsorbed onto the catalyst surface. The adsorbed reactant then interacts with the other reactant which is still in the gas phase. Subsequently, the formed products are desorbed from the catalyst surface. Seimanides and Stoukides [157] reported that this mechanism could well predict the CMC over Pd/ZrO_2 catalyst in the range of 450 to 600 ^{o}C. It is likely to be the only adsorbed atomic oxygen that reacts with the gaseous methane. Veldsink et al. [164] illustrated that the Eley-Rideal mechanism was adequate to describe the experiment data, and the reaction rate equation over $CuO/\gamma-Al_2O_3$ catalyst was proposed without the limitation of heat and mass transfer.

The Mars-van Krevelen mechanism is widely supported by a large amount of experimental results on CMC [165,166]. Different from the above two mechanisms, the Mars-van Krevelen mechanism suggests that the adsorbing surface is an active participant. Firstly, one of the reactants in the gas phase forms a chemical bond with the catalyst surface in the form of a thin layer (e.g., of metal oxide). Then, the remaining gas phase reactant can interact with the chemically bonded reactant, leaving behind a vacancy upon desorption of the products. However, it is not easy to distinguish between Mars-van Krevelen and Eley-Rideal mechanisms because of the existence of both the lattice and adsorbed oxygen species on the catalyst surface. Pfefferle et al. [160] further reported that one ^{16}O atom (lattice phase) in PdO was bounded to two Pd atoms, using the in-situ technology of isotopically labeled reaction. It was found that the ^{16}O atom in PdO was responsible to oxidize methane rather than the adsorbed ^{18}O atom in the gas phase. This conclusion is in line with the findings of Au-Yeung et al. [167]. In addition, the variation in the oxidation valence of Pd plays an important role in the reaction, indicating that the Mars-van Krevelen mechanism is more adequate to be used for the CMC [57,168,169]. Similarly for $NiCo_2O_4$ perovskite catalyst, Tao et al. [77] reported that the chemisorbed lattice oxygen played an important role. The oxidized products (CO_2 and H_2O) were generated by the competitive adsorption, and surface vacancies subsequently left behind by the fast re-oxidation

on the catalyst surface. Note that the DRIFT associated with Raman and X-ray fluorescence spectroscopies has been applied as important in-situ technologies by Jodłowski et al. [163] for the CMC over Co-Pd/Al_2O_3 catalyst. The proposed mechanism is slightly different from the Mars-van Krevelen mechanism, in that only the adsorbed active oxygen species on the catalyst surface was responsible to oxidize methane instead of the bulk oxygen atoms. Furthermore, the presence of -OCH_3 species was detected, rather than HCHO and H_2 in the gas phase. These results are also supported by other studies [170,171].

Therefore, there is no unanimous mechanism so far to fully elaborate the CMC, given the whole processes being rather complex and strongly dependent on the reaction conditions and used catalysts [172,173]. The Mars-van Krevelen mechanism seems to be more widely accepted than the Langmuir-Hinselwood and Eley-Rideal mechanisms. In this respect, more in-depth understanding is still needed to better elucidate the reaction pathway [174]. More details on the reaction mechanisms may be found in the literature [138-143].

Table 2.3 Main literature results on kinetic parameters for CMC.

Reference	Catalyst	Reactant	Temperature (^{o}C)	Conversion (%)	E_a (kJ mol^{-1})	Reaction rates (μmol g^{-1} min^{-1})
[19]	0.5 % Pt/Al_2O_3	O_2/CH_4 = 2:1	350-425	1.8-13.7	101 ± 10	
	1 % Pt/Al_2O_3				104 ± 1.0	
	2 % Pt/Al_2O_3				91.4 ± 5	
	4 % Pt/Al_2O_3				98.1 ± 11	
	0.5 % Pt/Al_2O_3	O_2/CH_4 = 5:1	350-500	0-28	108 ± 1.5	
	1 % Pt/Al_2O_3				121 ± 10	
	2 % Pt/Al_2O_3				100 ± 5	
	4 % Pt/Al_2O_3				83.8 ± 5	
[175]	$NiFe_2O_4$	CH_4: 3 vol.% O_2: 7.2 vol.%	350-400	~2-13	210.8	
[176]	$Co_{(0.95)}ZrO_2$		750-800		23	11880
	$Co_{(1.9)}ZrO_2$		750-800		26	18000
	$Co_{(1.9)}La/ZrO_2$		770-820		29	52200
[177]	Ru/γ-Al_2O_3	CH_4: 0.8 vol.%	361	10 %	116	2.53
	Ru_{90}-Re_{10}/γ-Al_2O_3	O_2: 22 vol.%	337	10 %	104	5.17
	Ru_{75}-Re_{25}/γ-Al_2O_3	N_2: 78 vol.%	359	10 %	117	2.00
[178]	γ-Al_2O_3	CH_4: 0.5-3 vol.%				
	Cu/γ-Al_2O_3 (600 ^{o}C)		525	50 %	21200	1.11×10^{11}
	Cu/γ-Al_2O_3 (800 ^{o}C)		540	50 %	21330 Cal mol^{-1}	0.91×10^{11}

Reference	Catalyst	Reactant	Temperature (°C)	Conversion (%)	E_a (kJ mol^{-1})	Reaction rates (µmol g^{-1} min^{-1})
[179]	AuPd$_{1.95}$/CoCr$_2$O$_4$	CH$_4$: 2.5 vol.%	305	10 %		60
		O$_2$: 20 vol.%	353	50 %		
		N$_2$: 77.5 vol.%	394	90 %		
[180]	ZrO$_2$/LaMnO$_3$	CH$_4$: 3 vol.%	417	10 %	19.3	3.30
		O$_2$: 10 vol.%	539	50 %		
		N$_2$: balance	632	90 %		
[181]	Cu-Cr/CuCr$_2$O$_4$	air/CH$_4$ = 30	550		105.9 ± 10.4	
			600		118.2 ± 0.6	

2.4. Effect of operational conditions on CMC

In this section, main factors that should be carefully assessed are reviewed so as to determine the appropriate working conditions for CMC, including the temperature, the ratio of methane to oxygen, the flow rate, the reactant composition and the pressure. The reaction behavior addressed in this section, unless otherwise specified, is assumed to be intrinsic. A summary of the studies over various catalysts and the key influential factors can be found in Table 2.4.

2.4.1. Effect of temperature

In general, the intrinsic reaction rate for CMC is correlated to temperature and activation energy according to the Arrhenius equation [182,183]. The reaction rate presents a great increase with the increasing reaction temperature.

Light-off temperature is one of the most crucial parameters used to indicate the catalyst activity [116,184,185]. Fig. 2.7 shows the reaction regime as a function of the temperature. At the beginning, the temperature over the catalyst is low and thus the reaction rate is limited by the intrinsic kinetics (regime A-B). The light-off is commonly defined by the regime where the temperature has no significant change when the conversion is increased from 10 %, 20 % up to 50 % (regime B-C) [186]. As light-off happens at comparatively high temperature levels, the intrinsic reaction rate rapidly increases but gradually the mass transfer rate cannot keep up with (regime B-C). Hence, the overall reaction rate tends to be limited more by the mass transfer rate. Upon further increase of the reaction temperature, the intrinsic reaction rate is increased so fast that the reaction falls in the mass transfer controlled regime (regime C-D). In this regime, the rate of increase in the overall reaction rate becomes slower. Eventually at substantially high temperature levels, the homogeneous combustion of methane dominates (regime D). The latter two regimes impose high requirements on the reactor design in terms of maintaining the

catalyst stability and enhancing the mass and heat transfer rates. The effect of high working temperatures on the shortened life-time due to the catalyst sintering should be considered, especially for noble metal catalysts.
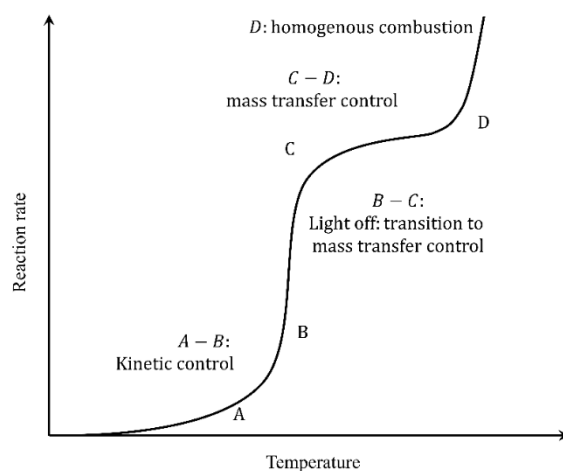
Fig. 2.7. Reaction rate as a function of temperature [186].

As for wall-coated plate-type/microchannel reactor, the temperature distribution along the catalytic reactor commonly displays a rapid increase at the entrance region, and a smooth decrease along the reactor length thereafter, as shown in Fig. 2.8. This is because that methane is mainly converted at the front section of the reactor [187]. However, the peak temperature region moves slowly towards the downstream with the increasing oxygen/methane ratio. The variation of temperature along the reactor mainly depends on the reactant flow pattern and the reactor structure, which will be elaborated in the following section 5.
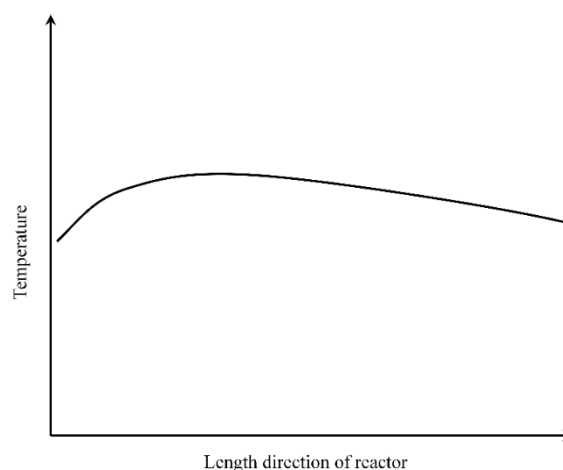
Fig. 2.8. Temperature distribution along the reactor length.

Moreover, the pollutant emission could be significantly affected by the operational temperature. With the presence of N_2 in the reactant feed, it was reported that NO_x emission showed a

growing trend with the increasing temperature [188]. The formation of CO is often due to the incomplete methane combustion under low temperatures and/or with a methane rich mixture.

In addition, it is worth noting that the catalyst deactivation is significantly influenced by the operational temperature. For instance, the active PdO phase is decomposed to the less active metallic palladium (PdO → Pd) at above 800 ᵒC, followed by the agglomeration and deactivation of catalysts [95]. It is thus essential to maintain the operational temperature below the thermal decomposition temperature of PdO. Another solution is to increase the decomposition temperature by optimizing the catalyst, e.g., by introducing metal oxides [189]. Farrauto et al. [90] pointed out that the addition of ZrO_2 into PdO/Al_2O_3 catalyst exhibited a superior synergistic effect between the temperature hysteresis and the active site reformation. The decomposition temperature of PdO was thus increased to ca. 900 ᵒC. In order to regenerate the catalyst, Farrauto et al. [90] suggested that the reoxidation temperature of metallic Pd occurred at ca. 650 ᵒC, and methane conversion increased after reoxidation process [90]. Another reason causing the catalyst deactivation at low temperatures (e.g., below 450 ᵒC) may be the overwhelming accumulation of hydroxyl group over the catalyst surface [190]. It hinders the migration and exchange of the active oxygen species between the catalyst support and active sites (PdO/Pd), resulting in the catalyst sintering. This is further confirmed by the water vapor effect on the methane conversion to be discussed in the section 2.4.4.

2.4.2. Effect of space velocity and residence time

Theoretically, the methane conversion presents an inverse proportion to the space velocity, as shown in Fig. 2.9. It was observed that the methane conversion at 400 ᵒC increased from 72 % to 100 % over Au-Pd catalyst when decreasing the space velocity of reactants from 40 000 to 10 000 mL g_{cat}^{-1} h^{-1} [179] (cf. the detailed experimental data in Table 2.4). A similar tendency over various catalysts has also been reported by other researchers [88,114]. This can be theoretically explained by the fact that the more accessibility of reactants (at longer residence time) over the active sites of catalyst favors the conversion of the adsorbed methane molecules. However, the side reactions and coke deposition are more likely to occur under long residence time [191].
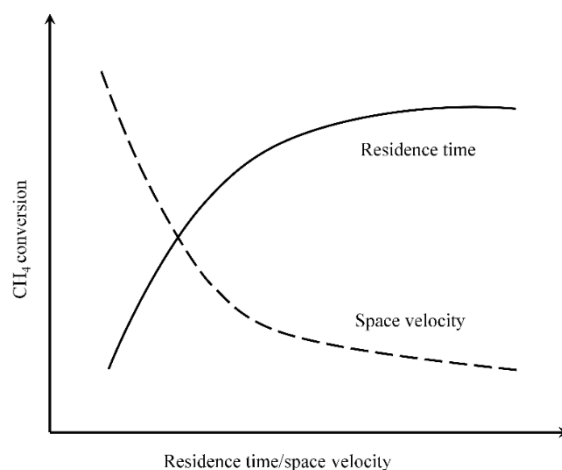
Fig. 2.9. CH$_4$ conversion as a function of the space velocity or residence time.

The methane conversion is directly relevant to the intrinsic reaction kinetics and mass transfer. The internal mass transfer mostly depends on the catalyst properties (e.g., diffusion in the pore structure, size and volume). The external mass transfer from gas phase to the catalyst surface is limited by the residence time (i.e., the flow rate of reactants). As for the exothermic reaction, the effect of the temperature gradient on the reaction rate should also be considered. It has been reported that at a certain temperature, a steady-state conversion rate could be reached with the increasing flow rate. After that, a further increase in the flow rate could not have any influence on the methane conversion. The mass transfer limitation is thus negligible at higher flow rates [192].

Moreover, in order to obtain sufficient reaction heat for heating purposes, higher reactant space velocity is required, but usually accompanied with a lower methane conversion. Hence, a compromise between the space velocity and the methane conversion should be reached for a certain application.

2.4.3. Effect of oxygen to methane molar ratio

The selectivity variation of products strongly depends on the molar ratio of oxygen to methane. Mouaddib et al. [193] investigated the effect of oxygen to methane molar ratio in the range of 4 to 0.66 over Pd/Al$_2$O$_3$ catalyst. It was observed that CO was formed under oxygen deficient conditions (O$_2$/CH$_4$ < 2) due to the side reaction of methane steam reforming. And CO became a main product when O$_2$/CH$_4$ molar ratio reached 0.66 [193]. Similarly, Lee et al. [186] reported that CO was formed over Pt/Al$_2$O$_3$, Pd/Al$_2$O$_3$ and Rh/Al$_2$O$_3$ catalysts in the presence of oxygen deficient mixtures as feedstock. The selectivity of CO also depended on the reaction temperature. With the increasing reaction temperature, the CO selectivity constantly increased

and became a main product under low O_2/CH_4 molar ratio. But the methane conversion was independent to the presence of CO in the feedstock [186].
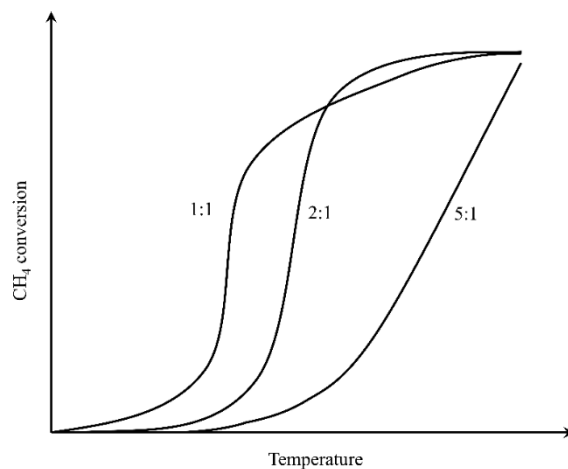
Fig. 2.10. CH_4 conversion as a function of temperature under different oxygen-to-methane molar ratios over Pt/Al_2O_3 catalyst [19].

Burch et al. [19] investigated the effect of different molar ratios of oxygen to methane on Pt/Al_2O_3 and Pd/Al_2O_3 catalysts. Pt/Al_2O_3 catalyst became more active from the oxygen-rich (O_2/CH_4 = 5:1) condition to methane rich (O_2/CH_4 = 1:1) condition, because the less oxidized platinum was more active than the oxidized platinum. As for Pt-based catalyst, Drozdov et al. [194] further explained that a weaker bond existed between oxygen and metallic platinum than that with platinum oxides. Thus, Pt-based catalyst is less active in oxygen-rich mixtures. On the contrary, as for Pd-based catalyst, it has been found that the oxygen is weakly bound to palladium oxides compared with metallic palladium [194]. Thus, the Pd-based catalyst is more active in oxygen-rich mixture [19,136].

The methane conversion at different oxygen-to-methane molar ratios does not display the same augmentation as the reaction temperature increases. More interestingly, the light-off phenomenon was observed to be significantly influenced by the oxygen to methane molar ratio and the resulted degree of reactant surface coverages [19]. It was found that the methane conversion over Pt/Al_2O_3 increased with the decreasing oxygen-to-methane molar ratio (e.g., from 5:1 to 1:1 as shown in Fig. 2.10; cf. detailed experimental results listed in Table 2.4) at lower temperatures (ca. 300 - 425 °C, in terms of different Pt loading) [19]. At higher temperatures (ca. 450 - 550 °C), the methane conversion at such a molar ratio of 1:1 became lower than that at 2:1, due to the insufficient oxygen supply, and the light-off was observed in the latter case. This phenomenon could be explained by the fact that the favorable concentration

of CH_4 and O_2 over the catalyst surface and/or the more significant local heat release greatly accelerate the reaction rate. However, no light-off was found under an oxygen-to-methane molar ratio of 5:1 because the excessively adsorbed oxygen resulted in a non-optimized surface coverage of methane, eventually hindering the light-off. The competitive adsorption between the adsorbed methane and oxygen species could affect the methane conversion. The lower methane conversion at the case of 5:1 molar ratio (Fig. 2.10) could be explained by the fact that more adsorbed oxygen species over the catalytic surface suppress the methane absorption due to the high methane adsorption energy [147,150].

Regarding the pollutant emissions, a lean reactant mixture is preferred in order to lower the emissions of CO, NO_x and the unburned hydrocarbon [195]. It has been reported that CO was detected at a methane concentration higher than 9.5 vol.% and carbon deposition occurred on catalyst surfaces at a methane concentration above 26.5 vol.% [196].

2.4.4. Effect of (synthetic) natural gas composition

Besides methane, natural gas is commonly composed of varying amounts of higher alkanes (e.g., ethane, propane) and other species depending on the resources. In this section, the effect of H_2S, H_2O, NO and CO_2 on the catalytic methane conversion is discussed, more details can be found in the references [179,197].

Noble metal catalysts are easily poisoned when exposed to natural gas containing sulfur compounds (Fig. 2.11a). For instance, the irreversible deactivation by SO_2 might be attributed to its occupation of the active sites, and/or the transformation of the highly active compound PdO on the catalyst surface to less active $PdSO_3$ or $PdSO_4$. Similar results were also reported in the literature [198,199]. The highly challenging issue of the resistance to poisoning by sulfur containing compounds present in trace amounts in the natural gas (odorizer) should be fully addressed. Developing catalysts with improved resistance to sulfur poisoning and possible desulfurization pretreatment are possible measures.

The presence of water vapor acts as an inhibitor for CMC [165,200]. It was observed that the methane conversion over the $Au-Pd/Co_3O_4$ catalyst dropped remarkably when water vapor was introduced, but this process is reversible when the water vapor is removed (Fig. 2.11b) [201].Specifically, the hydroxyl group was formed by reaction of the chemisorbed oxygen species with the water vapor over the catalyst surface, preventing thereby the exchange of the oxygen species between the active sites and the support [190,202]. Moreover, the hydroxyl group also hindered the desorption of CO_2 and H_2O over the catalyst surface due to the

competitive adsorption. The kinetic study by Geng et al. [202] illustrated that the reaction order with respect to methane decreased from 1.07 to 0.86 after the water vapor addition, and the reaction order in water also decreased from -0.72 to -0.95 with the increasing water concentration. Thus, improving the catalyst stability in the presence of water vapor becomes one important challenge to deal with wet CMC. Recently, Toso et al. [93] reported that the solution combustion synthesis could improve the stability and water resistance of Pd-ceria and Pd-ceria-zirconia catalysts compared to the traditional impregnation method. Ciuparu et al. [203] also suggested that the influence of water vapor became insignificant at above 723 K.

Sadokhina et al. [204] observed the enhanced activity with NO addition under wet conditions. This can be explained by the reaction between NO and hydroxyl species to form HNO_3 on the catalyst surface, compensating the inhibition effect of water addition.

The reversible inhibition effect of CO_2 addition is depicted in Fig. 2.11c. The negative influence of CO_2 addition on the methane conversion is ascribed to the accumulation of carbonate species on the catalyst surface, thus preventing a further adsorption of CH_4 and O_2 over the surface [201] (cf. detailed experimental data in Table 2.4).
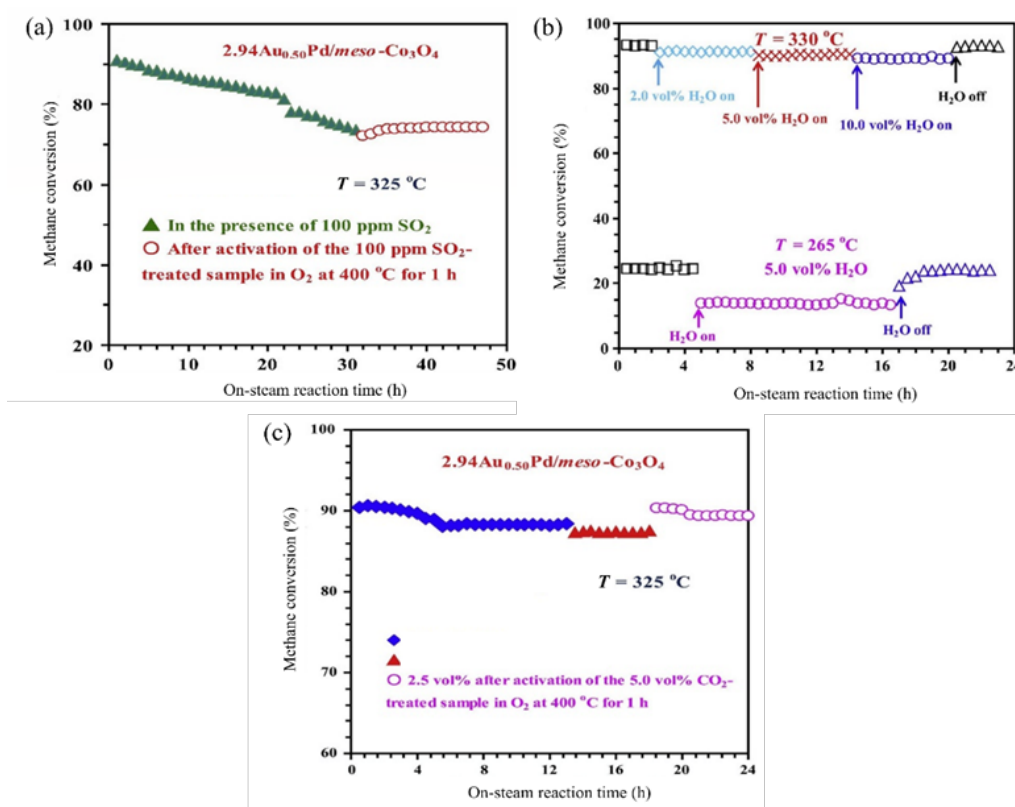
Fig. 2.11. Effect of (a) SO_2 (b) H_2O (c) CO_2 on the methane conversion. T in figures indicated the reaction temperature. Conditions: Au-Pd/ Co_3O_4 catalyst, space velocity at 20 000 mL g_{cat}^{-1} h^{-1} [201].

2.4.5. Effect of operating pressure

Most published studies have performed the CMC at the atmospheric pressure. High working pressure conditions (up to 30 bar or higher) are primarily applied for gas turbine purpose.

The methane conversion decreased (from ~7.2 % to ~3.5 %) with the increasing pressure (from 5 bar to 15 bar) over Pd-Pt/Al_2O_3 catalyst (cf. more details listed in Table 2.4) [103]. Moreover, it was reported that the effect of working pressure varied with the temperature [205]. At lower temperatures (500 - 600 ^{o}C), an increase in the pressure led to the decreased methane conversion and the lower combustion efficiency. In this case, the higher specific surface area was commonly required at high pressures so as to obtain a higher conversion. At higher temperatures (> 700 ^{o}C), homogenous combustion takes place. A higher combustion efficiency could thereby be obtained with an increasing pressure [205,206], probably due to the increasing mass throughputs [207].

Table 2.4 Summary of catalysts and reaction conditions for methane oxidation in various reactors.

Ref./ year [a]	Catalyst	Preparation method	BET surface area (m² g⁻¹)	Reactor (material, size)	Reactant	Total flow rate (mL min⁻¹)	Space velocity	T_{10} (°C) [b]	T_{50} (°C) [b]	T_{90} (°C) [b]	Tx (°C) [b] X=conv%	Remarks
Hexaaluminate catalyst												
[65] 1989	$BaAlAl_{11}O_{19-\alpha}$	Hydrolysis of metal alkoxides	15.3	Fixed-bed (quartz)	CH_4: 1 vol.% In air	800	48 000 h⁻¹	710		730		- Mn-substituted catalyst presented the best catalytic performance
	$BaCrAl_{11}O_{19-\alpha}$		15.7					700		770		
	$BaMnAl_{11}O_{19-\alpha}$		13.7					540		740		
	$BaFeAl_{11}O_{19-\alpha}$		11.1					560		780		
	$BaCoAl_{11}O_{19-\alpha}$		15.2					690		720		
	$BaNiAl_{11}O_{19-\alpha}$		11.1					710		770		
[208] 2000	BHA	Sol-gel	< 20	Flow reactor	CH_4: 1 vol.% In air		60 000 h⁻¹	710		~750		- Reverse microemulsions method presented a higher surface area and an excellent catalytic activity
	BHA	Reverse-micro emulsion	40-160					590	~650	~750		
	CeO_2-BHA							~400		600		
[209] 2007	$BaAl_{12}O_{19-\alpha}$	Co-precipitation and supercritical drying		Fixed-bed (quartz, i.d. 10 mm)	CH_4: 1 vol.% O_2: 4 vol.%, N_2: balance		15 000 h⁻¹	630	750	841		- Introduction of CeO_2 increased the surface area and enhanced the catalytic activity
	$BaMnAl_{11}O_{19-\alpha}$							470	580	655		
	$BaMn_2Al_{10}O_{19-\alpha}$							433	537	619		
	$CeO_2/BaAl_{12}O_{19-\alpha}$		83.5					535	618	690		
	$CeO_2/BaMnAl_{11}O_{19-\alpha}$		55.9					468	576	645		
	$CeO_2/BaMn_2Al_{10}O_{19-\alpha}$		47.8					426	534	611		

	$CeO_2/BaFeAl_{10}O_{19-\alpha}$		75.3					436	530	597	

Perovskite catalyst

Ref / Year	Catalyst	Method		Reactor	Feed gas		GHSV				Comments
[210] 2005	0 wt. %Pd/LaMnO$_3$ 2ZrO$_2$	Incipient wetness impregnation	29.82	Fixed-bed (quartz, i.d. 4 mm)	CH$_4$: 2 vol.% O$_2$: 14 vol.% He: balance	50			520		- ZrO$_2$ introduction increased the support thermal resistance
	0.5wt.%Pd/LaMnO$_3$ 2ZrO$_2$		28.88						509		
	1 wt. %Pd/LaMnO$_3$ 2ZrO$_2$		29.30						485		
	2 wt. %Pd/LaMnO$_3$ 2ZrO$_2$		28.64						432		
	3 wt. %Pd/LaMnO$_3$ 2ZrO$_2$		27.43						461		- Incipient wetness impregnation exhibited a higher catalytic performance
	0.5 wt. %Pd/La$_2$Zr$_2$O$_7$	Solution combustion							531		
	1 wt. %Pd/La$_2$Zr$_2$O$_7$								518		
	2 wt. %Pd/La$_2$Zr$_2$O$_7$								476		
	3 wt. % Pd/La$_2$Zr$_2$O$_7$								498		
[211] 2010	La$_2$CuO$_4$ -260	Co-precipitation		Fixed-bed (quartz, i.d. 4 mm)	CH$_4$: 2 vol.% O$_2$: 20 vol.% N$_2$: balance		50 000 mL g^{-1} h^{-1}	548	662	739	- An enhanced activity of La$_2$CuO$_4$ due to the Sr^{2+} doping
	La$_2$CuO$_4$ -220							587	677	759	
	La$_2$CuO$_4$ -180							625	722	766	- Excellent performance are attributed to more adsorbed oxygen species, better reducibility and single crystallinity.
	LaSrCuO$_4$ -260							482	620	667	

[Ref]/Year	Catalyst	Synthesis method	S_{BET}	Reactor	Reaction conditions		GHSV			Remarks
[212] 2012	$BaZr_{(1-x)}Me_xO_3$	Modified citrate method		Fixed-bed (quartz, i.d. 7 mm)	CH_4: 0.5 vol.%	150	150 000 mL g^{-1} h^{-1}			- Catalytic performance of substituted transition metals: Pd, Ru > Rh > Co > Mn > Ni
	Me = 5% Rh		15.3		O_2: 4 vol.%			625	T_{20} = 530	
	Me = 5 % Pd		18.3		N_2: 16 vol.%			600	T_{20} = 520	
	Me = 15 % Rh		7.3		He: balance			660	T_{20} = 570	
	Me = 20 % Rh		13.1					650	T_{20} = 570	
	Me = 2.73 % Mn		10.7					710	T_{20} = 635	
	Me = 2.91 % Ni		n.a.					790	T_{20} = 690	
	Me = 5.92 % Ni		n.a.					700	T_{20} = 625	
	Me = 4.91 % Ru		5.6					600	T_{20} = 520	
	Me = 1 % Pt		3.1					730	T_{20} = 645	
	Me = 2.93 % Co		13.8					640	T_{20} = 570	
	Me = 5.86 % Co		38.5					775	T_{20} = 675	
	$BaZrO_3$		6.3							
[213] 2014	$MgCr_2O_4$	Sol-gel	1.1	Fixed-bed	CH_4: 1 vol.% In air		48 000 mL g^{-1} h^{-1}	400	684	- $MgCr_2O_4$ exhibited a higher activity than $CoCr_2O_4$ due to the presence of Cr^{6+} and bulk structure
	$CoCr_2O_4$		0.4					480	750	
	MgO							618.8	742.4	
	Cr_2O_3							593.6	736.7	

Ref / Year	Catalyst	Method	SSA	Reactor	Feed		GHSV					Comments
[77] 2015	$NiCo_2O_4$	Co-deposition precipitation	218.7 (calculated surface area with average size of 4.5 nm)	Fixed-bed (quartz, i.d. 6 mm)	CH_4: 5 vol.% O_2: 25 vol.% Ar: balance	200	24 000 mL g^{-1} h^{-1}	~230	~262		T$_{100}$: 350	- $NiCo_2O_4$ showed a higher catalytic performance than Pd/Al_2O_3 under the same conditions
					CH_4:0.2vol.% O_2:5 vol.% CO_2:15vol.% H_2O:10vol.% Ar: balance			~240	~300		T$_{100}$: 425	
					CH_4:0.2vol.% O_2:5 vol.% NO:0.15vol.% H_2O:10vol.% Ar: balance			~300	~335		T$_{100}$: 475	
[214] 2016	3DOM $La_{0.6}Sr_{0.4}MnO_3$	Templating method	32.4	Fixed-bed (quartz, i.d. 6 mm)	CH_4: 5 vol.% O_2: 30 vol.% Ar: balance	42.8	50 000 mL g^{-1} h^{-1}	344	384	508		- Au addition weakens the bonding between intermediates and Pd atoms, improving the adsorbed oxygen over catalyst surface
	1Au/3DOM $La_{0.6}Sr_{0.4}MnO_3$		32.6					338	375	402		
	1Pd/3DOM $La_{0.6}Sr_{0.4}MnO_3$		32.0					323	358	378		
	1AuPd/3DOM $La_{0.6}Sr_{0.4}MnO_3$		33.6					304	350	382		
	2AuPd/3DOM $La_{0.6}Sr_{0.4}MnO_3$		33.3					280	331	354		
	3AuPd/3DOM $La_{0.6}Sr_{0.4}MnO_3$		33.8					265	314	336		
[215] 2016	$LaFeO_3$	Nitrate-citrate combustion		Fixed-bed	CH_4: 5 vol.% O_2: 50 vol.%	1000	240000 h^{-1}		~650		T$_{25}$: 600	- Perovskite nanopowder synthesized by
	$La_{0.8}Sr_{0.2}FeO_3$								~550		T$_{65}$: 600	

Ref / Year	Material	Method / Role	BET	Reactor	Feed gas		GHSV	T	T	T	T	Notes
	$La_{0.6}Sr_{0.4}FeO_3$	synthesis		(quartz)	N_2: 45 vol.%				~640		T_{35}: 600	solution combustion
												- Partial substitution of La^{3+} by Sr^{2+} greatly increased the catalytic activity
[216] 2018	CeO_2	Support	28.9	Fixed-bed (stainless steel, i.d. 8 mm)	CH_4: 10 vol.% O_2: 25 vol.% Ar: balance		24 000 mL g^{-1} h^{-1}	523	641			- Catalytic activity of different methods: CeO$_2$ (Plasma treatment) > CoAlO$_x$/CeO$_2$ (Impregnation combustion) > CoAlO$_x$/CeO$_2$ (Microwave in-situ grown) > CoAlO$_x$/CeO$_2$ (Impregnation)
	$CoAlO_x/CeO_2$	Impregnation	20.1					460	511	614		
	$CoAlO_x/CeO_2$	Microwave in-situ grown	28.4					418	481	601		
	$CoAlO_x/CeO_2$	Impregnation combustion	27.7					405	464	590		
	$CoAlO_x/CeO_2$	Plasma treatment	27.2					335	415	580		
[76] 2018	$LaMnO_3$ $La_{0.8}Sr_{0.2}MnO_3$	Sol-gel	11 27	Fixed-bed (quartz)	CH_4: 0.6 vol.% O_2: 21 vol.% Ar: balance	133	40 000 h^{-1}	313 270	379 333	443 397		-Effect of different preparation methods on the catalytic performance: - Chemical combustion ≈ Solvothermal > Sol-gel > Spray-pyrolysis - Catalytic performance 1 % Pd/Al$_2$O$_3$ > LaMnO$_3$/La$_{0.8}$Sr$_{0.2}$Mn
		Chemical combustion	15 18					237 266	351 329	375 389		
		Microwave-assisted solvothermal	16 19					269 280	331 363	392 439		
		Spray-										

Ref / Year	Catalyst	Method	S_{BET}	Reactor	Feed gas		GHSV	T_{10}	T_{50}	T_{90}	Remarks
	pyrolysis										O_3
			6					330	410	496	> 0.5% Pt/Al$_2$O$_3$
			11					359	452	537	
	0.5 wt.% Pt/Al$_2$O$_3$							278	446	499	
	1 wt.% Pd/Al$_2$O$_3$							205	252	296	
[217] 2018	Bulk LaMnAl$_{11}$O$_{19}$	Polymethyl methacrylate templating method	12	Fixed-bed (quartz, i.d. 8 mm)	CH$_4$: 2.5 vol.% O$_2$: 20 vol.% N$_2$: balance	16.7	20 000 mL g^{-1} h^{-1}	475	615	-	- Catalytic activity: 1.91AuPd$_{1.80}$/3DOM LaMnAl$_{11}$O$_{19}$ > 0.94AuPd$_{1.86}$/3DOM LaMnAl$_{11}$O$_{19}$ > 0.44AuPd$_{1.86}$/3DOM LaMnAl$_{11}$O$_{19}$ > 3DOM LaMnAl$_{11}$O$_{19}$ > Bulk LaMnAl$_{11}$O$_{19}$
	3DOM LaMnAl$_{11}$O$_{19}$		27.7					432	540	651	
	0.44AuPd$_{1.86}$/3DOM LaMnAl$_{11}$O$_{19}$		26.7					355	432	510	
	0.94AuPd$_{1.86}$/3DOM LaMnAl$_{11}$O$_{19}$		24.4					332	375	443	
	1.91AuPd$_{1.80}$/3DOM LaMnAl$_{11}$O$_{19}$		28.2					305	342	402	
[218] 2018	CeO$_2$	Co-precipitation	64	Fixed-bed (quartz)	CH$_4$: 1 vol.% O$_2$: 20 vol.% N$_2$: balance	100	30 000 mL g^{-1} h^{-1}				- Catalytic activity: Ce$_{0.6}$Fe$_{0.4}$O$_{2-\delta}$ > Ce$_{0.65}$Fe$_{0.35}$O$_{2-\delta}$ > Ce$_{0.7}$Fe$_{0.3}$O$_{2-\delta}$ > Ce$_{0.8}$Fe$_{0.2}$O$_{2-\delta}$ > Ce$_{0.9}$Fe$_{0.1}$O$_{2-\delta}$ > Ce$_{0.95}$Fe$_{0.05}$O$_{2-\delta}$ > CeO$_2$
	Ce$_{0.95}$Fe$_{0.05}$O$_{2-\delta}$		98								
	Ce$_{0.9}$Fe$_{0.1}$O$_{2-\delta}$		70								
	Ce$_{0.8}$Fe$_{0.2}$O$_{2-\delta}$		83								
	Ce$_{0.7}$Fe$_{0.3}$O$_{2-\delta}$		109							458	
	Ce$_{0.65}$Fe$_{0.35}$O$_{2-\delta}$		110								
	Ce$_{0.6}$Fe$_{0.4}$O$_{2-\delta}$		114					333	378	438	

Noble catalyst and metal oxides

Ref./Year	Catalyst	Preparation	SSA	Reactor	Feed	Flow / Gas velocity	GHSV			T (conversion)	Remarks
[19] 1994	4wt.% Pt/Al_2O_3	Dry impregnation		Fix-bed (i.d. 5 mm)	O_2/CH_4 = 5:1	200					T_{14}:400 $T_{49.2}$:475 $T_{93.8}$: 550	- Methane conversion in order of O_2/CH_4 molar ratio: 5:1 < 2:1 < 1:1
					O_2/CH_4 = 2:1						T_8:375 T_{28}:425 T_{96}: 450	
					O_2/CH_4 = 1:1						T_4:350 T_{59}:375 $T_{94.6}$: 475	
	4wt.% Pd/Al_2O_3				O_2/CH_4 = 5:1						T_{23}:300 $T_{40.6}$:325 $T_{94.5}$: 400	- Methane conversion in order of O_2/CH_4 molar ratio: 5:1 > 2:1 > 1:1
					O_2/CH_4 1:1						$T_{9.1}$:300 $T_{50.7}$:375 $T_{91.1}$:500	
[219] 1994	Pd-ZSM-5 PdO/Al_2O_3	Ion-exchange		Fixed-bed (quartz, o.d.1/4 inch at inlet, 3/8 inch at outlet)	CH_4: 1 vol.% In air	74	30 000 h^{-1}	~220 ~275	~255 ~325	~270 ~350		- Catalytic activity: Pd-ZSM-5 > PdO/Al_2O_3 - Higher metal dispersion and lattice oxygen of PdO/Al_2O_3 catalyst
[178] 2002	γ-Al_2O_3 Cu/γ-Al_2O_3(600 ºC) Cu/γ-Al_2O_3(800 ºC)	Wet impregnation	180 170 144	Fluidized bed reactor (stainless steel, i.d. 100 mm)	CH_4:0.5vol.% In air	Gas velocity: 0.4 to 0.8 cm s^{-1}			525 540			- Unreacted CH_4 > 100 ppm at 0.8 m·s^{-1} gas velocity and below 700 ºC - Unreacted CH_4 < 10 ppm at 0.4 m·s^{-1} gas velocity and below 700 ºC

Ref / Year	Catalyst	Preparation method	SSA	Reactor	Feed	GHSV					Notes
[220] 2004	Pd/Al$_2$O$_3$	Washcoated monolith	334	Fixed-bed (quartz, i.d. 26 mm)	CH$_4$: 1 vol. % In air	5800 h^{-1}	300	367	497		- Catalytic activity and thermal resistance increased by introducing SiO$_2$ and ZrSiO$_4$
	Pd/Al$_2$O$_3$-ZrSiO$_4$		217				285	360	415		
	Pd/Al$_2$O$_3$-SiO$_2$		356				285	360	447		
[92] 2004	Pd-3CeO$_2$/Al$_2$O$_3$	Sol-gel	680	Fixed-bed				648			- The higher Ce content, the higher catalytic activity
	Pd-5CeO$_2$/Al$_2$O$_3$		343					623			- La addition resulted in a lower catalytic activity due to less oxygen donor species present
	Pd-3La$_2$O$_3$/Al$_2$O$_3$		369					705			
	Pd-5La$_2$O$_3$/Al$_2$O$_3$		650					723			
[221] 2005	2 wt.% Pd/CeO$_2$	Deposition-precipitation	58.8	Fix-bed (quartz	CH$_4$: 1 vol.% In air	50 000 h^{-1}	224	257		T$_{100}$: 300	- Highest catalytic activity with 2 wt% Pd/CeO$_2$ prepared by DP method
	2 wt.% Pd/CeO$_2$	Impregnation	53.6				458	557			- Strong interaction between Pd and CeO$_2$ produced a large amount of active oxygen
	2 wt.% Pd/Al$_2$O$_3$	Deposition-precipitation	193				307	349		T$_{100}$: 410	
[103] 2005	Pd/Al$_2$O$_3$	Incipient wetness impregnation	102	flow reactor		250 000 h^{-1}					- Effect of pressure on catalytic performance: 5 bar: ~5.8 % 7.5 bar: ~3.5 % 10 bar: ~2.5 % 12.5 bar: ~2.2 % 15 bar: ~1.7 %
	PdPt/Al$_2$O$_3$		91								5 bar: ~7.2 % 7.5 bar: ~5.2 % 10 bar: ~4 % 12.5 bar:

Ref/Year	Catalyst	Method	SA	Reactor	Gas composition		GHSV	T_a	T_b	T_c	Light-off	Remarks
[184] 2007	Pd/HZSM-5	Precipitation	498.1	Fixed-bed (quartz)	CH$_4$: 2 vol.% O$_2$: 8 vol.% N$_2$: balance		48 000 h^{-1}	317	351		T$_{100}$: 351	- The highest catalytic activity with Pd-Ce/HZSM-5 - The addition of CeO$_2$ promoted the catalytic activity
	Pd-Ce/HZSM-5		493.5					290	336		T$_{100}$: 336	
	Pd-La/HZSM-5		438.4					331	387		T$_{100}$: 387	
	Pd-Sm/HZSM-5		455.0					326	374		T$_{100}$: 374	
	Pd-Nd/HZSM-5		462.2					322	371		T$_{100}$: 371	
	Pd-Tb/HZSM-5		419.1					329	388		T$_{100}$: 388	
	Pd/γ-Al$_2$O$_3$							352	443		T$_{100}$: 443	
	Pd/SiO$_2$							410	526		T$_{100}$: 526	
[222] 2008	Au/Fe$_2$O$_3$	Deposition-precipitation	33	Fixed-bed (quartz)	CH$_4$: 1 vol.% In air	100	51 000 h^{-1}	410	496		T$_{95}$: 565	- Catalyst prepared by HDP method showed a higher catalytic activity than DP method for methane combustion
	Au/Fe$_2$O$_3$	Homogeneous deposition precipitation	24					302	387		T$_{95}$: 488	
	Fe$_2$O$_3$		51					468	575		T$_{95}$: 650	
[223] 2009	Co$_{10}$Mn$_0$	Co-precipitation Powder	62.55	Fixed-bed (quartz i.d. 8mm)	CH$_4$: 1 vol.% O$_2$: 10 vol.% N$_2$: balance	150	36 000 h^{-1}		297	339	T$_{20}$: 265	- Appropriate Mn addition led to disorders in the spinel structure, and thus increased crystal defects and increased activity
	Co$_5$Mn$_1$		147.65						293	324	T$_{20}$: 280	
	Co$_3$Mn$_1$		158.46						306	333	T$_{20}$: 282	
	Co$_1$Mn$_1$		150.25						350	386	T$_{20}$: 323	
	Co$_1$Mn$_3$		154.49						351	392	T$_{20}$: 323	
	Co$_0$Mn$_{10}$		183.94						358	393	T$_{20}$: 331	

[224] 2009	Pd/SiO₂	Sol-gel	688	Fixed-bed (quartz, i.d. 12 mm)	CH₄:0.3 vol.% O₂: 2.4 vol.% He: balance (SO₂-free)	50	60 000 mL g⁻¹ h⁻¹		355			- The combination of TiO₂ and SiO₂ promoted the catalytic performance - TiO₂ and SiO₂ increased the catalyst SO₂ poisoning tolerance
	Pd/Ti5Si		328						332			
	Pd/Ti10Si		284						312			
	Pd/Ti15Si		243						321			
	Pd/Ti20Si		170						326			
	Pd/TiO₂		38						337			
	Pd/SiO₂				CH₄:0.3 vol.% O₂: 2.4 vol.% He: balance (with 10 vol. SO₂)				395			
	Pd/Ti5Si								379			
	Pd/Ti10Si								365			
	Pd/Ti15Si								n.a.			
	Pd/Ti20Si								381			
	Pd/TiO₂								346			
[116] 2009	Pt-W/γ-Al₂O₃ commercial	Washcoated	214	Microchannel	CH₄: 9.1 vol.%	107	74 000 h⁻¹	399	493		T₁₀₀: 600	- Pt-W/γ-Al₂O₃ showed 100% methane combustion and 99% CO₂ formation at 600 °C for 60 h test, 98% CH₄ conversion after 100 h
	Pt-W/γ-Al₂O₃ home-made		123					430	528		T₁₀₀: 625	
	Pt-Mo/γ-Al₂O₃ commercial		242					443	526		T₁₀₀: 625	
	Pt-Mo/γ-Al₂O₃ home-made		150					470	554		T₁₀₀: 650	
[225] 2010	2 wt% Pd/CeO₂ 2ZrO₂	Solution combustion synthesis		Fixed-bed (quartz, i.d. 4 mm)	CH₄: 2 vol.% O₂: 16 vol.% He: balance	50						- Lower catalytic activity with catalyst aging time: Pd/CeO₂ 2ZrO₂; - Increased catalytic activity with catalyst aging time: Pd/LaMnO₃ 2ZrO₂ Pd/BaCeO₃ 2ZrO₂
	fresh		74.6					340	382	429		
	1week aged		65.8					336	383	419		
	2 weeks aged		34.8					345	421	498		
	2 wt.% Pd/LaMnO₃ 2ZrO₂											
	fresh		132.5					450	570	645		
	1week aged		69.8					500	625	6905		

Ref./Year	Catalyst	Method		Reactor	Feed gas		GHSV				Notes
	2 weeks aged		21.6					360	450	0	
	2 wt.% Pd/BaCeO₃ 2ZrO₂										
	fresh		26.4					414	512	592	
	1week aged		22.7					540	628	694	
	2 weeks aged		15.4					330	443	540	
[88] 2010	Pd$_{(1.0)}$/Al₂O₃ Pt$_{(1.5)}$Rh$_{(0.3)}$/Al₂O₃ Pt$_{(1.0)}$Pd$_{(0.75)}$Rh$_{(0.25)}$/Al₂O₃ (molar ratio)	Impregnation		Fixed-bed (quartz, i.d. 8 mm)	CH₄: 0.1 vol.% O₂:16.74 vol.% N₂: 83.16 vol.%		10 000 h⁻¹		474 415 388	520 460 442	- Trimetallic catalytic activity depended on noble metal composition: PtPdRh/Al₂O₃>PtRh/Al₂O₃>Pd/Al₂O₃
[226] 2015	CoAlO-500 °C CoAlO-600 °C CoAlO-700 °C *Ag NPs:* Ag-CoAlO-500 °C Ag-CoAlO-600 °C Ag-CoAlO-700 °C	Deposition	88.6 262.6 29.1 96.2 69.5 212.4	Fixed-bed (quartz, i.d. 6 mm)	CH₄: 2 vol.% O₂: 20 vol.% N₂: 78 vol.%	41.6	30 000 mL g⁻¹ h⁻¹	462 471 477 393 343 371	538 562 585 516 444 475	618 629 656 571 522 555	- Catalytic activity: CoAlO - 700 °C < CoAlO - 600 °C < CoAlO - 500 °C <Ag-CoAlO - 500 °C <Ag-CoAlO - 700 °C <Ag-CoAlO - 600 °C - The highest catalytic activity with Ag-CoAlO-600 °C due to abundant Co³⁺ and adsorbed oxygen
[201] 2015	2.94Au$_{0.50}$Pd/meso-Co₃O₄		114.5	Fixed-bed (quartz)	SO₂ addition		20 000 mL g⁻¹ h⁻¹	230 263 242 269	280 312 288 321	324 378 334 397	*SO₂ addition (irreversible)* -100 ppm SO₂ addition: Conversion drop from 90.5% to

		73.6% after 31h
		- *regeneration:* CH$_4$ conversion slightly increased to 74.2% after 16 h
	H$_2$O addition	*H$_2$O addition (reversible)*
		-2 vol.% H$_2$O addition:
		Conversion drop from 93% to 91%
		-5 vol.% H$_2$O addition:
		Conversion drop from 91% to 90%
		-10 vol.% H$_2$O addition:
		Conversion drop from 90% to 89%
	CO$_2$ addition	*CO$_2$ addition (reversible)*
		-2.5 vol.% CO$_2$ addition:
		ca.2% decrease in methane conversion after 13h
		-5 vol.% CO$_2$ addition:
		ca.1% decrease in methane conversion after 4h

												-regeneration: restore to original ca.90.5% conversion
[114] 2015	Fe-Ni 3.2 wt.% Pd/Al$_2$O$_3$/Fe-Ni 4.8 wt.% Pd/Al$_2$O$_3$/Fe-Ni 4.8 wt.% Pd/Al$_2$O$_3$/Fe-Ni 4.8 wt.% Pd/Al$_2$O$_3$/Fe-Ni 4.8 wt.% Pd/Al$_2$O$_3$/Fe-Ni 4.8 wt.% Pd/Al$_2$O$_3$/Fe-Ni 4.8 wt.% Pd/Al$_2$O$_3$/Fe-Ni 4.8 wt.% Pd/Al$_2$O$_3$/Fe-Ni	Washcoated		Tubular (inner i.d. 20 mm, outer: i.d. 32 mm)	CH$_4$: 5 vol.% CH$_4$: 5 vol.% CH$_4$: 5 vol.% CH$_4$: 5 vol.% CH$_4$: 5 vol.% CH$_4$: 2 vol.% CH$_4$: 3 vol.% CH$_4$: 4 vol.%		50 50 50 100 150 200 50 50 50		T_{10}: 550 T_{10}: 350 T_{16}: 350 T_{10}: 400 T_9: 400 T_7: 400 T_{10}: 350 T_{12}: 350 T_{15}: 350	T_{35}: 400 T_{40}: 400 T_{50}: 500 T_{45}: 500 T_{35}: 500 T_{60}: 450 T_{68}: 450 T_{70}: 450	T_{98}: 500 T_{98}: 550 T_{95}: 550 T_{65}: 550 T_{62}: 550 T_{88}: 500 T_{90}: 500 T_{93}: 500	- Catalyst activity vs. Pd loading: 4.8% >3.2% - CH$_4$ conversion decreased with the increasing flow rate - CH$_4$ conversion slightly increased with the increasing CH$_4$ concentration
[177] 2016	3wt.%Re/γ-Al$_2$O$_3$ 5wt.%Pd/γ-Al$_2$O$_3$ (degussa) 5wt.%Ru/γ-Al$_2$O$_3$ (fluka) 5wt%Ru/γ-Al$_2$O$_3$ Ru$_{90}$-Re$_{10}$/γ-Al$_2$O$_3$ Ru$_{75}$-Re$_{25}$/γ-Al$_2$O$_3$	Wet impregnation	316 90 183 174 147	Fixed bed (i.d. 8 mm)	CH$_4$: vol.% In air	0.8	100	60 000 h^{-1}	535 300 386 361 337 359	650 331 436 407 391 411	T_{95}: 800 T_{95}: 403 T_{95}: 555 T_{95}: 525 T_{95}: 506 T_{95}: 538	- Pretreatment of catalyst greatly affected the activity - Re addition improved the activity

Ref / Year	Catalyst	SSA	Reactor	Feed		Space velocity	T10	T50	T90	T	Notes
[227] 2016	0.5wt.% Pd/γ-Al$_2$O$_3$		Fluidized reactor (i.d. 102 mm)	CH$_4$: 0.15 vol %	velocity 0.1 m s^{-1}					T$_{62.2}$: 450 T$_{94.5}$: 550	- At 550 °C, 0.3 %CH$_4$ velocity from 0.1 to 0.25 m s^{-1}, CH$_4$ conversion: 98% to 73%
[228] 2016	Co$_3$O$_4$ - 200 °C Co$_3$O$_4$ - 400 °C Co$_3$O$_4$ - 600 °C	136.2 41.5 7.4		CH$_4$: 1 vol.% O$_2$: 20 vol.%		18 000 mL g^{-1}h^{-1}	270 292 373				- Catalytic activity: Co$_3$O$_4$ - 200 °C > Co$_3$O$_4$ - 400 °C > Co$_3$O$_4$ - 600 °C
[179] 2017	3DOM CoCr$_2$O$_4$ (Three-dimensionally ordered macroporous) 0.98AuPd$_{1.93}$/3DOM CoCr$_2$O$_4$ 1.93AuPd$_{1.95}$/3DOM CoCr$_2$O$_4$ 1.98AuPd$_{1.96}$/Bulk CoCr$_2$O$_4$ Bulk CoCr$_2$O$_4$ 1.93AuPd$_{1.95}$/3DOM CoCr$_2$O$_4$ 1.93AuPd$_{1.95}$/3DOM CoCr$_2$O$_4$	33.2 35.6 34.9 8.8 7.2	Fixed-bed (quartz, i.d. 6 mm)	CH$_4$: 2.5 vol.% O$_2$: 20 vol.% N$_2$: 77.5 vol.%	16.7	20 000 mL g^{-1}h^{-1} 10 000 mL g^{-1}h^{-1} 40 000 mL g^{-1}h^{-1}	320 310 305 325 335 ~290 ~325	370 362 353 385 400 ~345 ~380	440 410 394 467 490 ~382 ~43		- Catalytic performance decreased with the increasing space velocity - 1.93AuPd$_{1.95}$/ 3DOM CoCr$_2$O$_4$ presented the best activity - Addition of H$_2$O(g) and SO$_2$ resulted in catalyst deactivation

Ref / Year	Catalyst	Synthesis method		Reactor	Feed		GHSV				Remarks
[229] 2017	Pd/CoAl$_2$O$_4$/Al$_2$O$_3$	Galvanic deposition Impregnation		Fixed-bed (Pyrex glass, i.d. 4 mm)	CH$_4$: 0.4 vol.% O$_2$: 10 vol.% He: balance	100	300 000 mL g^{-1}h^{-1}	266 285	~295 ~335		- Catalyst by galvanic deposition method performed better
[230] 2017	Pd/ZrO$_2$ Co/ZrO$_2$ Cu/ZrO$_2$ Cr/ZrO$_2$ Pd/ZrO$_2$/SDS Co/ZrO$_2$/SDS Cu/ZrO$_2$/SDS Cr/ZrO$_2$/SDS (SDS: sodium dodecyl sulphate)	Sonochemically aided impregnation synthesis	24.23 22.91 24.76 22.93 25.10 24.97 22.28 23.04	Fixed-bed	CH$_4$: 2000 ppm in air		150 000 mL g^{-1}h^{-1}			T$_{\sim95}$ = 300 T$_{\sim35}$ = 300 T$_{\sim14}$ = 300 T$_{\sim22}$ = 300 T$_{\sim20}$ = 300 T$_{\sim8}$ = 300 T$_{\sim10}$ = 300 T$_{\sim14}$ = 300	- Catalytic activity: Co/ZrO$_2$ > Pd/ZrO$_2$/SDS > Cr/ZrO$_2$ > Cu/ZrO$_2$ > Cu/ZrO$_2$/SDS > Cr/ZrO$_2$/SDS > Co/ZrO$_2$/SDS > Pd/ZrO$_2$
[231] 2019	CoO$_x$ @ SiO$_2$ - 400 °C CoO$_x$ @ SiO$_2$ - 600 °C CoO$_x$ @ SiO$_2$ - 800 °C	Deposition	389 290 225	Fixed-bed (quartz)	CH$_4$: 2 vol.% O$_2$: 20 vol.% N$_2$: balance	250	15 000 mL g^{-1}h^{-1}			T$_{100}$ = 330 T$_{100}$ = ~380 T$_{\sim85}$ = ~400	- Catalytic activity: CoO$_x$ @ SiO$_2$ - 400 °C > CoO$_x$ @ SiO$_2$ - 600 °C > CoO$_x$ @ SiO$_2$ - 800 °C

a. Mentioned studies in Table 2.4 are listed in the order of published year;

b. T$_{10}$/T$_{50}$/T$_{90}$: the temperature at which the methane conversion is 10 %, 50 % and 90 %.

2.5. Types of catalytic reactors

In this section, some representative types of reactor used for CMC are discussed. Special focuses are laid on the geometry, the way of reaction heat recovery and the improvement of thermal efficiency by the enhancement of heat and mass transfer. Table 2.5 recapitulates some key facts of the relevant studies reported in the literature and Table 2.6 provides a comparison on the advantages and disadvantages of these reactors.

2.5.1. Fixed-bed reactor

A fixed-bed catalytic reactor is commonly made up of a cylindrical tube with a certain amount of catalysts being fixed in certain locations inside the tube. The shapes of catalyst can be powder, spherical, cylindrical or randomly shaped pellets. This type of reactor is the most commonly used, suitable not only for catalyst activity test and kinetic study, but also for practical applications in the chemical and process industries. The advantages of fixed-bed reactors include easy operation, low cost, high catalyst spatial density, etc. Poor temperature distribution, low surface area, and high-pressure drop are their main disadvantages.

Besides being used individually as a single-stage reactor, several fixed-bed reactor modules may be combined to form a multi-stage reactor system. Different catalysts may be used for each stage. A two-stage combustor combining a conventional flame reactor with a catalytic reactor has been proposed by Sadamori et al. [205,232], with the purpose of improving the combustion efficiency and further reducing the gas exhaust emission. In their study, three monolithic catalysts with Pd and/or Pt based catalysts were loaded in the catalytic stage. Combustion efficiency higher than 99.5 % and the NO_x emission less than 2 ppm (80 % reduction) could be achieved by controlling the inlet temperature between 500 and 700 ^{o}C. In terms of thermal behavior, the conventional stationary fixed-bed reactor with a separated heat exchanger (Fig. 2.12a) has the problem such that the reaction heat is difficult to be fully utilized. Multifunctional or extended autothermal reactors having higher interfacial surface areas and more efficient heat transfer thus become more attractive, especially for strongly or moderately exothermic reactions [233]. This concept combines catalytic reaction with an effective thermal management (i.e. heat removal or addition) in an integrated and compact device (Fig. 2.12b), so as to largely reduce the heat losses. Compared to the ex-situ configuration, lower CO and NO_x emissions and higher heat power could be achieved for the multifunctional reactor with an integrated heat exchanger [31]. Detailed information about the autothermal fixed-bed reactor can be found in the literature [234-236].

Fig. 2.12. Autothermal fixed-bed reactor with (a) a separate heat exchanger; (b) an integrated heat exchanger; (c) a periodic flow reversal mode (central heat exchange); (d) hot gas withdrawal on two side ends of the catalyst section.

In order to further enhance the heat transfer capability, the fixed-bed reactor can be operated in the reversal flow mode [237,238], where the feeds are alternately introduced from either end

of the reactor (Fig. 2.12c). The continuous heat extraction is a viable way to provide necessary amount of heat in the reactor, and to maintain the catalyst activity without overheating. A high amount of heat withdrawal could result in a high instability of the reaction due to a remarkably decreased temperature of the reactor. Moreover, a periodic steady state in temperature can be achieved by switching the direction of reactant flow. The reversal time is one of the significant factors not only to stabilize the reactor and the heat exchanger but also to maintain a stable temperature in the catalytic section. A longer reversal time is commonly accompanied with a higher heat loss. On the contrary, a shorter reversal time can result in a lower heat generation and a reduced methane conversion [239,240]. Many simulations studied the relative position of the catalyst bed and the heat exchanger as well as the flow pattern in order to find out the most efficient way to recover heat from reversal-flow reactors [241-243]. Gosiewski et al. [241] found that a higher heat recovery efficiency can be approached by the hot gas withdrawal (Fig. 2.12d) than by the central heat exchange (Fig. 2.12c). Detail experimental data are listed in Table 2.5. Their results showed that more than 70% of heat can be recovered when withdrawing only around 30 % of the hot gas. Furthermore, Hunter et al. [244] studied different patterns of heat recovery with respect to the heat withdrawal location (central or end) and the possibilities of returning the cooled gas to exchange heat. It was found that a higher heat recovery efficiency could be obtained by positioning the heat exchanger at the two side ends of the catalytic bed without any returned cold gas. Hence, a high thermal recovery efficiency and the best methane conversion may be achieved by considering both the flow reversal mode (e.g., the hot gas withdrawal at the end of the catalyst bed) and the reversal time. More description of the flow-reversal reactors can be found in the references [235,241,245-247].

2.5.2. Wall-coated reactor

Conventional fixed-bed reactors have the drawback of limited heat transfer rate due to the low surface-to-volume ratio. On the contrary, the wall-coated reactors have features like lower pressure drop and higher surface area by depositing the catalyst layer on the reactor wall surface, so as to augment the catalyst contact surface area and to enhance the mass/heat transfer. Hence, this type of reactor is more suitable to be employed for coupling exothermic reactions with endothermic reactions. A lower temperature difference and a shorter distance between the heat source (exothermic reaction) and heat sink (endothermic reaction) are beneficial to increase the heat exchange efficiency. The so-called wall-coated reactor could be further divided into (folded) plate-type, tubular-type, micro/mini channel plate-type and monolithic reactors.

2.5.2.1 (Folded) plate-type reactor

Fig. 2.13a shows a basic plate-type reactor coupling CMC with methane steam reforming reaction. The two reactions happen on the opposite sides of the same plate with overlapped temperature profiles. The two flow modes (i.e., co-current and counter-current) were intensively investigated [248]. The hot spots could be avoided by optimizing the overlapping zone of reactions with the proper co-current arrangement. However, the complete overlapping is not able to be achieved by utilizing the counter-current flow mode. Regarding the distance between plates (thickness: 0.5 mm), it has been reported that no significant effect on the catalytic performance was observed when the plate distance varied between 1-4 mm [249].
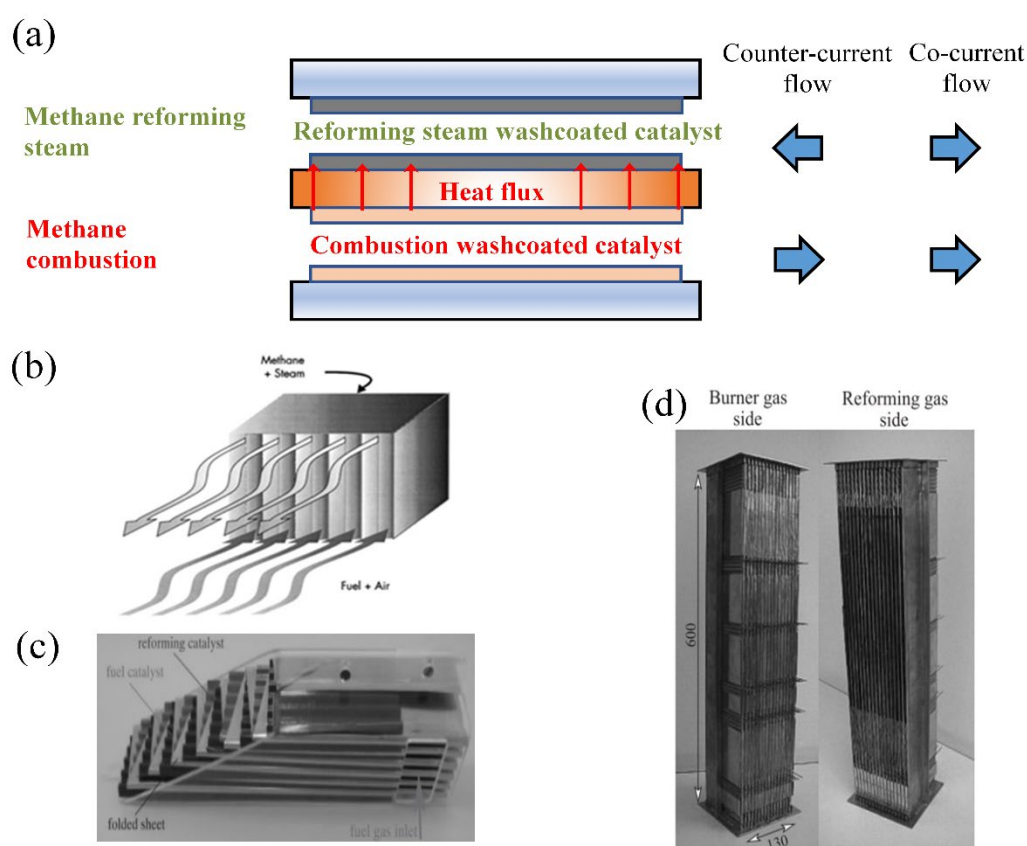
Fig. 2.13. Wall-coated reactor. (a) co-current and counter-current flow mode of wall-coated reactor; (b) folded metal sheet [250]; (c) folded sheet reactor with corrugated spacers as catalyst carriers [44]; (d) pilot-scale multifunctional folded sheet reactor [251].

A folded sheet structure reactor for the coupled CMC and steam reforming reaction was investigated by Polman et al. [250]. A relatively simple design with two separated chambers was formed by the folded metal sheet, as shown in Fig. 2.13b. In order to avoid the high heat loss and to enhance the heat transfer, a novel folded sheet reactor with rectangular adjacent channels was proposed by Kolios et al. [44]. The spacers with rectangular ducts in between are

responsible to support the whole structure, providing additional effective heat exchange areas as well (increased by a factor of 3). The gas distributor with channels is located on the right side of the entire reactor, as shown in Fig. 2.13c [44]. Fig. 2.13d shows a pilot-scale multifunctional folded sheet reactor combining methane combustion with methanol reforming [251].

2.5.2.2 Coated tubular reactor

A novel tube-type reactor (i.d. 25 mm, o.d. 38.5 mm) with external fins (fin height 14.3 mm) was proposed by Seo et al. (Fig. 2.14a) [32]. The external surfaces of tube with fins were coated with Pd/ZrO$_2$ catalysts for CMC while the cold air as the heat transfer fluid (HTF) was circulated inside the tube to remove the released reaction heat. From practical point of view, this compact design with a high surface area is capable of achieving 100 % methane conversion and a high heat transfer rate under high methane flow rate conditions. Moreover, nearly 100 % methane conversion could be obtained by 16 finned-tube reactors even under high gas velocity conditions (0.12-0.31 m s^{-1}). However, the same conversion for 10 finned-tube reactors is required under a much lower velocity (< 0.11 m s^{-1}). Moreover, it has been reported that the conversion at 400 °C decreased from 88 % to 70 % with the increasing catalyst thickness from 1 mm to 3 mm (cf. more details shown in Table 2.5). A washcoated finned tubular reactors with thinner catalyst thickness (e.g., <1 mm) was more favorable to reach a high conversion.
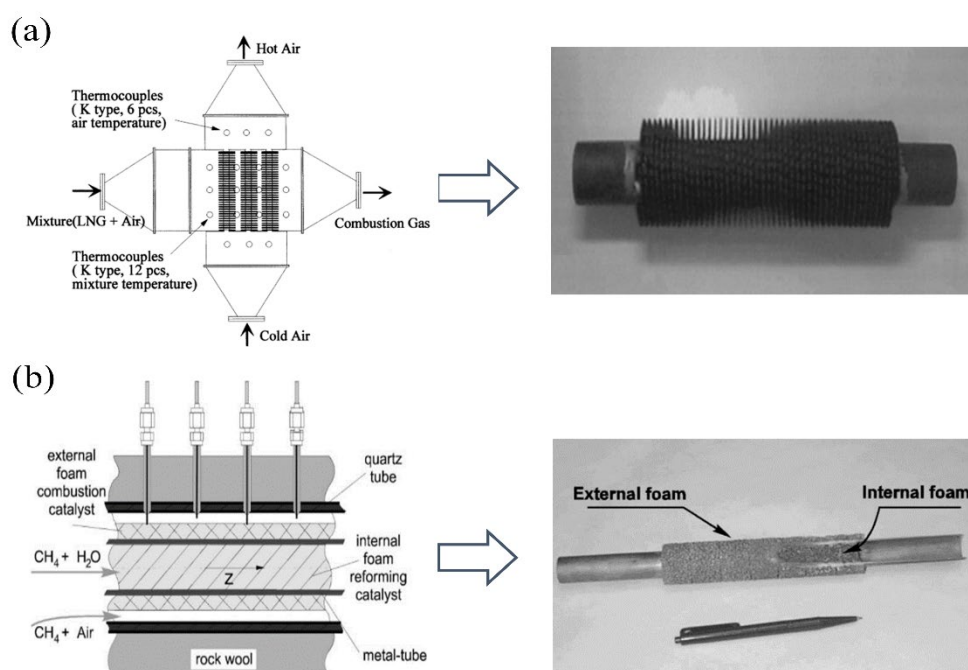
Fig. 2.14. Coated-tubular reactor. (a) tube-fin geometry and laboratory prototype [32]; (b) external surface coated with Ni-Cr catalyst, and internal surface coated with Ni catalyst [119].

Ismagilov et al. [119] investigated a tubular reactor (i.d. 18 mm, o.d. 20 mm) with coated metal

foams both on the external (Ni-Cr) and internal (Ni) tube surfaces (Fig. 2.14b). A stable catalytic performance and uniform temperature distribution in the reactor could be obtained by optimizing the gas mixture composition and the catalyst thickness. Moreover, the thickness of catalytic layer in the range of 4-5 mm was favorable to reach a more stable combustion than that of 2.5 mm. Thus, a suitable surface area and catalyst thickness are required not only for increasing the diffusion rate of reactants, but also for higher catalytic combustion efficiency.

Unlike the traditional straight combustor, Yan et al. [252] numerically investigated three different designs of the micro tube combustors for CMC. The improved combustion efficiency can be obtained from the design of multi-step separated baffles (two groups of three separated zones). One of the key advantages of this design is that the separated baffles provided chances for the premixed methane and air to enter the reaction zone from different locations, which enhanced the combustion efficiency and heat recirculation.

2.5.2.3 Micro/mini channel plate-type reactor

Micro/mini channel reactor has attracted more attention in the past several decades [253-255]. The high surface area of microchannel reactors as well as excellent mass/heat transfer presents great benefits for the catalytic performance [256-258]. Thus, highly exothermic reactions are better handled in the microchannel reactor, due to the suppression of the hot spot formation. However, it is worth noting that the high surface area may also result in the thermal quenching problem due to the high heat loss if the reactor is not properly insulated. An extra heat source may have to be provided to the microchannel reactor when the released heat from CMC is insufficient to compensate the heat loss to maintain a continuous combustion in practice [257,259,260].

Fig. 2.15a shows a basic geometry of microreactor with washcoated catalyst on multiple straight channels, where the CMC reaction takes place. O'Connell et al. [116] investigated methane combustion on a microstructured reactor (51 cm length × 14 cm width) with the microchannels (500 μm × 250 μm, 14 channels in total) over washcoated Pt-W/Mo-Al_2O_3 catalyst, as shown in Fig. 2.15b [116]. A methane conversion of 50% has been obtained at 493 °C under the total flow rate of 107 mL min^{-1}. The CMC was experimentally investigated by He et al. [118] in a parallel microchannels reactor (317.5 mm length × 50 mm width × 3 mm thickness) over washcoat Pt/γ-Al_2O_3 catalyst, as shown in Fig. 2.15c. A methane conversion of 95.75 % could be obtained at 450 °C and 110 mL min^{-1} (at a residence time of 14.41 s). A compact microchannel reactor (15 cm × 3.9 cm × 1.5 cm) was used for the coupled CMC with methane

steam reforming, as shown in Fig. 2.15d [261]. Each plate consists of 5 parallel straight channels (10 cm × 0.5 cm × 0.5 cm). The methane catalytic reactor with $Pt-Sn/Al_2O_3$ catalyst is located on the two sides of the steam reforming reactor with $Ni/CaAl_2O_4$ catalyst. The heat released from the CMC was provided for steam reforming reaction to produce hydrogen. The improved heat efficiency of 67 % and methane conversion of 96 % were obtained under optimized feed ratio (1.5) of combustion to reforming and at 700 ^oC. Enough hydrogen was expected to be generated to operate a 30 W fuel cell. Mundhwa et al. [117,262] proposed a microstructured reactor design (Fig. 2.15e) composed of two methane combustion reactors with segmented channels (1 mm × 5 cm × 20 μm, 20 channels) and two reforming reactor without channels. The plates were stacked alternatively one above another to form the autothermal microstructured reactor. Washcoated Pt/Al_2O_3 catalysts were applied in methane combustion microchannels while Ni/Al_2O_3 catalysts were coated on the steam reforming side. Based on this design, about 7~8 % less reactants and 70 % less catalysts were required for methane combustion to power a 1 kW fuel cell. A better methane conversion and heat transfer efficiency (in terms of better temperature distribution) could be obtained under the co-current flow mode (Fig. 2.15e). Contrarily, the counter-current flow mode generated undesirable high temperatures, resulting in the degraded catalyst life-time.

In order to improve the stability of methane combustion, Nui et al. [263] proposed different trapezoidal bluff bodies in the microchannel reactor. The numerical results presented that the combustion recirculation zone was broadened due to the formation of vortex by increasing the blockage ratio of bluff bodies.

The thickness of the catalyst layer has a significant impact on the catalytic performance. The increased thickness of the catalyst layer usually results in a decrease in the methane conversion due to the increased internal mass transfer limitation [119]. However, Rodrigues et al. [260] reported that a higher catalytic activity could be obtained by the thicker catalyst film. The porous catalyst prepared by the electrodeposited method offered the reactants easier access to the inner surface.
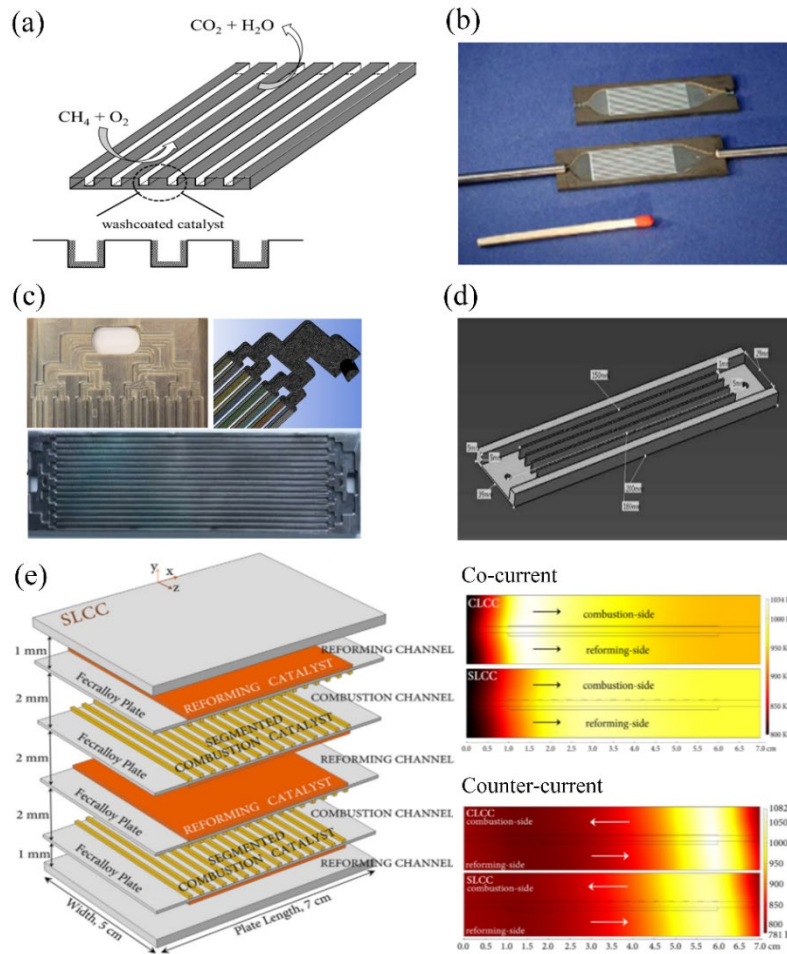
Fig. 2.15. Microchannel reactor. (a) basic geometry; (b) Washcoated Pt-W/Mo-Al₂O₃ catalyst on a microchannel reactor for CMC [116]; (c) Pt/γ-Al₂O₃ catalyst on multichannel reactor for CMC [118]; (d) coupling steam reforming over a microchannel reactor [261]; (e) integration of multi-plates coupling with methane steam reforming over a microchannel reactor [117].

2.5.2.4 Monolithic reactor

Monolithic reactors with open structures present a low pressure drop, high surface-to-volume ratio, high mass/heat transfer rates and high thermal stability. Thus, this type of reactor is widely applied to gas turbines and automobiles for power generation and/or for pollutant emission purification [264,265]. Numerous types of interconnected channels (e.g., square/round/triangle, as shown in Fig. 2.16a) and various types of substrate (e.g., honeycombs, foams or fibers) are oriented to different applications [266,267]. A higher monolithic surface area can be obtained by triangular interconnected channels. It was reported that monolith with a high specific surface area (400 cells cm⁻²) presented enhanced mass and heat transfer characteristics compared to the lower one (60 cells cm⁻²) [268]. Ceramic and metallic substrates are the most common materials used in studies due to the high mechanical stability and the low

thermal expansion.

Usually, the catalyst was loaded on the upper section of the reactor and the heat exchanger was located on the bottom. The thermal efficiency was found to be between 20 % and 30 % for such system [269]. In order to better utilize the heat released from reaction, a two-stage monolith prototype with two heat exchangers was designed. This compact design of premixed burner comprises two honeycombs in between the two heat exchangers on the opposite side, similar model as shown in Fig. 2.16b [29]. The thermal efficiency for this design could reach 101.1 %, implying an effective way to satisfactorily recover the released reaction heat [33]. Fig. 2.16c shows a monolith and folded wall reactor [35] for the CMC coupled with the steam reforming reaction, the inner pipe for CMC reaction and the annular part for steam reforming reaction (co-flow model). The temperature difference can be managed by adjusting the feed ratio of methane steam reforming to combustion. Furthermore, the heat transfer can be obviously improved by proper channel arrangement or catalyst distribution.
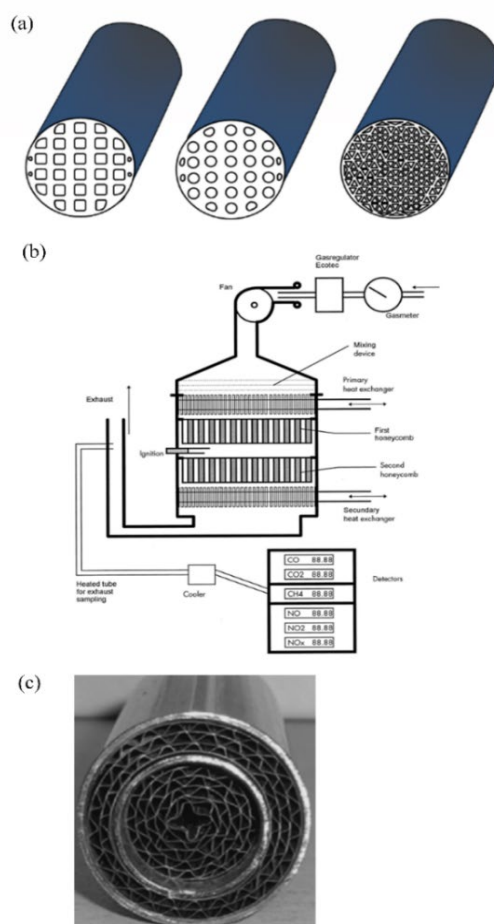
Fig. 2.16. Monolithic reactor. (a) various internal channel shapes (round/square/triangle); (b) catalytic monolithic reactor with two monolithic exchangers [29]; (c) folded-wall monolithic reactor coupled with steam reforming reaction [35].

2.5.3. Membrane reactor

A membrane reactor commonly comprises a membrane coated with catalysts or as a barrier that only allows certain component(s) to pass through. Lanthanum cobaltite perovskite ceramic is one of the most widely used materials for membranes. Other materials with improved properties, such as thin dual-phase membranes, ceramic metal dual-phase membranes and ion transport membranes are also very promising for enhanced oxygen permeation [270]. The increasing motivation for their industrial applications is the reduction of CO_2 emissions from methane combustion.

The basic principle of membrane reactor for CMC is shown in Fig. 2.17a. CH_4 and air pass through the membrane, and the permeated O_2 reacts with CH_4. CO_2 in the products can be successfully separated and captured. It has been reported that the nitrogen with a purity of 98-99 % could be produced and the system remained stable over 120 h [271].The membrane reactor used for CMC could achieve a high methane conversion mainly by varying the partial pressure of oxygen permeation. However, the high costs of membrane reactors potentially limit their industrial applications.
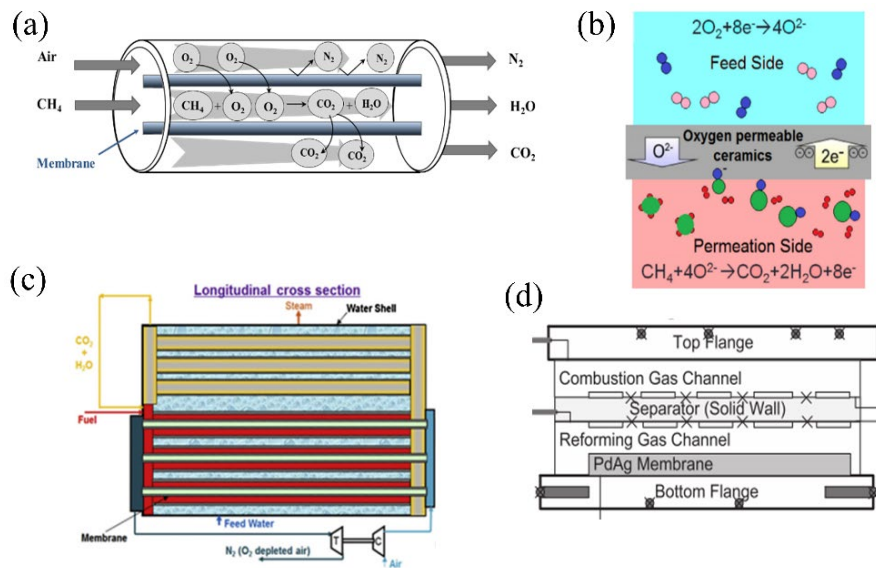
Fig. 2.17. Membrane reactor for CMC. (a) basic principle; (b) oxygen transport across the membrane [272]; (c) ion transport membranes reactor [273]; (d) multi-channel membrane reactor coupled with steam reforming reaction [274].

The membrane reaction efficiency is affected by the feed flow rate, the temperature, and the permeability of oxygen. Fig. 2.17b depicts the oxygen transport over the membrane reactor [272]. The oxygen is firstly adsorbed on the surface of the membrane. The charged oxygen

vacancy (O^{2-}) is diffused to the other side, due to the formation of the chemical potential gradient across the membrane. The electrons on the other side are transferred in a reversed-direction so as to compensate for the oxygen vacancies. The results of Falkenstein et al. [272] present that the oxygen permeation flux increased with the increasing methane flow rate and reaction temperature. However, the oxygen permeation flux remained fairly constant at high methane flow rates (e.g., >20 mL min^{-1}), probably due to the limitation of the effective membrane surface area. CO_2 selectivity was thus not significantly varied under higher flow rates in this case. This is in agreement with the results reported by Tan et al. [275], that is, the high methane and air flow rates resulted in a lower oxygen permeation and reaction rate over $La_{0.6}Sr_{0.4}Co_{0.2}Fe_{0.8}O_{3-\alpha}$ hollow fiber membrane reactor. Moreover, the membrane, coated with platinum catalyst, showed that the membrane reactor effectively facilitated the oxygen permeation and improved the methane conversion, owing to the reduced oxygen permeation resistance [275].

Habib et al. [273] proposed a two-pass ion transport membrane reactor (ITM) for CMC, as shown in Fig. 2.17c. The first pass is responsible for oxygen permeation, where methane combustion and partial heat exchange between the mixture gas and the water also happened. The second pass is for further permeation. Moreover, the counter-current flow configuration in this ITM provided high methane conversion than that with the co-current flow configuration, owing to the higher oxygen permeation in the first case. In fact, the increased oxygen partial pressure and the accumulated oxygen flux may lead to the reduced oxygen permeation under the co-current flow mode. Moreover, the membrane reactors have also been applied for coupling with steam reforming [276] (Fig. 2.17d) or ammonia decomposition [277] reactions. An effective way to improve the performance for this system is to increase the membrane effectiveness and to reduce the membrane thickness.

2.5.4. Fluidized bed reactor

Fluidized bed reactor is a kind of typical catalytic reactors in which solid catalysts (frequently with a diameter of 10-300 μm) are fluidized during the reaction. It is capable of handling a larger amount of reactants or catalysts owing to the large reactor size, and the feed flow rate is required to suspend the catalysts. A porous plate as gas distributor is responsible for supporting the material in the fluidized bed, as shown in Fig. 2.18. The high gas flow results in an efficient contact between the reactants and the catalysts, leading to the enhanced heat and mass transfer rates on the catalyst surfaces. As a result, the non-uniform temperature distribution that commonly exists in fixed-bed reactor could be avoided. One of its main disadvantages is the

great mass loss of the catalyst due to the in-bed attrition after long-term operation.

The experiment measurement by Yang et al. [278] illustrated that the methane conversion increased with the increasing temperature in the fluidized bed reactor, and decreased with the increasing methane inlet concentration. The methane conversion was also reported to decrease with the increasing gas velocity [227]. The fluctuation of temperature and the variation of mixture concentration may occur, due to the intensive motion of solid particles rising up and falling back [279]. Meanwhile, the enhanced mass and heat transfer can be realized between the reactants and the catalyst particles, due to the strong oscillations in the fluidized bed. Furthermore, the kinetic experiments conducted by Yang et al. [278] in the fluidized bed confirmed that the reaction was only controlled by the kinetics at a bed temperature below 450 ^{o}C, and by the mass transfer and kinetics together at temperatures above. Dubinina et al. [280] reported $CuO/Al_2O_3MgO-Cr_2O_3$ catalyst to be the one of the most promising catalysts in the fluidized bed reactor for CMC.
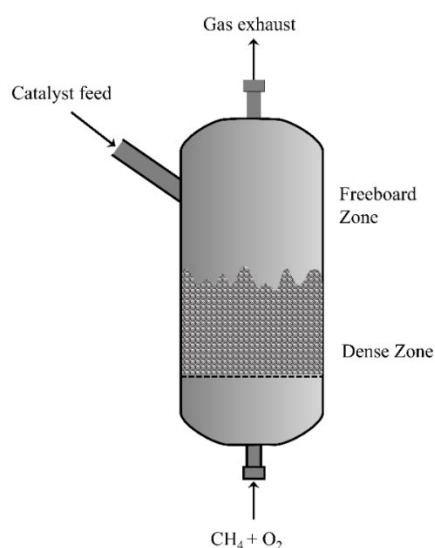
Fig. 2.18. Fluidized bed reactor for CMC.

Table 2.5 Summary of thermal parameters for various reactors.

Ref.	Reactor	Catalyst	Reactant	Tx (ºC) X=conv%	Heat transfer	Heat released	Heat recovery efficiency	Input power	Gas exhaust	Remarks
[29] 1999	Monolith (Fig. 2.16b)	One monolith	Air/CH$_4$ 1.1-1.5			15-40 W cm^{-2}			NO$_x$: 5 ppm CO: 0 ppm	- Long coating → CO emission
										- Short coating → NO$_x$ emission
		Two monoliths							NO$_x$: 0 ppm CO: 0 ppm	- Completely catalytic boiler:
									CH$_4$: 0 ppm	No emissions, and lower sensitivity to gas quality
[187] 1999	Monolith	Pd-NiO/Al$_2$O$_3$	E_a: 1.0 1.25 1.5 2.0			6.2-13.4 kcal h^{-1} cm^{-2}	~90 % ~100 % ~100 % ~100 %			- E_a 1.0-1.5: catalytic combustion
										E_a: 1.75-2.0: flame occurred
										E_a > 2.1: flame blown off
										E_a 1.25-1.75: stable catalytic combustion
										- Over 95% methane was converted within 8 mm from the entrance
[279] 2000	Fluidized-bed (i.d.: 96 mm L: 400 mm)	Mn/Al$_2$O$_3$	650 -720 ºC: 30 - 65 %							- Oscillations and heat losses of bed temperature attributed to the instability of oxygen consumption and products

Ref.	Reactor	Catalyst	Reactant	Tx (^oC) X=conv%	Heat transfer	Heat released	Heat recovery efficiency	Input power	Gas exhaust	Remarks
[32] 2003	Fin reactor (Fig. 2.14a)	Pd/ZrO$_2$	0.19 m s^{-1} 0.11 m s^{-1} 0.15 m s^{-1} 0.23 m s^{-1} 0.12-0.31m s^{-1}	T_{35}: 400 T_{70}: 450 T_{78}: 500 T_{80}: 600 $T_{99.9}$: 500 $T_{99.9}$: 500 T_{76}: 500 $T_{98.5}$: 500	Air as HTF (heat transfer fluid)		$T_{fin\ surface}$: ~300-750 ^oC T_{outlet}: ~727-927 ^oC			- <500 ^oC: methane conversion was greatly affected by the inlet temperature - >500 ^oC: methane conversion was slightly affected by the inlet temperature - Higher flowrate → more heat removed → lower surface temperature → decreased conversion - Surface area should be as large as possible
[33] 2005	Monolith	Co$_3$O$_4$/Fe$_2$O$_3$/ MnO$_2$	CH$_4$: O$_2$: N$_2$ 1:4:5	T_{10}: 358 ^oC T_{90}: 378 ^oC	T_{inlet}: 16.8 ^oC T_{outlet}: 42.0 ^oC (to heat water: 11.2 kg·min^{-1})	19.9 kW 80 W cm^{-2}	101.1 %		CO: 0.01 % NO$_x$: 22 ppm O$_2$: 5.6 % Hydrocarbon: 0 ppm	- Burner with two heat exchanger on two sides of monolith catalyst is able to enhance heat efficiency and reduce the pollutant
[281] 2006	Monolith (450×200× 700 mm)	Pt-based	1.00 m^3 s^{-1} 1.17 m^3 s^{-1} 1.33 m^3 s^{-1} 1.50 m^3 s^{-1} 1.67 m^3 s^{-1} (natural gas flow rate)		$T_{exhaust}$: 73 ^oC $T_{exhaust}$: 90 ^oC $T_{exhaust}$: 93 ^oC $T_{exhaust}$: 106 ^oC $T_{exhaust}$: 114 ^oC		99 % -99.5 %	3.5 kW 4.0 kW 4.6 kW 5.2 kW 5.7 kW	NO: 3ppm, CO:1, SO$_2$:1 NO: 2ppm, CO:1, SO$_2$:1 NO: 2ppm, CO:0, SO$_2$:2 NO: 0ppm, CO:0, SO$_2$:2 NO: 0ppm, CO:0, SO$_2$:4	- E_a:2.08, 6.88 % heat loss at an exhaust temperature of 114 ^oC - High combusiton efficiency and near-zero emission

Ref.	Reactor	Catalyst	Reactant	Tx (^{o}C) X=conv%	Heat transfer	Heat released	Heat recovery efficiency	Input power	Gas exhaust	Remarks
[241] 2007	Fixed-bed central heat exchange (Fig. 2.12c)	MnO_2		99.9 %	T_{inlet}: 833 ^{o}C T_{outlet}: 683 ^{o}C	1.89 MW [a]	63.3 %			- Heat recovery efficiency: hot gas withdrawal > central heat exchange - MnO_2 > Pd catalyst - Conversion: central heat exchange > hot gas withdrawal
	Hot gas withdrawal (Fig. 2.12d)	MnO_2		97.1 %	T_{inlet}: 878 ^{o}C T_{outlet}: 60 ^{o}C	2.85 MW	95.5 %			
		Pd		92.4 %	T_{inlet}: 670 ^{o}C T_{outlet}: 60 ^{o}C	2.16 MW	72.0 %			
[282] 2007	Fixed-bed	$Pd/LaMnO_3$ $2ZrO_2$	E_a: 2 -45 %		T_{inlet}: 30-60 ^{o}C T_{outlet}: 50-80 ^{o}C			10 - 25 kW		- Great improvement of catalytic performance was observed after sulfur aging

Ref.	Reactor	Catalyst	Reactant	Tx (°C) X=conv%	Heat transfer	Heat released	Heat recovery efficiency	Input power	Gas exhaust	Remarks
[31] 2009	Fixed-bed (i.d.: 50 mm L: 120 mm)	Pd/LaMnO$_3$/ZrO$_2$ Pd/CeO$_2$/ZrO$_2$ Pd/BaCeO$_3$/ZrO$_2$ (catalyst coating on FeCrAl fibre mat)	E_a: 5 % [b]	T_{50}: 570 T_{50}: 382 T_{50}: 512	T_{inlet}: 30 °C T_{outlet}: 50 °C (heat up water)			10 kW 22 kW 35 kW	~65-85 mg kWh^{-1} ~150-160 ~160-175	- NO increased at low input power - NO decreased at high air excess
			E_a: 30 %					10 kW 22 kW 35 kW	~40-50 ~45-50 ~55-65	
			E_a: 60 %					10 kW 22 kW 35 kW	~0 ~0 ~0	
[244] 2009	Fixed-bed hot gas withdrawal without returning cold gases	Pd-washcoated monolith	3000 ppm 5000 ppm 7000 ppm 9000 ppm	T_{97-99}: 400 T_{97-99}: 420-460 T_{98-99}: 430-550 T_{99-100}: 440-650		9.8 MW 16.4 MW 23.0 MW 29.5 MW	10-100 %			- Stability: withdrawal hot gas at bed end > withdrwal hot gas at center; no returning cold gas > returning - At the end of bed without returning cold gas showed the best conversion and heat recovery efficiency
	With returning cold gases		3000-9000 ppm	T_{98-100}: 400-500			0-73 %			

Ref.	Reactor	Catalyst	Reactant	Tx (^{o}C) X=conv%	Heat transfer	Heat released	Heat recovery efficiency	Input power	Gas exhaust	Remarks
[278] 2014	Fluidized-bed (i.d.: 0.1 m L: 0.66 m)	0.5 wt% Pd/Al$_2$O$_3$	0.15 % methane	T$_{97}$ = 500					CO < 10 ppm	- Methane conversion presented an increase with increasing bed temperature, and showed a slightly decrease as increasing the inlet methane concentration.
			3 % methane	T$_{88}$ = 500						
[283] 2015	Fixed-bed L: 40 mm	Pt/Al$_2$O$_3$ Pt/ZSM-5	Flow rate (mL min^{-1}) 800 1400	T$_{76}$: ~230 T$_{57}$: ~395	Q$_{surface}$ ^{c} ~7 W ~9.6 W			35.2 W 61.7 W		- 20 mm catalyst bed length showed better catalytic performance and combustion efficiency than 40 mm and 10 mm bed length, because it balanced the catalyst spatial density and the residence time
	L: 20 mm		2000 800 1400	T$_{36}$: ~350 T$_{58}$: ~310 T$_{80}$: ~335	~8.2 W ~7.7 W ~8.9 W			88.1 W 35.2 W 61.7 W		
	L: 10 mm		2000 800 1400 1800	T$_{90}$: ~350 T$_{33}$: ~250 T$_{25}$: ~255 T$_{18}$: ~210	~9.2 W ~6.4 W ~6.8 W ~6.2 W			88.1 W 35.2 W 61.7 W 79.2 W		
[274]	Membrane	Pd/γ-Al$_2$O$_3$	3-4 % CH$_4$	T$_{73.5-91.2}$:	Yield of H$_2$:					- 91 % methane conversion in steam reforming, and

Ref.	Reactor	Catalyst	Reactant	Tx (°C) X=conv%	Heat transfer	Heat released	Heat recovery efficiency	Input power	Gas exhaust	Remarks
2015	reactor Coupled with steam reforming rector (Fig. 2.17d)	Ru-MgO-La$_2$O$_3$/ γ-Al$_2$O$_3$	In air	555-575 °C T$_{\sim91}$: 570 °C	103-153 kg day^{-1} kg$_{cat}^{-1}$					99.99 % purity hydrogen can be obtained by the provived heated from methane combustion
[227] 2016	Fluidized-bed (i.d.: 0.102 m L: 1.88 m)	0.5 wt% Pd/Al$_2$O$_3$	0.30 % methane 0.10 m s^{-1} 0.25 m s^{-1}	 T$_{98}$ = 550 T$_{73}$ = 550						- Methane conversion presented a decrease with increasing velocity

a. Amount of heat flux withdrawal;

b. E_a: air excess;

c. Q$_{surface}$: heat release rate transferred via combustor surface.

Table 2.6 Advantages and disadvantages of various reactor types for CMC.

Reactor type	Advantages	Disadvantages
Fixed-bed	- Easy operation - Low cost - Suitable for industrial uses - Enhanced catalyst spatial density	- Low reactor surface area - Poor temperature uniformity - High pressure drop
Micro/mini structured	- High surface-to-volume ratio - High mass/heat transfer rate - Low pressure drop - Inherent safety (e.g., hazardous reaction mixtures can be handled safely due to channel dimensions below the quenching distance) - Compact design	- High manufacture cost - Not easy to replace the catalyst if washcoated
Monolithic	- Regular and well-defined structure - High surface-to-volume ratio - High mass/heat transfer rate - Low pressure drop - High thermal stability - Low cost	- Not easy to replace the catalyst if washcoated
Membrane	- Reaction and product separation in one reactor - By changing oxygen permeation and partial pressure to achieve the high conversion, and products are easy to withdrawal under high pressures	- High cost of membrane replacement
Fluidized bed	- Enhanced gas-solid catalyst contact - Enhanced heat/mass transfer - Low pressure drop - Good temperature distribution	- Large-scale device - Catalyst mass loss and high heat loss - Reactor bed temperature fluctuation

2.6. Summary and prospect

This work provides an extensive review on the CMC. Different catalysts, mechanisms, effect of operational parameters and reactor types are discussed. The main conclusions may be summarized as follows.

Noble metal catalysts with high activity are favorable for CMC at low temperatures (<700 ^{o}C). The bi-metallic catalysts have a better catalytic activity due to the more active sites and electronic synergy effects. The hexaaluminate and perovskite mixed metal-oxide catalysts with different microstructured features exhibit a high thermal stability, thus more suitable for high temperature applications (700-1300 ^{o}C).

The Mars-van Krevelen mechanism is more widely accepted than the Langmuir-Hinselwood and Eley-Rideal mechanisms. It has been observed by in-situ (spectroscopic) technologies that the adsorbed oxygen species in PdO catalyst are responsible for the methane oxidation, rather than oxygen in gas phase.

The light-off temperature is mainly influenced by the operating temperature and the oxygen to methane molar ratio. It varies depending on different catalyst properties. The optimized O_2/CH_4 molar ratio is beneficial for a full methane conversion due to the optimized coverage of the adsorbed mixtures over the surface.

The natural gas containing the sulfur compound, carbon dioxide and water vapor can suppress the catalytic activity due to the competitive adsorption and the blockage of active sites. The deactivation due to water and carbon dioxide is reversible whereas the sulfur poisoning is irreversible.

The reversal flow mode for fixed-bed reactors with hot gas withdrawal at the end of the bed and without the return of cold gas is highly recommended in order to maximize the heat recovery and methane conversion.

The recent development of mini/microstructured reactor with compact design has been broadly investigated for coupling the CMC with endothermic reaction (methane steam reforming) at different flow modes. The co-current flow mode presents a better thermal efficiency than the counter-current flow one.

Some scientific and technological barriers remain to be overcome for the wide spread industrial application of CMC, which are also the key issues and challenges of the current research and development:

To improve the thermal stability and to prolong the lifetime of noble metal catalysts by avoiding the possible sintering at high temperature levels.

To improve the current understanding into CMC reaction mechanisms and the corresponding kinetic models, including the deactivation mechanism (e.g., CMC with the presence of water and sulfides etc.).

To lower the light-off temperature and to maintain the long-term high catalytic activity of hexaaluminate and perovskite catalysts.

To develop effective desulfurization pre-treatment and measures in order to extend the catalyst lifetime.

To improve mechanical and chemical stabilities of the catalyst coating, and to cope with the deactivation issue by proposing replacement and/or regeneration methods.

To further enhance the heat and mass transfer in compact and integrated catalytic reactor-heat exchangers.

References

[1]   G. Karavalakis, T.D. Durbin, M. Villela, J.W. Miller, Air pollutant emissions of light-duty vehicles operating on various natural gas compositions, J Nat. Gas Sci. Eng,. 4 (2012) 8-16. https://doi.org/10.1016/j.jngse.2011.08.005.

[2]   U.S. Energy Information Administration. International energy outlook, https://www.eia.gov/todayinenergy/detail.php?id=32912; 2017 [Accessed 22 September 2014].

[3]   B. Durand, Petroleum, natural gas and coal: Nature, formation mechanisms, future prospects in the energy transition, EDP sciences, 101-152, 2019.

[4]   Centre for Energy Economics Research and Policy, UK. BP Statistical review of world energy, https://www.bp.com/en/global/corporate/energy-economics/statistical-review-of-world-energy; 2018 [Accessed 19 April 2019].

[5]   C. Zou, Q. Zhao, G. Zhang, B. Xiong, Energy revolution: from a fossil energy era to a new energy era, Nat. Gas Ind. B. 3 (2016) 1-11. https://doi.org/10.1016/j.ngib.2016.02.001.

[6]   A.W. Petrov, D. Ferri, F. Krumeich, M. Nachtegaal, J.A. van Bokhoven, O. Kröcher, Stable complete methane oxidation over palladium based zeolite catalysts, Nat. Commun. 9 (2018) 2545-2553. http://dx.doi.org/10.1038/s41467-018-04748-x.

[7]   M. Mehrpooya, M. Khalili, M.M.M. Sharifzadeh, Model development and energy and exergy analysis of the biomass gasification process (Based on the various biomass sources), Renew Sust Energ Rev. 91 (2018) 869-887. https://doi.org/10.1016/j.rser.2018.04.076.

[8]   F. Ahmad, E.L. Silva, M.B.A. Varesche, Hydrothermal processing of biomass for anaerobic digestion-A review, Renew Sust Energ Rev. 98 (2018) 108-124. https://doi.org/10.1016/j.rser.2018.09.008.

[9]   S.N. Naik, V.V. Goud, P.K. Rout, A.K. Dalai, Production of first and second generation biofuels: a comprehensive review, Renew Sust Energ Rev. 14 (2010) 578-597. https://doi.org/10.1016/j.rser.2009.10.003.

[10]   H. Li, E. Larsson, E. Thorin, E. Dahlquist, X. Yu, Feasibility study on combining anaerobic digestion and biomass gasification to increase the production of biomethane, Energy Convers. Manage. 100 (2015) 212-219. https://doi.org/10.1016/j.enconman.2015.05.007.

[11]   S. Sansaniwal, M. Rosen, S. Tyagi, Global challenges in the sustainable development of biomass gasification: an overview, Renew Sust Energ Rev. 80 (2017) 23-43. https://doi.org/10.1016/j.rser.2017.05.215.

[12]   R. Zwart, H. Boerrigter, E. Deurwaarder, C. Van der Meijden, S. Van Paasen. Production of synthetic natural gas (SNG) from biomass, http://www.ecn.nl/docs/library/report/2006/e06018.pdf; 2006 [Accessed 3 June 2013].

[13]   C.R. Vitasari, M. Jurascik, K.J. Ptasinski, Exergy analysis of biomass-to-synthetic natural gas (SNG) process via indirect gasification of various biomass feedstock, Energy. 36 (2011) 3825-3837. https://doi.org/10.1016/j.energy.2010.09.026.

[14]   F.L. Ricciardolo, P.J. Sterk, B. Gaston, G. Folkerts, Nitric oxide in health and disease of the respiratory system, Physiol. Rev. 84 (2004) 731-765. https://doi.org/10.1152/physrev.00034.2003.

[15]   Y.S. Najjar, Gaseous pollutants formation and their harmful effects on health and environment, Innovative energy policies. 1 (2011) 1-9. https://doi.org/10.4303/iep/E101203.

[16]   Official Journal of the European Union. Commision regulation (EU) No. 813/2013, http://data.europa.eu/eli/reg/2013/813/oj; [Accessed 2 August 2013].

[17]   J. Chen, H. Arandiyan, X. Gao, J. Li, Recent advances in catalysts for methane combustion, Catal. Surv. Asia. 19 (2015) 140-171. https://doi.org/10.1007/s10563-015-9191-5.

[18]   P. Gélin, M. Primet, Complete oxidation of methane at low temperature over noble metal based catalysts: a review, Appl. Catal., B. 39 (2002) 1-37. http://dx.doi.org/10.1016/S0926-3373(02)00076-0.

[19]   R. Burch, P.K. Loader, Investigation of Pt/Al$_2$O$_3$ and Pd/Al$_2$O$_3$ catalysts for the combustion of methane at low concentrations, Appl. Catal., B. 5 (1994) 149-164. http://dx.doi.org/10.1016/0926-3373(94)00037-9.

[20]   P. Gélin, L. Urfels, M. Primet, E. Tena, Complete oxidation of methane at low temperature over Pt and Pd catalysts for the abatement of lean-burn natural gas fuelled vehicles emissions: influence of water and sulphur containing compounds, Catal. Today. 83 (2003) 45-57. http://dx.doi.org/10.1016/s0920-5861(03)00215-3.

[21]   H. Hao, Z. Liu, F. Zhao, W. Li, Natural gas as vehicle fuel in China: A review, Renew Sust Energ Rev. 62 (2016) 521-533. https://doi.org/10.1016/j.rser.2016.05.015.

[22]   P. Forzatti, Status and perspectives of catalytic combustion for gas turbines, Catal. Today. 83 (2003) 3-18. http://dx.doi.org/10.1016/s0920-5861(03)00211-6.

[23]   M. Lyubovsky, L.L. Smith, M. Castaldi, H. Karim, B. Nentwick, S. Etemad, R. LaPierre, W.C. Pfefferle, Catalytic combustion over platinum group catalysts: fuel-lean versus fuel-rich operation, Catal. Today. 83 (2003) 71-84. http://dx.doi.org/10.1016/s0920-5861(03)00217-7.

[24]   S. Su, X. Yu, A 25 kWe low concentration methane catalytic combustion gas turbine prototype unit, Energy. 79 (2015) 428-438. http://dx.doi.org/10.1016/j.energy.2014.11.031.

[25]   Z.R. Ismagilov, N.V. Shikina, S.A. Yashnik, A.N. Zagoruiko, M.A. Kerzhentsev, V.A. Ushakov, V.A. Sazonov, V.N. Parmon, V.M. Zakharov, B.I. Braynin, O.N. Favorski, Technology of methane combustion on granulated catalysts for environmentally friendly gas turbine power plants, Catal. Today. 155 (2010) 35-44. http://dx.doi.org/10.1016/j.cattod.2010.04.008.

[26]   H. Sadamori, Application concepts and evaluation of small-scale catalytic combustors for natural gas, Catal. Today. 47 (1999) 325-338. https://doi.org/10.1016/S0920-5861(98)00314-9.

[27]   K.I. Khidr, Y.A. Eldrainy, M.M. EL-Kassaby, Towards lower gas turbine emissions: Flameless distributed combustion, Renew Sust Energ Rev. 67 (2017) 1237-1266. https://doi.org/10.1016/j.rser.2016.09.032.

[28]   T.M. Gür, Comprehensive review of methane conversion in solid oxide fuel cells: prospects for efficient electricity generation from natural gas, Prog. Energy Combust. Sci. 54 (2016) 1-64. https://doi.org/10.1016/j.pecs.2015.10.004.

[29]   S.R. Vaillant, A.S. Gastec, Catalytic combustion in a domestic natural gas burner, Catal. Today. 47 (1999) 415-420. http://dx.doi.org/10.1016/S0920-5861(98)00324-1.

[30]   S. Jugjai, N. Rungsimuntuchart, High efficiency heat-recirculating domestic gas burners, Exp. Therm Fluid Sci. 26 (2002) 581-592. http://dx.doi.org/10.1016/S0894-1777(02)00164-4.

[31]   S. Specchia, G. Toniato, Natural gas combustion catalysts for environmental-friendly domestic burners, Catal. Today. 147 (2009) 99-106. http://dx.doi.org/10.1016/j.cattod.2009.07.033.

[32]   Y.S. Seo, S.P. Yu, S.J. Cho, K.S. Song, The catalytic heat exchanger using catalytic fin tubes, Chem. Eng. Sci. 58 (2003) 43-53. http://dx.doi.org/10.1016/S0009-2509(02)00475-X.

[33]   D. X.Chun, Applied studies on methane catalytic combustion development of a natural gas premixed catalytic burner and boiler for household applications. 2005; Sichuan University. Thesis in chinese.

[34]   M. Rahimpour, M. Dehnavi, F. Allahgholipour, D. Iranshahi, S. Jokar, Assessment and comparison of different catalytic coupling exothermic and endothermic reactions: a review, Appl. Energy. 99 (2012) 496-512. https://doi.org/10.1016/j.apenergy.2012.04.003.

[35]   H. Mei, C. Li, S. Ji, H. Liu, Modeling of a metal monolith catalytic reactor for methane steam reforming-combustion coupling, Chem. Eng. Sci. 62 (2007) 4294-4303. http://dx.doi.org/10.1016/j.ces.2007.05.011.

[36]   Y. Chen, H. Xu, X. Jin, G. Xiong, Integration of gasoline prereforming into autothermal reforming for hydrogen production, Catal. Today. 116 (2006) 334-340. http://dx.doi.org/10.1016/j.cattod.2006.05.065.

[37]   M. Van Sint Annaland, H.A.R. Scholts, J.A.M. Kuipers, W.P.M. Van Swaaij, A novel reverse flow reactor coupling endothermic and exothermic reactions, part II: Sequential reactor conguration for reversible endothermic reactions, Chem. Eng. Sci. 57 (2002) 855-872. http://dx.doi.org/10.1016/S0009-2509(01)00423-7.

[38]   K. Venkataraman, J.M. Redenius, L.D. Schmidt, Millisecond catalytic wall reactors: dehydrogenation of ethane, Chem. Eng. Sci. 57 (2002) 2335-2343. http://dx.doi.org/10.1016/S0009-2509(02)00132-X.

[39]   M. Zanfir, A. Gavriilidis, Modelling of a catalytic plate reactor for dehydrogenation-combustion coupling, Chem. Eng. Sci. 56 (2001) 2671-2683. http://dx.doi.org/10.1016/S0009-2509(00)00522-4.

[40]   S.B. T.V. Choudhary, V.R. Choudhary, Catalysts for combustion of methane and lower alkanes review, Appl. Catal. A. 234 (2002) 1-23. https://doi.org/10.1016/S0926-860X(02)00231-4.

[41]   Z. Li, G.B. Hoflund, A review on complete oxidation of methane at low temperatures, J. Nat. Gas Chem. 12 (2003) 153-160.

[42]   L.M. Quick, S. Kamitomai, Catalytic combustion reactor design and test results, Catal. Today. 26 (1995) 303-308. https://doi.org/10.1016/0920-5861(95)00152-0.

[43]   Z. Anxionnaz, M. Cabassud, C. Gourdon, P. Tochon, Heat exchanger/reactors (HEX reactors): Concepts, technologies: State-of-the-art, Chem. Eng. Process. 47 (2008) 2029-2050. https://doi.org/10.1016/j.cep.2008.06.012.

[44]   G. Kolios, A. Gritsch, A. Morillo, U. Tuttlies, J. Bernnat, F. Opferkuch, G. Eigenberger, Heat-integrated reactor concepts for catalytic reforming and automotive exhaust purification, Appl. Catal., B. 70 (2007) 16-30. https://doi.org/10.1016/j.apcatb.2006.01.030.

[45]   J.G. McCarty, Kinetics of PdO combustion catalysis, Catal. Today. 26 (1995) 283-293. http://dx.doi.org/10.1016/0920-5861(95)00150-7.

[46]   R.G.W. Norrish, S.G. Foord, The kinetics of the combustion of methane, Proc. R. Soc. London, Ser. A. 157 (1936) 503-525. https://doi.org/10.1098/rspa.1936.0211.

[47]   K. Otto, Methane oxidation over Pt on gamma-alumina: kinetics and structure sensitivity, Langmuir. 5 (1989) 1364-1369. http://dx.doi.org/10.1021/la00090a018.

[48]   P. Dagaut, J.C. Boettner, M. Cathonnet, Methane oxidation: experimental and kinetic modeling study, Combust. Sci. Technol. 77 (1991) 127-148. https://doi.org/10.1080/00102209108951723.

[49]   G. Kolb, V. Hessel, Micro-structured reactors for gas phase reactions, Chem. Eng. J. 98 (2004) 1-38. https://doi.org/10.1016/j.cej.2003.10.005.

[50]   J. Yue, Multiphase flow processing in microreactors combined with heterogeneous catalysis for efficient and sustainable chemical synthesis, Catal. Today. 308 (2018) 3-19. https://doi.org/10.1016/j.cattod.2017.09.041.

[51]   Y. Lei, W. Chen, J. Lei, Combustion and direct energy conversion inside a micro-combustor, Appl. Therm. Eng. 100 (2016) 348-355. https://doi.org/10.1016/j.applthermaleng.2016.01.162.

[52]   M. Tian, X.D. Wang, T. Zhang, Hexaaluminates: a review of the structure, synthesis and catalytic performance, Catal. Sci. Technol. 6 (2016) 1984-2004. https://doi.org/10.1039/C5CY02077H.

[53]   J. Zhu, H. Li, L. Zhong, P. Xiao, X. Xu, X. Yang, Z. Zhao, J. Li, Perovskite Oxides: Preparation, Characterizations, and Applications in Heterogeneous Catalysis, ACS Catal. 4 (2014) 2917-2940. https://doi.org/10.1021/cs500606g.

[54]   A. Hepbasli, Y. Kalinci, A review of heat pump water heating systems, Renew Sust Energ Rev. 13 (2009) 1211-1229. https://doi.org/10.1016/j.rser.2008.08.002.

[55]   O. Ibrahim, F. Fardoun, R. Younes, H. Louahlia-Gualous, Review of water-heating systems: General selection approach based on energy and environmental aspects, Build. Environ. 72 (2014) 259-286. https://doi.org/10.1016/j.buildenv.2013.09.006.

[56]   J. Kopyscinski, T.J. Schildhauer, S.M. Biollaz, Production of synthetic natural gas (SNG) from coal and dry biomass - A technology review from 1950 to 2009, Fuel. 89 (2010) 1763-1783. https://doi.org/10.1016/j.fuel.2010.01.027.

[57]   D. Ciuparu, M.R. Lyubovsky, E. Altman, L.D. Pfefferle, A. Datye, Catalytic combustion of methane over palladium-based catalysts, Catal. Rev. 44 (2002) 593-649. https://doi.org/10.1081/CR-120015482.

[58]   A. Cruellas, T. Melchiori, F. Gallucci, M. van Sint Annaland, Advanced reactor concepts for oxidative coupling of methane, Catal. Rev. 59 (2017) 234-294. https://doi.org/10.1080/01614940.2017.1348085.

[59]   J. Yang, Y. Guo, Nanostructured perovskite oxides as promising substitutes of noble metals catalysts for catalytic combustion of methane, Chin. Chem. Lett. 29 (2018) 252-260. https://doi.org/10.1016/j.cclet.2017.09.013.

[60]   R.W. Sidwell, H. Zhu, B.A. Kibler, R.J. Kee, D.T. Wickham, Experimental investigation of the activity and thermal stability of hexaaluminate catalysts for lean methane-air combustion, Appl. Catal. A. 255 (2003) 279-288. http://dx.doi.org/10.1016/s0926-860x(03)00566-0.

[61]   H. Inoue, K. Sekizawa, K. Eguchi, H. Arai, Thermal stability of hexaaluminate film coated on SiC substrate for high-temperature catalytic application, J. Am. Ceram. Soc. 80 (1997) 584-588. https://doi.org/10.1111/j.1151-2916.1997.tb02870.x.

[62]   H. Inoue, K. Sekizawa, K. Eguchi, H. Arai, Thick-film coating of hexaaluminate catalyst on ceramic substrates for high-temperature combustion, Catal. Today. 47 (1999) 181-190. http://dx.doi.org/10.1016/S0920-5861(98)00298-3.

[63]   G. Groppi, C. Cristiani, P. Forzatti, $BaFe_xAl_{(12-x)}O_{19}$ system for high-temperature catalytic combustion: physico-chemical characterization and catalytic activity, J. Catal. 168 (1997) 95-103. https://doi.org/10.1006/jcat.1997.1632.

[64]   N. Iyi, S. Takekawa, S. Kimura, Crystal chemistry of hexaaluminates: β-alumina and magnetoplumbite structures, J. Solid State Chem. 83 (1989) 8-19. http://dx.doi.org/10.1016/0022-4596(89)90048-0.

[65]   M. Machida, K. Eguchi, H. Arai, Catalytic properties of $BaMAl_{11}O_{19-\alpha}$ (M = Cr, Mn, Fe, Co, and Ni) for high-temperature catalytic combustion, J. Catal. 120 (1989) 377-386. https://doi.org/10.1016/0021-9517(89)90277-7.

[66]   P. Artizzu-Duart, Y. Brullé, F. Gaillard, E. Garbowski, N. Guilhaume, M. Primet, Catalytic combustion of methane over copper- and manganese-substituted barium hexaaluminates, Catal. Today. 54 (1999) 181-190. https://doi.org/10.1016/S0920-5861(99)00179-0.

[67]   D. Wickham, R. Cook, Thermally stable catalysts for methane combustion. United States patent US 20030176278. 2003 September 18.

[68]   Y. Zhang, X. Wang, Y. Zhu, X. Liu, T. Zhang, Thermal evolution crystal structure and Fe crystallographic sites in $LaFe_xAl_{12-x}O_{19}$ hexaaluminates, The Journal of Physical Chemistry C. 118 (2014) 10792-10804. https://doi.org/10.1021/jp500682d.

[69]   X. Wang, K. Huang, W. Ma, Y. Cong, C. Ge, S. Feng, Defect engineering, electronic structure, and catalytic properties of perovskite oxide $La_{0.5}Sr_{0.5}CoO_{3-\delta}$, Chem. Eur. J. 23 (2017) 1093-1100. https://doi.org/10.1002/chem.201604065.

[70]   J. Shen, R.W. Scott, R.E. Hayes, N. Semagina, Structural evolution of bimetallic Pd-Ru catalysts in oxidative and reductive applications, Appl. Catal. A. 502 (2015) 350-360. https://doi.org/10.1016/j.apcata.2015.06.025.

[71]   M. Machida, K. Eguchi, H. Arai, Effect of additives on the surface area of oxide supports for catalytic combustion, J. Catal. 103 (1987) 385-393. http://dx.doi.org/10.1016/0021-9517(87)90129-1.

[72]   M. Pena, J. Fierro, Chemical structures and performance of perovskite oxides, Chem. Rev. 101 (2001) 1981-2018. https://doi.org/10.1021/cr980129f.

[73]   H. Arai, T. Yamada, K. Eguchi, T. Seiyama, Catalytic combustion of methane over various perovskite-type oxides, Appl. Catal., A. 26 (1986) 265-276. https://doi.org/10.1016/S0166-9834(00)82556-7.

[74]   S. Cimino, L. Lisi, R. Pirone, G. Russo, M. Turco, Methane combustion on perovskites-based structured catalysts, Catal. Today. 59 (2000) 19-31. https://doi.org/10.1016/S0920-5861(00)00269-8.

[75]   S. Laassiri, N. Bion, D. Duprez, S. Royer, H. Alamdari, Clear microstructure-performance relationships in Mn-containing perovskite and hexaaluminate compounds prepared by activated reactive synthesis, Phys. Chem. Chem. Phys. 16 (2014) 4050-4060. https://doi.org/10.1039/C3CP54363C.

[76]   N. Miniajluk, J. Trawczyński, M. Zawadzki, W. Tylus, LaMnO$_3$ (La$_{0.8}$Sr$_{0.2}$MnO$_3$) perovskites for lean methane combustion: effect of synthesis method, Adv. Mater. Phys. Chem. 8 (2018) 193. https://doi.org/10.4236/ampc.2018.84013.

[77]   F.F. Tao, J.-j. Shan, L. Nguyen, Z. Wang, S. Zhang, L. Zhang, Z. Wu, W. Huang, S. Zeng, P. Hu, Understanding complete oxidation of methane on spinel oxides at a molecular level, Nat. Commun. 6 (2015) 7798. https://doi.org/10.1038/ncomms8798.

[78]   F. Miao, F. Wang, D. Mao, X. Guo, J. Yu, H. Huang, G. Lu, Effect of different reaction conditions on catalytic activity of La(Mn, Fe)O$_{3+\lambda}$ catalyst for methane combustion, Materials Research Express. 6:5 (2019). https://doi.org/10.1088/2053-1591/aaff8a.

[79]   J. Li, H. Fu, L. Fu, J. Hao, Complete combustion of methane over indium tin oxides catalysts, Environ. Sci. Technol. 40 (2006) 6455-6459. https://doi.org/10.1021/es061629q.

[80]   R. Polini, A. Falsetti, E. Traversa, O. Schäf, P. Knauth, Sol-gel synthesis, X-ray photoelectron spectroscopy and electrical conductivity of Co-doped (La, Sr)(Ga, Mg)O$_{3-\delta}$ perovskites, J. Eur. Ceram. Soc. 27 (2007) 4291-4296. https://doi.org/10.1016/j.jeurceramsoc.2007.02.147.

[81]   A. Bhalla, R. Guo, R. Roy, The perovskite structure-a review of its role in ceramic science and technology, Mater. Res. Innovations. 4 (2000) 3-26. https://doi.org/10.1007/s100190000062.

[82]   F. Polo-Garzon, Z. Wu, Acid–base catalysis over perovskites: a review, J. Mater. Chem. A. 6 (2018) 2877-2894. https://doi.org/10.1039/C7TA10591F.

[83]   H. Zhu, P. Zhang, S. Dai, Recent advances of lanthanum-based perovskite oxides for catalysis, ACS Catal. 5 (2015) 6370-6385. https://doi.org/10.1021/acscatal.5b01667.

[84]   P. Granger, V.I. Parvulescu, S. Kaliaguine, W. Prellier, Perovskites and related mixed oxides: concepts and applications, Wiley, 2015.

[85]   A. Ersson, K. Persson, I.K. Adu, S.G. Järås, A comparison between hexaaluminates and perovskites for catalytic combustion applications, Catal. Today. 112 (2006) 157-160. https://doi.org/10.1016/j.cattod.2005.11.024.

[86]   G.B. Hoflund, Z. Li, W.S. Epling, T. Göbel, P. Schneider, H. Hahn, Catalytic methane oxidation over Pd supported on nanocrystalline and polycrystalline TiO$_2$, Mn$_3$O$_4$, CeO$_2$ and ZrO$_2$, React. Kinet. Catal. Lett. 70 (2000) 97-103. https://doi.org/10.1023/A:1010362632223.

[87]   A. Ersson, H. Kušar, R. Carroni, T. Griffin, S. Järås, Catalytic combustion of methane over bimetallic catalysts a comparison between a novel annular reactor and a high-pressure reactor, Catal. Today. 83 (2003) 265-277. https://doi.org/10.1016/s0920-5861(03)00247-5.

[88]   M. Bhagiyalakshmi, R. Anuradha, S.D. Park, T.S. Park, W.S. Cha, H.T. Jang, Effect of bimetallic Pt-Rh and trimetallic Pt-Pd-Rh catalysts for low temperature catalytic combustion of methane, Bull. Korean Chem. Soc. 31 (2010) 120-124. https://doi.org/10.5012/bkcs.2010.31.01.120.

[89]   N. Kinnunen, M. Suvanto, M. Moreno, A. Savimäki, K. Kallinen, T.-J. Kinnunen, T. Pakkanen, Methane oxidation on alumina supported palladium catalysts: effect of Pd precursor and solvent, Appl. Catal. A. 370 (2009) 78-87. https://doi.org/10.1016/j.apcata.2009.09.018.

[90]   R.J. Farrauto, M. Hobson, T. Kennelly, E. Waterman, Catalytic chemistry of supported palladium for combustion of methane, Appl. Catal. A. 81 (1992) 227-237. https://doi.org/10.1016/0926-860X(92)80095-T.

[91]   R.J. Farrauto, T. Kennelly, E.M. Waterman, M.C. Hobson Jr, Process conditions for operation of ignition catalyst for natural gas combustion. 1993; Google Patents.

[92]   G. Pecchi, P. Reyes, T. López, R. Gómez, Pd-CeO$_2$ and Pd-La$_2$O$_3$/alumina-supported catalysts: their effect on the catalytic combustion of methane, J. Non-Cryst. Solids. 345 (2004) 624-627. https://doi.org/10.1016/j.jnoncrysol.2004.08.110.

[93]   A. Toso, S. Colussi, S. Padigapaty, C. de Leitenburg, A. Trovarelli, High stability and activity of solution combustion synthesized Pd-based catalysts for methane combustion in presence of water, Appl. Catal., B. 230 (2018) 237-245. https://doi.org/10.1016/j.apcatb.2018.02.049.

[94]   V.A. Drozdov, P.G. Tsyrulnikov, V.V. Popovskii, N.N. Bulgakov, E.M. Moroz, T.G. Galeev, Comparative study of the activity of Al-Pd and Al-Pt catalysts in deep oxidation of hydrocarbons, React. Kinet. Catal. Lett. 27 (1985) 425-427. https://doi.org/10.1007/bf02070487.

[95]   P. Euzen, J.-H. Le Gal, B. Rebours, G. Martin, Deactivation of palladium catalyst in catalytic combustion of methane, Catal. Today. 47 (1999) 19-27. https://doi.org/10.1016/S0920-5861(98)00280-6.

[96]   R.F. Hicks, H. Qi, M.L. Young, R.G. Lee, Structure sensitivity of methane oxidation over platinum and palladium, J. Catal. 122 (1990) 280-294. https://doi.org/10.1016/0021-9517(90)90282-O.

[97]   K. Persson, A. Ersson, K. Jansson, N. Iverlund, S. Jaras, Influence of co-metals on bimetallic palladium catalysts for methane combustion, J. Catal. 231 (2005) 139-150. https://doi.org/10.1016/j.jcat.2005.01.001.

[98]   K. Persson, A. Ersson, K. Jansson, J. Fierro, S.G. Järås, Influence of molar ratio on Pd-Pt catalysts for methane combustion, J. Catal. 243 (2006) 14-24. https://doi.org/10.1016/j.jcat.2006.06.019.

[99]   N.M. Kinnunen, J.T. Hirvi, M. Suvanto, T.A. Pakkanen, Methane combustion activity of Pd-PdO$_x$-Pt/Al$_2$O$_3$ catalyst: the role of platinum promoter, J. Mol. Catal. A: Chem. 356 (2012) 20-28. https://doi.org/10.1016/j.molcata.2011.12.023.

[100]   P. Stefanov, S. Todorova, A. Naydenov, B. Tzaneva, H. Kolev, G. Atanasova, D. Stoyanova, Y. Karakirova, K. Aleksieva, On the development of active and stable Pd-Co/γ-Al$_2$O$_3$ catalyst for complete oxidation of methane, Chem. Eng. J. 266 (2015) 329-338. http://dx.doi.org/10.1016/j.cej.2014.12.099.

[101]   S. Zhang, P. Kang, M. Bakir, A.M. Lapides, C.J. Dares, T.J. Meyer, Polymer-supported CuPd nanoalloy as a synergistic catalyst for electrocatalytic reduction of carbon dioxide to methane, Proc. Natl. Acad. Sci. U. S. A. 112 (2015) 15809-15814. https://doi.org/10.1073/pnas.1522496112.

[102]   K. Persson, K. Jansson, S. Jaras, Characterisation and microstructure of Pd and bimetallic Pd-Pt catalysts during methane oxidation, J. Catal. 245 (2007) 401-414. https://doi.org/10.1016/j.jcat.2006.10.029.

[103]   K. Persson, A. Ersson, A.M. Carrera, J. Jayasuriya, R. Fakhrai, T. Fransson, S. Järås, Supported palladium-platinum catalyst for methane combustion at high pressure, Catal. Today. 100 (2005) 479-483. https://doi.org/10.1016/j.cattod.2004.08.018.

[104]   P. Briot, A. Auroux, D. Jones, M. Primet, Effect of particle size on the reactivity of oxygen-adsorbed platinum supported on alumina, Applied Catalysis. 59 (1990) 141-152. http://dx.doi.org/10.1016/S0166-9834(00)82193-4.

[105]   E. Marceau, M. Che, J. Saint-Just, J.M. Tatibouët, Influence of chlorine ions in Pt/Al$_2$O$_3$ catalysts for methane total oxidation, Catal. Today. 29 (1996) 415-419. http://dx.doi.org/10.1016/0920-5861(95)00313-4.

[106]   A.T. Gremminger, H.W. Pereira de Carvalho, R. Popescu, J.D. Grunwaldt, O. Deutschmann, Influence of gas composition on activity and durability of bimetallic Pd-Pt/Al2O3 catalysts for total oxidation of methane, Catal. Today. 258 (2015) 470-480. https://doi.org/10.1016/j.cattod.2015.01.034.

[107]   Y. Hajar, B. Venkatesh, E. Baranova, Electrochemical promotion of nanostructured palladium catalyst for complete methane oxidation, Catalysts. 9 (2019) 48. https://doi.org/10.3390/catal9010048.

[108]   Y.M. Hajar, B. Venkatesh, M.S. Houache, H. Liu, R. Safari, S. Prabhudev, G.A. Botton, E.A. Baranova, Electrochemical promotion of Bi-metallic Ni9Pd core double-shell nanoparticles for complete methane oxidation, J. Catal. 374 (2019) 127-135. https://doi.org/10.1016/j.jcat.2019.04.026.

[109]   K. Li, D. Xu, K. Liu, H. Ni, F. Shen, T. Chen, B. Guan, R. Zhan, Z. Huang, H. Lin, Catalytic combustion of lean methane assisted by an electric field over Mn$_x$Co$_y$ catalysts at low temperature, The Journal of Physical Chemistry C. 123 (2019) 10377-10388. https://doi.org/10.1021/acs.jpcc.9b00496.

[110]   K. Li, K. Liu, H. Ni, B. Guan, R. Zhan, Z. Huang, H. Lin, Electric field promoted ultra-lean methane oxidation over Pd-Ce-Zr catalysts at low temperature, Molecular Catalysis. 459 (2018) 78-88. https://doi.org/10.1016/j.mcat.2018.08.021.

[111]   K. Liu, K. Li, D. Xu, H. Lin, B. Guan, T. Chen, Z. Huang, Catalytic Combustion of Lean Methane Assisted by Electric Field over Pd/Co$_3$O$_4$ Catalysts at Low Temperature, Journal of Shanghai Jiaotong University (Science). 23 (2018) 8-17. https://doi.org/10.1007/s12204-018-2017-7.

[112]   M. Adamowska, P. Da Costa, Structured Pd/γ-Al$_2$O$_3$ prepared by washcoated deposition on a ceramic honeycomb for compressed natural gas applications, J. Nanopart. 2015 (2015) 1-9. https://doi.org/10.1155/2015/601941.

[113]   O. Deutschmann, L.I. Maier, U. Riedel, A.H. Stroemman, R.W. Dibble, Hydrogen assisted catalytic combustion of methane on platinum, Catal. Today. 59 (2000) 141-150. http://dx.doi.org/10.1016/S0920-5861(00)00279-0.

[114]   Y. Li, C. Luo, Z. Liu, L. Sang, Catalytic oxidation characteristics of CH$_4$-air mixtures over metal foam monoliths, Appl. Energy. 156 (2015) 756-761. https://doi.org/10.1016/j.apenergy.2015.05.053.

[115]   H. Yang, J. Li, H. Yu, F. Peng, H. Wang, Metal-foam-supported Pd/Al$_2$O$_3$ catalysts for catalytic combustion of methane: effect of interaction between support and catalyst, Int. J. Chem. React. Eng. 13 (2015). http://dx.doi.org/10.1515/ijcre-2014-0009.

[116]   M. O'Connell, G. Kolb, R. Zapf, Y. Men, V. Hessel, Bimetallic catalysts for the catalytic combustion of methane using microreactor technology, Catal. Today. 144 (2009) 306-311. https://doi.org/10.1016/j.cattod.2008.10.053.

[117]   M. Mundhwa, R.D. Parmar, C.P. Thurgood, A comparative parametric study of a catalytic plate methane reformer coated with segmented and continuous layers of combustion catalyst for hydrogen production, J. Power Sources. 344 (2017) 85-102. http://dx.doi.org/10.1016/j.jpowsour.2017.01.082.

[118]   L. He, Y. Fan, L. Luo, J. Bellettre, J. Yue, Preparation of Pt/γ-Al$_2$O$_3$ catalyst coating in microreactors for catalytic methane combustion, Chem. Eng. J. 380 (2020) 122424. https://doi.org/10.1016/j.cej.2019.122424.

[119]   Z.R. Ismagilov, V.V. Pushkarev, O.Y. Podyacheva, N.A. Koryabkina, H. Veringa, A catalytic heat-exchanging tubular reactor for combining of high temperature exothermic and endothermic reactions, Chem. Eng. J. 82 (2001) 355-360. https://doi.org/10.1016/S1385-8947(00)00349-1.

[120]   V. Meille, Review on methods to deposit catalysts on structured surfaces, Appl. Catal. A. 315 (2006) 1-17. https://doi.org/10.1016/j.apcata.2006.08.031.

[121]   R. Zapf, C. Becker-Willinger, K. Berresheim, H. Bolz, H. Gnaser, V. Hessel, G. Kolb, P.Löb, A.K. Pannwitt, A. Ziogas, Detailed characterization of various porous alumina-based catalyst coatings within microchannels and their testing for methanol steam reforming, Chem. Eng. Res. Des. 81 (2003) 721-729. https://doi.org/10.1205/026387603322302887.

[122]   N.R. Peela, A. Mubayi, D. Kunzru, Washcoating of γ-alumina on stainless steel microchannels, Catal. Today. 147 (2009) S17-S23. https://doi.org/10.1016/j.cattod.2009.07.026.

[123]   M. Liauw, M. Baerns, R. Broucek, O. Buyevskaya, J. Commenge, J. Corriou, L. Falk, K. Gebauer, H. Hefter, O. Langer, Microreaction Technology: Industrial Prospects. Springer, 2000, pp. 224-234.

[124]   X. Xu, H. Vonk, A. Cybulski, J.A. Moulijn, Alumina washcoating and metal deposition of ceramic monoliths, Stud. Surf. Sci. Catal., Elsevier, 1995, pp. 1069-1078.

[125]   K. Haas-Santo, M. Fichtner, K. Schubert, Preparation of microstructure compatible porous supports by sol-gel synthesis for catalyst coatings, Appl. Catal. A. 220 (2001) 79-92. https://doi.org/10.1016/S0926-860X(01)00714-1.

[126]   M. Karches, M. Morstein, P. Rudolf von Rohr, R.L. Pozzo, J.L. Giombi, M.A. Baltanás, Plasma-CVD-coated glass beads as photocatalyst for water decontamination, Catal. Today. 72 (2002) 267-279. https://doi.org/10.1016/S0920-5861(01)00505-3.

[127]   T. Aaltonen, M. Ritala, T. Sajavaara, J. Keinonen, M. Leskelä, Atomic layer deposition of platinum thin films, Chem. Mater. 15 (2003) 1924-1928. https://doi.org/10.1021/cm021333t.

[128]   L.L. Pranevicius, P. Valatkevicius, V. Valincius, C. Montassier, Catalytic behavior of plasma-sprayed Al-Al$_2$O$_3$ coatings doped with metal oxides, Surf. Coat. Technol. 125 (2000) 392-395. https://doi.org/10.1016/S0257-8972(99)00584-8.

[129]   L. Pranevicius, L.L. Pranevicius, P. Valatkevicius, V. Valincius, Plasma spray deposition of Al-Al$_2$O$_3$ coatings doped with metal oxides: catalytic applications, Surf. Coat. Technol. 123 (2000) 122-128. https://doi.org/10.1016/S0257-8972(99)00520-4.

[130]   R. Zapf, G. Kolb, H. Pennemann, V. Hessel, Basic study of adhesion of several alumina-based washcoats deposited on stainless steel microchannels, Chem. Eng. Technol. 29 (2006) 1509-1512. https://doi.org/10.1002/ceat.200600204.

[131]   P.A.R. Cebollada, E. Garcia Bordejé, Optimisation of physical properties of γ-alumina coating microreactors used for the growth of a carbon nanofiber layer, Chem. Eng. J. 149 (2009) 447-454. https://doi.org/10.1016/j.cej.2009.02.016.

[132]   J. Bravo, A. Karim, T. Conant, G.P. Lopez, A. Datye, Wall coating of a CuO/ZnO/Al$_2$O$_3$ methanol steam reforming catalyst for micro-channel reformers, Chem. Eng. J. 101 (2004) 113-121. http://dx.doi.org/10.1016/j.cej.2004.01.011.

[133]   F. Behrendt, O. Deutschmann, R. Schmidt, J. Warnatz, Ignition and extinction of hydrogen-air and methane-air mixtures over platinum and palladium, Heterogeneous Hydrocarbon Oxidation. American Chemical Society, 1996, pp. 48-57.

[134]   M. Valden, J. Pere, N. Xiang, M. Pessa, Influence of preadsorbed oxygen on activated chemisorption of methane on Pd(110), Chem. Phys. Lett. 257 (1996) 289-296. http://doi.org/10.1016/0009-2614(96)00554-4.

[135]   J. Xu, L. Ouyang, W. Mao, X.J. Yang, X.C. Xu, J.J. Su, T.Z. Zhuang, H. Li, Y.F. Han, Operando and kinetic study of low-temperature, lean-burn methane combustion over a Pd/γ-Al$_2$O$_3$ catalyst, ACS Catal. 2 (2012) 261-269. https://doi.org/10.1021/cs200694k.

[136]   Y. Yao, F. Yu, Oxidation of alkanes over noble metal catalysts, Ind. Eng. Chem. Prod. Res. Dev. 19 (1980) 293-298. https://doi.org/10.1021/i360075a003.

[137]   F. Duprat, Light-off curve of catalytic reaction and kinetics, Chem. Eng. Sci. 57 (2002) 901-911. https://doi.org/10.1016/S0009-2509(01)00409-2.

[138]   W. Qi, J. Ran, R. Wang, X. Du, J. Shi, J. Niu, P. Zhang, M. Ran, Kinetic consequences of methane combustion on Pd, Pt and Pd-Pt catalysts, RSC Advances. 6 (2016) 109834-109845. https://doi.org/10.1039/C6RA21150J.

[139]   Y.H. Chin, E. Iglesia, Elementary steps, the role of chemisorbed oxygen, and the effects of cluster size in catalytic CH$_4$-O$_2$ reactions on palladium, J. Phys. Chem. C. 115 (2011) 17845-17855. https://doi.org/10.1021/jp203324y.

[140]   L. Ma, D.L. Trimm, C. Jiang, The design and testing of an autothermal reactor for the conversion of light hydrocarbons to hydrogen I. The kinetics of the catalytic oxidation of light hydrocarbons, Appl. Catal. A. 138 (1996) 275-283. http://doi.org/10.1016/0926-860X(95)00301-0.

[141]   D. Trimm, C.-W. Lam, The combustion of methane on platinum-alumina fibre catalysts-II design and testing of a convective-diffusive type catalytic combustor, Chem. Eng. Sci. 35 (1980) 1731-1739. https://doi.org/10.1016/0009-2509(80)85008-1.

[142]   K. Gosiewski, A. Pawlaczyk, K. Warmuzinski, M. Jaschik, A study on thermal combustion of lean methane-

air mixtures: Simplified reaction mechanism and kinetic equations, Chem. Eng. J. 154 (2009) 9-16. https://doi.org/10.1016/j.cej.2009.03.045.

[143]   A. Pawlaczyk, K. Gosiewski, Combustion of lean methane-air mixtures in monolith beds: Kinetic studies in low and high temperatures, Chem. Eng. J. 282 (2015) 29-36. http://doi.org/10.1016/j.cej.2015.02.081.

[144]   W. Tsang, R. Hampson, Chemical kinetic data base for combustion chemistry. Part I. Methane and related compounds, J. Phys. Chem. Ref. Data. 15 (1986) 1087-1279. https://doi.org/10.1063/1.555759.

[145]   E. Ranzi, A. Sogaro, P. Gaffuri, G. Pennati, T. Faravelli, A wide range modeling study of methane oxidation, Combust. Sci. Technol. 96 (1994) 279-325. https://doi.org/10.1080/00102209408935359.

[146]   A. Burcat, W.C.J. Gardiner, G. Dixon-Lewis, M. Frenklach, R.K. Hanson, S. Salimian, J. Troe, J. Warnatz, R. Zellner, Combustion Chemistry, Springer New York, 1984.

[147]   S. Oh, P. Mitchell, R. Siewert, Methane oxidation over noble metal catalysts as related to controlling natural gas vehicle exhaust emissions, Catalytic control of air pollution. ACS Publication, Washington, DC, 1992.

[148]   R.W. McCabe, D.F. McCready, Formaldehyde oxidation on Pt: Kinetic evidence for adsorbed carbon monoxide intermediate, Chem. Phys. Lett. 111 (1984) 89-93. http://dx.doi.org/10.1016/0009-2614(84)80442-X.

[149]   M.P. Lapinski, R.G. Silver, J.G. Ekerdt, R.W. McCabe, Formaldehyde oxidation on silica-supported platinum: Spectroscopic evidence for adsorbed carbon monoxide intermediate, J. Catal. 105 (1987) 258-262. http://dx.doi.org/10.1016/0021-9517(87)90026-1.

[150]   O. Deutschmann, R. Schmidt, F. Behrendt, J. Warnat, Numerical modeling of catalytic ignition, Symposium (International) on Combustion. 26 (1996) 1747-1754. http://dx.doi.org/10.1016/S0082-0784(96)80400-0.

[151]   T. Engel, G. Ertl, Elementary steps in the catalytic oxidation of carbon monoxide on platinum metals, Adv. Catal. 28 (1979) 1-78. http://doi.org/10.1016/S0360-0564(08)60133-9.

[152]   A. Frennet, Chemisorption and exchange with deuterium of methane on metals, Catal. Rev. - Sci. Eng. 10 (1974) 37-68. https://doi.org/10.1080/01614947408079626.

[153]   T.G. Bond, B.A. Noguchi, C.-P. Chou, R.K. Mongia, J.-Y. Chen, R.W. Dibble. Catalytic oxidation of natural gas over supported platinum: Flow reactor experiments and detailed numberical modeling. in Symposium (international) on combustion. 1996. Elsevier.

[154]   J. Firth, H. Holland, Catalytic oxidation of methane over noble metals, Transactions of the Faraday Society. 65 (1969) 1121-1127. https://doi.org/10.1039/TF9696501121.

[155]   O.P. Ahuja, G. Mathur, Kinetics of catalytic oxidation of methane: Application of initial rate technique for mechanism determination, Can. J. Chem. Eng. 45 (1967) 367-371. https://doi.org/10.1002/cjce.545045060.

[156]   G. Groppi, Combustion of CH_4 over a PdO/ZrO_2 catalyst: an example of kinetic study under severe conditions, Catal. Today. 77 (2003) 335-346. https://doi.org/10.1016/s0920-5861(02)00378-4.

[157]   S. Seimanides, M. Stoukides, Catalytic oxidation of methane on polycrystalline palladium supported on stabilized zirconia, J. Catal. 98 (1986) 540-549. https://doi.org/10.1016/0021-9517(86)90342-8.

[158]   E. Garbowski, C. Feumi-Jantou, N. Mouaddib, M. Primet, Catalytic combustion of methane over palladium supported on alumina catalysts: Evidence for reconstruction of particles, Appl. Catal. A. 109 (1994) 277-291. https://doi.org/10.1016/0926-860X(94)80124-X.

[159]   C.A. Müller, M. Maciejewski, R.A. Koeppel, A. Baiker, Combustion of methane over palladium/zirconia: effect of Pd-particle size and role of lattice oxygen, Catal. Today. 47 (1999) 245-252. https://doi.org/10.1016/S0920-5861(98)00305-8.

[160]   D. Ciuparu, E. Altman, L. Pfefferle, Contributions of lattice oxygen in methane combustion over PdO-Based catalysts, J. Catal. 203 (2001) 64-74. http://doi.org/10.1006/jcat.2001.3331.

[161]   C.A. Müller, M. Maciejewski, R.A. Koeppel, R. Tschan, A. Baiker, Role of lattice oxygen in the combustion of methane over PdO/ZrO_2: combined pulse TG/DTA and MS study with ^{18}O-labeled catalyst, The Journal of Physical Chemistry. 100 (1996) 20006-20014. https://doi.org/10.1021/jp961903a.

[162]   D.L. Trimm, C.-W. Lam, The combustion of methane on platinum-alumina fibre catalysts-I: kinetics and mechanism, Chem. Eng. Sci. 35 (1980) 1405-1413. https://doi.org/10.1016/0009-2509(80)85134-7.

[163]   P.J. Jodłowski, R.J. Jędrzejczyk, D. Chlebda, M. Gierada, J. Łojewska, In situ spectroscopic studies of methane catalytic combustion over Co, Ce, and Pd mixed oxides deposited on a steel surface, J. Catal. 350 (2017) 1-12. https://doi.org/10.1016/j.jcat.2017.03.022.

[164]   J. Veldsink, G. Versteeg, W.P.M. van Swaaij, Intrinsic kinetics of the oxidation of methane over an industrial copper (II) oxide catalyst on a γ-alumina support, The Chemical Engineering Journal and the Biochemical Engineering Journal. 57 (1995) 273-283. https://doi.org/10.1016/0923-0467(94)02872-8.

[165]   P. Hurtado, S. Ordóñez, H. Sastre, F.V. Dıez, Development of a kinetic model for the oxidation of methane over Pd/Al_2O_3 at dry and wet conditions, Appl. Catal., B. 51 (2004) 229-238. https://doi.org/10.1016/j.apcatb.2004.03.006.

[166]   M. Jørgensen, H. Grönbeck, First-principles microkinetic modeling of methane oxidation over Pd (100) and Pd (111), ACS Catal. 6 (2016) 6730-6738. https://doi.org/10.1021/acscatal.6b01752.

[167]   J. Au-Yeung, K. Chen, A.T. Bell, E. Iglesia, Isotopic Studies of Methane Oxidation Pathways on PdO Catalysts, J. Catal. 188 (1999) 132-139. http://doi.org/10.1006/jcat.1999.2643.

[168]   M. Lyubovsky, L. Pfefferle, Methane combustion over the α-alumina supported Pd catalyst: Activity of the mixed Pd/PdO state, Appl. Catal. A. 173 (1998) 107-119. https://doi.org/10.1016/S0926-860X(98)00149-5.

[169]   A.K. Datye, J. Bravo, T.R. Nelson, P. Atanasova, M. Lyubovsky, L. Pfefferle, Catalyst microstructure and methane oxidation reactivity during the Pd↔PdO transformation on alumina supports, Appl. Catal. A. 198 (2000) 179-196. https://doi.org/10.1016/S0926-860X(99)00512-8.

[170]   O. Demoulin, M. Navez, P. Ruiz, Investigation of the behaviour of a Pd/γ-Al2O3 catalyst during methane combustion reaction using in situ DRIFT spectroscopy, Appl. Catal. A. 295 (2005) 59-70. https://doi.org/10.1016/j.apcata.2005.08.008.

[171]   S.H. Oh, P.J. Mitchell, R.M. Siewert, Methane oxidation over alumina-supported noble metal catalysts with and without cerium additives, J. Catal. 132 (1991) 287-301. https://doi.org/10.1016/0021-9517(91)90149-X.

[172]   M.V.d. Bossche, H. Gronbeck, Methane oxidation over PdO (101) revealed by first-principles kinetic modeling, J. Am. Chem. Soc. 137 (2015) 12035-12044. https://doi.org/10.1021/jacs.5b06069.

[173]   P. Aghalayam, Y.K. Park, N. Fernandes, V. Papavassiliou, A.B. Mhadeshwar, D.G. Vlachos, A C1 mechanism for methane oxidation on platinum, J. Catal. 213 (2003) 23-38. http://dx.doi.org/10.1016/S0021-9517(02)00045-3.

[174]   M. Chrzan, D. Chlebda, P. Jodłowski, E. Salomon, A. Kołodziej, A. Gancarczyk, M. Sitarz, J. Łojewska, Towards methane combustion mechanism on metal oxides supported catalysts: ceria supported palladium catalysts, Top. Catal. 62 (2019) 403-412. https://doi.org/10.1007/s11244-019-01143-8.

[175]   S. Feng, W. Yang, Z. Wang, Synthesis of porous NiFe2O4 microparticles and its catalytic properties for methane combustion, Mater. Sci. Eng., B. 176 (2011) 1509-1512. https://doi.org/10.1016/j.mseb.2011.09.007.

[176]   V.G. Milt, M.A. Ulla, E.A. Lombardo, Cobalt-containing catalysts for the high-temperature combustion of methane, Catal. Lett. 65 (2000) 67-73. https://doi.org/10.1023/a:1019061103878.

[177]   J. Okal, M. Zawadzki, K. Baranowska, Methane combustion over bimetallic Ru-Re/γ-Al2O3 catalysts: Effect of Re and pretreatments, Appl. Catal., B. 194 (2016) 22-31. https://doi.org/10.1016/j.apcatb.2016.04.038.

[178]   M. Iamarino, R. Chirone, L. Lisi, R. Pirone, P. Salatino, G. Russo, Cu/γ-Al2O3 catalyst for the combustion of methane in a fluidized bed reactor, Catal. Today. 75 (2002) 317-324. https://doi.org/10.1016/S0920-5861(02)00084-6.

[179]   Z. Wang, J. Deng, Y. Liu, H. Yang, S. Xie, Z. Wu, H. Dai, Three-dimensionally ordered macroporous CoCr2O4-supported Au-Pd alloy nanoparticles: Highly active catalysts for methane combustion, Catal. Today. 281, Part 3 (2017) 467-476. https://doi.org/10.1016/j.cattod.2016.05.035.

[180]   S. Cimino, R. Pirone, L. Lisi, Zirconia supported LaMnO3 monoliths for the catalytic combustion of methane, Appl. Catal., B. 35 (2002) 243-254. https://doi.org/10.1016/S0926-3373(01)00262-4.

[181]   G. Comino, A. Gervasini, V. Ragaini, Z.R. Ismagilov, Methane combustion over copper chromite catalysts, Catal. Lett. 48 (1997) 39-46. https://doi.org/10.1023/a:1019070819421.

[182]   I. Chorkendorff, J.W. Niemantsverdriet, Concepts of modern catalysis and kinetics, John Wiley & Sons, 524 2017.

[183]   J.W. Geus, J.C. van Giezen, Monoliths in catalytic oxidation, Catal. Today. 47 (1999) 169-180. http://doi.org/10.1016/S0920-5861(98)00297-1.

[184]   C. Shi, L. Yang, J. Cai, Cerium promoted Pd/HZSM-5 catalyst for methane combustion, Fuel. 86 (2007) 106-112. https://doi.org/10.1016/j.fuel.2006.05.029.

[185]   A.L. Barbosa, J. Herguido, J. Santamaria, Methane combustion over unsupported iron oxide catalysts, Catal. Today. 64 (2001) 43-50. http://doi.org/10.1016/S0920-5861(00)00507-1.

[186]   J.H. Lee, D.L. Trimm, Catalytic combustion of methane, Fuel Process. Technol. 42 (1995) 339-359. http://doi.org/10.1016/0378-3820(94)00091-7.

[187]   Y.S. Seo, S.K. Kang, M.H. Han, Y.S. Baek, Development of a catalytic burner with Pd/NiO catalysts, Catal. Today. 47 (1999) 421-427. http://doi.org/10.1016/S0920-5861(98)00325-3.

[188]   M. Anna Poskart, The control of NOx concentration in natural gas combustion process, CHEMIK. 67 (2013) 848-855.

[189]   R.J. Farrauto, J.K. Lampert, M.C. Hobson, E.M. Waterman, Thermal decomposition and reformation of PdO catalysts; support effects, Appl. Catal., B. 6 (1995) 263-270. https://doi.org/10.1016/0926-3373(95)00015-1.

[190]   W.R. Schwartz, D. Ciuparu, L.D. Pfefferle, Combustion of Methane over Palladium-Based Catalysts: Catalytic Deactivation and Role of the Support, The Journal of Physical Chemistry C. 116 (2012) 8587-8593. https://doi.org/10.1021/jp212236e.

[191]   M. Fleys, Y. Simon, D. Swierczynski, A. Kiennemann, P.M. Marquaire, Investigation of the reaction of partial oxidation of methane over Ni/La2O3 catalyst, Energy Fuels. 20 (2006) 2321-2329. https://doi.org/10.1021/ef0602729.

[192]   M. Halabi, M. De Croon, J. Van Der Schaaf, P. Cobden, J. Schouten, Intrinsic kinetics of low temperature

catalytic methane-steam reforming and water-gas shift over Rh/Ce$_\alpha$Zr$_{1-\alpha}$O$_2$ catalyst, Appl. Catal. A. 389 (2010) 80-91. https://doi.org/10.1016/j.apcata.2010.09.005.

[193]   N. Mouaddib, C. Feumi-Jantou, E. Garbowski, M. Primet, Catalytic oxidation of methane over palladium supported on alumina: Influence of the oxygen-to-methane ratio, Appl. Catal. A. 87 (1992) 129-144. https://doi.org/10.1016/0926-860X(92)80177-E.

[194]   V. Drozdov, P. Tsyrulnikov, V. Popovskii, N. Bulgakov, E. Moroz, T. Galeev, Comparative study of the activity of Al-Pd and Al-Pt catalysts in deep oxidation of hydrocarbons, React. Kinet. Catal. Lett. 27 (1985) 425-427. https://doi.org/10.1007/bf02070487.

[195]   M. Murru, A. Gavriilidis, Catalytic combustion of methane in non-permselective membrane reactors with separate reactant feeds, Chem. Eng. J. 100 (2004) 23-32. https://doi.org/10.1016/j.cej.2003.11.015.

[196]   W. Liu, Y. Xu, Z. Tian, Z. Xu, A thermodynamic analysis on the catalytic combustion of methane, J. Nat. Gas Chem. 12 (2003) 237-242.

[197]   L. Urfels, P. Gélin, M. Primet, E. Tena, Complete oxidation of methane at low temperature over Pt catalysts supported on high surface area SnO$_2$, Top. Catal. 30 (2004) 427-432. https://doi.org/10.1023/B:TOCA.0000029785.34330.57.

[198]   Z. Yang, J. Liu, L. Zhang, S. Zheng, M. Guo, Y. Yan, Catalytic combustion of low-concentration coal bed methane over CuO/γ-Al$_2$O$_3$ catalyst: effect of SO$_2$, RSC Advances. 4 (2014) 39394-39399. https://doi.org/10.1039/C4RA05334F.

[199]   D.L. Mowery, R.L. McCormick, Deactivation of alumina supported and unsupported PdO methane oxidation catalyst: the effect of water on sulfate poisoning, Appl. Catal., B. 34 (2001) 287-297. http://doi.org/10.1016/S0926-3373(01)00222-3.

[200]   G. Dixon-Lewis, D. Williams, The oxidation of hydrogen and carbon monoxide, Comprehensive chemical kinetics. Elsevier, 1977, pp. 1-248.

[201]   Z. Wu, J. Deng, Y. Liu, S. Xie, Y. Jiang, X. Zhao, J. Yang, H. Arandiyan, G. Guo, H. Dai, Three-dimensionally ordered mesoporous Co$_3$O$_4$-supported Au-Pd alloy nanoparticles: High-performance catalysts for methane combustion, J. Catal. 332 (2015) 13-24. http://doi.org/10.1016/j.jcat.2015.09.008.

[202]   H. Geng, Z. Yang, L. Zhang, J. Ran, Y. Chen, Experimental and kinetic study of methane combustion with water over copper catalyst at low-temperature, Energy Convers. Manage. 103 (2015) 244-250. https://doi.org/10.1016/j.enconman.2015.06.076.

[203]   D. Ciuparu, N. Katsikis, L. Pfefferle, Temperature and time dependence of the water inhibition effect on supported palladium catalyst for methane combustion, Appl. Catal. A. 216 (2001) 209-215. https://doi.org/10.1016/S0926-860X(01)00558-0.

[204]   N. Sadokhina, G. Smedler, U. Nylén, M. Olofsson, L. Olsson, The influence of gas composition on Pd-based catalyst activity in methane oxidation-inhibition and promotion by NO, Appl. Catal., B. 200 (2017) 351-360. http://doi.org/10.1016/j.apcatb.2016.07.012.

[205]   S. Hayashi, H. Yamada, K. Shimodaira, High-pressure reaction and emissions characteristics of catalytic reactors for gas turbine combustors, Catal. Today. 26 (1995) 319-327. https://doi.org/10.1016/0920-5861(95)00154-4.

[206]   A. Di Benedetto, G. Landi, V. Di Sarli, P.S. Barbato, R. Pirone, G. Russo, Methane catalytic combustion under pressure, Catal. Today. 197 (2012) 206-213. https://doi.org/10.1016/j.cattod.2012.08.032.

[207]   R. Carroni, T. Griffin, J. Mantzaras, M. Reinke, High-pressure experiments and modeling of methane/air catalytic combustion for power-generation applications, Catal. Today. 83 (2003) 157-170. https://doi.org/10.1016/s0920-5861(03)00226-8.

[208]   A.J. Zarur, J.Y. Ying, Reverse microemulsion synthesis of nanostructured complex oxides for catalytic combustion, Nature. 403 (2000) 65. https://doi.org/10.1038/47450.

[209]   S. Li, X. Wang, The Ba-hexaaluminate doped with CeO$_2$ nanoparticles for catalytic combustion of methane, Catal. Commun. 8 (2007) 410-415. https://doi.org/10.1016/j.catcom.2006.07.011.

[210]   A. Civera, G. Negro, S. Specchia, G. Saracco, V. Specchia, Optimal compositional and structural design of a LaMnO$_3$/ZrO$_2$/Pd-based catalyst for methane combustion, Catal. Today. 100 (2005) 275-281. https://doi.org/10.1016/j.cattod.2004.09.062.

[211]   L. Zhang, Y. Zhang, H. Dai, J. Deng, L. Wei, H. He, Hydrothermal synthesis and catalytic performance of single-crystalline La$_{2-x}$Sr$_x$CuO$_4$ for methane oxidation, Catal. Today. 153 (2010) 143-149. https://doi.org/10.1016/j.cattod.2010.02.059.

[212]   K. Gallucci, P. Villa, G. Groppi, N. Usberti, G. Marra, Catalytic combustion of methane on BaZr$_{(1-x)}$Me$_x$O$_3$ perovskites synthesised by a modified citrate method, Catal. Today. 197 (2012) 236-242. https://doi.org/10.1016/j.cattod.2012.08.034.

[213]   J. Hu, W. Zhao, R. Hu, G. Chang, C. Li, L. Wang, Catalytic activity of spinel oxides MgCr$_2$O$_4$ and CoCr$_2$O$_4$ for methane combustion, Mater. Res. Bull. 57 (2014) 268-273. https://doi.org/10.1016/j.materresbull.2014.06.001.

[214]   Y. Wang, H. Arandiyan, J. Scott, M. Akia, H. Dai, J. Deng, K.-F. Aguey-Zinsou, R. Amal, High performance Au-

Pd supported on 3D hybrid strontium-substituted lanthanum manganite perovskite catalyst for methane combustion, ACS Catal. 6 (2016) 6935-6947. https://doi.org/10.1021/acscatal.6b01685.

[215]   F. Zaza, I. Luisetto, E. Serra, S. Tuti, M. Pasquali. Catalytic combustion of methane by perovskite-type oxide nanoparticles as pollution prevention strategy. in AIP Conference Proceedings. 2016. AIP Publishing.

[216]   X. Fan, L. Li, F. Jing, J. Li, W. Chu, Effects of preparation methods on $CoAlO_x/CeO_2$ catalysts for methane catalytic combustion, Fuel. 225 (2018) 588-595. https://doi.org/10.1016/j.fuel.2018.03.006.

[217]   X. Li, Y. Liu, J. Deng, Y. Zhang, S. Xie, X. Zhao, Z. Wang, G. Guo, H. Dai, 3DOM LaMnAl11O19-supported AuPd alloy nanoparticles: Highly active catalysts for methane combustion in a continuous-flow microreactor, Catal. Today. 308 (2018) 71-80. https://doi.org/10.1016/j.cattod.2017.07.024.

[218]   D. Li, K. Li, R. Xu, H. Wang, D. Tian, Y. Wei, X. Zhu, C. Zeng, L. Zeng, $Ce_{1-x}Fe_xO_{2-\delta}$ catalysts for catalytic methane combustion: role of oxygen vacancy and structural dependence, Catal. Today. 318 (2018) 73-85. https://doi.org/10.1016/j.cattod.2017.12.015.

[219]   Y. Li, J.N. Armor, Catalytic combustion of methane over palladium exchanged zeolites, Appl. Catal., B. 3 (1994) 275-282. https://doi.org/10.1016/0926-3373(94)0006Z-H.

[220]   B. Kucharczyk, W. Tylus, L. Kpiński, Pd-based monolithic catalysts on metal supports for catalytic combustion of methane, Appl. Catal., B. 49 (2004) 27-37. https://doi.org/10.1016/j.apcatb.2003.11.006.

[221]   L.H. Xiao, K.P. Sun, X.L. Xu, X.N. Li, Low-temperature catalytic combustion of methane over Pd/CeO_2 prepared by deposition-precipitation method, Catal. Commun. 6 (2005) 796-801. https://doi.org/10.1016/j.catcom.2005.07.015.

[222]   V. Choudhary, V. Patil, P. Jana, B. Uphade, Nano-gold supported on Fe_2O_3: A highly active catalyst for low temperature oxidative destruction of methane green house gas from exhaust/waste gases, Appl. Catal. A. 350 (2008) 186-190. https://doi.org/10.1016/j.apcata.2008.08.008.

[223]   J. Li, X. Liang, S. Xu, J. Hao, Catalytic performance of manganese cobalt oxides on methane combustion at low temperature, Appl. Catal., B. 90 (2009) 307-312. https://doi.org/10.1016/j.apcatb.2009.03.027.

[224]   A. Venezia, G. Di Carlo, G. Pantaleo, L. Liotta, G. Melaet, N. Kruse, Oxidation of CH_4 over Pd supported on TiO_2-doped SiO_2: Effect of Ti(IV) loading and influence of SO_2, Appl. Catal., B. 88 (2009) 430-437. https://doi.org/10.1016/j.apcatb.2008.10.023.

[225]   S. Specchia, P. Palmisano, E. Finocchio, G. Busca, Ageing mechanisms on PdO_x-based catalysts for natural gas combustion in premixed burners, Chem. Eng. Sci. 65 (2010) 186-192. https://doi.org/10.1016/j.ces.2009.05.007.

[226]   S. Zhao, J. Li, Silver-cobalt oxides derived from silver nanoparticles deposited on layered double hydroxides for methane combustion, ChemCatChem. 7 (2015) 1966-1974. https://doi.org/10.1002/cctc.201500254.

[227]   Z. Yang, P. Yang, L. Zhang, M. Guo, J. Ran, Experiment and modeling of low-concentration methane catalytic combustion in a fluidized bed reactor, Appl. Therm. Eng. 93 (2016) 660-667. https://doi.org/10.1016/j.applthermaleng.2015.10.028.

[228]   Z. Han, H. Zhang, B. Dong, Y. Ni, A. Kong, Y. Shan, High efficient mesoporous Co_3O_4 nanocatalysts for methane combustion at low temperature, ChemistrySelect. 1 (2016) 979-983. https://doi.org/10.1002/slct.201600211.

[229]   Y. Mahara, T. Tojo, K. Murata, J. Ohyama, A. Satsuma, Methane combustion over $Pd/CoAl_2O_4/Al_2O_3$ catalysts prepared by galvanic deposition, RSC Advances. 7 (2017) 34530-34537. https://doi.org/10.1039/c7ra06150a.

[230]   P. Jodłowski, R. Jędrzejczyk, D. Chlebda, A. Dziedzicka, Ł. Kuterasiński, A. Gancarczyk, M. Sitarz, Non-noble metal oxide catalysts for methane catalytic combustion: sonochemical synthesis and characterisation, Nanomaterials. 7 (2017) 174. https://doi.org/10.3390/nano7070174.

[231]   L. Li, H. Chen, C. Zhang, Z. Fei, Ultrafine cobalt oxide nanoparticles embedded in porous SiO_2 matrix as efficient and stable catalysts for methane combustion, Molecular Catalysis. 469 (2019) 155-160. https://doi.org/10.1016/j.mcat.2018.12.028.

[232]   T.T. H. Sadamori, T. Matsuhisa., Proceedings of the international workshop on catalytic combustion. Tokyo, Japan., (1994) 166-169.

[233]   G. Kolios, J. Frauhammer, G. Eigenberger, Autothermal fixed-bed reactor concepts, Chem. Eng. Sci. 55 (2000) 5945-5967. http://doi.org/10.1016/S0009-2509(00)00183-4.

[234]   G. Kolios, J. Frauhammer, G. Eigenberger, Efficient reactor concepts for coupling of endothermic and exothermic reactions, Chem. Eng. Sci. 57 (2002) 1505-1510. http://doi.org/10.1016/S0009-2509(02)00022-2.

[235]   U. Nieken, G. Kolios, G. Eigenberger, Control of the ignited steady state in autothermal fixed-bed reactors for catalytic combustion, Chem. Eng. Sci. 49 (1994) 5507-5518. http://doi.org/10.1016/0009-2509(94)00381-5.

[236]   B. Glöckler, A. Gritsch, A. Morillo, G. Kolios, G. Eigenberger, Autothermal reactor concepts for endothermic fixed-bed reactions, Chem. Eng. Res. Des. 82 (2004) 148-159. http://doi.org/10.1205/026387604772992710.

[237]   C. Devals, A. Fuxman, F. Bertrand, J. Forbes, R. Hayes. Combustion of lean methane in a catalytic flow reversal reactor. in The proceeding of the Comsol users conference. 2006.

[238]	R.F. Blanks, T.S. Wittrig, D.A. Peterson, Bidirectional adiabatic synthesis gas generator, Chem. Eng. Sci. 45 (1990) 2407-2413. http://doi.org/10.1016/0009-2509(90)80122-U.

[239]	Y.W. Budhi, M. Effendy, Y. Bindar, S. Subagjo, Dynamic behavior of reverse flow reactor for lean methane combustion, J. Eng. Technol. Sci. 46 (2014) 299-317. http://doi.org/10.5614/j.eng.technol.sci.2014.46.3.5.

[240]	S. Balaji, S. Lakshminarayanan, Heat removal from reverse flow reactors used in methane combustion, Can. J. Chem. Eng. 83 (2005) 695-704. http://doi.org/10.1002/cjce.5450830410.

[241]	K. Gosiewski, K. Warmuzinski, Effect of the mode of heat withdrawal on the asymmetry of temperature profiles in reverse-flow reactors. Catalytic combustion of methane as a test case, Chem. Eng. Sci. 62 (2007) 2679-2689. http://doi.org/10.1016/j.ces.2007.02.013.

[242]	K. Gosiewski, A. Pawlaczyk, M. Jaschik, Energy recovery from ventilation air methane via reverse-flow reactors, Energy. 92 (2015) 13-23. http://doi.org/10.1016/j.energy.2015.06.004.

[243]	K. Gosiewski, Efficiency of heat recovery versus maximum catalyst temperature in a reverse-flow combustion of methane, Chem. Eng. J. 107 (2005) 19-25. http://doi.org/10.1016/j.cej.2004.12.005.

[244]	P. Marín, S. Ordóñez, F.V. Díez, Procedures for heat recovery in the catalytic combustion of lean methane-air mixtures in a reverse flow reactor, Chem. Eng. J. 147 (2009) 356-365. http://doi.org/10.1016/j.cej.2008.11.041.

[245]	Y.S. Matros, Catalytic processes under unsteady-state conditions, Elsevier, 1988.

[246]	K. Gosiewski, Y.S. Matros, K. Warmuzinski, M. Jaschik, M. Tanczyk, Homogeneous vs. catalytic combustion of lean methane-air mixtures in reverse-flow reactors, Chem. Eng. Sci. 63 (2008) 5010-5019. https://doi.org/10.1016/j.ces.2007.09.013.

[247]	K. Gosiewski, A. Pawlaczyk, M. Jaschik, Thermal combustion of lean methane-air mixtures: Flow reversal research and demonstration reactor model and its validation, Chem. Eng. J. 207-208 (2012) 76-84. https://doi.org/10.1016/j.cej.2012.07.044.

[248]	T. Ioannides, X. Verykios, Catalytic partial oxidation of methane in a novel heat-integrated wall reactor, Catal. Lett. 47 (1997) 183-188. https://doi.org/10.1023/A:1019077626264.

[249]	M. Zanfir, A. Gavriilidis, Catalytic combustion assisted methane steam reforming in a catalytic plate reactor, Chem. Eng. Sci. 58 (2003) 3947-3960. https://doi.org/10.1016/S0009-2509(03)00279-3.

[250]	E.A. Polman, J.M. Der Kinderen, F.M.A. Thuis, Novel compact steam reformer for fuel cells with heat generation by catalytic combustion augmented by induction heating., Catal. Today. 47 (1999) 347-351. https://doi.org/10.1016/S0920-5861(98)00316-2.

[251]	G. Kolios, B. Glöckler, A. Gritsch, A. Morillo, G. Eigenberger, Heat-integrated reactor concepts for hydrogen production by methane steam reforming, Fuel Cells. 5 (2005) 52-65. https://doi.org/10.1002/fuce.200400065.

[252]	Y. Yan, G. Wu, W. Huang, L. Zhang, L. Li, Z. Yang, Numerical comparison study of methane catalytic combustion characteristic between newly proposed opposed counter-flow micro-combustor and the conventional ones, Energy. 170 (2019) 403-410. https://doi.org/10.1016/j.energy.2018.12.114.

[253]	X. Guo, Y. Fan, L. Luo, Multi-channel heat exchanger-reactor using arborescent distributors: A characterization study of fluid distribution, heat exchange performance and exothermic reaction, Energy. 69 (2014) 728-741. https://doi.org/10.1016/j.energy.2014.03.069.

[254]	Y. Fan, L. Luo, Recent applications of advances in microchannel heat exchangers and multi-scale design optimization, Heat Transfer Eng. 29 (2008) 461-474. https://doi.org/10.1080/01457630701850968.

[255]	J.J. Brandner, L. Bohn, T. Henning, U. Schygulla, K. Schubert, Microstructure heat exchanger applications in laboratory and industry, Heat Transfer Eng. 28 (2007) 761-771. https://doi.org/10.1080/01457630701328528.

[256]	G. Kolb, J. Schürer, D. Tiemann, M. Wichert, R. Zapf, V. Hessel, H. Löwe, Fuel processing in integrated micro-structured heat-exchanger reactors, J. Power Sources. 171 (2007) 198-204. https://doi.org/10.1016/j.jpowsour.2007.01.006.

[257]	C.M. Miesse, R.I. Masel, C.D. Jensen, M.A. Shannon, M. Short, Submillimeter-scale combustion, AlChE J. 50 (2004) 3206-3214. https://doi.org/10.1002/aic.10271.

[258]	J. Hua, M. Wu, K. Kumar, Numerical simulation of the combustion of hydrogen–air mixture in micro-scaled chambers. Part I: Fundamental study, Chem. Eng. Sci. 60 (2005) 3497-3506. http://doi.org/10.1016/j.ces.2005.01.041.

[259]	J. Chen, X. Gao, D. Xu, Stability limits and chemical quenching of methane-air flame in plane micro-channels with different walls, RSC Advances. 5 (2015) 39375-39383. https://doi.org/10.1039/C5RA02813B.

[260]	J.M. Rodrigues, M.F. Ribeiro, E.C. Fernandes, Catalytic activity of electrodeposited cobalt oxide films for methane combustion in a micro-channel reactor, Fuel. 232 (2018) 51-59. https://doi.org/10.1016/j.fuel.2018.05.114.

[261]	A. Irankhah, M. Rahimi, M. Rezaei, Performance research on a methane compact reformer integrated with catalytic combustion, Chem. Eng. Technol. 37 (2014) 1220-1226. https://doi.org/10.1002/ceat.201300469.

[262]	M. Mundhwa, C.P. Thurgood, Numerical study of methane steam reforming and methane combustion over the segmented and continuously coated layers of catalysts in a plate reactor, Fuel Process. Technol. 158 (2017) 57-72. http://doi.org/10.1016/j.fuproc.2016.12.002.

[263]   J. Niu, J. Ran, L. Li, X. Du, R. Wang, M. Ran, Effects of trapezoidal bluff bodies on blow out limit of methane/air combustion in a micro-channel, Appl. Therm. Eng. 95 (2016) 454-461. https://doi.org/10.1016/j.applthermaleng.2015.11.061.

[264]   P. Jiang, G. Lu, Y. Guo, Y. Guo, S. Zhang, X. Wang, Preparation and properties of a γ-Al$_2$O$_3$ washcoat deposited on a ceramic honeycomb, Surf. Coat. Technol. 190 (2005) 314-320. https://doi.org/10.1016/j.surfcoat.2004.05.029.

[265]   S. Govender, H. Friedrich, Monoliths: A review of the basics, preparation methods and their relevance to oxidation, Catalysts. 7 (2017) 62. https://doi.org/10.3390/catal7020062.

[266]   J. Llorca, Monolithic reactor, Encyclopedia of Membranes. Springer Berlin Heidelberg, Berlin, Heidelberg, 2015, pp. 1-3.

[267]   J.L. Williams, Monolith structures, materials, properties and uses, Catal. Today. 69 (2001) 3-9. https://doi.org/10.1016/S0920-5861(01)00348-0.

[268]   M. Lyubovsky, H. Karim, P. Menacherry, S. Boorse, R. LaPierre, W.C. Pfefferle, S. Roychoudhury, Complete and partial catalytic oxidation of methane over substrates with enhanced transport properties, Catal. Today. 83 (2003) 183-197. http://doi.org/10.1016/S0920-5861(03)00231-1.

[269]   V. Dupont, F. Moallemi, A. Williams, S.H. Zhang, Combustion of methane in catalytic honeycomb monolith burners, Int. J. Energy Res. 24 (2000) 1181-1201. https://doi.org/10.1002/1099-114X(20001025)24:13<1181::AID-ER669>3.0.CO;2-Y.

[270]   Y. Lin, Microporous and dense inorganic membranes: current status and prospective, Sep. Purif. Technol. 25 (2001) 39-55. https://doi.org/10.1016/S1383-5866(01)00089-2.

[271]   T. Hu, H. Zhou, H. Peng, H. Jiang, Nitrogen production by efficiently removing oxygen from air using a perovskite hollow-fiber membrane with porous catalytic layer, Front. Chem. 6 (2018). http://doi.org/10.3389/fchem.2018.00329.

[272]   R. Falkenstein Smith, P. Zeng, J. Ahn, Investigation of oxygen transport membrane reactors for oxy-fuel combustion and carbon capture purposes, Proc. Combust. Inst. 36 (2017) 3969-3976. http://doi.org/10.1016/j.proci.2016.09.005.

[273]   M.A. Habib, M.A. Nemitallah, Design of an ion transport membrane reactor for application in fire tube boilers, Energy. 81 (2015) 787-801. http://doi.org/10.1016/j.energy.2015.01.029.

[274]   A. Vigneault, J.R. Grace, Hydrogen production in multi-channel membrane reactor via steam methane reforming and methane catalytic combustion, Int. J. Hydrogen Energy. 40 (2015) 233-243. http://doi.org/10.1016/j.ijhydene.2014.10.040.

[275]   X. Tan, K. Li, A. Thursfield, I.S. Metcalfe, Oxyfuel combustion using a catalytic ceramic membrane reactor, Catal. Today. 131 (2008) 292-304. http://doi.org/10.1016/j.cattod.2007.10.081.

[276]   D.S. Simakov, M. Sheintuch, Experimental optimization of an autonomous scaled-down methane membrane reformer for hydrogen generation, Ind. Eng. Chem. Res. 49 (2009) 1123-1129. https://doi.org/10.1021/ie900938n.

[277]   J. Chen, L. Yan, Ammonia decomposition coupled with methane combustion in catalytic microreactors for hydrogen production, Chem. Biomol. Eng. 2 (1994) 19-26. http://doi.org/10.11648/j.cbe.20170201.14.

[278]   Z. Yang, P. Yang, L. Zhang, M. Guo, Y. Yan, Investigation of low concentration methane combustion in a fluidized bed with Pd/Al$_2$O$_3$ as catalytic particles, RSC Advances. 4 (2014) 59418-59426. https://doi.org/10.1039/C4RA08534E.

[279]   W. Zukowski, The role of two-stage combustion in the development of oscillations during fluidized bed combustion of gases, Fuel. 79 (2000) 1757-1765. http://doi.org/10.1016/S0016-2361(00)00038-7.

[280]   Y.V. Dubinin, N. Tsereshko, A. Saraev, O. Bulavchenko, V. Yakovlev, Studying the effect of magnesium on the activity of a deep oxidation catalyst for a fluidized bed in methane and CO oxidation reactions, Catalysis in Industry. 10 (2018) 237-243. http://doi.org/10.1134/S2070050418030030.

[281]   Q. Dong, S. Zhang, Z. Duan, Q. Zhou, An energy analysis of the catalytic combustion burner, Heat. Technol. Energy Eff. (2006). http://hdl.handle.net/1969.1/5530.

[282]   S. Specchia, M.A. Ahumada Irribarra, P. Palmisano, G. Saracco, V. Specchia, Aging of premixed metal fiber burners for natural gas combustion catalyzed with Pd/LaMnO$_3$·2ZrO$_2$, Ind. Eng. Chem. Res. 46 (2007) 6666-6673. http://doi.org/10.1021/ie061665y.

[283]   C. Deng, W. Yang, J. Zhou, Z. Liu, Y. Wang, K. Cen, Catalytic combustion of methane, methanol, and ethanol in microscale combustors with Pt/ZSM-5 packed beds, Fuel. 150 (2015) 339-346. http://doi.org/10.1016/j.fuel.2015.02.018.

Chapter 3

Preparation of Pt/γ-Al₂O₃ catalyst coating in microreactors for catalytic methane combustion

ABSTRACT: A catalyst preparation method, consisting of slurry washcoating with γ-Al_2O_3 followed by impregnating platinum on the microreactor walls, has been investigated. The effect of various factors in the preparation procedures on the adhesion of the washcoated γ-Al_2O_3 was studied, including the slurry property (i.e., the binder type, concentration and molecular weight, γ-Al_2O_3 concentration and particle size, pH), and the (micro)reactor substrate and channel shape. The results show that the adhesion of γ-Al_2O_3 washcoat strongly depended on the slurry rheological characteristics. A good adhesion on FeCrAlloy substrates was obtained using the slurry with polyvinyl alcohol as the binder (typical concentration at 3 to 5 wt% and molecular weight of 57,000 - 186,000), 20 wt% γ-Al_2O_3 (particle size being around 3 μm) and pH = 3.5. FeCrAlloy as the substrate exhibited an excellent coating adhesion in rectangular or round channels, primarily due to the formation of alumina film over the surface during thermal pretreatment. The aluminum-free stainless steel as the substrate only showed a good adhesion in a round channel. Well-adhered Pt/γ-Al_2O_3 catalysts were then applied in a microreactor comprising parallelized microchannels made of FeCrAlloy under the optimized coating procedures, and investigated in terms of its performance in the catalytic methane combustion. It is shown that the reaction temperature has a greater influence on the methane conversion than the flow rate, and a favorable coverage of methane and oxygen on the catalyst surface is essential to obtain a good catalytic performance. These reaction results are in line with the temperature behavior measured along the microreactor.

Nomenclature

$F_{CH_4,i}$	Inlet molar flow rate of CH_4, mol s^{-1}
$F_{CH_4,o}$	Outlet molar flow rate of CH_4, mol s^{-1}
$F_{CO_x,o}$	Outlet molar flow rate of CO or CO_2, mol s^{-1}
ΔH_R	Heat of reaction for methane combustion, kJ mol^{-1}
i.d.	Inner diameter of the channel, m
L	Length of the channel, m
L^*	Normalized length of the channel (Eq. (3.3))
Q_{tot}	Total volumetric flow rate, m^3 s^{-1}
S_{CO_x}	Selectivity of CO or CO_2 (Eq. (3.2))
ΔT_{ad}	Adiabatic temperature rise, ^{o}C or K
V_{tot}	Total volume of channels for reaction in a multi-channel microreactor, m^3
X_{CH_4}	CH_4 conversion (Eq. (3.1))

Greek symbols

τ	Residence time, s (Eq. (3.4))
Φ	Inlet molar ratio of oxygen to methane

Abbreviation

BET	Brunauer-Emmett-Teller
GC	Gas chromatography
2-HEC	2-Hydroxyethyl cellulose

MW	Molecular weight
PEG	Polyethylene glycol
PVA	Polyvinyl alcohol
SEM	Scanning electron microscopy
TGA	Thermogravimetric analysis
Tylose	Methyl 2-hydroxyethyl cellulose

3.1. Introduction

Microreactors, with characteristic channel dimensions on the order of ca. 1 mm or below, have shown great potentials in intensifying reaction processes in comparison to conventional reactors (e.g. fixed-bed reactors for solid-catalyzed gas phase and multiphase reactions) [1-3]. The specific surface area of microreactors could reach 10,000 to 50,000 m^2 m^{-3} [4,5], compared to around 100 m^2 m^{-3} for traditional reactors, thereby leading to substantially enhanced mass and heat transfer rates [6,7]. The improved mass transfer can lead to enhanced reaction rates (e.g., in the presence of multiphase fluids or solid catalysts). The heat transfer enhancement avoids the presence of temperature hot spots due to the local accumulation of reaction heat in the microreactor, a feature especially favorable for handling strongly exothermic reactions or coupled exothermic and endothermic catalytic reactions [8]. Moreover, the modular, flexible and compact microreactor design allows an easy upscaling from the laboratory to the industrial scale aiming at mass production [4]. One challenge is how to deliver reaction fluids, as well as heat transfer fluids (if present), uniformly across a multitude of microchannels in order to ensure that the optimal microreactor performance is not lost during the numbering-up process (i.e., a replication of basic microchannel units) [9-11].

Solid catalysts (e.g., noble metal-based) can be incorporated into microreactors as wall coatings, and γ-Al_2O_3 represents one of the most common catalyst supports in use. Thus, a successful application of microreactors for solid-catalyzed catalytic reactions strongly depends on the formation of a well-adhered and uniform catalyst layer on the microreactor substrate [12,13]. Based on the properties of the catalyst and substrate surface, various methods have been used to deposit catalysts onto the microreactor wall, as summarized in some reviews [12,14,15]. Different coating methods and the corresponding preparation procedures have been investigated, including suspension [16-18], sol-gel deposition [19,20], electrophoretic deposition [21,22], chemical vapor deposition [23,24], physical vapor deposition [25,26], etc. The suspension technique (or slurry washcoating) is one of the most commonly used methods for depositing catalysts in microreactors, which typically consists of the following steps: microreactor surface pretreatment, slurry preparation and deposition, impregnation of the catalytically active component (e.g., noble metal), heat treatment (e.g., drying and calcination). Sometimes, a primer coating is used before the slurry deposition to further enhance the coating adhesion. Alternatively, the catalytically active component can be mixed with the prepared slurry prior to the coating step, allowing to attach the entire catalyst onto the microreactor wall in one step. It has been reported that the slurry properties (e.g., the binder nature, viscosity, pH

and particle size) could greatly influence the rheological properties of the washcoated layer as well as its adhesion [27]. A brief literature survey of key factors in these steps is presented below, including the substrate pretreatment, nature of binder, pH and particle sizes used in the slurry for washcoating, and primer coating.

The thermal pretreatment of the (microreactor) substrate is the most commonly used method to increase the substrate surface roughness. In the case of Al-containing substrates, such pretreatment also causes the migration of aluminum species over the substrate surface to form a thin film, effectively enhancing the adhesion between the coating layer and substrate. For instance, the thermal pretreatment of FeCrAlloy material could be conducted in a range of 800 to 1000 $^\circ$C for 5 to 10 h [28-30]. It has been reported that alumina crystals appeared at about 700 $^\circ$C. When the calcination temperature was increased to 900 $^\circ$C, the needle-like α-Al_2O_3 was substantially formed and tended to cover the whole surface. This is beneficial for anchoring the deposited washcoated layer. The rapid growth of α-Al_2O_3 grains and the agglomeration occurred at 1000 °C, forming the globular morphology. Other pretreatment methods such as the anodic oxidation on aluminum or aluminum alloy plates [31,32] and the chemical pretreatment on substrates made of aluminum, FeCrAlloy or stainless steel [33,34] were also reported.

The suspension method was characterized typically by adding the binder into a slurry (e.g., of γ-Al_2O_3), in order to finally form a smooth and well-adhered layer onto the walls of microreactors [35,36]. Binders are generally divided into two categories: organic binder (e.g., polymers) and inorganic binder (e.g., boehmite and colloidal alumina). The effect of different binders on the coating adhesion was investigated by Germani et al. [37]. A compromise between the shrinking behavior and particle packing of the coating could be reached using methyl 2-hydroxyethyl cellulose (Tylose) as the binder which has a better thickening effect compared to polyvinyl alcohol (PVA). Besides the binder structure, its molecular weight and concentration may also have a noticeable effect on the slurry viscosity and subsequently the prepared coating adhesion. An excessive addition of organic binders could result in cracks during calcination due to the polymer thermal decomposition [37]. Details on the binder characterization may be found elsewhere [38-40].

For washcoating of γ-Al_2O_3, the slurry stability also depends on whether γ-Al_2O_3 particles are well dispersed in the suspension. The viscosity and stability of the slurry greatly increase with the increasing pH value. This is because the net surface charge of particles is changed by adjusting the pH [41]. The initial particle size of γ-Al_2O_3 is also a key factor that affects the adhesion strength. Particle sizes of 2-5 μm were reported to be a suitable range to obtain a

stable slurry [27,39,42], because a smaller particle size improved the affinity and interlocking between particles in the coating.

Apart from directly applying slurry onto the microreactor wall, an intermediate layer of primer coating can be deposited in a previous step, acting as a link to enhance the adhesion between the substrate and the slurry deposition. Moreover, the difference in thermal expansion coefficients between the washcoated layer and the substrate could be decreased to some extent by applying primer coating in between. Various primer compositions have been investigated and optimized [17,43]. In order to further improve the coating adhesion on Al-free substrates like stainless steel, the substrate could be treated by the pack aluminisation technique before the primer coating step [44,45]. A thin alumina layer is expected to form on stainless steel by the diffusion of metal atoms over the surface.

Microreactors with wall-coated catalysts are promising for carrying out the catalytic combustion of methane efficiently. Compared with the conventional flame combustion, the catalytic methane combustion has been performed towards achieving a lower light-off or working temperature, less exhaust emission and more stable combustion [46]. Catalyst development, reactor design and operational conditions should be thus well addressed for obtaining an optimal process performance. Noble metal-based catalysts with high specific surface areas were reported to have a better catalytic performance than perovskites or hexaaluminate catalysts in the catalytic methane combustion, with lower activation energy, less pollutant and lower light-off temperature allowing more stable combustion [47,48]. Pd, Pt, Rh and Au as the active component have been widely studied [49]. Among them, Pd and Pt-based catalysts were reported as the most active one by far. The base/acid properties of the support affect the catalytic activity by interacting with the oxidized/metallized state of noble metals. It was reported that the decreased acidity strength of Al_2O_3 support (e.g., with Pd as the active component) could enhance the catalytic performance of methane combustion [50]. Pt/Al_2O_3 catalyst has also shown to be more active when the O_2/CH_4 molar ratio was varied from the oxygen-rich to methane-rich conditions [48]. So far, many studies have been performed to characterize the performance of catalytic methane combustion, but mostly in conventional fixed-bed reactors [51,52] or monolithic reactors [53,54]. Fewer studies were devoted to wall-coated microreactors that are promising owing to their enhanced mass and heat transfer rates, leading to a better process control in terms of high reaction rates and suppressing temperature excursion [55-57]. Especially, plate-type multi-channel microreactors, with appropriate catalyst coatings, seem very attractive for use in the catalytic methane combustion, allowing a

modular and compact coupling with heat transfer (for the utilization of the combustion reaction heat) or with an endothermic reaction (e.g., steam reforming), which becomes a research hotspot in the recent decade for the foreseeable industry benefits [58-60].

From the above literature survey, one may find that the research on how to obtain a good adhesion and dispersion of the catalytic layer onto the walls of microreactors is still needed, especially when it comes to γ-Al$_2$O$_3$ supported noble metal catalysts for use in the catalytic methane combustion. Thus, the main objective of this study is to investigate and characterize the slurry washcoating method of γ-Al$_2$O$_3$ onto microreactor walls, so as to ensure the formation of a stable, homogeneous and well-adhered catalyst layer. The effect of various factors in the preparation procedures was systematically studied, including the slurry property (i.e., the binder nature and its concentration and molecular weight, the pH value, the γ-Al$_2$O$_3$ content and particle size), and the (micro)reactor substrate material and channel shape. Then, washcoating of γ-Al$_2$O$_3$ under the optimized preparation conditions, followed by the impregnation of platinum, was used to prepare Pt/γ-Al$_2$O$_3$ catalyst on the walls of a laboratory-scale multi-channel microreactor made of FeCrAlloy. The microreactor performance was tested in the catalytic methane combustion, where the influence of operating conditions and the temperature distribution along the microreactor have been particularly addressed.

3.2. Experimental

3.2.1. Materials

γ-Al$_2$O$_3$ (3 μm, 99.97 % on metals basis), PVA (98-99 % hydrolyzed), acetic acid, tetraammineplatinum (II) nitrate (Pt(NH$_3$)$_4$(NO$_3$)$_2$, 99.99 % on metals basis) were purchased from Alfa Aesar. Tylose MH300 (methyl 2-hydroxyethyl cellulose, molecular weight (MW) of 95,000), 2-HEC (2-hydroxyethyl cellulose, MW of 90,000), PEG (polyethylene glycol, MW of 20,000) were obtained from Sigma-Aldrich. γ-Al$_2$O$_3$ with other particle sizes (20 nm - 180 μm) were also studied and obtained from Sigma-Aldrich. Boehmite (AlO(OH)) and dispersal P2 were obtained from Sasol.

The multi-channel platelets used for the coating adhesion test were made of FeCrAlloy (Kanthal A-1, 22 % Cr, 5.8 % Al and Fe for balance) and 316 L stainless steel, having an overall dimension of 50 mm (length) × 22 mm (width) × 3 mm (height). 10 parallel microchannels of rectangular shape with a dimension of 50 mm × 1.5 mm × 1 mm were machined on each platelet. Round capillaries made of FeCrAlloy and 316 L stainless steel having a dimension of 10 mm (outer diameter; o.d.) × 8 mm (inner diameter; i.d.) ×100 mm (length) and square capillaries made of

316 L stainless steel with a dimension of 8 mm (width) × 8 mm (height) × 100 mm (length) were used for coating adhesion test as well.

The catalytic methane combustion was performed in plate-type multi-channel microreactors. The microreactor basically consisted of two multi-channel platelets (made of FeCrAlloy or 316 L stainless steel) back-to-back and enclosed by two additional blind stainless steel plates (350 mm × 80 mm × 5 mm). Each platelet (317.5 mm × 50 mm × 3 mm) has 16 parallelized straight channels of 275 mm × 1.5 mm × 1 mm, the total number of machined microchannels in the microreactor being 32 (Fig. 3.1). Each platelet has an inlet fluid distributor and an outlet fluid collector, having a bifurcated tree-like geometry (Fig. 3.1) that guarantees a uniform fluid flow distribution across parallel microchannels [61,62]. Only the two sides and bottom of the rectangular microchannel on the platelets were coated with Pt/γ-Al$_2$O$_3$ catalyst, the fluid distributor and collector being not coated.
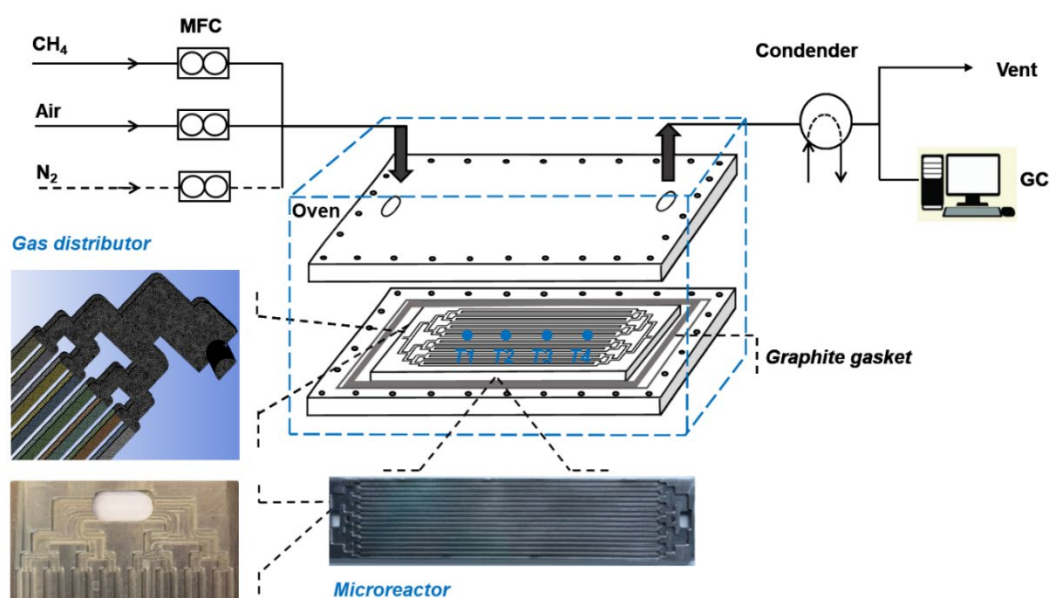
Fig. 3.1. Scheme of the catalytic methane combustion in the multi-channel microreactor coated with Pt/γ-Al$_2$O$_3$ catalyst. Thermocouples were placed at an axial distance to the beginning of the microchannels (T1: 55 mm, T2: 110 mm, T3: 165 mm, T4: 220 mm).

3.2.2. Catalyst preparation

3.2.2.1. Pretreatment

The platelets and capillaries made of FeCrAlloy were first immersed with acetone for 30 min in the ultrasonic bath at 45 $^\circ$C, in order to remove oil, grease and other dirt [63]. Thermal pretreatment was subsequently performed at 900 $^\circ$C (ramp from room temperature: 20 $^\circ$C min^{-1}; 10 h at final temperature), to generate a thin alumina layer over the substrate surface which

could be a strong bonding between the coating layer and the substrate [28,43]. In the case of platelets and capillaries made of 316 L stainless steel, sandblasting was first applied before the calcination pretreatment to remove the anti-corrosion layer on the surface as well as to increase its roughness.

3.2.2.2. Washcoating procedures

The γ-Al_2O_3 slurry was prepared by mixing γ-Al_2O_3 powders, binder and acetic acid [18]. Various binders (including Tylose, PVA, 2-HEC, PEG or boehmite) with different concentrations and/or molecular weights have been added in the slurry. γ-Al_2O_3 concentration was varied from 10 to 40 wt%, with its initial particle size ranging from 0.02 to 180 μm. pH of the slurry was changed from 1.5 (by adding acetic acid) to 9.35 (by adding NH_4OH). The slurry was then heated up to 65 ^{o}C for 2 h under 300 rpm stirring and stored at room temperature for at least 2 weeks to remove the inside bubbles before use.

Thus prepared slurry as the catalyst support precursor was first deposited on the walls of the parallelized microchannels on the microreactor platelets (made of FeCrAlloy and stainless steel) using syringe injection. The excessive suspension outside the microchannel was immediately removed with a razor blade. The platelets were then dried at room temperature overnight for at least 8 h, dehydrated at 120 ^{o}C for 8 h and finally calcined at 600 ^{o}C (ramp from room temperature: 2 ^{o}C min^{-1}; 2 h at final temperature). Multiple layers of coatings were obtained by repeating the same washcoating procedure as described above. A similar washcoating procedure was applied for coating inside circular or square capillaries, except that after the slurry washcoating, a rotary motor held one end of the capillary with a fixed rotation speed (ca. 30 rpm), keeping it at room temperature overnight. The same drying and calcination processes were then followed (see Appendix 3.A for more details about washcoating in such capillaries).

The primer coating was only tested on the 316 L stainless steel multi-channel platelet (with 10 parallel microchannels; dimensions shown in Section 2.1) before coating the slurry. The alumina sol-gel composed of 10 wt% dispersal P2, 3 % PVA (MW of 146,000-186,000) and 1 % HNO_3 was coated on the platelet by using syringe injection. Subsequently, the substrate was dried at room temperature overnight (for at least 8 h) and then dehydrated at 120 ^{o}C for 8 h. Then, calcination at 600 ^{o}C for 2 h took place before applying the same slurry deposition procedure as describe above.

3.2.2.3. Impregnation of catalytically active component

The incipient wetness impregnation was performed by immersing the coated multi-channel

platelet in a $Pt(NH_3)_4(NO_3)_2$ solution with a certain concentration. The impregnated coating was dried at room temperature overnight for at least 8 h, and then calcined at 450 °C (ramp from room temperature: 2 °C min^{-1}; 2 h at final temperature). The nominal Pt loading over the catalyst is about 3.8 wt% for the FeCrAlloy platelet, and about 3.5 wt% for the 316 L stainless steel platelet.

3.2.3. Washcoat adhesion test

The adhesion test of the prepared γ-Al_2O_3 washcoat was firstly performed by immersing the coated substrate in a glass beaker (containing acetone) that was placed in the ultrasonic bath (PCE-UC 20) for typically 3 h, the frequency of ultrasonic bath being 40 kHz. The weight loss of the substrate (i.e., multi-channel platelets or capillaries) was calculated based on its weight difference before and after the ultrasonic treatment combined with drying at room temperature. Another method used to test the adhesion is the thermal shock test, by rapidly heating the coated substrate to 800 °C (ramp: 20 °C min^{-1}) and cooling it down quickly to room temperature in the air, and repeating the cycle for 5 runs. The weight loss (i.e., the weight difference before and after the thermal shock test) was also measured.

3.2.4. Catalytic methane combustion in microreactors

Two mass flow controllers (MFC, Brooks SLA5850) were used to adjust the flow rates of methane and the synthetic air for the experiment (Fig. 3.1). The total gas flow rate was typically adjusted from 110 to 880 mL min^{-1} (based on ca. 20 °C and 1 atm). Methane-air mixture (concentration of methane at 2 to 10 vol. %) first passed the inlet stainless steel tube (i.d.: 3.7 mm, o.d.: 6 mm). A part of this tube (15 cm in length) was kept inside an oven to preheat the mixture gas to the required reaction temperature. Then, the gas mixture was introduced into the multi-channel microreactor (i.e., with parallel microchannels on the platelet made of FeCrAlloy or 316 L stainless steel) placed in the oven. It has to be mentioned that the microreactor was first heated up (ramp: 10 °C min^{-1}) to the targeted reaction temperature under the nitrogen atmosphere to avoid any reaction occurrence during this startup process, and then the gas was switched to the methane-air mixture for the reaction to start. The reaction temperature tested ranged from 300 to 450 °C, and refers to the measured oven temperature by a thermocouple located in its right corner (Fig. 3.1). Four thermocouples (T1-T4) were placed on the top surface of the microreactor at different axial positions (i.e., at 20 %, 40 %, 60 % and 80 % of the microchannel length from the inlet), touching the top of the middle microchannel (Fig. 3.1). The product gas first flew through a condenser at the outlet of the

microreactor to remove water, and was collected and analyzed using a gas chromatography (GC).

3.2.5. Analytical procedure

Gas product was collected by a Tedlar sample bag (SKC 3 L, 9.5×10 inch) with a single polypropylene septum fitting, and then analyzed by GC (Hewlett-Packard 5890 Series II) equipped with a thermal conductivity detector. A Porablot Q Al_2O_3/Na_2SO_4 column (length: 50 m; i.d.: 0.5 mm) and a CP-Molsieve 5 Å column (length: 25 m; i.d.: 0.53 mm) were used. The concentrations of the reference gas used were 20.7 % CH_4, 17.9 % CO_2, 2.99 % CO, 1.5 % C_2H_6, 1.49 % C_3H_8, 5088 ppm C_2H_4, 5122 ppm C_3H_6 and H_2 for the rest. The GC oven temperature was heated from 40 ^oC up to 90 ^oC (ramp: 20 ^oC min^{-1}) and maintained for 7.5 min. The detector temperature was kept at 200 ^oC.

The rheological characteristics of slurries used for washcoating were evaluated by a rheometer (HAAKE Mars III, Thermo Scientific). The diameter of cone-and-plate geometry is 60 mm, the angle 2 ^oC. The slurry viscosity was measured based on a shear rate in a range of 0.05 to 1500 s^{-1} at 20 ^oC.

Zeta potential of the slurry as a function of pH was measured on a ZetaPALS instrument (Brookhaven) by the use of an electrophoretic technique. The mobility of charged particles can be determined via this technique by the phase analysis light scattering (PALS).

Thermogravimetric analysis (TGA) of the γ-Al_2O_3 slurry was performed on a PerkinElmer TGA 4000 thermogravimetric analyzer. The slurry was heated up in nitrogen from 30 ^oC to 1000 ^oC (at 10 ^oC min^{-1}). Data were recorded by Pyris thermal analysis software.

Scanning electron microscopy (SEM) was performed on an XL30 ESEM (Philips) operating at 20 keV, to characterize the smoothness and thickness of the washcoated γ-Al_2O_3 layer on the microchannel. The specific surface area of the washcoated γ-Al_2O_3 or Pt/γ-Al_2O_3 catalyst was measured using a Micromeritics ASAP 2420 apparatus by nitrogen physisorption at -196 ^oC. The coating was scraped from the substrate and ground to a particle size below 25 μm. The samples were firstly degassed in the vacuum at 200 ^oC for 8 h before nitrogen adsorption. The surface area and pore size were evaluated using the Brunauer-Emmett-Teller (BET) method, and the micropore area was quantified by the t-plot method.

Transmission electron microscopy (TEM) analysis of the coated Pt/γ-Al_2O_3 catalyst was performed using an electron microscope CM12 (Philips) at 120 keV. The catalyst was scraped from the substrate and ground to a particle size below 25 μm, and prepared by ultrasonication

in acetone.

3.2.6. Definitions

The loading (unit: g m^{-2}) of γ-Al$_2$O$_3$ or Pt/γ-Al$_2$O$_3$ deposited on a multi-channel platelet is calculated as its weight gained on the substrate (i.e., after calcination) divided by the microchannel surface area subject to coating.

The CH$_4$ conversion (X_{CH_4}) and CO$_2$ (CO) selectivity (S_{CO_x}) are calculated based on Eqs. (3.1) and (3.2), respectively.

$$X_{CH_4} = \frac{F_{CH_4,i} - F_{CH_4,o}}{F_{CH_4,i}} \times 100\ \% \tag{3.1}$$

$$S_{CO_x} = \frac{F_{CO_x,o}}{F_{CH_4,i} - F_{CH_4,o}} \times 100\ \% \tag{3.2}$$

Here F means the molar flow rate. The subscripts i and o indicate the microreactor inlet and outlet, respectively.

The normalized length (L^*) is used to infer the thermocouple location in the multi-channel microreactor (Fig. 3.1). It is defined as the distance from the thermal couple to the beginning of the parallel microchannel in which it was inserted (x) divided by the entire length of the microchannel (L).

$$L^* = \frac{x}{L} \tag{3.3}$$

The residence time (τ) in the multi-channel microreactor is defined as the total volume of the parallel microchannels (V_{tot}) divided by the total volumetric flow rate of the gas entering the microreactor (Q_{tot}).

$$\tau = \frac{V_{tot}}{Q_{tot}} \tag{3.4}$$

3.3. Results and discussion

3.3.1. Effect of preparation procedures on the washcoat adhesion

Many factors can have an important effect on the adhesion and thickness of the washcoated γ-Al$_2$O$_3$ layer over the metal substrate surface, including among others the binder characteristics and the slurry properties. The influence of these key factors is discussed in the following sub-sections.

3.3.1.1. Effect of binder

The multi-channel FeCrAlloy platelets were initially coated with slurries containing different binders. The slurry composition is listed in Table 3.1. Fig. 3.2 shows that the results from the ultrasonic test are in good agreement with the thermal shock test results in Table 3.1, with regard to the influence of binder addition on the washcoat adhesion strength: PVA (5 wt%) ≈ Tylose (1.6 wt%) > PVA (5 wt%) + boehmite (1 wt%) > 2-HEC (1.6 wt%) > PEG (15 wt%) > without binder. Typically, well-adhered and stable washcoated layers were obtained on the parallel microchannels of the platelets by employing PVA or Tylose as the binder. No weight loss of the washcoat was observed for the case with PVA in the ultrasonic test after 3 h and only 1.2 wt% weight loss for the case with Tylose, with no weight loss found in the thermal shock test. A higher weight loss of 8 wt% according to the ultrasonic test was caused by adding boehmite with PVA in the slurry. In this case, a strong shrinkage behavior was observed during drying overnight at room temperature, which resulted in a higher washcoat detachment. PEG or 2-HEC as the binder presented a much higher detachment from the microchannel wall, finally resulting in 78.9 wt% or 69.5 wt% weight losses in the ultrasonic test, respectively (Fig. 3.2). Fig. 3.2 also shows that the weight loss curves with all binders tested reach a plateau after 1 or 2 h ultrasonic treatment, indicating that at least part of (if not all) the washcoated layer was strongly anchored to the microchannel wall in all cases.

Table 3.1

Effect of binder addition in the slurry on the surface area and adhesion of the γ-Al_2O_3 washcoat on FeCrAlloy platelets.[a]

Slurry composition		pH of the slurry	Surface area[b]	Weight loss[c]
γ-Al_2O_3	Binder			
(wt%)	(wt%)	(-)	(m^2 g^{-1})	(wt%)
20	Without binder	3.5	101.25	62.5
20	1.6 wt% 2-HEC	3.5	82.78	35.9
20	1.6 wt% Tylose	3.5	82.60	0
20	15 wt% PEG	3.5	74.25	45.2

| 20 | 5 wt% PVA | 3.5 | 78.53 | 0 |
| 20 | 5 wt% PVA +1 wt% boehmite | 3.5 | 83.10 | 5.2 |

[a] Other slurry preparation conditions: γ-Al_2O_3 initial particle size at 3 μm, PVA MW of 146,000-186,000, other binder MW information listed in Section 2.1. [b] Measured surface area of the γ-Al_2O_3 washcoat based on the BET method. [c] Weight loss of the washcoat according to the thermal shock test.
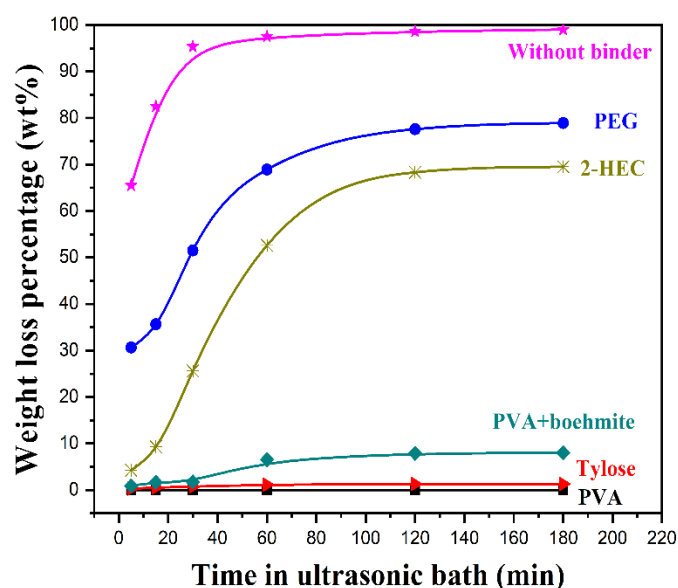
Fig. 3.2. Weight loss of the washcoated γ-Al_2O_3 layer as a function of the ultrasonic test time and the binder nature. Substrate: FeCrAlloy multi-channel platelet. Other slurry washcoating parameters are shown in Table 3.1.

The slurry viscosity can be adjusted by changing the binder and its concentration (Fig. 3.3). The slurry viscosity exponentially rises with the increasing binder percentage, especially for PVA. It was reported that the hydroxyl methyl cellulose could act as an associative function group in the acid environment [64]. The high amount of hydroxyl group is able to aid the adhesion and the bond between particles [65]. Thus, binders (like PVA and Tylose) with a large amount of hydroxyl group on their surface could form a stronger bridge between particles, enhancing effectively the adhesion. However, the hydroxyl group of PEG is located only at the end of polymer chains, which is not enough to form a firm bonding with alumina, thus causing a poor washcoat adhesion as shown in Table 3.1 and Fig. 3.2 [5,66].

As shown in Fig. 3.3, Tylose and 2-HEC carrying methyl and hydroxyethyl groups have a more significant effect on the slurry viscosity increase even at a lower concentration than the case with PVA. As for PEG, in order to obtain a similar viscosity, a factor of 15 in terms of concentration is required than for Tylose or 2-HEC. The slurry viscosity is not always directly related to the washcoat adhesion strength. However, the viscosity reflects the interaction of the entangled long-chain binder with γ-Al_2O_3. Hence, an enhanced adhesion is expected to be obtained by using the slurry with a suitable viscosity.
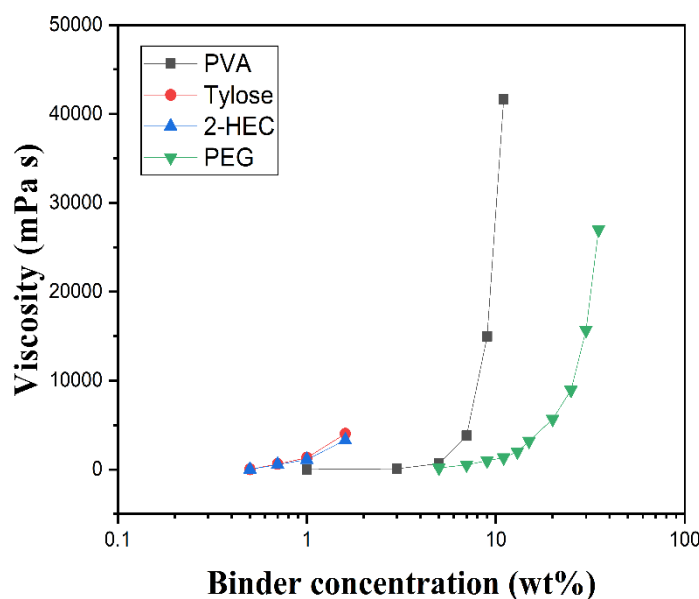
Fig. 3.3. Slurry viscosity in the presence of different binders (measured at a shear rate of 5 s^{-1}). Slurry preparation conditions: 20 wt% γ-Al_2O_3, pH at 3.5, other details listed in Table 3.1.

During the drying process of the washcoated layer, the binder particles were attached to the surface of alumina and strong bridges could thus be formed. Different types of hydrogen bridges could be formed in terms of different surface groups of γ-Al_2O_3 [67]. On one hand, PVA carrying the hydroxyl group (-OH) may serve as the anchoring site for the formation of hydrogen bridges with γ-Al_2O_3. $Al-O-H\cdots OH$ or $Al-O^-\cdots OH$ long chain could be formed in the suspension [67], which could effectively enhance the coating adhesion. On the other hand, partly dissolved alumina could form $Al-O-Al$ group, which may enhance the particle cohesion during drying. Furthermore, γ-Al_2O_3 particles of small sizes can be easily filled into the space between the large polymer binder particles. Alumina particles could migrate with the shrinking process to the contact points between particles during drying, leading to a remarkably increased interlocking between the polymer and alumina. Tylose and PVA have been evaluated to be the best binder

considering the negligible weight loss percentage from the ultrasonic and thermal shock tests (Table 3.1 and Fig. 3.2). A smaller concentration is required for Tylose than for PVA to achieve the same viscosity (Fig. 3.3). Also, Tylose is much easier to dissolve in water than PVA. However, the SEM image in Fig. 3.4a shows some obvious cracks between the side walls and the bottom of the microchannel. The strong shrinkage behavior of Tylose during drying hindered the formation of a smooth and crack-free washcoated layer at the two corners of the rectangular microchannel. In contrast, PVA could be a good option to form a smooth and crack-free washcoated layer, as shown in the SEM image of Fig. 3.4b.

Although the specific surface area of the obtained washcoat did not vary significantly in the case of adding different binders (Table 3.1), it was obviously decreased compared with the case without binders. This could be attributed to the modification of the washcoat pore structure to some extent associated with the thermal decomposition of binders during calcination [68,69]. Moreover, binders (e.g. PVA, Tylose, 2-HEC) were completely removed during calcination at ca. 600 ^{o}C, as confirmed by TGA results (cf. Fig. 3.B.1 in Appendix 3.B). The choice of this calcination temperature throughout the current work for washcoating was also based on the consideration of maintaining an appreciable specific surface area of the γ-Al$_2$O$_3$ washcoat (cf. Table 3.B.1 in Appendix 3.B).
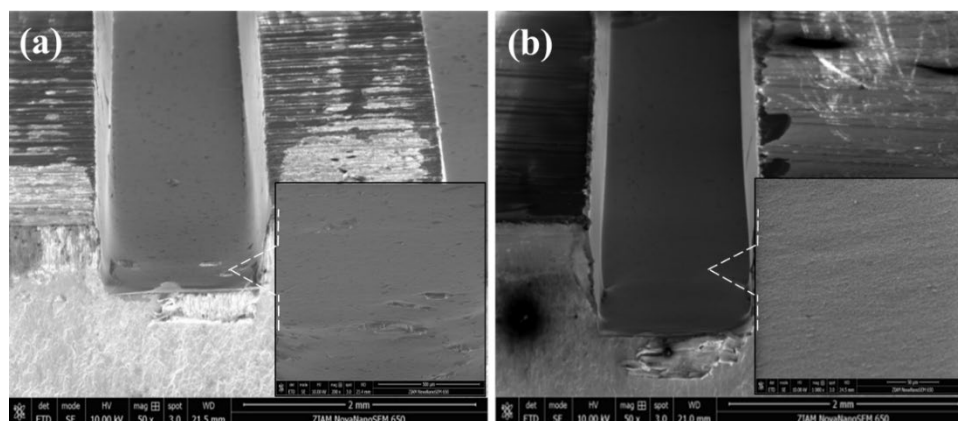
Fig. 3.4. SEM micrographs of the cross-section of the washcoated γ-Al$_2$O$_3$ layer in the microchannel of the multi-channel FeCrAlloy platelet using 1.6 wt% Tylose (a) and 5 wt% PVA (b) as the binder in the slurry. Other slurry washcoating parameters are shown in Table 3.1.

3.3.1.2. Effect of concentration and molecular weight of PVA

As described above, PVA as the binder used in the slurry deposition presents the best washcoat adhesion onto the microchannel wall. The slurry characteristics depend not only on the chemical structure of the binder, but also on its concentration and molecular weight (MW).

Higher MW results in an increased slurry viscosity even at low concentrations of PVA (Table 3.2). The results in Fig. 3.5 indicate that a stable washcoated layer on the FeCrAlloy platelet with negligible weight loss during the ultrasonic treatment was obtained when using a PVA concentration of 3 - 5 wt% with the MW at 57,000 - 186,000, or of 1 wt%, but only with the MW at the highest range tested (146,000 - 186,000). Upon increasing the MW, longer PVA polymer chains could better disperse alumina particles and better prevent particle agglomeration in the slurry, thus it is possible to provide a better spatial stabilization of alumina in the slurry. However, when the PVA concentration is higher than 5 wt%, the weight loss of the washcoat in the ultrasonic treatment increased obviously with the increasing MW. This could be explained by the fact that a higher MW with a higher concentration commonly results in a stronger shrinkage behavior, which could easily generate cracks on the surface of the finished washcoated layer. Moreover, the excessive polymer binder could occupy a large fraction of the spatial structure in the washcoat than was required, and was not able to form a bond bridge with alumina. The structure was thus much easier to break under high temperature calcination. As for the MW of 13,000 - 23,000, Fig. 3.5 shows that the weight loss exhibited an obvious reduction as the PVA concentration was increased from 1 to 11 wt%. The high weight loss at lower PVA concentrations is mainly due to the insufficient amount of polymer and thus less hydrogen bridge links to alumina, especially when considering the fact that a good dispersion of alumina particles in the slurry could not be promoted with such low MW PVA.

Table 3.2

Effect of PVA concentration and molecular weight on the slurry viscosity and the property of the obtained washcoat on FeCrAlloy platelets.[a]

PVA concentration (wt%)	Molecular weight (g mol^{-1})	Viscosity[b] (mPa s)	Surface area[c] (m^2 g^{-1})	Pore volume (cm^3 g^{-1})	Average pore size (Å)
1	88,000-97,000	7.75	64.99	0.32	195.39
5	88,000-97,000	653.10	66.85	0.35	211.43
11	88,000-97,000	36898.20	81.84	0.48	226.92

| 5 | 146,000-186,000 | 784.69 | 78.53 | 0.35 | 198.20 |
| 5 | 13,000-23,000 | 56.50 | 62.82 | 0.45 | 224.62 |

[a] Other slurry preparation conditions: γ-Al$_2$O$_3$ initial particle size at 3 μm, pH = 3.5. [b] Measured at a shear rate of 10.34 s -1. [c] Measured surface area of the γ-Al$_2$O$_3$ washcoat based on the BET method.
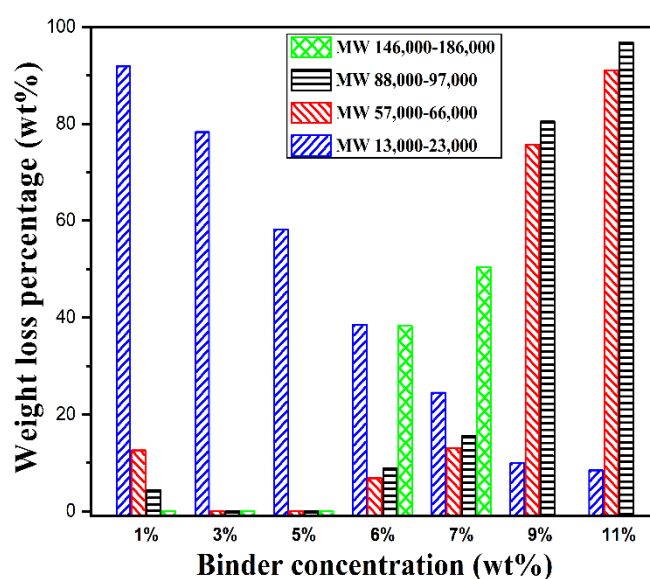
Fig. 3.5. Weight loss of the washcoated γ-Al$_2$O$_3$ layer prepared using PVA as the binder at different concentrations and molecular weights after 3 h ultrasonic treatment. Other slurry preparation conditions: 20 wt% γ-Al$_2$O$_3$ (initial particle size at 3 μm), pH = 3.5. Substrate: FeCrAlloy platelet.

In addition, it is seen from Table 3.2 that the BET surface area of the prepared washcoat layer slightly increased with the PVA MW and concentration. A high surface area might be attributed to a better particle dispersion and less agglomeration using PVA (5 wt%) with a higher MW [70,71]. However, a lower pore volume and average pore size appeared when using a higher PVA MW, possibly due to the disruption of pore structure order with long-chain PVA to some extent [72]. A higher BET surface area obtained at a higher PVA concentration (i.e., at the MW of 88,000 - 97,000; Table 3.2) could be explained by the fact that a larger amount of spatial structure was occupied by PVA, which inhibited the close packing of alumina particles. Accordingly, a higher surface area with a larger pore volume and pore size was observed thereof.

Thus, the washcoat adhesion and specific surface area could be varied by adjusting the concentration and MW of PVA. Typically, the PVA MW of 57,000 - 186,000 with the concentration in a range of 3 to 5 wt% could be considered as an appropriated range for the slurry preparation.

3.3.1.3. Effect of pH

The pH value determines the fluidity and stabilization of the slurry. PVA with the MW of 146,000 - 186,000 and concentration of 5 wt% was selected as the optimized binder composition during the slurry preparation. The influence of pH (1.5 - 9.35) of the slurry was investigated on the weight loss of the finally obtained γ-Al_2O_3 washcoat on FeCrAlloy platelets after 3 h in the ultrasonic bath, as shown in Fig. 3.6. The weight loss first decreased with the increasing pH value, but then remarkably increased with the pH value reaching 9.35. A distinctive feature may be seen, namely no weight loss at pH = 3.5.
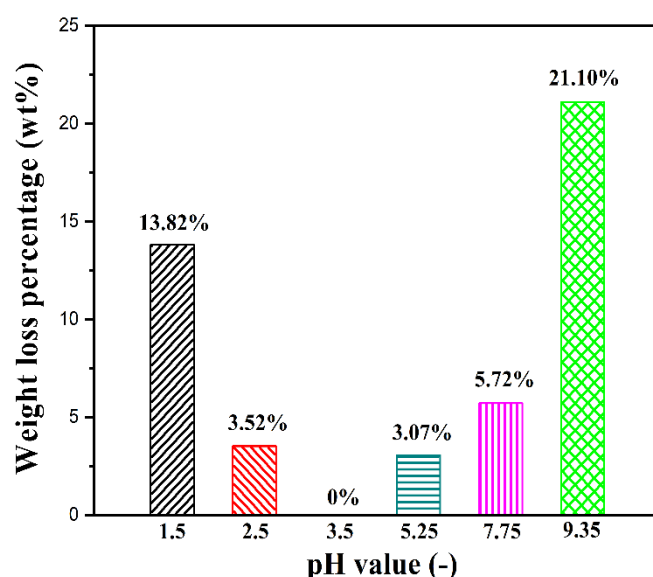
Fig. 3.6. Weight loss of γ-Al_2O_3 washcoat after 3 h ultrasonic treatment as a function of the pH value of the slurry used for the deposition. Other slurry preparation conditions: 20 wt% γ-Al_2O_3 (initial particle size at 3 μm), 5 wt% PVA (MW of 146,000-186,000). Substrate: FeCrAlloy platelet.

Fig. 3.7 shows the variation of the slurry viscosity and the zeta potential as a function of the pH value. The viscosity obviously rises, whereas the zeta potential gradually decreases with the increasing pH from 1.5 to 9.35. The larger zeta potential (higher than that of the isoelectric point) indicated that the (negative) particle surface charges increase with the increasing pH. Under a strong base environment, alumina particles in the slurry carry a negative electric charge

($Al_2O_3 + 2OH^- + 3H_2O \rightarrow 2Al(OH)_4^-$). High viscosity values could be explained by the increased adsorption rate of free ions of the negatively charged particles (Al(OH)$_4^-$) over the alumina surface at high pH values [73,74]. The higher amount of free ions carrying more current could remarkably reduce the movement speed of the particles. Thus, an unevenly washcoated layer could be caused by the formation of particle agglomerations and poor particle dispersion at pH = 9.35, as confirmed by the SEM image shown in Fig. 3.8. This eventually resulted in a high weight loss under the ultrasonic treatment (Fig. 3.6).

In comparison, low slurry viscosities at lower pH values (< 3.5) resulted in a higher weight loss (Fig. 3.6). This observation is in good agreement with the tendency of the zeta potential curve (Fig. 3.7), an important factor to reflect the mobility and stability of the suspension. At lower pH values (e.g., 1.5), the dissolution of alumina particles took place in the acidic solution ($Al_2O_3 + 6H^+ \rightarrow 2Al^{3+} + 3H_2O$) [75]. Al^{3+} dissolution and the surface charging became the main reaction [76]. The mutual electrostatic repulsion forces between particles were enhanced due to the addition of H$^+$ ions [73,77]. It resulted in a high fluidity of the slurry with well-dispersed alumina particles. Thus at pH < 3.5, a worse coating adhesion was observed when decreasing pH. It is worth noting that the original pH of the prepared slurry was around 5 and the sedimentation took place during storage, and the obtained washcoated layer was also much easier to peel off. Therefore, a stable and uniform washcoated layer of alumina can be formed by preparing slurry at a slight acid environment of pH ≈ 3.5 under which the suitable zeta potential (not too high) and viscosity (not too low) values were ensured.
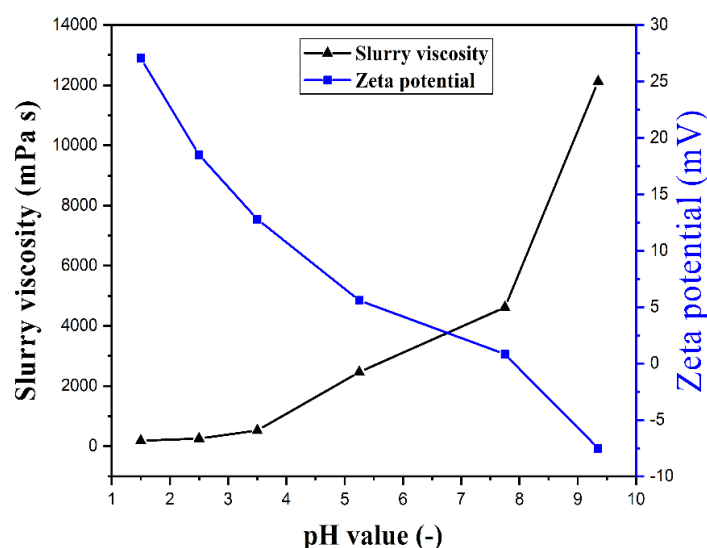
Fig. 3.7. Slurry viscosity and zeta potential as a function of the pH value. Shear rate for the viscosity measurement was at 10.34 s^{-1}. Other slurry preparation conditions: 20 wt% γ-Al$_2$O$_3$ (initial particle size at 3 μm), 5 wt% PVA (MW of 146,000 - 186,000).
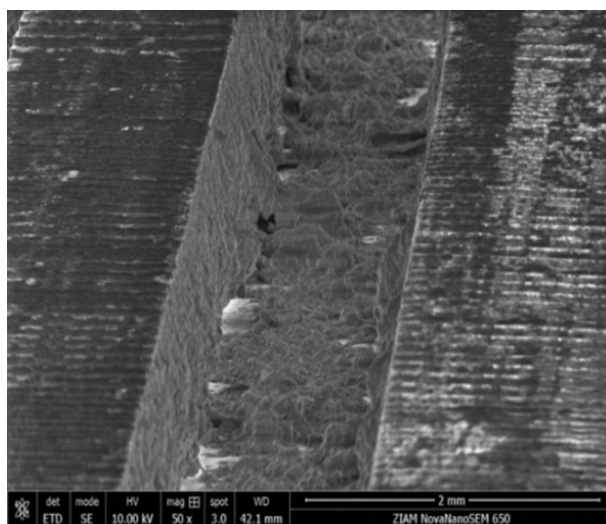
Fig. 3.8. SEM micrograph of the washcoated γ-Al_2O_3 layer on the microchannel of the FeCrAlloy platelet. Slurry preparation conditions: 20 wt% γ-Al_2O_3 (initial particle size at 3 μm), 5 wt% PVA (MW of 146,000 - 186,000), pH = 9.35.

3.3.1.4. Effect of initial γ-Al_2O_3 particle size

The weight loss curves of the washcoat subject to the ultrasonic treatment, when using different γ-Al_2O_3 particle sizes in the slurry for deposition on the FeCrAlloy platelet, are presented in Fig. 3.9a. In the case of particle sizes between 45 and 180 μm, 100 wt% weight loss was found within 1 h, and most of the weight loss took place within 5 min. It seems that the larger the particle size, the higher the weight loss for a given short ultrasonic test time. Here, a serious particle sedimentation in the slurry is expected to have occurred, which could be attributed to the significant liquid-solid density difference. For instance, the slurry prepared with 100 μm alumina exhibited an obvious sedimentation with the appearance of two separate phases within 10 h (Fig. 3.9b). Thus, the slurry composed of larger particles is generally less adhered onto the substrate than that of smaller particles. Larger γ-Al_2O_3 particles in the suspension are thus not favorable to form the extensive mechanical interlocking due to fewer contact points for anchorage.

As the alumina particle size decreased to 3 μm, more substantial contact points could be created between smaller particles, leading to a significantly improved anchorage and interlocking on the surface of the substrate [5]. Brownian motion usually overcomes the effect of gravity for smaller particles (e.g., with sizes around the sub-micron scale). Thus, no separate phases occurred for alumina with 3 μm even after 3 months (Fig. 3.9b). However, for the particle size in a range of 0.02 to 3 μm, the washcoat weight loss increased with the decreasing particle size in use (Fig. 3.9a). The maximum weight loss is 18 wt% after 3 h ultrasonic test in the case of

using a particle size of 0.02 μm. As shown in Fig. 3.9b, for this particle size the sedimentation of the slurry slowly occurred within 4 days (the reason of which is not clear yet). In this case, alumina particles seemed to be loosely bounded due to the weaker interlocking formed between particles in the deposited coating, and eventually could be easily peeled off under the ultrasonic vibration.

Furthermore, smaller particles are more capable of penetrating into the surface cavities, forming a strong interlocked with the substrate. The tighter packing of particles of smaller sizes (e.g., 3 μm), the stronger the mechanical/interfacial force formed between particles and the substrate. However, much larger particles are not favorable to form the extensive mechanical interlocking, due to a looser particle packing that can be easily carried away from the ultrasonic vibration [39].

Interestingly, it has been reported that a good adhesion of CeO_2/CuO washcoat on ceramic monoliths could be achieved starting from a slurry with a ceria particle size range from ca. 1 to 3 μm [78,79]. This size range is similar to our findings, suggesting that the optimal particle size in the slurry for a good adhesion might poorly depend on the chemical composition of the washcoated layer.
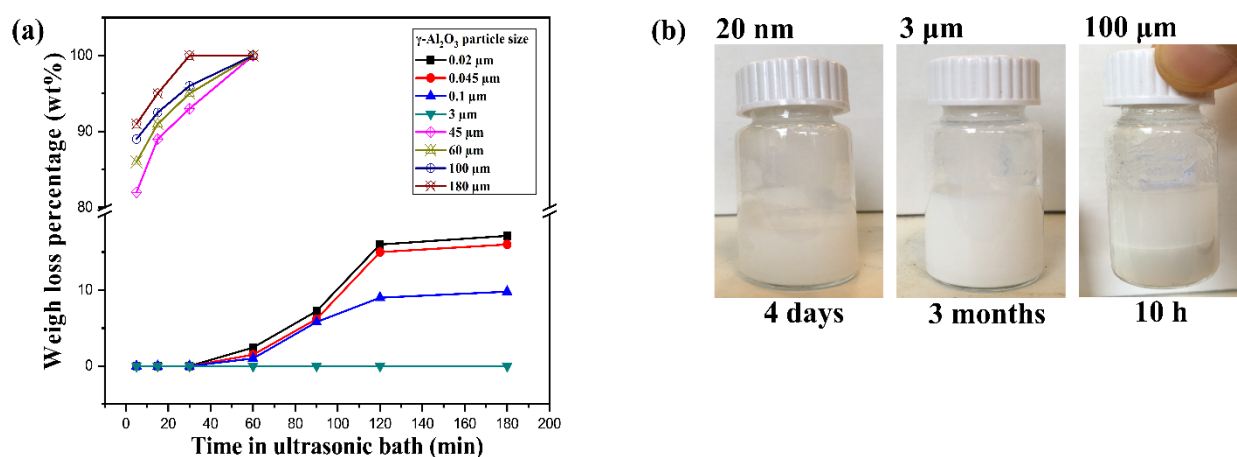
Fig. 3.9. (a) Weight loss of the washcoated γ-Al_2O_3 layer on the microchannel of the FeCrAlloy platelet as a function of γ-Al_2O_3 particle size used in the slurry preparation. (b) Photos of slurries prepared using 20 nm, 3 μm and 100 μm γ-Al_2O_3 particles at different storage times. Other slurry preparation conditions: 20 wt% γ-Al_2O_3, 5 wt% PVA (MW of 146,000-186,000), pH = 3.5.

All the above observations indicate that the initial γ-Al_2O_3 particle size is an essential factor that

affects the adhesion characteristics of the washcoated layer on the substrate. A higher mechanical stability of the washcoated layer can be obtained with relatively smaller initial particle sizes. A γ-Al$_2$O$_3$ particle size of about 3 µm seems appropriate for obtaining a well-adhered washcoated layer with endurance.

3.3.1.5. Effect of γ-Al$_2$O$_3$ content

The adhesion test results on the FeCrAlloy platelet under the ultrasonic treatment of washcoats prepared with various γ-Al$_2$O$_3$ concentrations in the slurry are presented in Table 3.3. Almost no weight loss was observed of the washcoat when the γ-Al$_2$O$_3$ concentration used was in a range of 10 - 20 wt%. The weight loss sharply increased to 10.03 wt% and 32.56 wt% when the γ-Al$_2$O$_3$ concentrations were at 30 wt% and 40 wt%, respectively. Moreover, the coating surface appeared to have irregularities in the latter cases (Fig. 3.10). This may be explained by the stronger attractive force caused by a closer distance between alumina particles at high concentrations. The surface cracks consequently appeared during calcination due to the particle agglomeration. Also, the slurry viscosity was found to exponentially increase with the increasing γ-Al$_2$O$_3$ concentration. Increasing the slurry viscosity (or γ-Al$_2$O$_3$ concentration) and/or the number of washcoated layers tended to increase the γ-Al$_2$O$_3$ loading on the microchannel (Table 3.3). SEM images (Figs. 10a and b) also visually confirm that the γ-Al$_2$O$_3$ loading on the microchannel was remarkably increased in the cases of using 30 wt% and 40 wt% γ-Al$_2$O$_3$ in the slurry compared with the case with 20 wt% γ-Al$_2$O$_3$ (Fig. 3.4b). The formation of an uneven washcoated layer was observed, however, in the cases with higher γ-Al$_2$O$_3$ concentrations (> 20 wt%).

The desired amount of the washcoat to support the catalytically active component on a microchannel commonly depends on the reaction type/conditions and the targeted application. In terms of the single layer loading, it could be increased from 28.01 to 123.97 g m^{-2} when using 10 to 40 wt% γ-Al$_2$O$_3$ in the slurry for deposition. Similar observations were reported by several researchers [27,80-82]. To reach a higher amount of the washcoat deposited on the microchannel, successive deposited layers are often needed.

Table 3.3

Effect of γ-Al_2O_3 concentration on the slurry viscosity, the loading and adhesion strength of the obtained washcoat on FeCrAlloy platelets.[a]

γ-Al_2O_3 concentration (wt%)	Viscosity of slurry (mPa s)[b]	Weight loss percentage[c] (wt%)	γ-Al_2O_3 loading (g m^{-2})			
			1st layer	2nd layer	3rd layer	4th layer
10	273.26	0.11	28.01	68.00	105.60	173.50
20	784.69	0	54.16	110.60	183.50	283.50
30	1652.72	10.03	90.41	198.50	296.50	510.00
40	18121.40	32.56	123.97	305.00	460.60	/

[a] Other slurry preparation conditions: γ-Al_2O_3 initial particle size at 3 μm, 5 wt% PVA (MW of 146,000-186,000, pH = 3.5. [b] Measured at a shear rate of 10.34 s^{-1}. [c] Weight loss tested on the single layer washcoat for 3 h ultrasonic treatment.
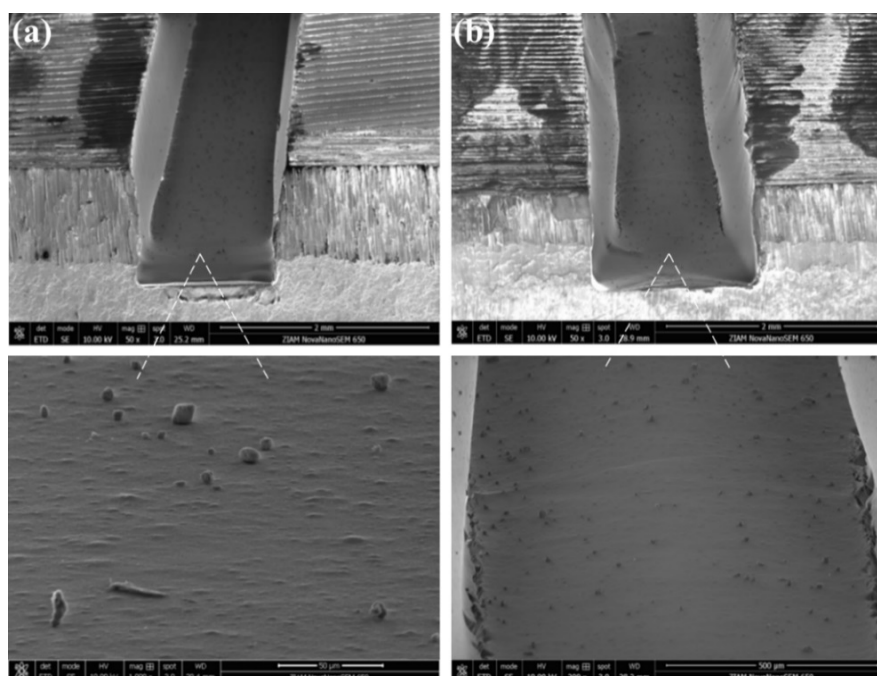
Fig. 3.10. SEM micrographs of the cross-section of the washcoat in the microchannel of the FeCrAlloy multi-channel platelet using 30 wt% (a) and 40 wt% (b) γ-Al_2O_3 in the slurry. Other slurry washcoating parameters are shown in Table 3.3.

3.3.1.6. Effect of reactor material and channel shape

Based on the optimal washcoating conditions on FeCrAlloy multi-channel platelets found from the experiments discussed above, γ-Al$_2$O$_3$ washcoating has been applied onto two different reactor materials (FeCrAlloy and 316 L stainless steel) in the form of capillaries or multichannel platelets with different channel shapes (round, rectangular and square). The coating conditions are characterized by using 20 wt% γ-Al$_2$O$_3$ (initial particle size at 3 μm), PVA as the binder (MW of 146,000 - 186,000), pH = 3.5 in the slurry. No weight loss under the ultrasonic treatment was observed when depositing the washcoated layer on FeCrAlloy substrates with (micro)channels of both round and rectangular shapes (Table 3.4). In contrast, 0.66 wt%, 8.24 wt% and 11.49 wt% weight losses in the washcoating have been observed for (micro)channels made of stainless steel material with round, rectangular and square shapes, respectively. Under such circumstances, the washcoat detachment mostly occurred at two bottom corners of the rectangular or square channels after the ultrasonic treatment (Fig. 3.11). The weight loss difference between the two materials is firstly due to that the surface of FeCrAlloy was much rougher than that of stainless steel. Thus, more anchoring sites existed over the FeCrAlloy surface, resulting in a stronger interlocking between the washcoated particles and surface irregularities over the substrate. More importantly, a thin layer of alumina was formed on the FeCrAlloy surface after calcination, which effectively improved the adhesion strength. For the stainless steel case, iron oxide was probably formed on the surface after calcination. It is thus assumed that the washcoated layer possibly has a stronger affinity with the alumina thin layer (e.g., via $Al - O - Al$ bonds) on FeCrAlloy than with iron oxide (e.g., via $Al - O - Fe$ bonds) on stainless steel.

In order to improve the coating adhesion on 316 L stainless steel, the primer coating (cf. details in Section 2.2.2) was employed before depositing alumina coating [17,83]. According to the literature [17,70], a strong bond between the primer coating and the peroxidized 316 L surface could be formed. However, the test results indicate that the use of the current primer coating could not reduce the washcoat weight loss during the ultrasonic treatment (cf. Table 3.C.1 in Appendix 3.C), where 23.84 wt% weight loss was observed on the stainless steel multi-channel platelet for 1 h ultrasonic test. This is even worse than the results without applying primer coating (Table 3.4). The reason for this is not clear yet, which indicates that the primer coating method deserves further investigation. Thus, the primer coating was not used in our following experiments.

Table 3.4

Weight loss of the γ-Al$_2$O$_3$ washcoated layer on different reactor materials with different channel shapes after 3 h ultrasonic treatment.[a]

Channel shape	Weight loss percentage (wt%)	
	FeCrAlloy	316 L stainless steel
Rectangular[b]	0	8.24
Circular[c]	0	0.66
Square[c]	Not tested	11.49

[a] Channel dimensions are shown in Section 2.1. Slurry preparation conditions: 20 wt% γ-Al$_2$O$_3$ with its initial particle size at 3 μm, 5 wt% PVA (MW of 146,000 - 186,000), pH = 3.5. [b] Tested on parallel microchannels in a multi-channel platelet. [c] Tested in capillaries.
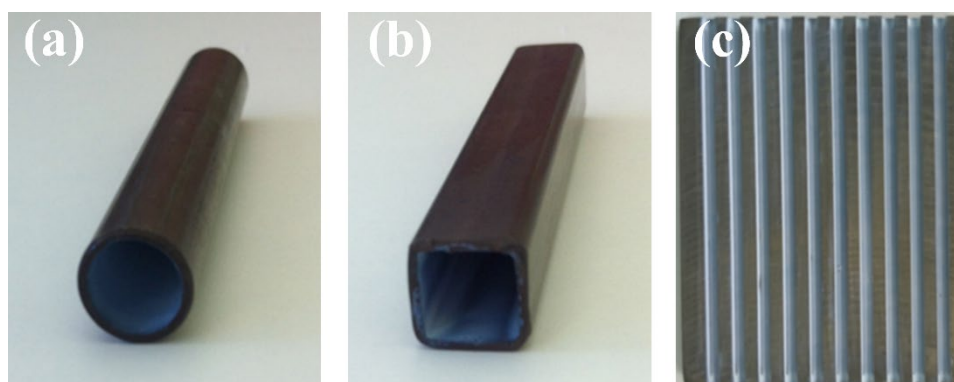
Fig. 3.11. Washcoated layer on 316 L stainless steel with different channel shapes: (a) circular (i.d. = 8 mm), (b) square (width × height × length = 8 × 8 × 100 mm), (c) rectangular (width × height × length = 1.5 × 1 × 50 mm). Slurry preparation conditions are shown in Table 3.4.

3.3.1.7. Effect of viscosity during the drying process

The washcoated layer (i.e., as tested on multi-channel platelets of this study) should have a uniform and constant thickness along the microchannel, for ensuring its good catalytic performance when impregnated with catalytically active components. The platelets were initially fully filled with the slurry. The excess slurry around the top of parallel microchannels was then scraped off. The slurry adhered to the bottom and the side walls of microchannels during drying. The drying process was characterized by the particle packing and the shrinkage degree, which is supposed to rationalize the washcoat shape as shown in Fig. 3.12. The water

evaporation in the washcoated layer is accompanied by the shrinkage behavior at the same time. During the experiment, it was observed that drying of highly viscous suspensions was faster to reach the finally stagnant film (due to less volatility) compared with suspensions with low viscosity. That is, in the latter case, a longer drying time was needed to reach the stagnant film for the same γ-Al_2O_3 loading. The film thickness further shrunk until a homogeneous solid washcoated layer was formed. For less viscous suspensions, part of the suspension at the top section of side channel walls may slowly slip down and accumulate at the bottom of the channels during drying. The coating layer thus appeared to be thicker on the bottom than on the two side walls. In contrast, the washcoated layer in the case of using highly viscous suspensions was much thicker at the lower part of the side walls than at the upper part. Thus, a suitable slurry viscosity is required for a uniform coating around the microchannel, which is in qualitative agreement with SEM images shown in Figs. 4b and 10).
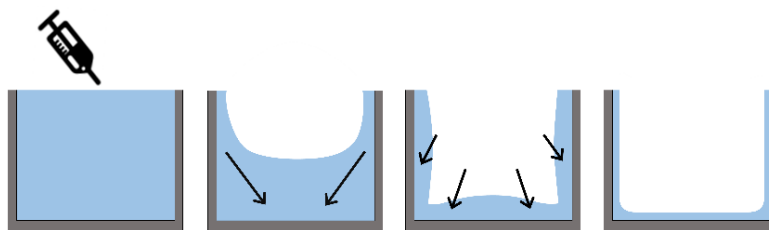
Fig. 3.12. Schematic of the drying process of the deposited γ-Al_2O_3 slurry in a rectangular microchannel (i.e., on a multi-channel platelet as tested in this study).

3.3.2. Catalytic methane combustion over the coated Pt/γ-Al_2O_3 catalyst in the multi-channel microreactor

The catalytic methane combustion was studied over the coated Pt/γ-Al_2O_3 catalyst in the multi-channel microreactor (containing the microchannel platelet made of FeCrAlloy or 316 L stainless steel). The coating was applied using the optimized slurry preparation conditions characterized by using 20 wt% γ-Al_2O_3 (3 μm particle size), 5 wt% PVA (MW of 146,000-186,000) at a slurry pH of 3.5, followed by the impregnation of Pt. The TEM picture confirms the successful dispersion of platinum particles in the catalyst (cf. Fig. 3.D.1 in Appendix 3.D). The reaction performance as a function of the key operational conditions was investigated, including the temperature, flow rate and O_2/CH_4 molar ratio. The temperature distribution along the microreactor was also studied under selected reaction conditions.

3.3.2.1. Effect of operating conditions on the methane conversion

The methane conversion as a function of the reaction temperature under different total flow

rates (i.e., the sum of air and methane flow rates, based on ca. 20 °C and 1 atm) is shown in Fig. 3.13a, for the multi-channel microreactor composed of FeCrAlloy platelet. At a total flow rate of 110 mL min^{-1}, the conversion presented a remarkable increase from 12.7 % to 95.75 % when the temperature was increased from 300 to 450 °C at an inlet O_2 to CH_4 molar ratio (Φ) of 2. The light-off was observed with a sharp conversion increase starting at ca. 350 °C. This light-off phenomenon is likely due to the local heating of the catalyst given the highly exothermic nature of the combustion reaction (the heat of the reaction, ΔH_R being ca. -810 kJ mol^{-1}) and the favorable fractional coverage of the catalyst surface by the adsorbed methane and oxygen under such conditions [47,48], leading to a significant increase of the catalytic activity. The smaller flow rate rendered a longer residence time (τ; cf. Eq. (3.4)) in the coated microchannel. For instance, the residence time was increased by a factor of 8 from 1.8 s (880 mL min^{-1}) to 14.41 s (110 mL min^{-1}) at 450 °C, and thus the methane conversion was increased from 78.53 % to 95.75 %. Fig. 3.13a further reveals that the reaction temperature has a greater influence than the flow rate, due to the remarkable increase of the intrinsic kinetic rate especially at the catalytic ignition temperature (where the light-off occurs) or above.

Fig. 3.13b shows that carbon monoxide was formed increasingly when prolonging the residence time ($\tau > 1.8$ s) at a reaction temperature of 450 °C and $\Phi = 2$ (stoichiometric ratio for a complete combustion), however, its selectivity is low (< 1.2%). One possibility for CO formation is that the adsorbed oxygen over the localized areas of the catalyst was not sufficient [48], giving rise to the incomplete combustion ($CH_4 + 1/2O_2 \rightarrow CO + 2H_2$). Moreover, H_2 produced herein could further react with the complete combustion product, CO_2, according to the reverse water-gas shift reaction to produce CO ($H_2 + CO_2 \rightarrow CO + H_2O$). It seems from Fig. 3.13b that the longer the residence time, the higher the chance for such reactions for CO formation to occur. It should be noted that no carbon monoxide was detected (i.e., the CO_2 selectivity being 100%), when Φ was set higher than 2, indicating a more sufficient coverage of the adsorbed oxygen on the catalyst surface.

Fig. 3.13c reveals that the methane conversion tended to decrease when increasing Φ from 2 to 10 (oxygen-rich). The lower conversion for the oxygen-rich case could be explained by the competitive adsorption between oxygen and methane over the catalyst surface. Since the methane adsorption energy is higher than that of oxygen [84], a competitive adsorption of oxygen prevented further oxidation by inhibiting the weakly adsorbed methane on the active sites [85]. Thus, a favorable surface coverage by the adsorbed methane and oxygen over the catalyst surface is essential for achieving a desired conversion. Another possibility is that the

bond between the absorbed oxygen and the oxidized platinum is stronger than that with metallic platinum [86], which is not favorable for methane and/or oxygen adsorption (rate determining step). Commonly, its metallic state presents a higher catalytic activity compared to its oxidized state (PtO_2), despite the high-dispersed phase of the latter state [87,88]. Thus, the platinum catalyst itself might be less active under the condition of the predominant oxygen-covered surface and thus not be able to fully catalyze methane oxidation especially when the present methane amount was high. Consequently, a low methane conversion would be expected when using an oxygen-rich mixture due to the insufficient adsorbed methane and/or less available metallic state of platinum on the catalyst surface.

Fig. 3.13d presents a comparison of the methane conversion in the multi-channel microreactors composed of FeCrAlloy and 316 L stainless steel reaction platelets. A slight lower conversion was obtained in the stainless steel microreactor under otherwise the same conditions, possibly due to a somewhat lower Pt loading. Considering the coating adhesion strength, FeCrAlloy microreactors appear to be a better option for long-term uses, whereas 316 L stainless steel microreactors represent a more cost-effective alternative (especially if the coating adhesion is better addressed).
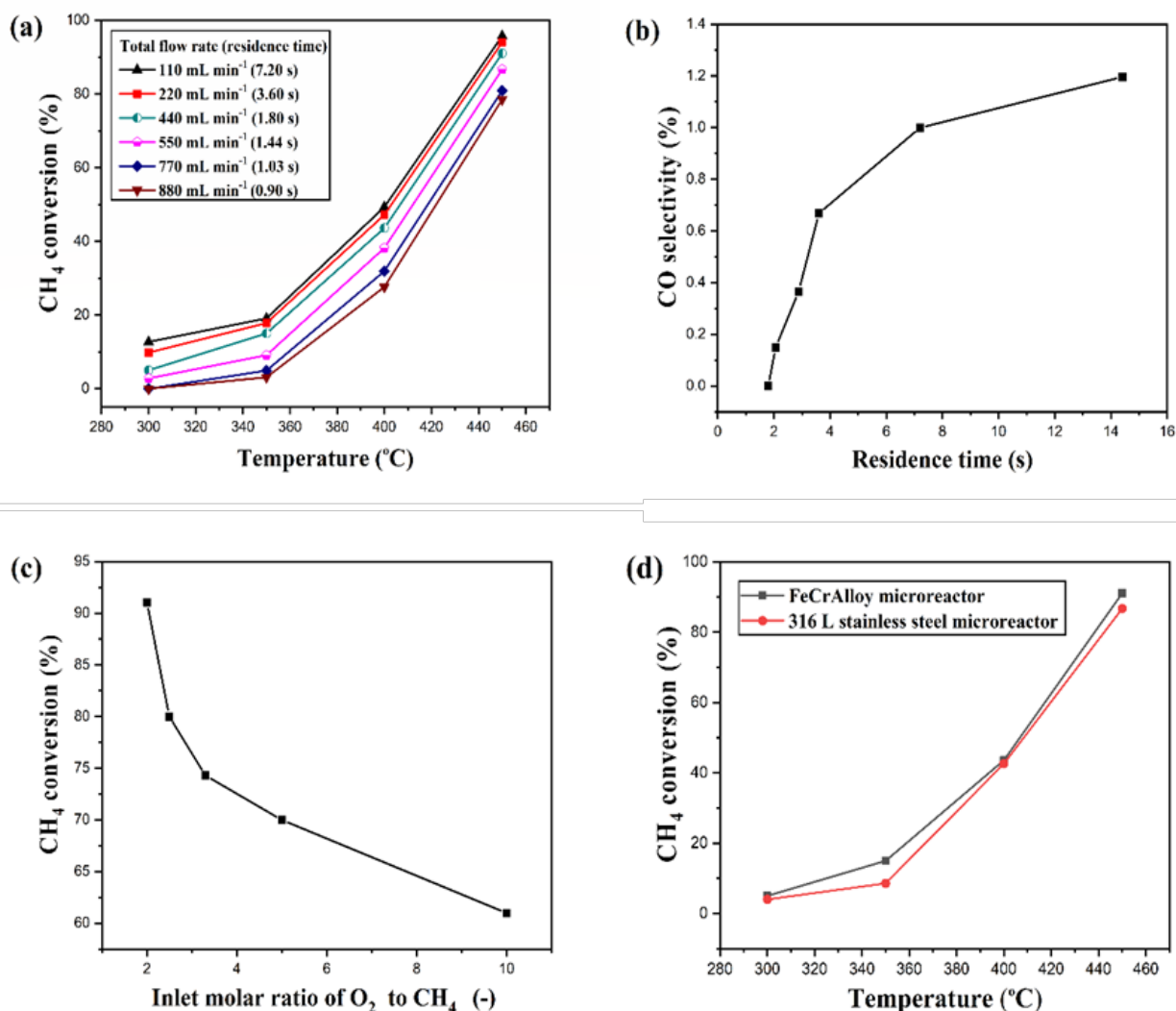
Fig. 3.13. Catalytic methane combustion over the coated Pt/γ-Al$_2$O$_3$ catalyst in the multi-channel microreactor with (a-c) FeCrAlloy platelets (3.8 wt% Pt loading) and (d) FeCrAlloy or stainless steel platelets (3.5 wt% Pt loading). (a) Methane conversion under different reaction temperatures and flow rates, Φ = 2. (b) CO selectivity under different residence times at 450 °C and Φ = 2. (c) Methane conversion under different inlet O$_2$/CH$_4$ molar ratios at 450 °C; the total flow rate at 400 mL min^{-1}. (d) Methane conversion under different reaction temperatures, for a total flow rate at 440 mL min^{-1} and Φ = 2. Loadings of Pt/γ-Al$_2$O$_3$ in the FeCrAlloy and 316 L stainless steel microreactors are 80.8 and 74.4 g m^{-2}, respectively.

3.3.2.2. Effect of operating conditions on the microreactor temperature distribution

The temperature distribution along the multi-channel microreactor (with FeCrAlloy platelets) was measured during the catalytic methane combustion, using the thermocouples that touched the top of the middle microchannel on the platelet. A blank experiment for temperature

measurement was also conducted with only air flowing through the microreactor, as a reference case for comparison.

It was observed in Fig. 3.14a that for a reaction temperate (i.e., the oven temperature) at 450 ^oC, the temperature along the microchannel was close to uniform in the reference case without reaction occurrence. Temperature values close to the middle of the microchannel appeared to be slightly higher than those at both ends, with a difference below ca. 5 ^oC. This is mainly a result of the oven temperature profile. Once the reaction started, such a (close to) uniform temperature profile was no longer sustained in the microchannel. For a total flow rate at 440 mL min^{-1} and Φ = 2 (Fig. 3.14a), the temperature in the front part of the microchannel increased more significantly (e.g., at the normalized length of the microchannel, L^* = 0.2), due to the released combustion reaction heat and the location of the reaction front in the middle section or further upstream (*vide infra*). At a given axial location, the temperature was gradually increased upon increasing the reaction test time on stream until 50 min, after which the temperature reached a stable state showing the thermal inertia of the microreactor. Moreover, the temperature was increased mainly in the front part, and then was gradually decreased to the trailing end of the microchannel. It may be concluded that the majority of methane was converted at the front section of the microreactor. And (much) less reaction took place at the latter section of the microreactor under these conditions, resulting in a somewhat insignificant temperature increase therein.

The effect of flow rate on the temperature distribution along the microreactor is illustrated in Fig. 3.14b. More heat would be released at a higher total flow rate due to the more involved methane, despite a slightly lower methane conversion (Fig. 3.13a). Thus, the temperature was noticeably raised along the microreactor at higher flow rates (Fig. 3.14b), and the axial location with the peak temperature seems to gradually move downstream along the microreactor. This is due to a shorter residence time at a higher flow rate, implying that more methane was converted at a longer distance from the microchannel inlet. This is in line with the literature observation during the catalytic combustion of methane over monolithic catalysts based on (Pt-)LaMnO$_3$ that the reaction front shifted upstream along the channel at a longer residence time [89,90]. At the reaction front, the fluid has reached the catalytic ignition temperature resulting a large reaction heat release and consequently a sharp increase in the fluid/catalyst temperature [91]. The remaining length of the reactor after the reaction front experienced either no reaction or an insignificant conversion, thus this part acted mainly as a heat exchanger and the fluid/catalyst was cooled down due to external heat losses [89-91]. With the increasing

flow rate, it tends to take a longer distance to heat the reactant mixture to the ignition temperature, resulting a downstream shift of the reaction front.

Similarly, the concentration variation of the adsorbed methane and oxygen over the catalyst surface significantly affected the temperature distribution. The obvious temperature gradient over the microreactor in this case can be observed in Fig. 3.14c. Both the methane conversion and the temperature increase could achieve a maximum at a stoichiometric ratio of 2 (cf. Fig. 3.13c as well). With the increasing inlet O_2/CH_4 molar ratio, the temperature in the microreactor at a given axial location was obviously decreased, an observation in line with the reduced methane conversion shown in Fig. 3.13c. Under such circumstances, there is less thermal power provided via combustion, and possibly less favorable surface coverage over the catalyst surface due to the competitive adsorption between oxygen and methane (as discussed in Section 3.2.1), leading to a temperature or conversion decrease. Apart from that, another reason for the lower temperature under the oxygen-rich conditions (at $\Phi > 2$) is that more balance gas (nitrogen) was involved. Thus, a part of the released heat was diluted and absorbed by the balance gas.

The actual maximum value present in the temperature profile and its position in the reactor (as shown in Figs. 14a-c) depend significantly on the pre-heating temperature, the thermal power of the reactant mixture (i.e., related to its composition and flow rate), as well as the heat losses of the reactor (realized in the current work via the conduction through the microreactor wall to the oven atmosphere). Moreover, in our experiments the temperature was only measured on the top surface of the middle microchannel (without coating), since the tips of thermocouples (o.d.: 3 mm) are not possible to touch the inner catalytic wall (Fig. 3.1). Thus, the temperature level and profile reported in this work are only indicative of that on the catalyst surface. Considering the good thermal conductivity of FeCrAlloy platelets and the reaction heat released, the actual surface temperature of the catalyst should be much higher than these measurements. To illustrate, the adiabatic temperature rise (ΔT_{ad}) can amount to ca. 2000 ^{o}C at $\Phi = 2$ (calculations not shown for brevity) [92]. Thus, it is reasonable to estimate that the actual temperature on the catalyst surface could be somewhat high under the present reaction conditions, which might accelerate the catalyst deactivation as well [93]. The high temperature level on the catalyst surface could also activate and thermally sustain the homogeneous combustion to a certain extent, as addressed in many literatures [89,90,93-95]. Investigation of the above-mentioned aspects would contribute to optimized operating conditions and microreactor design for the catalytic methane combustion. These findings, when coupled with

heat transfer studies (e.g., in the presence of the integrated heat exchanging modules), can provide insights into the potential uses of such wall-coated microreactors in energy-related applications (e.g., for heat supply in a small-scale boiler system [96]).
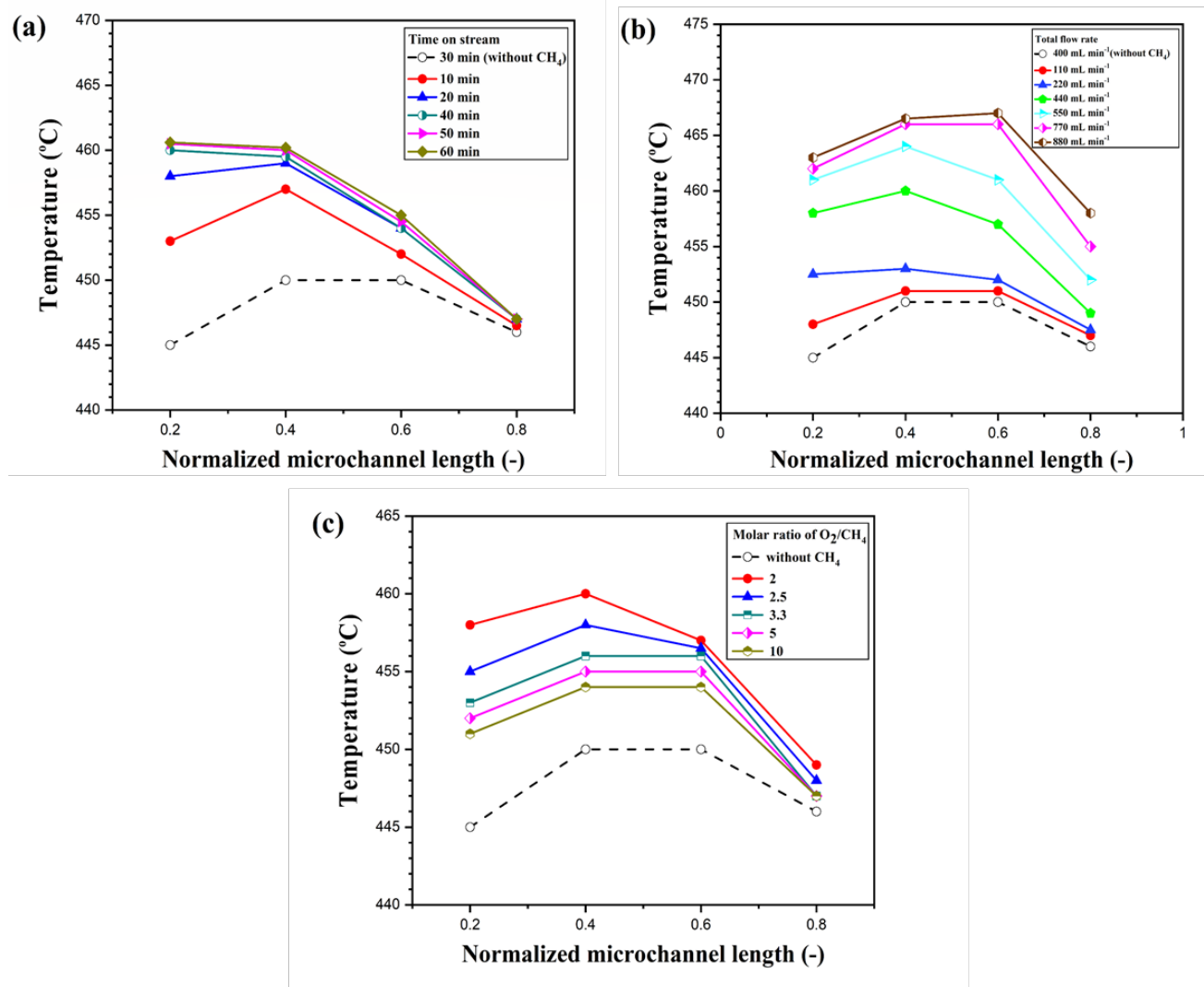
Fig. 3.14. Axial surface temperature distribution during the catalytic methane combustion in the multi-channel microreactor (with FeCrAlloy platelets). The oven temperature was fixed at 450 °C as the reported reaction temperature. (a) Effect of time on stream; the total flow rate at 440 mL min^{-1}, Φ = 2. (b) Effect of the total flow rate, Φ = 2 (c) Effect of the inlet O_2/CH_4 molar flow ratio; the air flow rate at 400 mL min^{-1}. In (b) and (c), data were collected after 30 min on stream.

3.3.2.3. Preliminary results of catalyst deactivation

Catalyst life is an important indicator for its performance, especially relevant to the long-term operation in the commercial applications. Regarding the coated Pt/γ-Al$_2$O$_3$ catalyst in the multi-channel microreactors, a detailed in-situ life time study has not been performed yet. However,

the coated Pt/γ-Al$_2$O$_3$ catalyst scrapped from the stainless steel substrate has been tested in the powder form in a fixed bed reactor for 100 h on stream. A somewhat significant decrease of the catalyst activity was already noticed (see Appendix 3.E for more details). This deactivation is possibly due to the catalyst sintering and the growth of Pt particles (e.g., as a result of the high temperature level generated by the released heat at the reaction front), or the formation of platinum species in the oxidized state (PtO$_2$) with a lower activity compared to its metallic state [97-99]. These preliminary results imply that the catalyst coating preparation in microreactors still needs to be further optimized (e.g., by improving the catalyst structural stability and the metal-support interaction), together with the catalyst regeneration, in order to maintain a stable catalyst activity.

3.4. Conclusions

In this work, the slurry washcoating followed by the incipient wetness impregnation has been used to prepare Pt/γ-Al$_2$O$_3$ catalytic coatings in microreactors. The effect of various factors in the slurry preparation procedures on the adhesion properties (tested typically via the ultrasonic treatment) of the washcoated γ-Al$_2$O$_3$ layer on the microreactor substrates with different channel shapes was investigated. The initial γ-Al$_2$O$_3$ particle size and pH were found as two important factors affecting the slurry stability and the washcoat adhesion strength. A strong particle attractive force could be maintained by using a particle size of around 3 μm in the slurry with a slightly acid environment (pH ≈ 3.5). PVA (typically at a concentration of 3 - 5 wt% and a MW of 57,000 - 186,000) was identified as a suitable binder to better disperse alumina particles and form sufficient hydrogen bridges with alumina, thus effectively enhancing the washcoat adhesion. FeCrAlloy as the (micro)reactor substrate exhibited an excellent coating adhesion with negligible weight loss during the ultrasonic treatment in either rectangular or round channels, primarily because of the formation of alumina film over the surface during thermal pretreatment. In contrast, 316 L stainless steel as the substrate only showed a relatively good adhesion in a round channel, presumably due to the lack of a strong chemical bonding between the washcoated layer and the pretreated substrate surface.

The catalyst performance in the catalytic methane combustion was further examined in microreactors comprising parallel microchannels made of FeCrAlloy or 316 L stainless steel. A higher total flow rate (of methane and air) was found to render higher heat generation rate and lead to a more significant temperature increase in the front part of the microreactor, despite a slightly decreased methane conversion due to a shorter residence time. Under the oxygen-rich conditions, the predominant adsorption of oxygen over methane species on the catalyst surface

could lead to a decreased methane conversion and thus a lower heat generation. Thus, an appropriate fractional coverage of the catalyst surface by these species and a proper reaction condition selection are needed for achieving the favorable methane conversion, as well as the sufficient heat release for the potential uses of such microreactors for energy-related applications. Somewhat significant deactivation of the coated $Pt/\gamma-Al_2O_3$ catalyst over a time scale of 100 hours, as observed in an ex-situ test in a fixed-bed reactor, represents a further direction of improvement to be addressed in our future work.

Appendix 3.A

Washcoating of $\gamma-Al_2O_3$ inside a capillary

For coating inside circular or square capillaries, a certain mass of the $\gamma-Al_2O_3$ slurry was injected inside via a syringe. One end of the coated capillary was then connected with the motor which rotated at a given speed (Fig. 3.A.1). During drying, the connection was switched from one to the other end of the capillary multiple times. Thus, the slurry near the open end side of the capillary was faster to be dried, whereas that in the middle of the capillary could be the last part to be dried. However, some imprints like 'tree-rings' may be observed on the washcoated layer after drying. Thus, a better method to dry the coating inside such capillaries might be to directly heat it up to a certain temperature in the oven with a low loading of alumina, so as to reduce the gravity influence. More alumina loading could be achieved by multilayer coating with the same method.
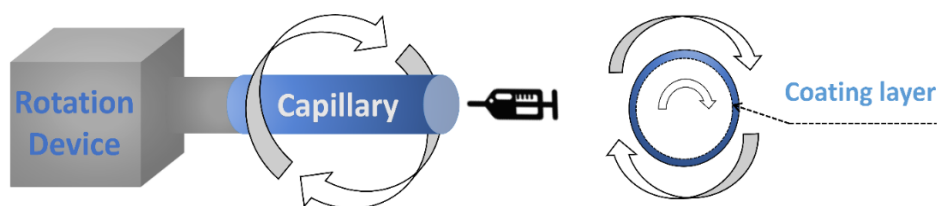
Fig. 3.A.1. Schematic of the drying process of the deposited $\gamma-Al_2O_3$ slurry in a circular capillary.

Appendix 3.B

TGA analysis of the slurry

The amount of slurries (prepared under the conditions mentioned in Table 3.1) for TGA analysis is 3-10 mg. The results of analysis in the case of using different binders are shown in Fig. 3.B.1, together with the first derivation of the TGA curve (DTG). The first weight loss (<100 °C) is ascribed to the desorption of the physically adsorbed water in the slurry. The second weight loss (at 200-300 °C) and third one (at 400-500 °C) are associated with the thermal

decomposition of binders. This indicates that binders were completely decomposed when being calcined at 600 °C. However, the specific surface area of the obtained washcoat decreased with the increasing calcination temperature due to the structure damage of alumina (e.g., pore collapse), as shown for the case of PVA as the binder in Table 3.B.1. Considering both the specific surface area and the binder removal, 600 °C was chosen as a suitable calcination temperature.
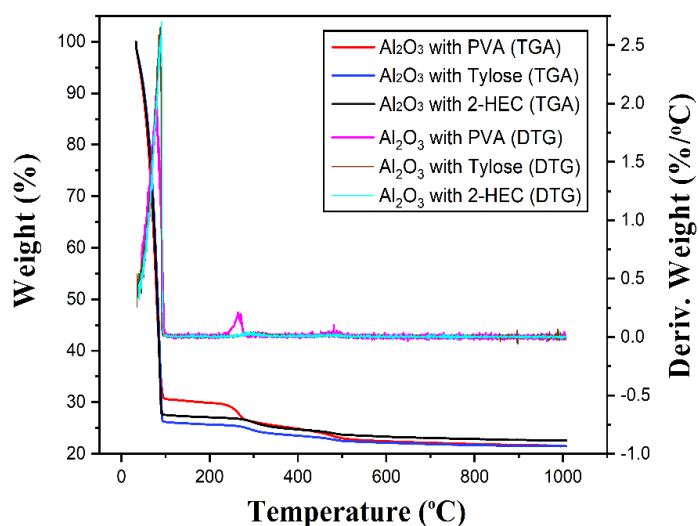
Fig. 3.B.1. TGA and DTG curves of slurries prepared under the conditions mentioned in Table 3.1.

Table 3.B.1.

BET surface area and pore properties of the washcoated γ-Al$_2$O$_3$ layer obtained on FeCrAlloy platelets under different calcination temperatures.[a]

Calcination temperature (°C)	BET surface area (m^2 g^{-1})	Micropore area (m^2 g^{-1})	Pore volume (cm^3 g^{-1})	Average pore size (Å)
800	54.05	0.51	0.41	277.78
700	61.81	1.40	0.38	200.44
600	78.53	1.73	0.35	198.20
500	86.24	4.39	0.31	160.43

[a] Slurry preparation conditions: 20 wt% γ-Al$_2$O$_3$ (initial particle size at 3 μm), 5 wt% PVA as the binder (MW of 146,000-186,000), pH = 3.5.

Appendix 3.C

Effect of primer coating on the adhesion of the γ-Al$_2$O$_3$ washcoated layer

Table 3.C.1 shows the weight loss in the ultrasonic treatment of the γ-Al$_2$O$_3$ washcoat obtained via applying the primer coating (details shown in Section 2.2.2), followed by the slurry deposition (other preparation conditions are the same as shown in Table 3.4) on the 316 L stainless steel multi-channel platelet. The weight loss was found to increase to a somewhat significant level upon increasing the treatment time from 5 to 60 min.

Table 3.C.1

Effect of primer coating on the adhesion of the γ-Al$_2$O$_3$ washcoated layer on the 316 L stainless steel multi-channel platelet.

Primer composition	Slurry composition[a]	Ultrasonic bath time (min)	Weight loss percentage (wt%)
10 wt% dispersal P2 + 3 wt% PVA	20 wt% γ-Al$_2$O$_3$ + 5 wt% PVA	5	0.66
		15	10.76
		30	16.56
		60	23.84

[a] Other preparation conditions are shown in Table 3.4.

Appendix 3.D

TEM analysis of Pt/γ-Al$_2$O$_3$ catalyst

3.5 wt% Pt/γ-Al$_2$O$_3$ catalyst was prepared on the FeCrAlloy platelet (with 10 parallel microchannels; see Section 2.1 for dimensions), according to the procedures described in Section 2.2. Herein, the slurry for coating was prepared using 20 wt% Al$_2$O$_3$ (3 μm), 5 wt% PVA (MW of 146,000 -186,000) and pH at 3.5. Then, the catalyst was scrapped off from the substrate and ground to a particle size below 25 μm. After ultrasonication in acetone for 10 min, the sample was dropped onto the carbon coated copper grid (400 mesh) for TEM analysis. The TEM

image is shown in Fig. 3.D.1. Pt particles (black dots) seemed to be well dispersed over the alumina support by using the incipient wet impregnation method.
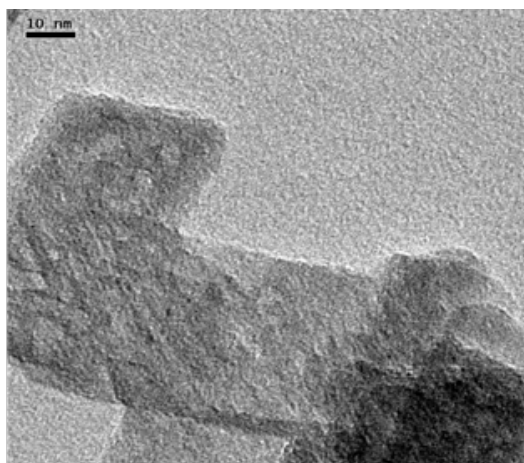
Figure D.1. TEM image of the 3.5 wt% $Pt/\gamma-Al_2O_3$ catalyst scrapped from the FeCrAlloy platelet.

Appendix 3.E

Catalyst life time test in a fixed-bed reactor

3.5 wt% $Pt/\gamma-Al_2O_3$ catalyst was prepared on the 316 L stainless steel platelet (with 16 parallel microchannels; see Section 2.1 for dimensions), using the same protocol as mentioned in Appendix 3.D. The fresh $Pt/\gamma-Al_2O_3$ catalyst was then scraped from the platelet and ground to a particle size of about 25 μm for the catalyst life time test in a fixed-bed reactor made of glass (U shape; i.d.: 5 mm) in a similar oven and experimental setup as shown in Fig. 3.1. A full methane conversion was achieved at 450 °C with 16 h on stream (Fig. 3.E.1). However, the catalyst gradually deactivated, with the methane conversion being dropped to 98.12 % at 22 h, and 84.61 % at 100 h. The CO_2 selectivity also seems to drop slowly over time. The measured BET surface areas of the fresh and used (after 100 h on stream) catalysts are listed in Table 3.E.1. An obvious reduction in the specific surface area of the used catalyst was observed, possibly due to the catalyst sintering after a long-term reaction. Meanwhile, the growth of Pt particles due to agglomeration could also have occurred, which would result in a catalyst activity loss [100-102]. Hence, the current catalyst preparation method still needs to be further improved to maintain a stable catalyst activity.
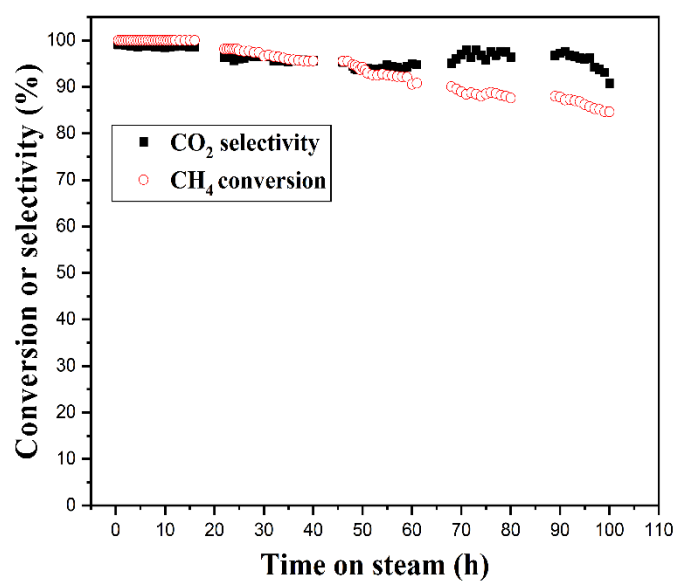
Fig. 3.E.1. Catalyst life time test in a fixed-bed reactor (i.d.: 5 mm). Other conditions: 3.5 wt% Pt/γ-Al$_2$O$_3$ catalyst (scrapped from the 316 L stainless steel platelet; 0.2 g; size at ca. 25 μm;), total gas flow rate (of air and methane) at 20 mL min^{-1}, 2.513 % CH$_4$ in the air (Φ = 7.8), 450 ^{o}C.

Table 3.E.1

BET surface area of the fresh and used Pt/γ-Al$_2$O$_3$ catalysts.

Catalyst	BET surface area (m^2 g^{-1})	Micropore area (m^2 g^{-1})	Pore volume (cm^3 g^{-1})	Average pore size (Å)
Fresh Pt/γ-Al$_2$O$_3$	66.07	0.20	0.41	249.42
Used Pt/γ-Al$_2$O$_3$[a]	52.38	/	0.40	305.70

[a] After 100 h reaction test (cf. Fig. 3.E.1).

References

[1]   D. Van Herk, P. Castano, M. Makkee, J.A. Moulijn, M.T. Kreutzer, Catalyst testing in a multiple-parallel, gas-liquid, powder-packed bed microreactor, Appl. Catal. A. 365 (2009) 199-206. https://doi.org/10.1016/j.apcata.2009.06.010.

[2]   A. Karim, J. Bravo, D. Gorm, T. Conant, A. Datye, Comparison of wall-coated and packed-bed reactors for steam reforming of methanol, Catal. Today. 110 (2005) 86-91. http://dx.doi.org/10.1016/j.cattod.2005.09.010.

[3]   W. Ehrfeld, V. Hessel, H. Löwe, Microreactors: new technology for modern chemistry, Wiley, Michigan, 2000.

[4]   J. Klaus, H. Volker, L. Holger, B. Manfred, Chemistry in microstructured reactors, Angew. Chem. Int. Ed. 43 (2004) 406-446. https://doi.org/10.1002/anie.200300577.

[5]   L.A. Truter, P.R. Makgwane, B. Zeelie, S. Roberts, W. Böhringer, J.C.Q. Fletcher, Washcoating of H-ZSM-5 zeolite onto steel microreactor plates-filling the void space between zeolite crystallite agglomerates particles, Chem. Eng. J. 257 (2014) 148-158. https://doi.org/10.1016/j.cej.2014.07.047.

[6]   B. Schmidt, M. Liauw, Mass transfer limitations in microchannel reactors, Catal. Today. 110 (2005) 15-25. https://doi.org/10.1016/j.cattod.2005.09.019.

[7]   P.L. Mills, D.J. Quiram, J.F. Ryley, Microreactor technology and process miniaturization for catalytic reactions-A perspective on recent developments and emerging technologies, Chem. Eng. Sci. 62 (2007) 6992-7010. https://doi.org/10.1016/j.ces.2007.09.021.

[8]   M. Rahimpour, M. Dehnavi, F. Allahgholipour, D. Iranshahi, S. Jokar, Assessment and comparison of different catalytic coupling exothermic and endothermic reactions: a review, Appl. Energy. 99 (2012) 496-512. https://doi.org/10.1016/j.apenergy.2012.04.003.

[9]   J. Yue, R. Boichot, L. Luo, Y. Gonthier, G. Chen, Q. Yuan, Flow distribution and mass transfer in a parallel microchannel contactor integrated with constructal distributors, AlChE J. 56 (2010) 298-317. https://doi.org/10.1002/aic.11991.

[10]   X. Guo, Y. Fan, L. Luo, Multi-channel heat exchanger-reactor using arborescent distributors: A characterization study of fluid distribution, heat exchange performance and exothermic reaction, Energy. 69 (2014) 728-741. https://doi.org/10.1016/j.energy.2014.03.069.

[11]   A. Günther, K.F. Jensen, Multiphase microfluidics: from flow characteristics to chemical and materials synthesis, Lab Chip. 6 (2006) 1487-1503. https://doi.org/10.1039/B609851G.

[12]   V. Meille, Review on methods to deposit catalysts on structured surfaces, Appl. Catal. A. 315 (2006) 1-17. https://doi.org/10.1016/j.apcata.2006.08.031.

[13]   V. Paunovic, V. Ordomsky, M.F. Neira D'Angelo, J.C. Schouten, T.A. Nijhuis, Catalyst coating on prefabricated capillary microchannels for the direct synthesis of hydrogen peroxide, Ind. Eng. Chem. Res. 54 (2015) 2919-2929. https://doi.org/10.1021/ie504762y.

[14]   V. Hessel, P. Angeli, A. Gavriilidis, H. Löwe, Gas-liquid and gas-liquid-solid microstructured reactors: contacting principles and applications, Ind. Eng. Chem. Res. 44 (2005) 9750-9769. https://doi.org/10.1021/ie0503139.

[15]   J. Yue, Multiphase flow processing in microreactors combined with heterogeneous catalysis for efficient and sustainable chemical synthesis, Catal. Today. 308 (2018) 3-19. https://doi.org/10.1016/j.cattod.2017.09.041.

[16]   M. Liauw, M. Baerns, R. Broucek, O. Buyevskaya, J. Commenge, J. Corriou, L. Falk, K. Gebauer, H. Hefter, O. Langer, Periodic operation in microchannel reactors, Microreaction technology: industrial prospects. Springer, Berlin, 2000, pp. 224-234.

[17]   N.R. Peela, A. Mubayi, D. Kunzru, Washcoating of γ-alumina on stainless steel microchannels, Catal. Today. 147 (2009) S17-S23. https://doi.org/10.1016/j.cattod.2009.07.026.

[18]   R. Zapf, C. Becker-Willinger, K. Berresheim, H. Bolz, H. Gnaser, V. Hessel, G. Kolb, P.Löb, A.K. Pannwitt, A. Ziogas, Detailed characterization of various porous alumina-based catalyst coatings within microchannels and their testing for methanol steam reforming, Chem. Eng. Res. Des. 81 (2003) 721-729. https://doi.org/10.1205/026387603322302887.

[19]   X. Xu, H. Vonk, A. Cybulski, J.A. Moulijn, Alumina washcoating and metal deposition of ceramic monoliths, Stud. Surf. Sci. Catal., Elsevier, 1995, pp. 1069-1078.

[20]   K. Haas-Santo, M. Fichtner, K. Schubert, Preparation of microstructure compatible porous supports by sol-gel synthesis for catalyst coatings, Appl. Catal. A. 220 (2001) 79-92. https://doi.org/10.1016/S0926-860X(01)00714-1.

[21]   M.P. Vorob'eva, A.A. Greish, A.V. Ivanov, L.M. Kustov, Preparation of catalyst carriers on the basis of alumina supported on metallic gauzes, Appl. Catal. A. 199 (2000) 257-261. https://doi.org/10.1016/S0926-860X(99)00563-3.

[22]   K.S. Yang, Z. Jiang, J. Shik Chung, Electrophoretically Al-coated wire mesh and its application for catalytic oxidation of 1,2-dichlorobenzene, Surf. Coat. Technol. 168 (2003) 103-110. https://doi.org/10.1016/S0257-8972(02)00569-8.

[23]   M. Karches, M. Morstein, P. Rudolf von Rohr, R.L. Pozzo, J.L. Giombi, M.A. Baltanás, Plasma-CVD-coated glass beads as photocatalyst for water decontamination, Catal. Today. 72 (2002) 267-279. https://doi.org/10.1016/S0920-5861(01)00505-3.

[24]   T. Aaltonen, M. Ritala, T. Sajavaara, J. Keinonen, M. Leskelä, Atomic layer deposition of platinum thin films, Chem. Mater. 15 (2003) 1924-1928. https://doi.org/10.1021/cm021333t.

[25]   L.L. Pranevicius, P. Valatkevicius, V. Valincius, C. Montassier, Catalytic behavior of plasma-sprayed Al-Al$_2$O$_3$ coatings doped with metal oxides, Surf. Coat. Technol. 125 (2000) 392-395. https://doi.org/10.1016/S0257-8972(99)00584-8.

[26]   L. Pranevicius, L.L. Pranevicius, P. Valatkevicius, V. Valincius, Plasma spray deposition of Al-Al$_2$O$_3$ coatings doped with metal oxides: catalytic applications, Surf. Coat. Technol. 123 (2000) 122-128. https://doi.org/10.1016/S0257-8972(99)00520-4.

[27]   C. Agrafiotis, A. Tsetsekou, The effect of processing parameters on the properties of γ-alumina washcoats deposited on ceramic honeycombs, J. Mater. Sci. 35 (2000) 951-960. https://doi.org/10.1023/A:1004762827623.

[28]   L. Giani, C. Cristiani, G. Groppi, E. Tronconi, Washcoating method for Pd/γ-Al$_2$O$_3$ deposition on metallic foams, Appl. Catal., B. 62 (2006) 121-131. https://doi.org/10.1016/j.apcatb.2005.07.003.

[29]   X. Yu, S.T. Tu, Z. Wang, Y. Qi, Development of a microchannel reactor concerning steam reforming of methanol, Chem. Eng. J. 116 (2006) 123-132. https://doi.org/10.1016/j.cej.2005.11.008.

[30]   I. Cerri, M. Pavese, G. Saracco, V. Specchia, Premixed metal fibre burners based on a Pd catalyst, Catal. Today. 83 (2003) 19-31. https://doi.org/10.1016/S0920-5861(03)00213-X.

[31]   S.J. Lee, A. Gavriilidis, Au catalysts supported on anodised aluminium for low-temperature CO oxidation, Catal. Commun. 3 (2002) 425-428. https://doi.org/10.1016/S1566-7367(02)00161-9.

[32]   J. Ganley, K. Riechmann, E. Seebauer, R. Masel, Porous anodic alumina optimized as a catalyst support for microreactors, J. Catal. 227 (2004) 26-32. https://doi.org/10.1016/j.jcat.2004.06.016.

[33]   M. Valentini, G. Groppi, C. Cristiani, M. Levi, E. Tronconi, P. Forzatti, The deposition of γ-Al$_2$O$_3$ layers on ceramic and metallic supports for the preparation of structured catalysts, Catal. Today. 69 (2001) 307-314. http://dx.doi.org/10.1016/S0920-5861(01)00383-2.

[34]   J.P. Reymond, Structured supports for noble catalytic metals: stainless steel fabrics and foils, and carbon fabrics, Catal. Today. 69 (2001) 343-349. http://dx.doi.org/10.1016/S0920-5861(01)00388-1.

[35]   R. Zapf, G. Kolb, H. Pennemann, V. Hessel, Basic study of adhesion of several alumina-based washcoats deposited on stainless steel microchannels, Chem. Eng. Technol. 29 (2006) 1509-1512. https://doi.org/10.1002/ceat.200600204.

[36]   V. Sebastián, O. de la Iglesia, R. Mallada, L. Casado, G. Kolb, V. Hessel, J. Santamaría, Preparation of zeolite films as catalytic coatings on microreactor channels, Microporous Mesoporous Mater. 115 (2008) 147-155. https://doi.org/10.1016/j.ces.2007.02.034.

[37]   G. Germani, A. Stefanescu, Y. Schuurman, A.C. van Veen, Preparation and characterization of porous alumina-based catalyst coatings in microchannels, Chem. Eng. Sci. 62 (2007) 5084-5091. https://doi.org/10.1016/j.ces.2007.02.034.

[38]   Y.S. Lin, K.J. de Vries, A.J. Burggraaf, Thermal stability and its improvement of the alumina membrane top-layers prepared by sol-gel methods, J. Mater. Sci. 26 (1991) 715-720. https://doi.org/10.1007/BF00588309.

[39]   C. Agrafiotis, A. Tsetsekou, The effect of powder characteristics on washcoat quality. part I: alumina washcoats, J. Eur. Ceram. Soc. 20 (2000) 815-824. https://doi.org/10.1016/S0955-2219(99)00218-6.

[40]   V.T. Zaspalis, W. Van Praag, K. Keizer, J.R.H. Ross, A.J. Burggraaf, Synthesis and characterization of primary alumina, titania and binary membranes, J. Mater. Sci. 27 (1992) 1023-1035. https://doi.org/10.1007/BF01197657.

[41]   K. Birdi, Handbook of surface and colloid chemistry, second ed., CRC press, Boca Raton, 2002.

[42]   P. Jiang, G. Lu, Y. Guo, Y. Guo, S. Zhang, X. Wang, Preparation and properties of a γ-Al$_2$O$_3$ washcoat deposited on a ceramic honeycomb, Surf. Coat. Technol. 190 (2005) 314-320. https://doi.org/10.1016/j.surfcoat.2004.05.029.

[43]   P.A.R. Cebollada, E. Garcia Bordejé, Optimisation of physical properties of γ-alumina coating microreactors used for the growth of a carbon nanofiber layer, Chem. Eng. J. 149 (2009) 447-454. https://doi.org/10.1016/j.cej.2009.02.016.

[44]   X. Ying, L. Zhang, H. Xu, Y.L. Ren, Q. Luo, H.W. Zhu, H. Qu, J. Xuan, Efficient Fischer-Tropsch microreactor with innovative aluminizing pretreatment on stainless steel substrate for Co/Al$_2$O$_3$ catalyst coating, Fuel Process. Technol. 143 (2016) 51-59. https://doi.org/10.1016/j.fuproc.2015.11.005.

[45]   Z.D. Xiang, P.K. Datta, Pack aluminisation of low alloy steels at temperatures below 700 °C, Surf. Coat. Technol. 184 (2004) 108-115. https://doi.org/10.1016/j.surfcoat.2003.10.046.

[46]   J. Chen, H. Arandiyan, X. Gao, J. Li, Recent advances in catalysts for methane combustion, Catal. Surv. Asia. 19 (2015) 140-171. https://doi.org/10.1007/s10563-015-9191-5.

[47]   S.B. T.V. Choudhary, V.R. Choudhary, Catalysts for combustion of methane and lower alkanes review, Appl. Catal. A. 234 (2002) 1-23. https://doi.org/10.1016/S0926-860X(02)00231-4.

[48]   R. Burch, P.K. Loader, Investigation of Pt/Al$_2$O$_3$ and Pd/Al$_2$O$_3$ catalysts for the combustion of methane at low concentrations, Appl. Catal., B. 5 (1994) 149-164. http://dx.doi.org/10.1016/0926-3373(94)00037-9.

[49]   M. Bhagiyalakshmi, R. Anuradha, S.D. Park, T.S. Park, W.S. Cha, H.T. Jang, Effect of bimetallic Pt-Rh and trimetallic Pt-Pd-Rh catalysts for low temperature catalytic combustion of methane, Bull. Korean Chem. Soc. 31 (2010) 120-124. https://doi.org/10.5012/bkcs.2010.31.01.120.

[50]   N. Kinnunen, M. Suvanto, M. Moreno, A. Savimäki, K. Kallinen, T.-J. Kinnunen, T. Pakkanen, Methane oxidation on alumina supported palladium catalysts: effect of Pd precursor and solvent, Appl. Catal. A. 370 (2009) 78-87. https://doi.org/10.1016/j.apcata.2009.09.018.

[51]   J. Okal, M. Zawadzki, K. Baranowska, Methane combustion over bimetallic Ru-Re/γ-Al$_2$O$_3$ catalysts: Effect of Re and pretreatments, Appl. Catal., B. 194 (2016) 22-31. https://doi.org/10.1016/j.apcatb.2016.04.038.

[52]   Y. Mahara, T. Tojo, K. Murata, J. Ohyama, A. Satsuma, Methane combustion over Pd/CoAl$_2$O$_4$/Al$_2$O$_3$ catalysts prepared by galvanic deposition, RSC Advances. 7 (2017) 34530-34537. https://doi.org/10.1039/c7ra06150a.

[53]   Q. Dong, S. Zhang, Z. Duan, Q. Zhou, An energy analysis of the catalytic combustion burner, Heat. Technol. Energy Eff. (2006). http://hdl.handle.net/1969.1/5530.

[54]   D. X.Chun, Applied studies on methane catalytic combustion development of a natural gas premixed catalytic burner and boiler for household applications. 2005; Sichuan University. Thesis in chinese.

[55]   C.M. Miesse, R.I. Masel, C.D. Jensen, M.A. Shannon, M. Short, Submillimeter-scale combustion, AlChE J. 50 (2004) 3206-3214. https://doi.org/10.1002/aic.10271.

[56]   L. Olsson, B. Westerberg, H. Persson, E. Fridell, M. Skoglundh, B. Andersson, A kinetic study of oxygen adsorption/desorption and NO oxidation over Pt/Al$_2$O$_3$ catalysts, J. Phys. Chem. B. 103 (1999) 10433-10439. https://doi.org/10.1021/jp9918757.

[57]   M. O'Connell, G. Kolb, R. Zapf, Y. Men, V. Hessel, Bimetallic catalysts for the catalytic combustion of methane using microreactor technology, Catal. Today. 144 (2009) 306-311. https://doi.org/10.1016/j.cattod.2008.10.053.

[58]   H. Mei, C. Li, S. Ji, H. Liu, Modeling of a metal monolith catalytic reactor for methane steam reforming-combustion coupling, Chem. Eng. Sci. 62 (2007) 4294-4303. http://dx.doi.org/10.1016/j.ces.2007.05.011.

[59]   M. Mundhwa, C.P. Thurgood, Numerical study of methane steam reforming and methane combustion over the segmented and continuously coated layers of catalysts in a plate reactor, Fuel Process. Technol. 158 (2017) 57-72. http://doi.org/10.1016/j.fuproc.2016.12.002.

[60]   M. Mundhwa, R.D. Parmar, C.P. Thurgood, A comparative parametric study of a catalytic plate methane reformer coated with segmented and continuous layers of combustion catalyst for hydrogen production, J. Power Sources. 344 (2017) 85-102. http://dx.doi.org/10.1016/j.jpowsour.2017.01.082.

[61]   P. Zhou, D. Tarlet, Y. Fan, X. Hu, L. Luo, Water-in-oil emulsification in a bifurcated tree-like network: Flow distribution properties and their impact on the emulsion polydispersity, Chem. Eng. Res. Des. 134 (2018) 420-433. https://doi.org/10.1016/j.cherd.2018.04.031.

[62]   P. Zhou, D. Tarlet, M. Wei, Y. Fan, L. Luo, Novel multi-scale parallel mini-channel contactor for monodisperse water-in-oil emulsification, Chem. Eng. Res. Des. 121 (2017) 233-244. https://doi.org/10.1016/j.cherd.2017.03.010.

[63]   V. Meille, S. Pallier, G. Santacruzbustamante, M. Roumanie, J. Reymond, Deposition of γ-Al$_2$O$_3$ layers on structured supports for the design of new catalytic reactors, Appl. Catal. A. 286 (2005) 232-238. https://doi.org/10.1016/j.apcata.2005.03.028.

[64]   Christopher John Bennett, John P. Coll, Debnath DE, Andrea Hawkins, W. Manning, Method of applying washcoat to monolithic substrate, United States Patent, US9144796B1, Sep. 29, 2015.

[65]   E.B. Andrew, J.G. Stephen, J.L. Mark, Adhesion and coating integrity of washcoats and overcoats, Unite State Patent, US20100081563A1, Apr. 1, 2010

[66]   O. Ohara, Adhesives comprising polyvinyl alcohol bearing or mixed with substances bearing carboxyl groups, and a stabilizer, United States Patent. 1968.

[67]   M. Wiśniewska, S. Chibowski, T. Urban, D. Sternik, Investigation of the alumina properties with adsorbed polyvinyl alcohol, J. Therm. Anal. Calorim. 103 (2011) 329-337. https://doi.org/10.1007/s10973-010-1040-1.

[68]   C.C. Huang, Y.J. Huang, H.S. Wang, F.G. Tseng, Y.C. Su, A well-dispersed catalyst on porous silicon micro-reformer for enhancing adhesion in the catalyst-coating process, Int. J. Hydrogen Energy. 39 (2014) 7753-7764. https://doi.org/10.1016/j.ijhydene.2014.03.029.

[69]   Z. Chen, C. Weinberger, M. Tiemann, D. Kuckling, Organic polymers as porogenic structure matrices for mesoporous alumina and magnesia, Processes. 5 (2017) 70.

[70]   S. Katheria, G. Deo, D. Kunzru, Washcoating of Ni/MgAl$_2$O$_4$ catalyst on FeCralloy monoliths for steam reforming of methane, Energy Fuels. 31 (2017) 3143-3153. https://doi.org/10.1021/acs.energyfuels.6b03423.

[71]   S.S. Kim, S.J. Lee, S.C. Hong, Effect of CeO$_2$ addition to Rh/Al$_2$O$_3$ catalyst on N$_2$O decomposition, Chem. Eng. J. 169 (2011) 173-179. https://doi.org/10.1016/j.cej.2011.03.001.

[72]   H. Qin, R. Jian, J. Bai, J. Tang, Y. Zhou, B. Zhu, D. Zhao, Z. Ni, L. Wang, W. Liu, Q. Zhou, X. Li, Influence of molecular weight on structure and catalytic characteristics of ordered mesoporous carbon derived from lignin,

ACS Omega. 3 (2018) 1350-1356. https://doi.org/10.1021/acsomega.7b01870.

[73]   B.V. Velamakanni, J.C. Chang, F.F. Lange, D.S. Pearson, New method for efficient colloidal particle packing via modulation of repulsive lubricating hydration forces, Langmuir. 6 (1990) 1323-1325. https://doi.org/10.1021/la00097a023.

[74]   B. Delmon, P.A. Jacobs, R. Maggi, J.A. Martens, G. Poncelet, Preparation of catalysts VII: proceedings of the 7th international symposium on scientific bases for the preparation of heterogeneous catalysts, Elsevier, Louvain-la-Neuve, Belgium, 1998.

[75]   M.D. Franke, W.R. Ernst, A.S. Myerson, Kinetics of dissolution of alumina in acidic solution, AlChE J. 33 (1987) 267-273. https://doi.org/10.1002/aic.690330213.

[76]   C. Cristiani, M. Valentini, M. Merazzi, S. Neglia, P. Forzatti, Effect of ageing time on chemical and rheological evolution in γ-Al_2O_3 slurries for dip-coating, Catal. Today. 105 (2005) 492-498. https://doi.org/10.1016/j.cattod.2005.06.020.

[77]   A.S. Rao, Effect of the surface active agents on the rheology of aqueous alumina slips, Ceram. Int. 14 (1988) 17-25. https://doi.org/10.1016/0272-8842(88)90013-2.

[78]   J. Ayastuy, N. Gamboa, M. González-Marcos, M. Gutiérrez-Ortiz, CuO/CeO_2 washcoated ceramic monoliths for CO-PROX reaction, Chem. Eng. J. 171 (2011) 224-231. https://doi.org/10.1016/j.cej.2011.03.006.

[79]   G. Landi, P.S. Barbato, A. Di Benedetto, L. Lisi, Optimization of the preparation method of CuO/CeO_2 structured catalytic monolith for CO preferential oxidation in H_2-rich streams, Appl. Catal., B. 181 (2016) 727-737. https://doi.org/10.1016/j.apcatb.2015.08.040.

[80]   M.A. Kumar, K. Deepak, Effect of method of preparation on activity of Pd/Al_2O_3 monolith catalysts, Can. J. Chem. Eng. 88 (2010) 367-375. https://doi.org/10.1002/cjce.20288.

[81]   J.M. Zamaro, M.A. Ulla, E.E. Miró, Zeolite washcoating onto cordierite honeycomb reactors for environmental applications, Chem. Eng. J. 106 (2005) 25-33. https://doi.org/10.1016/j.cej.2004.11.003.

[82]   M. Brishti, K. Deepak, Washcoating of different zeolites on cordierite monoliths, J. Am. Ceram. Soc. 91 (2008) 64-70. https://doi.org/10.1111/j.1551-2916.2007.02032.x.

[83]   S. Zhao, J. Zhang, D. Weng, X. Wu, A method to form well-adhered γ-Al_2O_3 layers on FeCrAl metallic supports, Surf. Coat. Technol. 167 (2003) 97-105. http://dx.doi.org/10.1016/S0257-8972(02)00859-9.

[84]   O. Deutschmann, R. Schmidt, F. Behrendt, J. Warnat, Numerical modeling of catalytic ignition, Symposium (International) on Combustion. 26 (1996) 1747-1754. http://dx.doi.org/10.1016/S0082-0784(96)80400-0.

[85]   S. Oh, P. Mitchell, R. Siewert, Methane oxidation over noble metal catalysts as related to controlling natural gas vehicle exhaust emissions, Catalytic control of air pollution. ACS Publication, Washington, DC, 1992.

[86]   V.A. Drozdov, P.G. Tsyrulnikov, V.V. Popovskii, N.N. Bulgakov, E.M. Moroz, T.G. Galeev, Comparative study of the activity of Al-Pd and Al-Pt catalysts in deep oxidation of hydrocarbons, React. Kinet. Catal. Lett. 27 (1985) 425-427. https://doi.org/10.1007/bf02070487.

[87]   L. Ma, D.L. Trimm, C. Jiang, The design and testing of an autothermal reactor for the conversion of light hydrocarbons to hydrogen I. The kinetics of the catalytic oxidation of light hydrocarbons, Appl. Catal. A. 138 (1996) 275-283. http://doi.org/10.1016/0926-860X(95)00301-0.

[88]   H. Arai, T. Yamada, K. Eguchi, T. Seiyama, Catalytic combustion of methane over various perovskite-type oxides, Appl. Catal., A. 26 (1986) 265-276. https://doi.org/10.1016/S0166-9834(00)82556-7.

[89]   P. Barbato, G. Landi, R. Pirone, G. Russo, A. Scarpa, Auto-thermal combustion of CH_4 and CH_4-H_2 mixtures over bi-functional Pt-$LaMnO_3$ catalytic honeycomb, Catal. Today. 147 (2009) S271-S278. https://doi.org/10.1016/j.cattod.2009.07.018.

[90]   P.S. Barbato, A. Di Benedetto, V. Di Sarli, G. Landi, R. Pirone, High-pressure methane combustion over a perovskyte catalyst, Ind. Eng. Chem. Res. 51 (2011) 7547-7558. https://doi.org/10.1021/ie201736p.

[91]   D.G. Norton, D.G. Vlachos, Combustion characteristics and flame stability at the microscale: a CFD study of premixed methane/air mixtures, Chem. Eng. Sci. 58 (2003) 4871-4882. https://doi.org/10.1016/j.ces.2002.12.005.

[92]   D. Neumann, G. Veser, Catalytic partial oxidation of methane in a high-temperature reverse-flow reactor, AlChE J. 51 (2005) 210-223. https://doi.org/10.1002/aic.10284.

[93]   M. Reinke, J. Mantzaras, R. Bombach, S. Schenker, A. Inauen, Gas phase chemistry in catalytic combustion of methane/air mixtures over platinum at pressures of 1 to 16 bar, Combust. Flame. 141 (2005) 448-468. https://doi.org/10.1016/j.combustflame.2005.01.016.

[94]   A. Di Benedetto, G. Landi, V. Di Sarli, P.S. Barbato, R. Pirone, G. Russo, Methane catalytic combustion under pressure, Catal. Today. 197 (2012) 206-213. https://doi.org/10.1016/j.cattod.2012.08.032.

[95]   M. Reinke, J. Mantzaras, R. Schaeren, R. Bombach, A. Inauen, S. Schenker, High-pressure catalytic combustion of methane over platinum: In situ experiments and detailed numerical predictions, Combust. Flame. 136 (2004) 217-240. https://doi.org/10.1016/j.combustflame.2003.10.003.

[96]   S.R. Vaillant, A.S. Gastec, Catalytic combustion in a domestic natural gas burner, Catal. Today. 47 (1999) 415-420. http://dx.doi.org/10.1016/S0920-5861(98)00324-1.

[97]   K. Narui, H. Yata, K. Furuta, A. Nishida, Y. Kohtoku, T. Matsuzaki, Effects of addition of Pt to PdO/Al$_2$O$_3$ catalyst on catalytic activity for methane combustion and TEM observations of supported particles, Appl. Catal. A. 179 (1999) 165-173. https://doi.org/10.1016/S0926-860X(98)00306-8.

[98]   K. Murata, Y. Mahara, J. Ohyama, Y. Yamamoto, S. Arai, A. Satsuma, The metal-support interaction concerning the particle size effect of Pd/Al$_2$O$_3$ on methane combustion, Angew. Chem. Int. Ed. 56 (2017) 15993-15997. https://doi.org/10.1002/anie.201709124.

[99]   C. Bozo, N. Guilhaume, E. Garbowski, M. Primet, Combustion of methane on CeO$_2$–ZrO$_2$ based catalysts, Catal. Today. 59 (2000) 33-45. https://doi.org/10.1016/S0920-5861(00)00270-4.

[100]   Y. Ozawa, Y. Tochihara, A. Watanabe, M. Nagai, S. Omi, Deactivation of Pt·PdO/Al$_2$O$_3$ in catalytic combustion of methane, Appl. Catal. A. 259 (2004) 1-7. https://doi.org/10.1016/j.apcata.2003.09.029.

[101]   J.H. Lee, D.L. Trimm, Catalytic combustion of methane, Fuel Process. Technol. 42 (1995) 339-359. http://doi.org/10.1016/0378-3820(94)00091-7.

[102]   W.R. Schwartz, D. Ciuparu, L.D. Pfefferle, Combustion of Methane over Palladium-Based Catalysts: Catalytic Deactivation and Role of the Support, The Journal of Physical Chemistry C. 116 (2012) 8587-8593. https://doi.org/10.1021/jp212236e.

Chapter 4

Capillary microreactors with single- and multi-layer Pt/γ-Al₂O₃ catalyst coatings for catalytic methane combustion

ABSTRACT: Capillary microreactors (made of stainless steel) coated with single- and multi-layer catalytic coatings of Pt/γ-Al₂O₃ were employed for the catalytic methane combustion. For the single-layer coating, the effect of Pt loading (i.e., Pt weight percentage in the catalyst), total flow rate and oxygen to methane molar ratio (Φ) on the reaction performance was studied. A best methane conversion of 95.17% was obtained under 500 °C at 30 mL min⁻¹ and Φ = 2. Upon increasing the Pt loading from 1.5 wt% to 3.0 wt% and further on to 4.5 wt%, the difference in the increment of methane conversion tended to slow down, possibly due to more significant internal diffusion limitation in the coating with the increased intrinsic kinetic rate. The multi-layer coating was characterized by the presence of the same Pt weight (case 1) or loading (case 2) as that in the single-layer case. A higher methane conversion at Φ = 2 or 5 was found in the single-layer system (at Pd loadings of 3.0 wt% and 4.5 wt%) when compared with the corresponding double-layer system in case 1, suggesting the increased internal diffusion resistance within the thicker catalytic coating. A lower methane conversion existed in the single-layer system (at a Pt loading of 1.5 wt%) than that in the double-layer system in case 2, indicating the active participation of multiple coatings layers and the reaction rate being more limited by catalyst amount than internal diffusion. These findings provide useful guidelines in the catalyst coating preparation and microreactor operation for the catalyst combustion of methane.

Nomenclature

$F_{CH_4,i}$	Inlet molar flow rate of CH_4, mol s^{-1}
$F_{CH_4,o}$	Outlet molar flow rate of CH_4, mol s^{-1}
$F_{CO_x,o}$	Outlet molar flow rate of CO or CO_2, mol s^{-1}
$F_{H_2,o}$	Outlet molar flow rate of H_2, mol s^{-1}
L	Length of the microreactor, m
Q_{tot}	Total volumetric flow rate, m^3 s^{-1}
S	Inner surface area of the microreactor subjected to Pt/γ-Al$_2$O$_3$ coating, m^2
S_{CO_x}	Selectivity of CO or CO_2, %
S_{H_2}	Selectivity of H_2, %
T	Temperature, ^{o}C
T_{50}	Temperature at 50% methane conversion, ^{o}C
V_{tot}	Total volume for reaction in a microreactor, m^3
W_{cat}	Catalyst mass, g
X_{CH_4}	Methane conversion, %

Greek symbols

τ	Mean residence time, s
Φ	Inlet molar ratio of oxygen to methane, -
φ	Specific catalyst loading, g m^{-2}

Abbreviation

BET   Brunauer-Emmett-Teller

CMC   Catalytic methane combustion

GC   Gas chromatography

2-HEC   2-Hydroxyethyl cellulose

ICP-OES   Inductively coupled plasma optical emission spectrometry

i.d.   Inner diameter

MFC   Mass flow controller

MW   Molecular weight

o.d.   Outer diameter

PVA   Polyvinyl alcohol

SEM-EDS   Scanning electron microscopy-energy dispersive spectroscopy

SNG   Synthetic natural gas

TCD   Thermal conductivity detector

4.1. Introduction

Natural gas, with methane as the major component, provides an attractive fossil energy source due to its high energy content (55.7 kJ g^{-1} if fully based on methane as its main component), and its consumption has been constantly increased in the past decades [1]. Besides the abundantly proven natural gas reserves, the synthetic natural gas (SNG) can be obtained by biomass digestion (e.g., of manure) and carbohydrate fermentation [2-4]. Moreover, biomass gasification (e.g., of wood, straw and crops) coupled with the methanation process is a promising way to produce the SNG [5,6]. Thus, methane has been proposed as a promising substitute for the future leading energy [7]. Compared to the non-catalytic methane combustion that requires high working temperatures (ca. 1400 °C) and leads to harmful emissions [8-10], the catalytic methane combustion (CMC), due to the reduced activation energy (40-80 kJ mol^{-1}) for the reaction and thus lower working temperatures, has become an attractive means for energy applications such as in gas vehicles [11], gas turbines [12], solid oxide fuel cells [13] and domestic heating system [14].

The CMC in different aspects have been reviewed in the literature, e.g., on catalysts [8,15,16], reaction kinetics and mechanisms [17,18], and reactor designs [19]. Regarding the catalyst development, noble metal-based catalysts (e.g., Pd-based [20,21] and Pt-based [22,23]) present a relatively higher catalytic activity compared with perovskite and hexaaluminate catalysts due to their higher specific surface area and capabilities of lowering the activation energy [16,24]. It is reported that bimetallic catalysts (e.g., Pd-Pt/Al_2O_3) offers a higher activity than that of monometallic counterparts [25,26], due to the synergetic effect between metal-metal interactions. Moreover, different supports (e.g., Al_2O_3, CeO_2 and ZrO_2) were introduced to increase the catalyst activity and prolong the catalyst life [27,28]. The acidity of the catalyst could be decreased by introducing Al_2O_3 as support, resulting in a higher activity for the methane combustion [29]. The presence of CeO_2 as support was shown to improve the exchange of oxygen species between PdO and CeO_2, towards obtaining the enhanced catalyst activity [27,30].

In the fixed-bed reactor commonly used for the CMC, catalysts are fixed at a certain location inside the reactor, and the suitable catalyst shapes could be the powder, cylindrical or randomly shaped pellets. The preparation methods of traditional powder-based catalysts for use in such conventional (fixed-bed) reactors mainly include the incipient wetness impregnation [31], co-precipitation [32], ion-exchange [33], etc. However, in order to avoid the high pressure drop and hot spot formation likely occurring in fixed-bed type reactors, structured reactors especially

microreactors incorporated with the coated catalyst hold a promising potential for the CMC [34-37]. The catalyst in the form of wall coatings is usually prepared via the suspension method [38-41] and sol-gel method [42,43]. The main influencing factors (e.g., the binder properties, pH value and particle size in the coating precursors) have been investigated in order to maintain a good catalyst adhesion with the microreactor substrate, due to its greatly influence on the rheological properties of slurry and its adhesion with substrate [44]. In our previous study [41], PVA and Tylose were considered as binders (at the concentrations of 5 wt% and 1.6 wt%, respectively) for the preparation of γ-Al_2O_3 slurry, and the optimized pH value of 3.5 and Al_2O_3 particle size of ca. 3 μm were identified. After applying the slurry coating technique and the subsequent thermal treatment, a well-adhered and uniform γ- Al_2O_3 layer could be formed on the FeCrAlloy microreactor substrate, as demonstrated by the ultrasonic test and SEM image. The incorporation of active catalytic component (in this case Pt) for the CMC could then be realized using impregnation with Pt precursor.

Regarding the performance in the CMC, O'Connell et al. [34] have tested a multichannel microreactor with the microchannel dimension of 500 μm (length) × 250 μm (width) coated with Pt-W/Mo-Al_2O_3 (4.6 wt% Pt and 9 wt% W) and Pt-Mo/γ-Al_2O_3 (4.6 wt% Pt and 9 wt% Mo) catalysts. Pt-W/γ-Al_2O_3 catalyst presented a higher catalytic activity (T_{50} = 493 °C, T_{100} = 600 °C) than Pt-Mo/γ-Al_2O_3 catalyst (T_{50} = 526 °C, T_{100} = 625 °C) at a total flow rate of 107 mL min^{-1} (corresponding to a space velocity of 74,000 h^{-1}; defined as the total flow rate of reactants divided by the reactor volume), where T_{50} and T_{100} designate the respective temperature values for reaching a methane conversion of 50% and 100%. In our previous study, a multichannel microreactor (275 mm length × 1.5 mm width × 1 mm height) with Pt/γ-Al_2O_3 catalytic coating was investigated [41]. The results show that a 95.75% methane conversion was obtained at 450 °C and 110 mL min^{-1} (space velocity: 6,557 h^{-1}). The lower working temperature required for a close to complete methane conversion in this case might mainly result from the lower space velocity used (translating into a longer residence time in the microreactor).

The high mass transfer rate is one of the outstanding features for microreactor operations. In the case of using microreactors with wall-coated catalyst (for carrying out among others the CMC), reactants have to be transported (perpendicularly to the flow direction) from the centre of the microchannel to the catalyst external surface (i.e., external mass transfer), followed by the reactant diffusion within the coating layer (i.e., internal mass transfer) [45], before the reaction happens on the internal surface of catalyst pores. The external mass transfer mainly depends on the flow pattern (e.g., reactant velocity) and concentration, microchannel geometry

and reactant diffusivities, etc. The internal mass transfer mainly relies on the washcoat properties (e.g., thickness, porosity, tortuosity) as well as the effective diffusivities of reactants within coating. Thus, apart from the influence of kinetics (e.g., via changing the reaction temperature and catalyst mass), such two inherently coupled external and internal mass transfer processes also play an important role in determining the overall microreactor performance (in the CMC) [46].

The simulation results on Fischer-Tropsch synthesis in microreactors with wall-coated 20 wt%Co-0.5wt%Re/γ-Al$_2$O$_3$ have been reported by Theampetch et al. [47]. A higher CO conversion could be obtained by the reduced cross-sectional area of the microchannel (0.3 mm width × 0.3 mm height) with a length of 50.18 mm, which was attributed to among others the reduced gas diffusion path towards the catalytic wall. To reduce the internal diffusion path within the coating, a relatively thin layer is commonly recommended [48]. Laguna et al. [49] investigated two microreactors composed of 100 microchannels, where the influence of coating thickness (with 150 mg and 300 mg CuO$_x$/CeO$_2$ catalysts) has been examined for CO oxidation in the presence of H$_2$. The microreactor with 150 mg coating catalyst (calculated thickness ca. 10 μm) was estimated to have a higher effectiveness factor than that with 300 mg catalyst (calculated thickness ca. 19 μm). In contrast, the same catalyst in the powder form (with an assumed average diameter of 150 μm) presented the lowest effectiveness factor with a more pronounced decrease at high temperatures. These calculation results are in line with the experimental results, where the microreactor with 150 mg catalyst mass showed a higher catalytic performance due to the better internal mass transfer characteristics. Holmgren et al. [50] investigated the influence of washcoat catalyst thickness on mass transfer in the monolithic reactor for CO oxidation. The effective diffusivity of reactant gas in the double layers of 1 wt% Pt/γ-Al$_2$O$_3$ washcoat was measured to be higher by a factor of 2-25 than the prediction by the Wakao-Simith model, due to the cracks, incomplete and non-uniform washcoat layer inside square monolithic channels [50]. So far, such mass transfer influence on the CMC reaction characteristics in microreactors has not been largely reported.

From the above literature survey, it is clear that optimization of the operating parameters and the coating properties are both important towards achieving a favorable methane conversion in microreactors, and thus dedicated experiments are required. The washcoat catalyst with a thin coating layer holds a great promise for increasing the catalyst efficiency, however, the catalyst mass required for the desired conversion has to be met (e.g., by increasing the active species loading or using long coated microchannels). Experimentally, the relative roles of the

external mass transfer, internal diffusion, and intrinsic kinetic rate in determining the overall reaction rate can be investigated by varying the relevant influencing factors (e.g., reactant flow rate and ratio, temperature, active species loading and coating thickness). Thus, in this work, single- and multi-layer Pt/γ-Al$_2$O$_3$ catalysts have been washcoated inside the stainless steel capillary microreactors. Pt loading and weight have been varied in the coating, combined with the change of the operating parameter (including the reaction temperature, total flow rate and molar ratio of oxygen to methane), in order to study their influence on the CMC reaction performance. The reaction results over single- and multi-layer catalyst systems have been compared and explained mainly based on the (external and internal) mass transfer effect, as well as the CMC reaction kinetics and mechanism. A further improvement direction was also discussed.

4.2. Experimental

4.2.1. Materials

γ-Al$_2$O$_3$ (3 µm, 99.97% on metals basis), tetraammineplatinum (II) nitrate (Pt(NH$_3$)$_4$(NO$_3$)$_2$, 99.99% on metals basis, ≥ 50.0% Pt), PVA (≥ 99% hydrolysed, MW = 146,000 - 186,000 g mol^{-1}) and acetic acid (ACS reagent, ≥ 99.8%) were purchased from Alfa Aesar. Synthetic air (UN1956, Linde) composed of 80% N$_2$ and 20% O$_2$ was used as the oxygen source, and methane (UN1971, Linde) was of 99.995%. The capillary microreactors were made of 316L stainless steel with an overall dimension of 100 mm (length) × 4.6 mm (i.d.), and 6.35 mm (o.d.).

4.2.2. Catalyst preparation and coating procedures

4.2.2.1. Catalyst slurry preparation

The γ-Al$_2$O$_3$ slurry was prepared by mixing γ-Al$_2$O$_3$ powders, binder and acetic acid [38]. Based on our previous study [41], the optimized composition of slurry (20 wt% γ-Al$_2$O$_3$, 5 wt% PVA and 1 wt% acetic acid) was used in the current experiments. The slurry was heated up from room temperature to the final temperature of 65 °C and maintained for 2 h under 300 rpm stirring. The desired concentration of the Pt(NH$_3$)$_4$(NO$_3$)$_2$ aqueous solution was then added into the slurry at room temperature, followed by stirring the whole mixture at 300 rpm for 30 min. The catalyst slurry was subsequently stored at room temperature for at least 2 weeks to remove bubbles inside before use.

4.2.2.2. Washcoating procedures

The file and drill with a metal brush were first used to polish the inside surface of capillary

microreactors, in order to remove the anti-corrosion layer over the surface and increase its roughness. This could result in an improved adhesion between the microreactor wall and the washcoated catalyst. The microreactor was then immersed in acetone for 30 min in the ultrasonic bath at 45 ^{o}C to further remove oil, grease and other dirt [51]. The thermal pretreatment of the microreactor was subsequently performed at 900 ^{o}C (ramp from room temperature: 20 ^{o}C min^{-1}; 10 h) to generate a thin layer of metal oxides over the substrate surface functioning as a strong bonding with the catalyst coating layer [52,53].

The slurry coating method of Pt/γ-Al$_2$O$_3$ catalyst over the flat, multichannel microreactor in our previous study via syringe injection [41] is hardly applicable to coat the current capillary microreactor. Thus, to coat a (close to) uniform layer of the catalyst slurry around the inner microreactor wall, the dynamic slug flow coating method was applied, inspired by the reported literature [54,55]. Before coating, the prepared Pt/γ-Al$_2$O$_3$ catalyst slurry was stirred at a low rotation speed (50 rpm) for 30 minutes to ensure an even distribution of components in the slurry as well as to prevent the bubble formation. As Fig. 4.1 shows, the coating started with the use of a syringe pump (model: NE-300, new era pump systems Inc.) to inject the catalyst slurry into the microreactor. A catalyst slug with a fixed mass was delivered by the pump (at a constant rate of 180 μL min^{-1} for 2 minutes) into the capillary microreactor placed horizontally. Subsequently, the pump was stopped and the microreactor inlet was switched to connect with nitrogen gas line the flow rate of which was regulated by a mass flow controller (ELFlow, type: F-200C-FA-11-V, Bronkhorst HI-TEC) at 3 mL min^{-1} under 2 bar. The bubble front of the gas then pushed the catalyst slug through the microreactor, leaving behind a uniform coating around the wall. The influence of the nitrogen gas flow rate pressure used to drain the excess Pt/γ-Al$_2$O$_3$ slurry may have a significant effect on the surface tension and viscosity forces that govern the residual film thickness. Such influence was not further investigated, since the focus of this work is on the CMC reaction behavior in the capillary microreactor. The coated microreactor was then dried in a muffle furnace (LM312, G800P controller, Linn High Therm) at 75 ^{o}C (ramp from room temperature: 2.5 ^{o}C min^{-1}) for 2 h, followed by calcination at 500 ^{o}C (ramp from 75 ^{o}C: 15 ^{o}C min^{-1}) for another 2 h in the same furnace. In order to investigate the impact of the coating thickness as well as the catalyst loading (defined as the Pt weight percentage in the catalyst) on the methane conversion, both single-layer (i.e., realized by one coating procedure) and multi-layer (realized by repeated coating procedures) catalyst systems were studied. Two cases of multi-layer systems were considered for their comparison with the single-layer system, as illustrated in Fig. 4.2. Taking a single-layer catalyst with 3 wt% Pt loading as an example, case 1

deals with a two-layer Pt/γ-Al$_2$O$_3$ catalyst coating (with 1.5 wt% Pt loading for each layer and thus for both layers as well), which compares with the single-layer system by maintaining the identical total mass of Pt in the catalyst (if we consider the same thickness of each layer obtained in one or multiple coating procedures), but with the Pt loading in the catalyst being proportionally decreased with the number of layers. In case 2, a two-layer Pt/γ-Al$_2$O$_3$ catalyst coating has 3 wt% Pt loading in each layer, which compares with the single-layer system by maintaining the same Pt loading in the catalyst, but with proportionally increased total mass of Pt with the number of layers. Table 4.1 summarizes all the tested Pt/γ-Al$_2$O$_3$ washcoated catalysts for both single-layer and multi-layer systems. The finally coated catalyst amount could be well controlled using this method, as confirmed by ICP-OES characterization (*vide infra*).
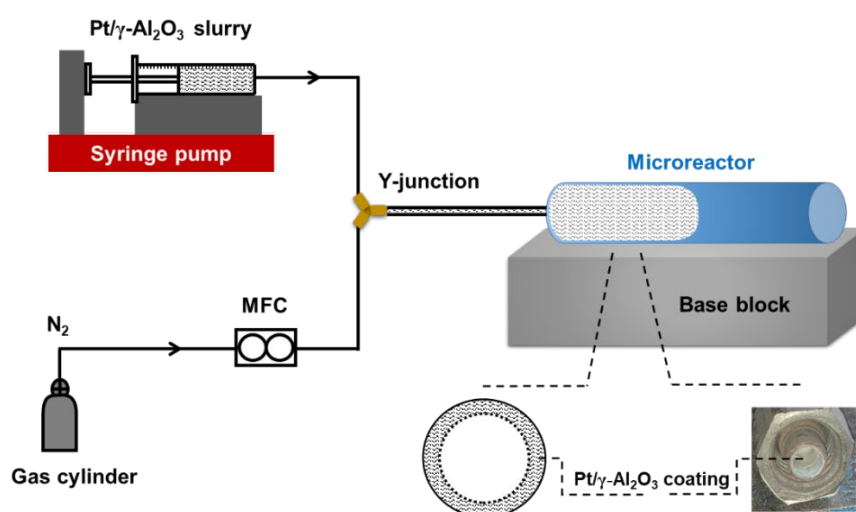
Fig. 4.1. Schematics of the washcoating process of the Pt/γ-Al$_2$O$_3$ slurry in the capillary microreactor.
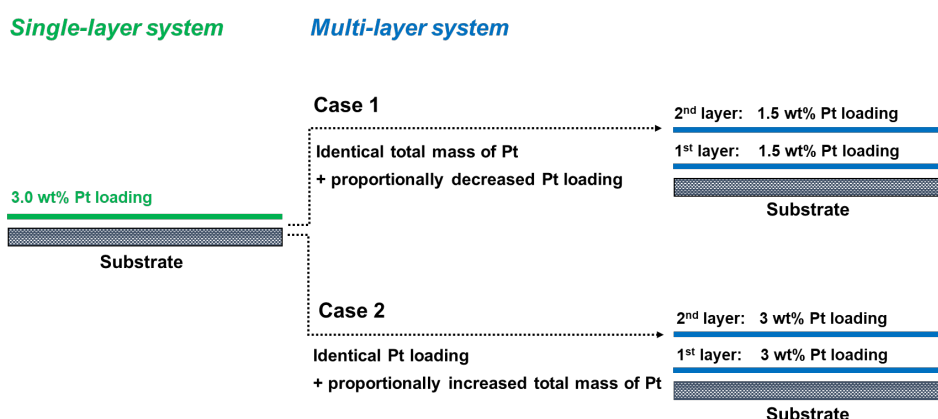
Fig. 4.2. Comparisons between single-layer system and two types of multi-layer systems of Pt/γ-Al$_2$O$_3$ catalyst in the capillary microreactor. A single-layer catalyst (3 wt% Pt/γ-Al$_2$O$_3$) and the corresponding double layer system in cases 1 and 2 are shown as an example.

Table 4.1

Summary of the investigated single- and multi-layer Pt/γ-Al$_2$O$_3$ coating systems in the capillary microreactor.

Entry	Pt loading by preparation [a] (wt%)	Number of layers (-)	Total catalyst mass [b] (g)	Total Pt mass by preparation (mg)	Specific catalyst loading φ [c] (g m^{-2})	Pt loading by ICP-OES [d] (wt%)
1	1.5	1	0.0775	1.163	53.6	1.31
2	3.0	1	0.0759	2.277	52.5	2.62
3	3.0	1	0.0814	2.442	56.3	
4	3.0	1	0.0789	2.367	54.6	
5	3.0	1	0.0635	1.905	43.9	
6	3.0	1	0.0787	2.361	54.5	
7	4.5	1	0.0817	3.677	56.5	
8	4.5	1	0.0725	3.263	50.2	3.92
9	1.5 (cases 1+2) [e]	2	0.1406	2.109	97.3	
10	1.5 (cases 1+2) [e]	3	0.1934	2.901	133.9	
11	2.25 (case 1) [e]	2	0.1461	3.287	101.1	2.11
12	3 (case 2) [e]	2	0.1249	3.747	86.4	
13	3 (case 2) [e]	3	0.2119	6.357	146.6	

[a] The same for each layer; calculated based on the slurry composition and the dry weight of the obtained coating.

[b] The measured weight of the coated catalyst (after drying and calcination) gained on the microreactor wall.

[c] Calculated with Eq. (4.5).

d ICP-OES: inductively coupled plasma optical emission spectrometry.

e Illustrations of cases 1 and 2 are exemplified in Fig. 4.2.

4.2.3. Catalytic methane combustion in microreactors

The setup for the catalytic methane combustion in the capillary microreactor is schematically presented in Fig. 4.3. Two mass flow controllers (EL-Flow, Type: F-200C-FA-11-V, Bronkhorst HI-TEC) were used to adjust the flow rates of methane and the synthetic air for the experiment. Methane and air were mixed in the gas line and the mixture flow rate was typically adjusted from 30 to 100 mL min^{-1} (based on ca. 20 ^oC and 1 atm). The methane-air mixture (concentration of methane at 0.5 to 5 vol. %) first passed a preheating coil tube (i.d.: 3.7 mm, o.d.: 6 mm, ca. 15 cm in length) to ensure the reactants reaching the set reaction temperature (i.e., the oven temperature) before entering the capillary microreactor. Both the coil tube and microreactor were placed in the oven. It has to be mentioned that the microreactor was first heated up from room temperate (ramp: 10 ^oC min^{-1}) to the targeted reaction temperature under the nitrogen atmosphere to avoid any reaction occurrence during this startup process, and then the feed line was switched to the methane-air mixture side for the reaction to start. Two thermocouples (Type K) were connected to external temperature loggers (USB-501-TC-LCD thermocouple data logger) and placed at the inlet and outlet of the microreactor (without touching the catalyst surface) to measure the corresponding gas temperatures therein (T_{inlet} and T_{outlet}). Subsequently, the product gas was guided out of the microreactor to a condenser to remove water. The remaining gas was then collected using a syringe (35 mL) fitted with luer lock tip valves (Terumo), and later analysed on an offline gas chromatography (GC).
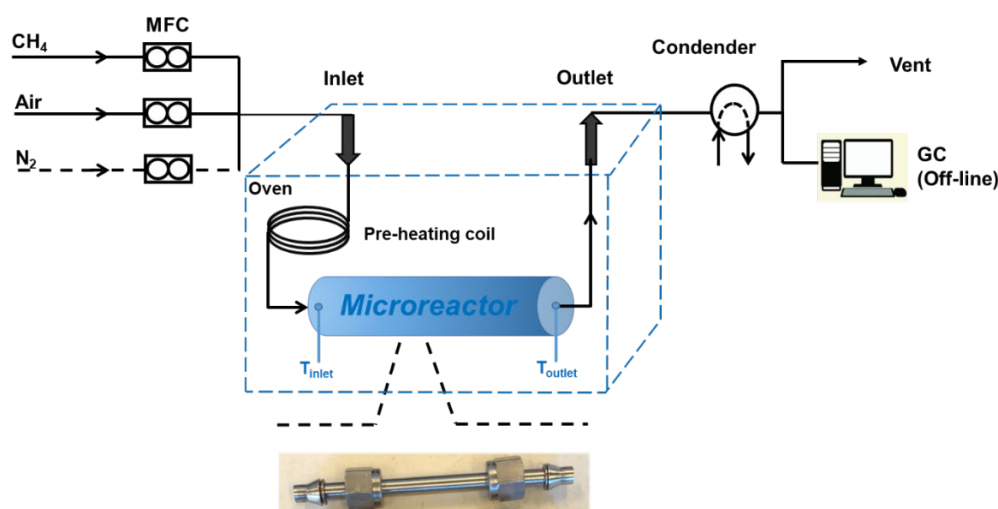
Fig. 4.3. Schematic presentation of the catalytic methane combustion in the capillary microreactor coated with Pt/γ-Al$_2$O$_3$ catalyst.

4.2.4. Analytics

Gas products were analyzed by GC (Hewlett-Packard 5890 Series II) equipped with a thermal conductivity detector (TCD) operated at 200 °C. A Porablot Q Al_2O_3/Na_2SO_4 column (length: 50 m; i.d.: 0.5 mm) and Agilent Technologies HP-Molesieve 5 Å column (length: 25 m; i.d.: 0.53 mm) were utilized for analysis. The applied program for analysis was at 40 °C for 3 min, and then increased to 90 °C (ramp: 20 °C min^{-1}; 8 min). The reference gas concentration is as follows: 20.7 % CH_4, 17.9 % CO_2, 2.99 % CO, 1.5 % C_2H_6, 1.49 % C_3H_8, 5088 ppm C_2H_4, 5122 ppm C_3H_6 and H_2 as the balance.

SEM-EDS (scanning electron microscopy-energy dispersive spectroscopy) analysis was performed on an XL30 ESEM (Philips) operating at 10 keV, a take-off between 37.1 - 38.2, live time of 50 s, amp time of 0.12 µs, and a resolution of 143.4 eV, to characterize the smoothness and thickness of the washcoated Pt/γ-Al_2O_3 layer on the microchannel. The sample was prepared by firstly cutting a small section of the capillary microreactor with a Buehler low-speed saw, and subsequently the sample was hot-mounted in a circular resin with 30 mm diameter. After that, in order to polish the cutting surface of the sample, a sandpaper (#1200) was used and then a polisher (Stuers TegroPol-11; with an application force of 15 N at 300 rpm combined with diamond suspensions of 9 µm, 3 µm and 1 µm) was applied. The procedure was repeated until all visible scratches were removed and checked by an Olympus VANOX-T microscope. In order to avoid the possible mass loss of the catalyst from the reactor wall, the resin was also placed inside the microreactor so that the exposed catalyst layer was not affected by the sample preparation procedures above.

The specific surface area of the washcoated Pt/γ-Al_2O_3 catalyst was measured using a Micromeritics ASAP 2420 apparatus by nitrogen physisorption at -196 °C. The coating was scraped from the microreactor substrate. The samples were firstly degassed in the vacuum at 200 °C for 8 h before nitrogen adsorption. The surface area and pore size were evaluated using the Brunauer-Emmett-Teller (BET) method, and the micropore area was quantified by the t-plot method.

Inductively coupled plasma optical emission spectrometry (ICP-OES) was used to determine the Pt loading in the catalyst. Selected catalyst washcoat samples scrapped from the microreactor wall were dissolved in 3% HF overnight prior to analysis. Analysis was performed using PerkinElmer Optima 7000 DV with the following operational parameters: 0.90 L min^{-1} nebulizer gas flow, 0.20 L min^{-1} auxiliary gas flow, 1.40 mL min^{-1} pump flow, and 1450 W RF

power. Each sample was measured twice to give the average Pt loading.

The coating adhesion measurements were performed in an ultrasonic bath (PCE-UC 20, 40 kHz) by immersing the coated microreactor in the glass beaker containing acetone for 1 to 3 h. After drying the capillary microreactor, the weight loss percentage of the microreactor was calculated based on the dry weight difference before and after the ultrasonic test.

4.2.5. Definitions

The CH$_4$ conversion (X_{CH_4}), CO$_2$ or CO selectivity (S_{CO_x}) and H$_2$ selectivity (S_{H_2}) are calculated based on Eqs. (4.1) - (4.3), respectively.

$$X_{CH_4} = \frac{F_{CH_4,i} - F_{CH_4,o}}{F_{CH_4,i}} \times 100\ \% \tag{4.1}$$

$$S_{CO_x} = \frac{F_{CO_x,o}}{F_{CH_4,i} - F_{CH_4,o}} \times 100\ \% \tag{4.2}$$

$$S_{H_2} = \frac{F_{H_2,o}}{F_{CH_4,i} - F_{CH_4,o}} \times 100\ \% \tag{4.3}$$

Here F means the molar flow rate (based on ca. 20 ^{o}C and 1 atm). The subscripts i and o denote the inlet and outlet of the microreactor, respectively.

The mean residence time (τ) in the microreactor is defined as the total inner volume of the microreactor (V_{tot}) divided by the total volumetric flow rate of the feed gases (Q_{tot}; based on 20 ^{o}C and 1 atm).

$$\tau = \frac{V_{tot}}{Q_{tot}} \tag{4.4}$$

The actual residence time under the reaction conditions is shorter due to the increased reaction temperature (cf. Table 4.A.1 in the appendix).

The catalyst specific loading (φ) of Pt/γ-Al$_2$O$_3$ coating is defined as the catalyst mass (W_{cat}) divided by the inner surface area (S) of the microreactor,

$$\varphi = \frac{W_{cat}}{S} \tag{4.5}$$

Here the calculation of τ and φ are based on the microreactor geometry without considering the presence of the coating (given its negligibly small thickness compared with the microreactor inner diameter).

4.2.6. Error analysis

Each data point (i.e., the methane conversion) presented in this work represents an average result of the two or three samples collected for each run. The relative deviation was found in a range of 3.33-15.97% at 350 °C (due to practically low conversion levels) and of 0.11 to 2.32% for temperatures of 400 - 500 °C. The reason for these errors might be due to the reaction operation process (e.g., manual sampling) and the sample analysis (by GC).

4.3. Results and discussion

4.3.1. Reaction performance of the single-layer Pt/γ-Al2O3 catalyst system

4.3.1.1 Effect of temperature

The methane conversion as a function of the reaction temperature (i.e., approximated as the oven temperature) under different Pt loadings and $O_2:CH_4$ molar ratios (Φ) for the single-layer Pt/γ-Al_2O_3 catalyst system is presented in Fig. 4.4. As shown in Fig. 4.4a ($\Phi = 2$), at a lower temperature (e.g., from 350 °C to 400 °C), the reaction could be mainly controlled by kinetics. At 350 °C, the methane conversion is very low (<3%) due to the reaction rate being very low at such temperatures and its difference is not noticeable between each Pt loading tested as the measurement could be more significantly affected by the experimental error. As the temperature increased to 400 °C, the methane conversion for each Pt loading case increased and the higher Pt loading gave rise to a higher methane conversion, due to the much increased reaction rate clearly unveiling the positive effect of increased Pt loading. As the temperature increased to 450 or 500 °C, the methane conversion increased more rapidly for each Pt loading tested, primarily due to the exponential increase of the kinetic rate with temperature (according to the Arrhenius equation). The methane conversion at 500 °C exhibited a remarkable increase from ca. 37.54% to 84.97% when the Pt loading was increased from 1.5 wt% to 4.5 wt%, and the CO_2 selectivity is approximately 100 % ± 3% without any other byproducts found (not shown for brevity). The Pt loading increase in the single-layer system resulted in the increased intrinsic kinetic rate, and thus increased the overall reaction rate leading to a higher methane conversion, although the reaction tended to be controlled by mass transfer at such high temperature levels.

The methane conversion obviously exhibited a remarkable increase starting from ca. 400 °C onwards (Fig. 4.4a). Given the higher adsorption energy of methane than that of oxygen, it is reported that the reaction rate determining step was shifted from the oxygen adsorption at the beginning to the methane adsorption with the increased surface temperature of catalyst [56].

The light-off phenomenon occurred once the favourable coverage of the adsorbed methane and oxygen over the catalyst surface was reached [57,58]. This light-off further boosted the local temperature of the catalyst, resulting a further increase in the methane conversion. Thus, the light-off temperature is one of the crucial parameters used to evaluate the catalyst activity. As shown in Table 4.2, for a higher Pt loading, the T_{50} value (i.e., the light-off temperature corresponding to 50% methane conversion; estimated by the polynomial fitting method [15]) is lower due to the enhanced catalyst activity.

It is worth noting that the difference in the methane conversion increase is generally reduced when increasing the Pt loading, which is more obvious at higher temperatures. For example, the difference in the methane conversion (54.67%) between 1.5 wt% and 3.0 wt% Pt loading at 500 ^{o}C is much larger than that (15.62%) between 3.0 wt% and 4.5 wt% Pt loading. This phenomenon might be attributed to the more significant (external) mass transfer limitation at the higher Pt loading system, especially at high temperatures between 450 ^{o}C to 500 ^{o}C where the kinetic rate is such fast that the reaction tended to be in the mass transfer-controlled regime. As a result, there existed a slower conversion increment with higher Pt loading systems (e.g., 4.5 wt% Pt loading). These results suggest that a higher methane conversion could be obtained at a higher temperature and preferably over a higher Pt loading system, although the mass transfer limitation has to be suppressed for the best use of the intrinsic catalytic activity.

Similar trends in the methane conversion as a function of the reaction temperature and Pt loading were found at $\Phi = 5$ (Fig. 4.4b). Comparing Figs. 4.4a and 4.4b, the methane conversion with Pt loading systems of 3.0 wt% and 4.5 wt% is generally higher at $\Phi = 2$ than that at $\Phi = 5$, which is more discernible at relatively higher temperatures (e.g., at 450 ^{o}C or above). This is in line with the lower light-off temperature (T_{50}) at $\Phi = 2$ for such Pt loading (Table 4.2). The difference in the light-off behavior at different Φ values could be due to the coverage variation between the adsorbed oxygen and methane over the catalyst surface. The adsorption rate of oxygen is faster than that for the methane [9], resulting in the catalyst surface being more covered by oxygen prior to ignition [59]. The more adsorbed oxygen could bring a lower methane conversion by preventing the weakly adsorbed methane over the catalyst surface [60]. A favourable coverage between the adsorbed methane and oxygen could be reached at ca. $\Phi = 2$ (i.e., the stoichiometric ratio for methane combustion), resulting in a better methane conversion and thus a lower T_{50} value.

On the contrary, at a Pt loading of 1.5 wt%, a slightly higher methane conversion has been observed at $\Phi = 5$ rather than at $\Phi = 2$ throughout the tested temperature from 350 to 500 ^{o}C

(Fig. 4.4). For example, a ca. 5% higher conversion was found at Φ = 5 for reaction temperatures of 450 and 500 ºC, in agreement with the light-off temperature difference shown in Table 4.2. Such difference is believed not caused by a significant experimental error. This might be further explained by the fact that at Φ = 2, the reactants were less significantly ignited due to the insufficient Pt loading though in the presence of a (close to) favourable catalyst coverage, and thus the adsorbed methane at Φ = 2 could not be effectively converted than that at Φ = 5 where there was less methane adsorbed in the presence of a dominant oxygen adsorption. This might be linked to the influence of catalyst properties (e.g., specific surface area, Pt particle size, the interaction between Pt and Al_2O_3 through bridging oxygen [61]) at such low Pt loading/mass on the catalytic performance. A further justification would require catalyst surface characterization.
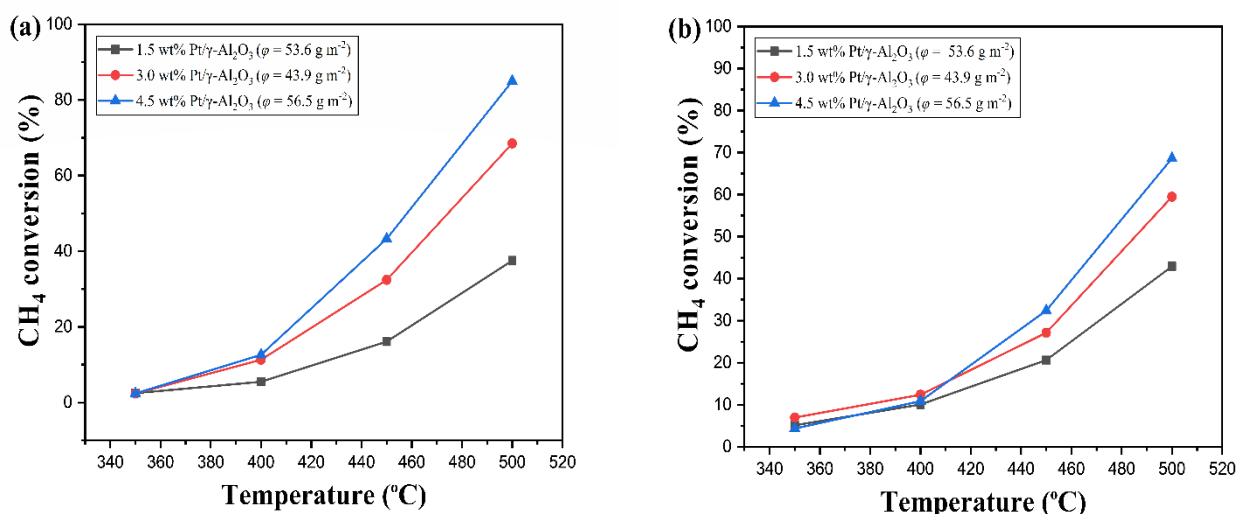
Fig. 4.4. Methane conversion as a function of the reaction temperature (T) over the single-layer Pt/γ-Al_2O_3 catalyst in the capillary microreactor: (a) Φ = 2, (b) Φ = 5. Conditions: T = 350 - 500 ºC, Q_{tot} = 70 mL min^{-1}, τ = 1.42 s, Pt loading from 1.5 to 4.5 wt% (cf. entries 1, 5 and 7 in Table 4.1).

Table 4.2

T_{50} values for the CMC experimental data presented in Fig. 4.4.

Pt loading (wt%)	T_{50} (°C) [a, b]	
	$\Phi = 2$	$\Phi = 5$
1.5	531.25	518.81
3.0	476.58	487.39
4.5	460.96	476.88

[a] T_{50} indicates the temperature to reach 50% methane conversion, and reaction conditions are the same as shown in Fig. 4.4.

[b] Estimated from the polynomial regression line used for fitting the measured conversion curve as a function of the reaction temperature for each Pt loading. The polynomial is in the form of $T_{50} = B_0 + B_1 X_{CH_4} + B_2 X_{CH_4}^2$, where B_0, B_1 and B_2 are the fitting constants.

4.3.1.2 Effect of molar ratio of O_2 to CH_4

The methane conversion as a function of Φ is presented for the single-layer 3 wt% Pt/γ-Al$_2$O$_3$ system in Fig. 4.5 by maintaining a constant total flow rate (Q_{tot} = 70 mL min^{-1}) and operating temperature (T = 400 or 450 °C). The methane conversion was found higher for all investigated Φ values at 450 °C than that at 400 °C. This is consistent with the results in the light-off experiments (Fig. 4.4), that is, a higher temperature improved the methane conversion due to the increased intrinsic catalytic activity. For each temperature, the methane conversion increased when increasing Φ from 0.5 to 1.5. At such methane-rich conditions ($\Phi < 2$), the coverage of the adsorbed methane is dominant over the catalyst surface, and the insufficient supply of oxygen is the main factor limiting the adsorbed methane to be further converted over the available active sites, as it is shown in the GC analysis that all oxygen has been consumed. In other words, with increasing Φ up to ca. 1.5, there is more oxygen available in the feed and subsequently over the catalyst surface, leading to a higher methane conversion. The limited oxygen supply at such low Φ values also explains the observed little effect of raising the temperature from 400 to 450 °C on the conversion improvement (i.e., the reaction has already proceeded 100% relative to oxygen). The slight increase of the methane conversion at 450 °C is possibly due to the more favored side reactions involving methane (e.g., methane partial oxidation and steam reforming [62]) compared to that at 400 °C, as supported by the higher

H$_2$/CO selectivity and lower CO$_2$ selectivity found in the former case (Fig. 4.6). The well-known path for methane partial oxidation is that CH$_4$ is first converted to CO$_2$ and H$_2$O, and the remaining CH$_4$ is converted with CO$_2$ or H$_2$O to form H$_2$ and CO when oxygen is completely consumed [63-65]. Meanwhile, CH$_4$ is reformed with H$_2$O for producing H$_2$ and CO (steam reforming reaction), and CO could react with H$_2$O to form CO$_2$ and H$_2$ (water-gas shift reaction). The highest conversion was found at ca. Φ = 1.5 instead of 2 (the stoichiometric ratio for methane combustion), due to the increased oxygen supply together with the additional consumption of methane in side reactions mentioned above that require less amount of oxygen. Moreover, it is also reported that there has to be a balance between the adsorbed oxygen and methane on the catalyst surface, and neither a fully oxidized nor a fully reduced Pt state was desired [66]. A further decrease or increase of the oxygen composition in the feed disturbs this balance and negatively impacts the conversion of methane. It seems that this balance has been achieved at Φ = 1.5 in the experiments relevant to Fig. 4.5, which also largely explains a remarkable decrease in the methane conversion at Φ = 2.

As further revealed in Fig. 4.5, the methane conversion slightly increased when increasing Φ from 2 to 5. This phenomenon is also not procedurally related, as an additional experiment by decreasing Φ from 5 to 2 (and further on to 0.5) at 400 ^{o}C led to exactly the same conversion behavior. The results in the current molar ratio experiment (Fig. 4.5) are not consistent with that in the light-off experiment (Fig. 4.4) where the methane conversion is higher at Φ = 2 than that at Φ = 5 under otherwise identical conditions (3 wt% Pt loading, 70 mL min^{-1}, 400 and 450 ^{o}C). In the light-off experiment, Φ was fixed and the temperature was gradually increased from 350 to 450 ^{o}C. In the molar ratio experiment, the temperature was fixed and Φ was varied from 0.5 to 5 (or vice versa), where a more complex surface behavior might have occurred. It is reported that the hysteresis phenomenon was present when switching the feed gas composition [62,67,68], due to the balance between the adsorbed methane and oxygen over the catalyst being disrupted. The hysteresis phenomenon is commonly considered in the case that when the catalyst is first induced to the high conversion state (e.g., after ignition), it still maintains a relatively high conversion even after switching to the low conversion state/or extinction conditions [66]. Moreover, Bugosh et al. [62] reported that in the high conversion state, increasing the oxygen to methane ratio (as high as 65) in the feed gas had no significant effect on the methane conversion. Thus, the oxygen coverage as well as the number of active sites could be considered as constant under such circumstances. In the current molar ratio experiment, such a (relatively) high conversion state has been triggered previously by operating

at $\Phi = 1.5$, and thus is expected to maintain when Φ was further switched to 2 all the way up to 5. Thus, the increased methane conversion upon increasing Φ from 2 to 5 in such experiment could be related to the decrease in the relative concentration of methane in the feed gas. To be more specific, under the oxygen-rich conditions ($\Phi > 2$), the catalyst surface is covered by a large amount of oxygen. It is reasonable to assume that the adsorbed oxygen concentration was sustained relatively as constant over the catalyst surface. Thus, the methane adsorption became the rate-determining step [57,58], and the decreased methane concentration in the feed gas with increasing Φ resulted in a higher methane conversion due to the less methane competing for a certain amount of active sites. In other words, a relatively large fraction of methane had the possibility to be adsorbed onto the active sites, resulting in higher oxidation chances and therefore an increased methane conversion. This theory also holds true when Φ was decreased from 5 to 2 as shown in Fig. 4.5. In more detail, given the high temperature level tested (400 ºC), a relatively high conversion state was already achieved at $\Phi = 5$. Thus, this state could be kept when further decreasing Φ towards 2. Here, it can be still assumed that the catalyst was with a constant oxygen coverage on the surface and therefore a constant number of active sites. Consequently, the methane conversion was reduced with decreasing Φ, based on a similar argument as above. In the light-off experiment, the high conversion state was only reached near the end (i.e., at relatively high temperature level) and thus, the hysteresis effect was not observed.
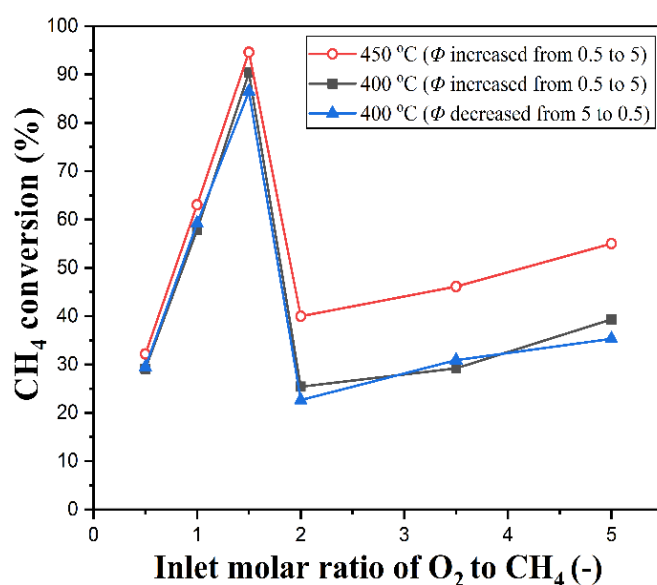
Fig. 4.5. Methane conversion as a function of the molar ratio of O_2 to CH_4 (Φ) over the single-layer 3 wt% Pt/γ-Al$_2$O$_3$ system (cf. entry 6 in Table 4.1) in the microreactor. Conditions: $T = 400$, and 450 ºC, $\Phi = 0.5 - 5$, $Q_{tot} = 70$ mL min^{-1}, $\tau = 1.42$ s.
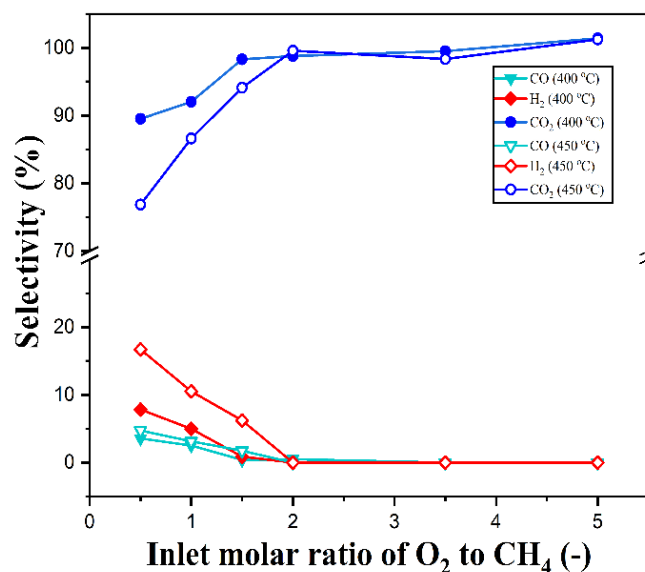
Fig. 4.6. Selectivities of H_2, CO and CO_2 as a function of Φ over the single-layer 3 wt% Pt/γ-Al$_2$O$_3$ system (cf. entry 6 in Table 4.1) in the microreactor. Other conditions are the same as in Fig. 4.5.

Table 3 provides a further comparison between the light-off experiment and the molar ratio experiment in Table 4.3. Under otherwise the same operating conditions, the methane conversion in the molar ratio experiment is (much) higher than that in the light-off experiment for Φ = 2 or 5. This difference can be also explained by the hysteresis effect as mentioned above. In our molar ratio experiment, the high conversion state in the catalyst has been induced, e.g., at Φ = 1.5. This could result in a higher methane conversion when raising Φ to 2 and further on up to 5 in the molar ratio experiment than that obtained in the light-off experiment where there is an absence of the hysteresis effect. Thus, the high conversion state theory and its effect on the competitive adsorption behavior over the catalyst therefore explains the performance difference between the light-off and molar ratio experiments.

In the light-off experiment, it was only operated by increasing the operating temperature from 350 to 500 °C, namely, from a low conversion state to high conversion state. Since the hysteresis phenomenon was observed by switching high temperature (ignition) and low temperature (extinction) operations [67], it can be applied to reach a high methane conversion even at a relative low temperature level, i.e., by first working at a high temperature region and then changing back [67]. However, this was not tested in the light-off experiment. Moreover, it is not clear about the duration of such high conversion state that can be maintained before extinction, which is beyond the current research scope and will be considered in our future studies.

Table 4.3

Comparison between the light-off experiment and the molar ratio experiment over the single-layer 3 wt% Pt/γ-Al$_2$O$_3$ catalyst in the microreactor.

Φ	X_{CH_4} in the light-off experiment [a]		X_{CH_4} in the molar ratio experiments [b]	
	400 °C	450 °C	400 °C	450 °C
2	11.33	32.44	25.42	39.98
5	12.40	27.12	39.35	55.00

[a] Conditions are shown in Fig. 4.4. [b] Conditions are shown in Fig. 4.5.

In this work, the reaction temperature is simply assumed as the oven temperature. In reality, the temperature inside the microreactor (i.e., in the gas mixture and over the catalyst surface) could be (much) higher than the oven temperature, due to the strongly exothermic nature of the methane combustion reaction. This has been partially revealed in our previous study with a plate-type multichannel microreactor [41], where a non-uniform temperature distribution was found in the microreactor and the reaction front (characterized by the presence of a temperature maximum) could shift from the inlet towards downstream at an increased total flow rate or oxygen to methane molar ratio. A similar trend was observed in the current capillary microreactor. As shown in Fig. 4.7, the gas temperatures measured at the microreactor inlet and outlet were found to be 470.4 °C and 472.6 °C (with an oven operational temperature of 450 °C) at Φ = 0.5, and to be 445.5 °C and 466.3 °C at Φ = 5, respectively. The difference in the inlet gas temperature shows that the reaction front moved further towards downstream of the microreactor with increasing oxygen concentration in the feed gas. In more details, at Φ = 0.5, the temperature in the front part of the microreactor significantly increased due to the released combustion reaction heat, with a little further increase of the gas temperature at outlet, indicating that the location of the reaction front was at or near the inlet. However, at Φ = 5, the gas temperature only slightly increased at the inlet and experienced a somewhat more significant increase at the outlet. The majority of methane was thus converted at the downstream of the microreactor, producing a larger temperature difference between the inlet and outlet at Φ = 5. It has to be noted that the temperature reported in this work was only measured at the inlet and outlet of the gas stream, and the tips of thermocouples did not touch the catalyst surface. The actual temperature of catalyst surface should be much higher than these measurements [41].
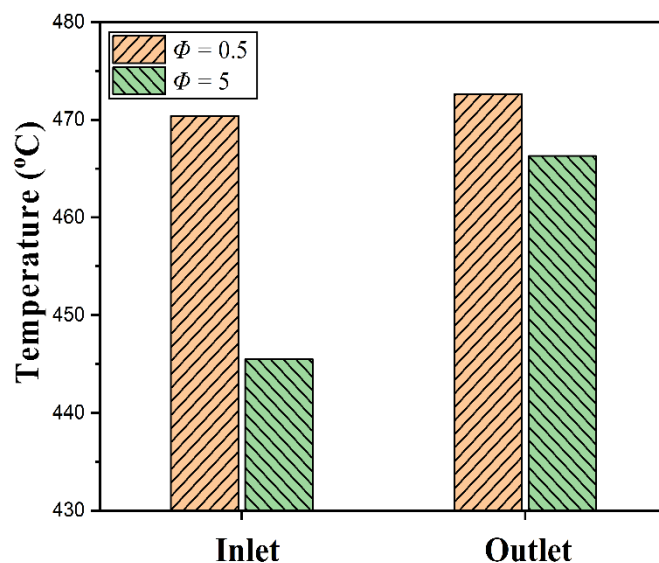
Fig. 4.7. Axial temperature profile along the capillary microreactor over the single-layer 3 wt% Pt/γ-Al$_2$O$_3$ catalyst (cf. entry 6 in Table 4.1). Conditions: T = 450 °C, Φ = 0.5 and 5, other conditions are the same as shown in Fig. 4.5.

4.3.1.3 Effect of total flow rate

The methane conversion in the microreactor as a function of the total flow rate over the single-layer catalyst (with Pd loadings of 1.5 – 4.5 wt%) is displayed in Fig. 4.8. An obvious decrease in the methane conversion was observed when increasing the total flow rate, as a result of the reduced residence time (Eq. (4.4)). For all flow rates studied (Q_{tot} = 30 - 100 mL min^{-1}) at 400 °C, a higher Pt loading gave rise to a higher methane conversion due to the enhanced catalytic activity. The decrease of the methane conversion tends to become indiscernible at sufficiently high flow rates. This could be explained by the significantly improved external mass transfer that compensated the methane conversion decrease from the shortened residence time. In more detail, under prevailing laminar flow conditions (also relevant to the current experiments), the external gas-solid mass transfer inside channels was usually found to increase somewhat significantly with the increasing flow rate (or more generally the Reynolds number) [50]. Moreover, it seems that such insignificant decrease of the methane conversion started at a larger total flow rate when increasing the Pt loading (e.g., from 1.5 to 3 wt% and further on to 4.5 wt%). This is likely due to the higher kinetic rate present at a higher Pt loading, making the mass transfer more easily limited, and thus a higher flow rate is required to improve the external mass transfer in order to sufficiently compensate the conversion loss. Herein, a

further increase of the methane conversion could be reached by increasing the operational temperature, as shown in the figure for the 3 wt% loading case at 450 °C.
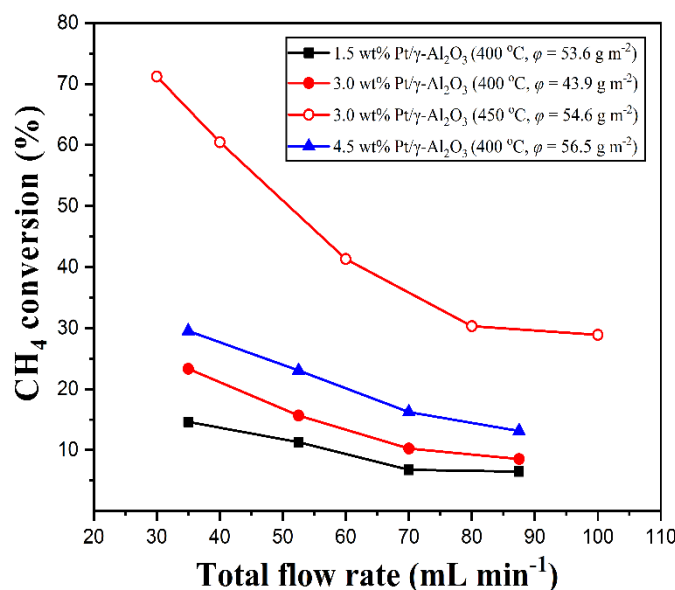
Fig. 4.8. Methane conversion as a function of the total flow rate under different Pt loadings over the single-layer Pt/γ-Al₂O₃ catalyst in the microreactor. Conditions: T = 400 and 450 °C, Φ = 2, Q_{tot} = 30 - 100 mL min⁻¹, τ = 1.00 s - 3.32 s, Pt loading from 1.5 to 4.5 wt% (cf. entries 1, 4, 5 and 7 in Table 4.1).

The methane conversion in the microreactor (with the single-layer 3 wt% Pt/γ-Al₂O₃) as a function of the reaction temperature (350 – 500 °C) under different flow rates is further depicted in Fig. 4.9. It is particularly noticed that at a total flow rate of 47.5 or 65.0 mL min⁻¹, a seemingly exponential increase in the methane conversion was found upon increasing the temperature from 350 to 500 °C. This is in contrast to a more or less linear conversion increase at the total flow rate of 30.0 mL min⁻¹. At such a lower flow rate, the external mass transfer tended to have a more significant influence, which was improved with temperature rise due to mainly the increased gaseous diffusivity of oxygen and methane (e.g., proportional with $T^{1.75}$ [69,70]) At higher flow rates, the external mass transfer was improved and the intrinsic kinetic rate (increasing exponentially with temperature according to the Arrhenius equation) played a more important role in determining the overall flow rate. Thus, under these circumstances, the methane conversion shows more like an exponential increase with temperature.
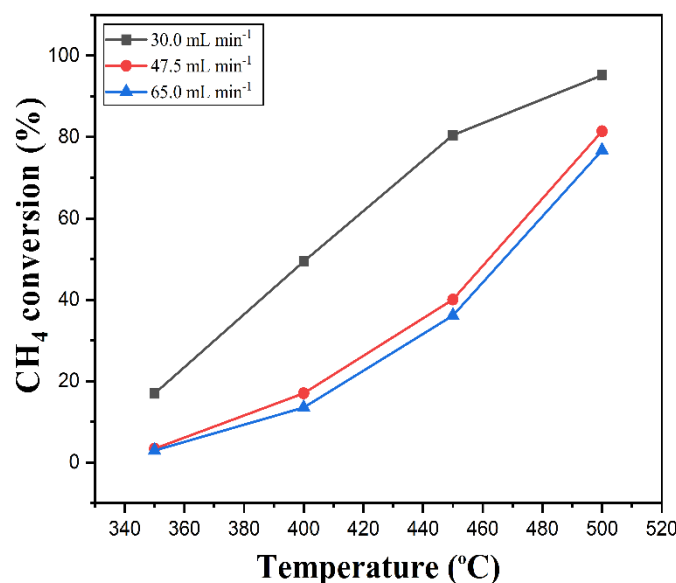
Fig. 4.9. Methane conversion as a function of the reaction temperature under different flow rates over the single-layer 3 wt% Pt/γ-Al$_2$O$_3$ catalyst (cf. entry 3 in Table 4.1) in the microreactor. Conditions: T = 350 - 500 °C, Φ = 2, Q_{tot} = 30 - 65 mL min^{-1}, τ = 1.53 - 3.32 s.

4.3.2. Reaction performance of the multi-layer Pt/γ-Al$_2$O$_3$ catalyst system

To further investigate the influence of internal diffusion within the coating layer, the multi-layer catalyst coatings were prepared inside the capillary microreactor. Two different cases of multi-layer Pt/γ-Al$_2$O$_3$ catalysts were designed (Fig. 4.2). The influence of temperature and molar ratio of O$_2$ to CH$_4$ was investigated in these two cases for the CMC and compared with the single-layer counterpart.

4.3.2.1 Effect of temperature

Fig. 4.10 compares the methane conversion at different temperatures between the single-layer (with 1.5 wt%, 3 wt% and 4.5 wt% Pt/γ-Al$_2$O$_3$) and double-layer (with 1.5 wt% and 2.25 wt% Pt/γ-Al$_2$O$_3$) system at Φ = 2. Case 1 was produced with the double-layer system of 1.5 or 2.25 wt% Pt loading to compare with the respective single-layer 3 or 4.5 wt% Pt loading system. The double-layer system of 1.5 wt% Pt loading also represents case 2 in relation to the single-layer system of 1.5 wt% Pt loading. For case 1, the total Pt mass of the double-layer and respective single-layer systems is theoretically consistent, and thus the Pd loading in the double-layer system is assumed half of that in the single-layer system. As for case 2, the total Pt loading in the double-layer and respective single-layer systems is theoretically identical, and thus the total Pt mass of the double-layer system is assumed twice of that in the single-layer system. For both

cases, the double-layer system is assumed to have a coating thickness around twice of that in the respective single-layer system (as also indicated by an almost doubled φ value in the former system; Table 4.1). The actual Pt loading in both layer systems could be found from the selected results of ICP-OES in Table 4.1. The actual Pt loading is about 6% to 13% lower than the theoretical one (i.e., estimated according to the preparation conditions), which could be due to the uncertainties associated with the experimental coating procedures. Such relatively low deviation also corroborates the reliability of the current coating preparation method.

Given the more significant internal diffusion limitation caused by thicker coating layers (with equal Pt mass), the double-layer system in case 1 tends to yield a lower methane conversion than the respective single-layer system. This trend is seen in Fig. 4.10 when one compares the methane conversion of the double-layer (with 1.5 or 2.25 wt% Pt/γ-Al$_2$O$_3$) system with that of the corresponding single-layer (with 3 or 4 wt% catalyst) system, especially at a relatively high operational temperature (e.g., > 400 or 450 ^{o}C) where the reaction is likely more limited by the (external and internal) mass transfer. At a relatively low temperature, the reaction tended to be controlled by kinetics, thus the conversion difference between the double-layer and respective single-layer systems is not pronounced.

A further comparsion between the double-layer (with 1.5 wt% Pt/γ-Al$_2$O$_3$) system in case 2 with the corresponding single-layer (with 1.5 wt% catalyst) system reveals a higher methane coversion in the former system, especially at temperatures above ca. 400 ^{o}C (Fig. 4.10). In case 2, the Pt loading (and thus mass) in each layer is the same as that of the single-layer system. Thus, the above results indicate that in case 2 besides the top coating layer, the bottom layer is also quite active in the reaction given the large increase of the methane conversion in the double-layer system (e.g., being 61.5% at 500 ^{o}C compared with 37.5% in the single-layer system). Another implication is that there is not a severe internal diffusion limitation in the single-layer system. In other words, the reactant could still diffusive through the coating to reach the inner surface of the pores (especially those near the microreactor wall), leading to the presence of non-zero reactant concentrations therein. Otherwise, the bottom layer in case 2 would not function actively in the reaction. This further suggests that although the coating thickness is thicker in case 2, the reaction rate seems to be more limited by the catalyst amount than the internal diffusion. The fact that the improved conversion in case 2 is more pronounced at relatively high temperature levels could be explained by the more significantly increased intrinsic kinetic rate therein. At relatively low temperature levels, the kinetic rate already became so slow controlling the overall reaction rate that essentially no conversion difference

existed in both the double- and single-layer systems.

Fig. 4.10 also correctly reflects the positive effect of increasing the Pt loading (or mass) on the reaction performance improvement, as supported by the increased methane conversion when the Pt loading was changed from 1.5 wt% all the way up to 4.5 wt% in the single-layer system, and from 1.5 wt% to 2.25 wt% in the double layer system.
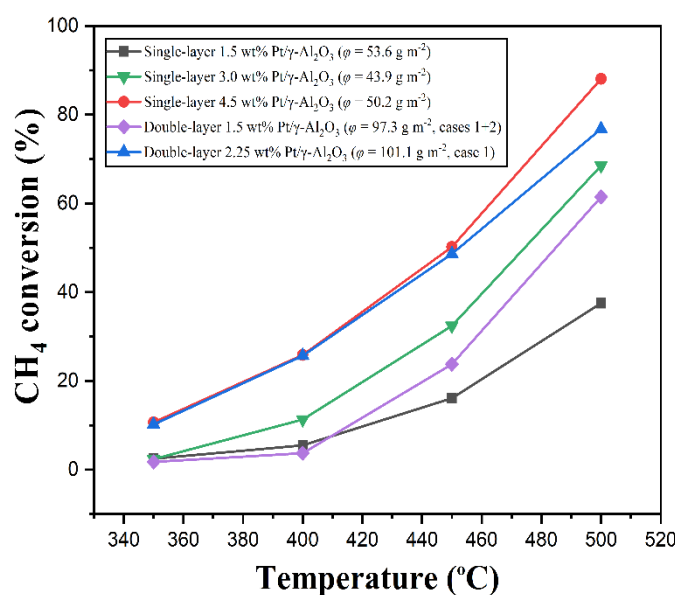
Fig. 4.10. Methane conversion as a function of the reaction temperature over the single-layer (with 1.5 wt%, 3 wt% and 4.5 wt% Pt/γ-Al$_2$O$_3$) and double-layer (with 1.5 wt% (cases 1 + 2) and 2.25 wt% (case 2) catalyst) systems in the microreactor. Conditions: T = 350 - 500 $^{\circ}$C, Φ = 2, Q_{tot} = 70 mL min^{-1}, τ = 1.42 s. The single-layer systems correspond with entries 1, 5 and 8 in Table 4.1, and the double-layer systems with entries 9 and 11 in Table 4.1.

The above discussions are limited to qualitative analysis, since it is not possible to directly quantify the rates of surface reaction and internal diffusion within the coating in the current experiment. It is reported that the internal diffusion rate is directly correlated to particle properties (e.g., size, pore structure and tortuosity). A small particle size facilitates more reactants to access the interior of the catalyst and is characterized by a low value of Thieles modulus (defined as the ratio of the surface reaction rate to the internal diffusion rate), so that catalyst and the surface reaction rate tends to be limiting [71]. Similarly, for thicker coatings in the double-layer system, an increased diffusion path is expected. Moreover, in, the repetitive coating procedures in cases 1 and 2 might cause the pore structure of the bottom coating layer to be modified to some extent by another coating layer on the top. These eventually may result

in an increase of the internal diffusion resistance within the (bottom layer of) coating. However, selected BET analyses have revealed no significant surface area or pore volume change of the catalyst in the double-layer system as compared with its single-layer counterpart, as indicated in Table 4.B.1 of the appendix. Thus, a more detailed study concerning the impact of the double-layer and single-layer systems on the coating structure and the diffusion/reaction behavior therein is still needed for an in-depth elucidation of the current experimental results. In addition, given the strongly exothermic nature of the methane combustion reaction, the adiabatic temperature rise is estimated ca. 2000 ^{o}C at Φ = 2 [72]. Thus, the external surface temperature of the catalyst could be much higher than that inside the catalyst, and with that a much higher reaction rate may be facilitated at the exterior of the catalyst. Such temperature effect should be also well taken into account in the analysis of diffusion/reaction behavior within the coating layer.

The impact of using single-layer and multi-layer catalyst systems on the methane conversion under methane-rich conditions (Φ = 1) is shown in Fig. 4.11. The multi-layer (double-/triple-layer) systems here are according to case 2, and were produced by maintaining the theorteically idential Pt loading (3.5 wt%) as that in the corresponding single-layer system. A generally insignificant difference in the methane conversion was found between the single-layer and double/triple-layer systems under the tempearture tested (350 – 500 ^{o}C). As shown in Fig. 4.10 (Φ = 2), a higher methane conversion for the double-layer stystem in case 2 could be obtained than that of the single-layer system, due to more Pt avaiable despite the thicker catalyst coating layer. The insignificant conversion difference noticed here at Φ = 1 is thus mainly due to the insufficient oxygen supply as the dominant factor to limit the adsorbed methane to be further converted some slight conversion difference could be due to the experimental uncertainties inccurred in either the coating preparation or reaction testing).
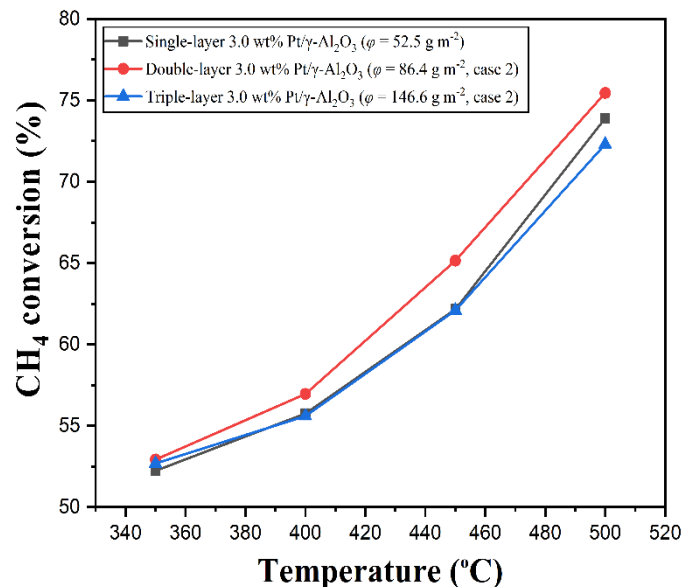
Fig. 4.11. Methane conversion as a function of the reaction temperature over the single-layer system and double-/triple-layer systems (case 2) in the microreactor. Conditions: T = 350 °C - 500 °C, Φ = 1, Q_{tot} = 70 mL min^{-1}, τ = 1.42 s, 3 wt% Pt/γ-Al$_2$O$_3$. The single-layer system corresponds with entry 2 in Table 4.1 and the multiple-layer systems with entries 12 and 13 in Table 4.1.

4.3.2.2 Effect of molar ratio of O$_2$ to CH$_4$

The methane conversion as a function of Φ for the single-layer and multi-layer (double-/triple-layer; case 2) 3 wt% Pt/γ-Al$_2$O$_3$ catalyst systems was investigated by maintaining the flow rate at 70 mL min^{-1} and operational temperature at 400 °C (Fig. 4.12). The methane conversion for the multi-layer catalyst system presented a significant increase in the order: Φ = 1 > Φ = 5 > Φ = 2, which is in line with the results demonstrated in the molar ratio experiment for the single-layer system (Fig. 4.5). This proves that the multi-layer system as a whole functioned well. There only exists a minor conversion difference at Φ = 1 for the single-, double-, and triple-layer systems, since the insufficient oxygen supply is limiting factor (as already presented in Fig. 4.11 above). At Φ = 2 and 5, the methane conversion was found to generally increase when the number of coating layer was further increased in case 2 (if one neglects the local anomaly present at Φ = 5, which might be due to experimental error). This finding is consistent with the results of Fig. 4.10 according to which a higher methane conversion could be obtained in the multi-layer system in case 2 than that in the single-layer system. Thus, it can be also assumed in both the double- and triple-layer systems, all coating layers (actively) contributed to the reaction.
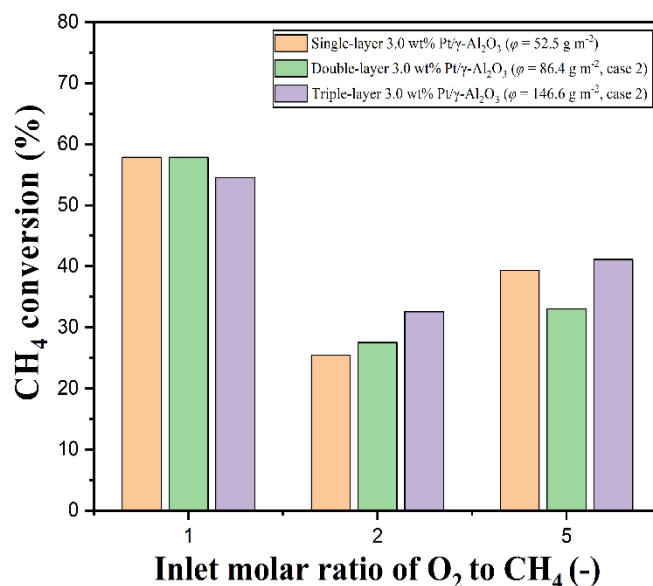
Fig. 4.12. Methane conversion as a function of Φ over the different catalyst layer systems in the miroreactor. Conditions: T = 400 °C, Φ = 1, 2 and 5, Q_{tot} = 70 mL min^{-1}, τ = 1.42 s. 3 wt% Pt/γ-Al$_2$O$_3$. The single-layer system corresponds with entry 2 in Table 4.1 and the multiple-layer systems with entries 12 and 13 in Table 4.1.

4.3.3. Catalyst stability

The catalyst stability under reaction conditions was tested in a span of 5 days over the single-layer 4.5 wt% Pt/γ-Al$_2$O$_3$ catalyst system in the microreactor (Fig. 4.13). The test was conducted at a total flow rate of 70 mL min^{-1} under 500 °C and Φ = 2, which consisted of each daily run for 6 hours, with the reaction being stopped in between, until five days' data were collected. The methane conversion was found at the highest level in the first 6 h (the average value being 86.4%), and the lowest was in the last 6 h (the average value being 79.3%). Thus, there is a gradual catalyst activity loss (indicated by ca. 7% conversion drop over a reaction time of 30 h). As Fig. 4.14 reveals, a considerable difference in the light-off curve was found when comparing the fresh catalyst (time on stream at 0 h) and aged catalyst (times on stream at 35 h and 40 h), with the more aged catalyst requiring a higher T_{50} value. A possible reason for catalyst activity loss is the catalyst sintering and the formation of less active species (PtO$_2$) during the reaction [9,73,74]. An aged catalyst probably resulted in the structural changes (e.g., Pt particle size, pores narrowing/blockages), which could further affect mass transfer within the coating layer and kinetics. Thus, an improved catalyst preparation method is required to enhance the catalyst stability. The above results also indicate that the coating adhesion on the microreactor wall was

strong enough under the applied reaction conditions, though the adhesion test using (possibly harsh) ultrasonic treatment caused a relatively large weight loss percentage of the coating and the SEM-EDS analysis seems to suggest some local structure imperfection in the coating (cf. Appendix 4.C for more details and discussion).
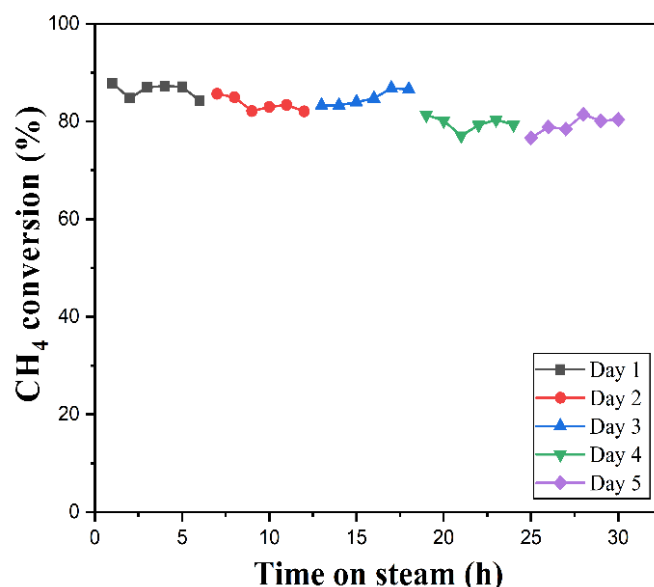
Fig. 4.13. Catalyst stability over the single-layer 4.5 wt% Pt/γ-Al$_2$O$_3$ catalyst system (cf. entry 8 in Table 4.1) in the microreactor. Conditions: T = 500 ^{o}C, Φ = 2, Q_{tot} = 70 mL min^{-1}, τ = 1.42 s.
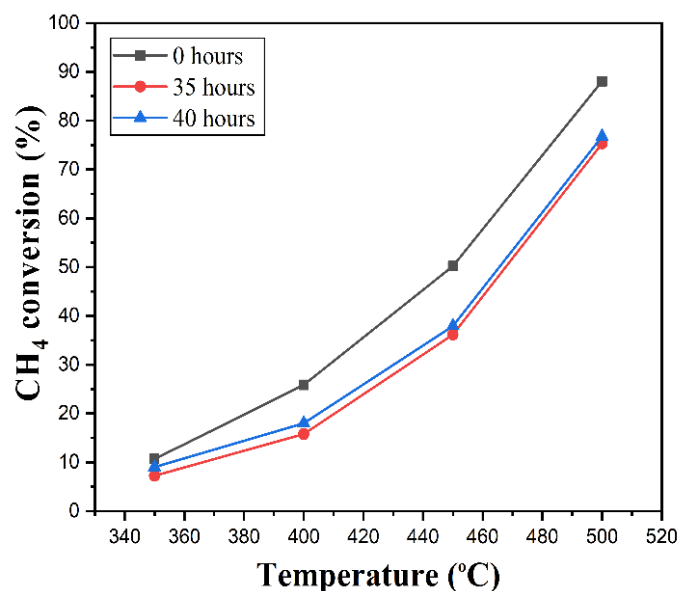
Fig. 4.14. Methane conversion at a function of the reaction temperature in the single-layer system with different catalyst ages in the microreactor. Conditions: T = 350 - 500 ^{o}C, Φ = 2, Q_{tot} = 70 mL min^{-1}, τ = 1.42 s, 4.5 wt% Pt/γ-Al$_2$O$_3$ (cf. entry 8 in Table 4.1).

4.4. Conclusions

In this work, the dynamic slug flow method was used to washcoat Pt/γ-Al$_2$O$_3$ catalyst in the capillary microreactor (made of stainless steel) in one step. Both the single- and multi-layer catalyst coating systems were prepared and tested for the catalytic methane combustion. Two different cases were designed in the multi-layer system. In case 1, the total weight of Pt in the multi-layer system was maintained theoretically the same as that in the respective single-layer system. In case 2, the theoretical Pt loading in the multi-layer system was kept identical to the single-layer system. For both cases, the coating thickness was assumed to increase proportionally with the number of layers coated.

For the single-layer system, the effect of the reaction temperature, molar ratio of O$_2$ to CH$_4$ (Φ), and total mixture flow rate was investigated over catalysts with different Pt loadings. A best methane conversion of 95.17% could be obtained under 500 ^{o}C at 30 mL min^{-1} and Φ = 2. The light-off curves exhibited a remarkable increase in the methane conversion as increasing Pt loading from 1.5 wt% to 4.5 wt% at Φ = 2 and 5, especially at relatively high temperatures (above ca. 400 ^{o}C). A lower methane conversion at Φ = 5 could be attributed to the increased competitive adsorption of reactants, where the predominantly adsorbed oxygen could prevent the weakly adsorbed methane over the catalyst surface for its further conversion. The increment of the methane conversion with increasing Pt loading tended to slow down, possibly due to the more significant internal diffusion limitation in the coating given the increased kinetic rate. A higher methane conversion was found in the molar ratio experiment than that in the light-off experiment under otherwise identical conditions possibly due to the hysteresis effect, since the high conversion state can be maintained by varying the molar ratio of O$_2$ to CH$_4$ in the experiment at a relatively high temperature level. A decrease of the methane conversion was found for each Pt loading upon increasing the total mixture flow rate due to the reduced residence time, though it became insignificant at sufficiently high flow rates at which the external mass transfer could be largely improved to compensate the conversion loss. In addition, a slight catalyst activity decrease over time was noticed. Thus, the catalyst preparation method in microreactors still needs further improvement.

The multi-layer (or more specifically, double-layer) system in case 1 was found to yield a lower methane conversion at Φ =2 and 5 than the respective single-layer system, possibly due to the increased internal diffusion resistance in the thicker coating layer. For case 2, the multi-layer (or more specifically, double- and triple-layer) system generally exhibited a higher methane conversion at Φ = 2 and 5 than the corresponding single-layer system, indicating the (active)

participation of all coating layers (instead of the top layer alone) in the reaction. This suggests that in case 2, the reaction rate tends to be more limited by the catalyst amount than the internal diffusion. The methane conversion is nearly identical between the single-, double- and triple-layer systems at Φ = 1 thoughout the temperature range of 350 to 500 ℃, due to the reaction rate being mainly limited by the insuffieinct oxygen supply.

The above findings may provide useful guidelines in the catalyst coating preparation and microreactor operation for the catalyst methane combustion. However, further studies of the reactant transport within the coating (as a function of local temperature profile and coating properties), reaction kinetics and mechanisms, are still required for a more in-depth understanding of the reaction behavior in microreactors.

Appendix 4.A

Influence of temperature on the residence time

The residence time in this work was calculated based on the total mixture flow rate at 20 ℃ and 1 atm (cf. Eq. (4.4)). Under the reaction conditions, the actual residence time is shorter due to the increased temperature, as shown in Table 4.A.1.

Table 4.A.1. Comparisons of the mean residence time as a function of the reaction temperature.

Reaction temperature (℃)	Total flow rate [a] (mL min^{-1})	Mean residence time [b] (s)	
		At 20 ℃	At the reaction temperature
350	70	1.42	0.67
400	70	1.42	0.62
450	70	1.42	0.58
500	70	1.42	0.54

[a] Based on 20 ℃ and 1 atm.

[b] Calculated with Eq. (4.4), assuming 1 atm pressure and the ideal gas behavior.

Appendix 4.B

BET analyses of the coated catalyst after reaction

The specific surface area of Pt/γ-Al$_2$O$_3$ catalyst coated in the capillary microreactor was measured after reaction, as presented in Table 4.B.1. No clear relation could be found between the Pt loading and the BET surface area or the pore volume/size. In all tested cases, the catalyst with a 3 wt% Pt loading provided the highest surface area. It might be due to the favorable catalyst structure (e.g., pore size and volume) formed therein with γ-Al$_2$O$_3$ as support. However, this is not conclusive since the evidence from such limited BET analyses is still insufficient. As the catalysts characterized here were after reaction uses for certain hours and scrapped from the microreactor surface, a small difference in the surface area and pore characteristics likely occurred as a result of the variation of different operational conditions, as also revealed in this table. However, the general similarity in these analysis results corroborates the good reproducibility of the catalyst coating procedures in both single- and double -layer systems with different Pt loadings.

Table 4.B.1

Summary of BET analyses for different used catalysts.

Entry [a]	Pt loading (wt%) [b]	φ (g m^{-2})	Catalyst age (h) [c]	BET surface area (m^2 g^{-1})	Pore volume (cm^3 g^{-1})	Pore size (nm)
1	1.5	53.6	25	74.34	0.459	24.71
5	3	43.9	18	92.28	0.643	27.88
7	4.5	56.5	25	78.49	0.482	24.56
11	2.25	101.1	8	81.42	0.458	22.51

[a] Corresponding with Table 4.1. [b] According to the preparation conditions; calculated based on the slurry composition and the dry weight of the obtained coating. [c] Time spent in the CMC reaction test.

Coating adhesion Test

In order to simplify the coating procedure, the one-step approach was used in this work to washcoat a mixture of the alumina slurry and $Pt(NH_3)_4(NO_3)_2$ solution under dynamic slug flow inside the capillary microreactor (cf. Section 2.2.2). The adhesion of the prepared $Pt/\gamma\text{-}Al_2O_3$ catalytic coating was investigated by measuring its weight loss in the ultrasonic test (cf. details in Section 2.4). The results are presented in Table 4.C.1. It seems that the addition of $Pt(NH_3)_4(NO_3)_2$ solution into the alumina slurry improved the coating adhesion onto the microreactor wall when comparing the adhesion test results of $\gamma\text{-}Al_2O_3$ alone and $Pt/\gamma\text{-}Al_2O_3$ catalyst. However, a high weight loss percentage was observed after ultrasonic tests, which amounts to be as high as 100% in the case of the single-layer 1.5 wt% $Pt/\gamma\text{-}Al_2O_3$ catalyst after 3 h in ultrasonic bath.

Despite this, it appears that the adhesion of the catalyst coating is strong enough under the applied reaction conditions, as a good catalytic activity could be sustained over long hours of operation (cf. Fig. 4.13). This is also supported by the fact that no signs of catalyst loss could be noticed when comparing the reactor weight before and after the reaction testing.

Table 4.C.1

Adhesion test of $Pt/\gamma\text{-}Al_2O_3$ washcoated catalyst on the stainless steel capillary microreactor.

Pt loading (wt%)	Initial mass of catalyst (g)	Total mass loss of catalyst (g)			Final mass of catalyst (g)	Weight loss percentage at 3 h (wt%)
		1 h [a]	2 h [a]	3 h [a]		
4.5 [b]	0.0817	0.0487	0.0553	0.0633	0.0181	77.8
1.5 [c]	0.1934	0.1740	0.1948	0.1985	0	100
0 [e]	0.0414	0.0289	0.0311	0.0328	0.0086	79.3
0 [e]	0.0433	0.0249	0.0260	0.0273	0.0201	63.0
3 [f]	0.0400	0.0097	0.0170	0.0199	0.0291	49.8
3 [f]	0.0404	0.0131	0.0139	0.0158	0.0246	39.1

[a] Ultrasonic bath time.

[b] Used catalyst after reaction (ca. 15 h on stream), cf. entry 7 in Table .4.1.

[c] Fresh catalyst, cf. entry 10 in Table 4.1.

[e] It refers to the γ-Al$_2$O$_3$ support and the length of capillary microreactor is 50 mm.

[f] Fresh catalyst and the length of capillary microreactor is 50 mm.

Fig. 4.C.1 presents the SEM-EDS analysis results of the triple-layer 3 wt% Pt/γ-Al$_2$O$_3$ catalyst. As shown in the SEM image (Fig. 4.C.1a), some internal cracks and disconnection between the catalyst and the microreactor wall could be clearly observed. Although these imperfections of the coating layer on the microreactor seem to not affect the reaction performance during the short time on stream tested in this work, the coating method needs to be improved (e.g., in the coating step and/or the thermal treatment) in order to keep a better coating integrity for its long-term durability. The EDS spectrum illustrates the presence of a thin layer of iron oxide over the microreactor surface (Figs. 4.C.1b and 4.C.1c). It was likely generated during the thermal pre-treatment of the microreactor at 900 °C for 10 h (cf. Section 2.2.2). Such oxide layer could function as a strong bonding with the catalyst coating layer, at least under the reaction conditions tested in this work.

Element	Weight %	Atomic %	Net Int.	Error %	Kratio	Z	A	F
Ti L	10.09	5.66	597.81	5.18	0.1105	0.8849	1.2381	1.0000
O K	42.04	70.60	21259.41	5.46	0.3179	1.1693	0.6486	1.0000
Fe L	23.26	11.19	2453.71	7.33	0.0987	0.8723	0.4865	1.0000
Ni L	6.53	2.99	869.03	7.81	0.0311	0.8832	0.5392	1.0000
Si K	0.52	0.50	235.28	8.49	0.0045	1.0446	0.8307	1.0031
Cr K	17.56	9.07	1048.85	5.65	0.1620	0.8593	0.9970	1.0769
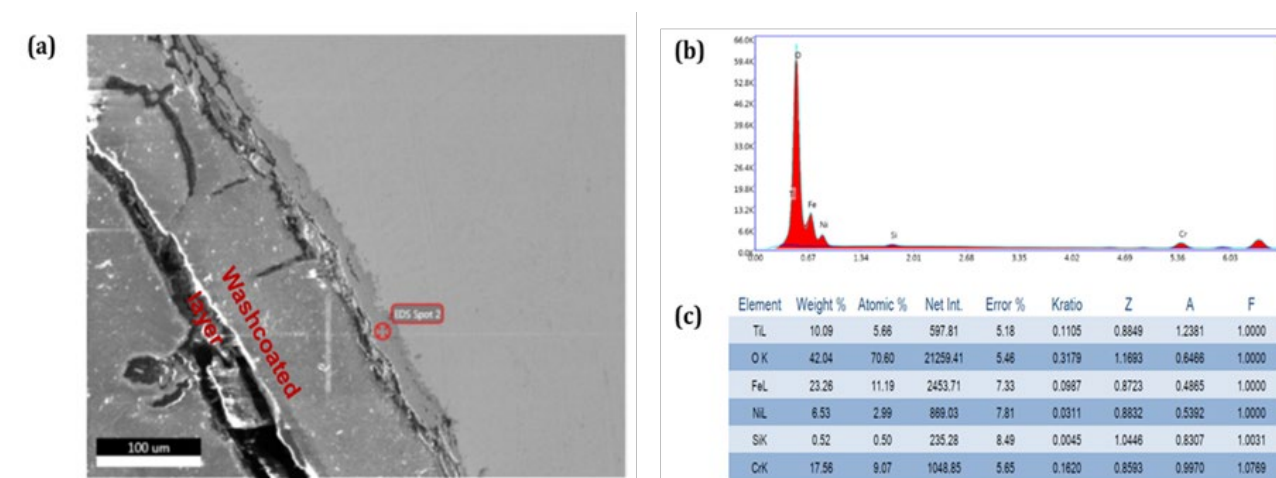
Fig. 4.C.1. Results of SEM-EDS annlysis for the triple-layer system with 3 wt% Pt/γ-Al$_2$O$_3$ catalyst (cf. entry 13 in Table 4.1). (a) SEM images, (b) EDS spectrum, (c) eZAF smart quant results.

The above results also suggest that the ultrasonic treatment herein might be a rather harsh procedure to test the adhesion of the catalytic coating prepared in 316 L stainless steel microreactor using the current one-step coating method. On the other hand, this ultrasonic treatment offers a convenient way for the catalyst removal from the microreactor, which opens up opportunities to recycle the deactivated/used catalyst and reuse the microreactors [75].

References

[1]   B. Durand, Petroleum, natural gas and coal: Nature, formation mechanisms, future prospects in the energy transition, EDP sciences, 101-152, 2019.

[2]   S.N. Naik, V.V. Goud, P.K. Rout, A.K. Dalai, Production of first and second generation biofuels: a comprehensive review, Renew Sust Energ Rev. 14 (2010) 578-597. https://doi.org/10.1016/j.rser.2009.10.003.

[3]   H. Li, E. Larsson, E. Thorin, E. Dahlquist, X. Yu, Feasibility study on combining anaerobic digestion and biomass gasification to increase the production of biomethane, Energy Convers. Manage. 100 (2015) 212-219. https://doi.org/10.1016/j.enconman.2015.05.007.

[4]   S. Sansaniwal, M. Rosen, S. Tyagi, Global challenges in the sustainable development of biomass gasification: an overview, Renew Sust Energ Rev. 80 (2017) 23-43. https://doi.org/10.1016/j.rser.2017.05.215.

[5]   R. Zwart, H. Boerrigter, E. Deurwaarder, C. Van der Meijden, S. Van Paasen. Production of synthetic natural gas (SNG) from biomass, http://www.ecn.nl/docs/library/report/2006/e06018.pdf; 2006 [Accessed 3 June 2013].

[6]   C.R. Vitasari, M. Jurascik, K.J. Ptasinski, Exergy analysis of biomass-to-synthetic natural gas (SNG) process via indirect gasification of various biomass feedstock, Energy. 36 (2011) 3825-3837. https://doi.org/10.1016/j.energy.2010.09.026.

[7]   G. Karavalakis, T.D. Durbin, M. Villela, J.W. Miller, Air pollutant emissions of light-duty vehicles operating on various natural gas compositions, J Nat. Gas Sci. Eng,. 4 (2012) 8-16. https://doi.org/10.1016/j.jngse.2011.08.005.

[8]   J. Chen, H. Arandiyan, X. Gao, J. Li, Recent advances in catalysts for methane combustion, Catal. Surv. Asia. 19 (2015) 140-171. https://doi.org/10.1007/s10563-015-9191-5.

[9]   J.H. Lee, D.L. Trimm, Catalytic combustion of methane, Fuel Process. Technol. 42 (1995) 339-359. http://doi.org/10.1016/0378-3820(94)00091-7.

[10]   R.J. Farrauto, Low-temperature oxidation of methane, Science. 337 (2012) 659-660. https://doi.org/10.1126/science.1226310.

[11]   P. Gélin, L. Urfels, M. Primet, E. Tena, Complete oxidation of methane at low temperature over Pt and Pd catalysts for the abatement of lean-burn natural gas fuelled vehicles emissions: influence of water and sulphur containing compounds, Catal. Today. 83 (2003) 45-57. http://dx.doi.org/10.1016/s0920-5861(03)00215-3.

[12]   P. Forzatti, Status and perspectives of catalytic combustion for gas turbines, Catal. Today. 83 (2003) 3-18. http://dx.doi.org/10.1016/s0920-5861(03)00211-6.

[13]   T.M. Gür, Comprehensive review of methane conversion in solid oxide fuel cells: prospects for efficient electricity generation from natural gas, Prog. Energy Combust. Sci. 54 (2016) 1-64. https://doi.org/10.1016/j.pecs.2015.10.004.

[14]   S.R. Vaillant, A.S. Gastec, Catalytic combustion in a domestic natural gas burner, Catal. Today. 47 (1999) 415-420. http://dx.doi.org/10.1016/S0920-5861(98)00324-1.

[15]   P. Gélin, M. Primet, Complete oxidation of methane at low temperature over noble metal based catalysts: a review, Appl. Catal., B. 39 (2002) 1-37. http://dx.doi.org/10.1016/S0926-3373(02)00076-0.

[16]   S.B. T.V. Choudhary, V.R. Choudhary, Catalysts for combustion of methane and lower alkanes review, Appl. Catal. A. 234 (2002) 1-23. https://doi.org/10.1016/S0926-860X(02)00231-4.

[17]   D. Ciuparu, M.R. Lyubovsky, E. Altman, L.D. Pfefferle, A. Datye, Catalytic combustion of methane over palladium-based catalysts, Catal. Rev. 44 (2002) 593-649. https://doi.org/10.1081/CR-120015482.

[18]   Z. Li, G.B. Hoflund, A review on complete oxidation of methane at low temperatures, J. Nat. Gas Chem. 12 (2003) 153-160.

[19]   L. He, Y. Fan, J. Bellettre, J. Yue, L. Luo, A review on catalytic methane combustion at low temperatures: Catalysts, mechanisms, reaction conditions and reactor designs, Renew Sust Energ Rev. (2019) 109589.

[20]   R.J. Farrauto, M. Hobson, T. Kennelly, E. Waterman, Catalytic chemistry of supported palladium for combustion of methane, Appl. Catal. A. 81 (1992) 227-237. https://doi.org/10.1016/0926-860X(92)80095-T.

[21]   D. Wang, J. Gong, J. Luo, J. Li, K. Kamasamudram, N. Currier, A. Yezerets, Distinct reaction pathways of methane oxidation on different oxidation states over Pd-based three-way catalyst (TWC), Appl. Catal. A. 572 (2019) 44-50. https://doi.org/10.1016/j.apcata.2018.12.022.

[22]   I.E. Beck, V.I. Bukhtiyarov, I.Y. Pakharukov, V.I. Zaikovsky, V.V. Kriventsov, V.N. Parmon, Platinum nanoparticles on Al_2O_3: Correlation between the particle size and activity in total methane oxidation, J. Catal. 268 (2009) 60-67. https://doi.org/10.1016/j.jcat.2009.09.001.

[23]   C.-P. Hwang, C.-T. Yeh, Platinum-Oxide Species Formed on Progressive Oxidation of Platinum Crystallites Supported on Silica and Silica–Alumina, J. Catal. 182 (1999) 48-55. http://dx.doi.org/10.1006/jcat.1998.2304.

[24]   R. Burch, P.K. Loader, Investigation of Pt/Al_2O_3 and Pd/Al_2O_3 catalysts for the combustion of methane at

low concentrations, Appl. Catal., B. 5 (1994) 149-164. http://dx.doi.org/10.1016/0926-3373(94)00037-9.

[25]   K. Persson, K. Jansson, S. Jaras, Characterisation and microstructure of Pd and bimetallic Pd-Pt catalysts during methane oxidation, J. Catal. 245 (2007) 401-414. https://doi.org/10.1016/j.jcat.2006.10.029.

[26]   K. Persson, A. Ersson, A.M. Carrera, J. Jayasuriya, R. Fakhrai, T. Fransson, S. Järås, Supported palladium-platinum catalyst for methane combustion at high pressure, Catal. Today. 100 (2005) 479-483. https://doi.org/10.1016/j.cattod.2004.08.018.

[27]   G. Pecchi, P. Reyes, T. López, R. Gómez, Pd-CeO$_2$ and Pd-La$_2$O$_3$/alumina-supported catalysts: their effect on the catalytic combustion of methane, J. Non-Cryst. Solids. 345 (2004) 624-627. https://doi.org/10.1016/j.jnoncrysol.2004.08.110.

[28]   S. Specchia, E. Finocchio, G. Busca, G. Saracco, V. Specchia, Effect of S-compounds on Pd over LaMnO$_3$·2ZrO$_2$ and CeO$_2$·2ZrO$_2$ catalysts for CH$_4$ combustion, Catal. Today. 143 (2009) 86-93. https://doi.org/10.1016/j.cattod.2008.10.035.

[29]   N. Kinnunen, M. Suvanto, M. Moreno, A. Savimäki, K. Kallinen, T.-J. Kinnunen, T. Pakkanen, Methane oxidation on alumina supported palladium catalysts: effect of Pd precursor and solvent, Appl. Catal. A. 370 (2009) 78-87. https://doi.org/10.1016/j.apcata.2009.09.018.

[30]   R.J. Farrauto, J.K. Lampert, M.C. Hobson, E.M. Waterman, Thermal decomposition and reformation of PdO catalysts; support effects, Appl. Catal., B. 6 (1995) 263-270. https://doi.org/10.1016/0926-3373(95)00015-1.

[31]   L.H. Xiao, K.P. Sun, X.L. Xu, X.N. Li, Low-temperature catalytic combustion of methane over Pd/CeO$_2$ prepared by deposition-precipitation method, Catal. Commun. 6 (2005) 796-801. https://doi.org/10.1016/j.catcom.2005.07.015.

[32]   J. Li, X. Liang, S. Xu, J. Hao, Catalytic performance of manganese cobalt oxides on methane combustion at low temperature, Appl. Catal., B. 90 (2009) 307-312. https://doi.org/10.1016/j.apcatb.2009.03.027.

[33]   Y. Li, J.N. Armor, Catalytic combustion of methane over palladium exchanged zeolites, Appl. Catal., B. 3 (1994) 275-282. https://doi.org/10.1016/0926-3373(94)0006Z-H.

[34]   M. O'Connell, G. Kolb, R. Zapf, Y. Men, V. Hessel, Bimetallic catalysts for the catalytic combustion of methane using microreactor technology, Catal. Today. 144 (2009) 306-311. https://doi.org/10.1016/j.cattod.2008.10.053.

[35]   M. Mundhwa, R.D. Parmar, C.P. Thurgood, A comparative parametric study of a catalytic plate methane reformer coated with segmented and continuous layers of combustion catalyst for hydrogen production, J. Power Sources. 344 (2017) 85-102. http://dx.doi.org/10.1016/j.jpowsour.2017.01.082.

[36]   C.M. Miesse, R.I. Masel, C.D. Jensen, M.A. Shannon, M. Short, Submillimeter-scale combustion, AlChE J. 50 (2004) 3206-3214. https://doi.org/10.1002/aic.10271.

[37]   M.H. Exchangers, Microreactors: new technology for modern chemistry, Weinheim: Wiley/VCH, 2000.

[38]   R. Zapf, C. Becker-Willinger, K. Berresheim, H. Bolz, H. Gnaser, V. Hessel, G. Kolb, P.Löb, A.K. Pannwitt, A. Ziogas, Detailed characterization of various porous alumina-based catalyst coatings within microchannels and their testing for methanol steam reforming, Chem. Eng. Res. Des. 81 (2003) 721-729. https://doi.org/10.1205/026387603322302887.

[39]   N.R. Peela, A. Mubayi, D. Kunzru, Washcoating of γ-alumina on stainless steel microchannels, Catal. Today. 147 (2009) S17-S23. https://doi.org/10.1016/j.cattod.2009.07.026.

[40]   M. Liauw, M. Baerns, R. Broucek, O. Buyevskaya, J. Commenge, J. Corriou, L. Falk, K. Gebauer, H. Hefter, O. Langer, Microreaction Technology: Industrial Prospects. Springer, 2000, pp. 224-234.

[41]   L. He, Y. Fan, L. Luo, J. Bellettre, J. Yue, Preparation of Pt/γ-Al$_2$O$_3$ catalyst coating in microreactors for catalytic methane combustion, Chem. Eng. J. 380 (2020) 122424. https://doi.org/10.1016/j.cej.2019.122424.

[42]   X. Xu, H. Vonk, A. Cybulski, J.A. Moulijn, Alumina washcoating and metal deposition of ceramic monoliths, Stud. Surf. Sci. Catal., Elsevier, 1995, pp. 1069-1078.

[43]   K. Haas-Santo, M. Fichtner, K. Schubert, Preparation of microstructure compatible porous supports by sol-gel synthesis for catalyst coatings, Appl. Catal. A. 220 (2001) 79-92. https://doi.org/10.1016/S0926-860X(01)00714-1.

[44]   C. Agrafiotis, A. Tsetsekou, The effect of processing parameters on the properties of γ-alumina washcoats deposited on ceramic honeycombs, J. Mater. Sci. 35 (2000) 951-960. https://doi.org/10.1023/A:1004762827623.

[45]   B. Schmidt, M. Liauw, Mass transfer limitations in microchannel reactors, Catal. Today. 110 (2005) 15-25. https://doi.org/10.1016/j.cattod.2005.09.019.

[46]   M. Bhattacharya, M.P. Harold, V. Balakotaiah, Shape normalization for catalytic monoliths, Chem. Eng. Sci. 59 (2004) 3737-3766. https://doi.org/10.1016/j.ces.2004.02.020.

[47]   A. Theampetch, W. Chaiwang, N. Jermkwan, P. Nararaturuksa, T. Sornchamni, C. Prapainainar, Design of microreactor flow channel for Fischer Tropsch synthesis using computational fluid dynamic, Energy Procedia. 100

(2016) 439-447. https://doi.org/10.1016/j.egypro.2016.10.199.

[48]   J.P. Lopes, S.S.S. Cardoso, A.E. Rodrigues, Effectiveness factor for thin catalytic coatings: Improved analytical approximation using perturbation techniques, Chem. Eng. Sci. 71 (2012) 46-55. https://doi.org/10.1016/j.ces.2011.12.006.

[49]   O.H. Laguna, M. González Castaño, M.A. Centeno, J.A. Odriozola, Microreactors technology for hydrogen purification: Effect of the catalytic layer thickness on CuO_x/CeO_2-coated microchannel reactors for the PROX reaction, Chem. Eng. J. 275 (2015) 45-52. https://doi.org/10.1016/j.cej.2015.04.023.

[50]   A. Holmgren, B. Andersson, Mass transfer in monolith catalysts-CO oxidation experiments and simulations, Chem. Eng. Sci. 53 (1998) 2285-2298. https://doi.org/10.1016/S0009-2509(98)00080-3.

[51]   V. Meille, S. Pallier, G. Santacruzbustamante, M. Roumanie, J. Reymond, Deposition of γ-Al_2O_3 layers on structured supports for the design of new catalytic reactors, Appl. Catal. A. 286 (2005) 232-238. https://doi.org/10.1016/j.apcata.2005.03.028.

[52]   L. Giani, C. Cristiani, G. Groppi, E. Tronconi, Washcoating method for Pd/γ-Al_2O_3 deposition on metallic foams, Appl. Catal., B. 62 (2006) 121-131. https://doi.org/10.1016/j.apcatb.2005.07.003.

[53]   P.A.R. Cebollada, E. Garcia Bordejé, Optimisation of physical properties of γ-alumina coating microreactors used for the growth of a carbon nanofiber layer, Chem. Eng. J. 149 (2009) 447-454. https://doi.org/10.1016/j.cej.2009.02.016.

[54]   V. Paunovic, V. Ordomsky, M.F. Neira D'Angelo, J.C. Schouten, T.A. Nijhuis, Catalyst coating on prefabricated capillary microchannels for the direct synthesis of hydrogen peroxide, Ind. Eng. Chem. Res. 54 (2015) 2919-2929. https://doi.org/10.1021/ie504762y.

[55]   M.F.N. D'Angelo, V. Ordomsky, V. Paunovic, J. Van Der Schaaf, J.C. Schouten, T.A. Nijhuis, Hydrogen production through aqueous‐phase reforming of ethylene glycol in a washcoated microchannel, ChemSusChem. 6 (2013) 1708-1716.

[56]   D. Trimm, C.-W. Lam, The combustion of methane on platinum-alumina fibre catalysts-II design and testing of a convective-diffusive type catalytic combustor, Chem. Eng. Sci. 35 (1980) 1731-1739. https://doi.org/10.1016/0009-2509(80)85008-1.

[57]   T.G. Bond, B.A. Noguchi, C.-P. Chou, R.K. Mongia, J.-Y. Chen, R.W. Dibble. Catalytic oxidation of natural gas over supported platinum: Flow reactor experiments and detailed numberical modeling. in Symposium (international) on combustion. 1996. Elsevier.

[58]   F. Behrendt, O. Deutschmann, R. Schmidt, J. Warnatz, Ignition and extinction of hydrogen-air and methane-air mixtures over platinum and palladium, Heterogeneous Hydrocarbon Oxidation. American Chemical Society, 1996, pp. 48-57.

[59]   P.-A. Bui, D. Vlachos, P. Westmoreland, Catalytic ignition of methane/oxygen mixtures over platinum surfaces: comparison of detailed simulations and experiments, Surf. Sci. 385 (1997) L1029-L1034. https://doi.org/10.1016/S0039-6028(97)00438-X.

[60]   S. Oh, P. Mitchell, R. Siewert, Methane oxidation over noble metal catalysts as related to controlling natural gas vehicle exhaust emissions, Catalytic control of air pollution. ACS Publication, Washington, DC, 1992.

[61]   A. Hinz, P.-O. Larsson, A. Andersson, Influence of Pt loading on Al2O3 for the low temperature combustion of methanol with and without a trace amount of ammonia, Catal. Lett. 78 (2002) 177-183.

[62]   G.S. Bugosh, V.G. Easterling, I.A. Rusakova, M.P. Harold, Anomalous steady-state and spatio-temporal features of methane oxidation on Pt/Pd/Al_2O_3 monolith spanning lean and rich conditions, Appl. Catal., B. 165 (2015) 68-78. https://doi.org/10.1016/j.apcatb.2014.09.058.

[63]   D. Dissanayake, M.P. Rosynek, K.C. Kharas, J.H. Lunsford, Partial oxidation of methane to carbon monoxide and hydrogen over a Ni/Al_2O_3 catalyst, J. Catal. 132 (1991) 117-127. https://doi.org/10.1016/0021-9517(91)90252-Y.

[64]   R. Schwiedernoch, S. Tischer, C. Correa, O. Deutschmann, Experimental and numerical study on the transient behavior of partial oxidation of methane in a catalytic monolith, Chem. Eng. Sci. 58 (2003) 633-642. https://doi.org/10.1016/S0009-2509(02)00589-4.

[65]   C. Diehm, O. Deutschmann, Hydrogen production by catalytic partial oxidation of methane over staged Pd/Rh coated monoliths: Spatially resolved concentration and temperature profiles, Int. J. Hydrogen Energy. 39 (2014) 17998-18004. https://doi.org/10.1016/j.ijhydene.2014.06.094.

[66]   I.Y. Pakharukov, A.Y. Stakheev, I.E. Beck, Y.V. Zubavichus, V.Y. Murzin, V.N. Parmon, V.I. Bukhtiyarov, Concentration hysteresis in the oxidation of methane over Pt/γ-Al_2O_3: X-ray absorption spectroscopy and kinetic study, ACS Catal. 5 (2015) 2795-2804. https://doi.org/10.1021/cs501964z.

[67]   A. Amin, A. Abedi, R. Hayes, M. Votsmeier, W. Epling, Methane oxidation hysteresis over Pt/Al_2O_3, Appl. Catal. A. 478 (2014) 91-97. https://doi.org/10.1016/j.apcata.2014.03.032.

[68]   S.H. Oh, P.J. Mitchell, R.M. Siewert, Methane oxidation over alumina-supported noble metal catalysts with

and without cerium additives, J. Catal. 132 (1991) 287-301. https://doi.org/10.1016/0021-9517(91)90149-X.

[69]   A.K. Coker, 3-Physical properties of liquids and gases, Ludwig's Applied Process Design for Chemical and Petrochemical Plants (Fourth Edition). Gulf Professional Publishing, Burlington, 2007, pp. 103-132.

[70]   M. Tang, R. Cox, M. Kalberer, Compilation and evaluation of gas phase diffusion coefficients of reactive trace gases in the atmosphere: volume 1. Inorganic compounds, Atmos. Chem. Phys. 14 (2014).

[71]   H.S. Fogler, Elements of chemical reaction engineering, Pearson Higher Education & Professional Group, 2013.

[72]   D. Neumann, G. Veser, Catalytic partial oxidation of methane in a high-temperature reverse-flow reactor, AIChE J. 51 (2005) 210-223. https://doi.org/10.1002/aic.10284.

[73]   Y. Ozawa, Y. Tochihara, A. Watanabe, M. Nagai, S. Omi, Deactivation of Pt·PdO/Al$_2$O$_3$ in catalytic combustion of methane, Appl. Catal. A. 259 (2004) 1-7. https://doi.org/10.1016/j.apcata.2003.09.029.

[74]   W.R. Schwartz, D. Ciuparu, L.D. Pfefferle, Combustion of Methane over Palladium-Based Catalysts: Catalytic Deactivation and Role of the Support, The Journal of Physical Chemistry C. 116 (2012) 8587-8593. https://doi.org/10.1021/jp212236e.

[75]   S. Kressirer, L. Protasova, M. de Croon, V. Hessel, D. Kralisch, Removal and renewal of catalytic coatings from lab-and pilot-scale microreactors, accompanied by life cycle assessment and cost analysis, Green Chem. 14 (2012) 3034-3046. https://doi.org/10.1039/C2GC35803D.

Chapter 5

Catalytic methane combustion in plate-type microreactors with different channel configurations: an experimental study

ABSTRACT: The straight parallel channel microreactor (made of FeCrAlloy) with washcoated Pt/γ-Al$_2$O$_3$ catalyst was firstly investigated for the catalytic methane combustion (CMC). A specific catalyst loading of 57.6 g m^{-2} was found to yield the highest methane conversion over 3.5 wt% Pt/γ-Al$_2$O$_3$ (at temperatures above ca. 350 ^{o}C). A higher or lower specific catalyst loading tended to decrease the methane conversion due to either the limited internal diffusion through the thicker coating layer or insufficient active sites in the thinner coating layer. Then, the CMC performance of the above microreactor was compared with other five plate-type microreactors of different geometries, covering simple channel geometries (i.e., cavity and double serpentine microchannels) and more complicated configurations (i.e., obstacled microchannels, meshed circuit and vascular network). The microreactor with double serpentine microchannels presented the highest methane conversion with the lowest light-off temperature (especially at a relatively low mixture flow rate), due to the appropriate control over the residence time and specific catalyst surface area compared with other channel configurations. The lowest methane conversion appeared in the microreactor with meshed circuit network, which could be attributed to the non-uniform flow distribution and inefficient usage of the coated catalysts over the surface. For all types of microreactors, the highest methane conversion was observed at an oxygen to methane molar ratio of 1.5 (instead of the stoichiometric ratio of 2), possibly due to the presence of side reactions involving methane (e.g., its partial oxidation and steam reforming). The findings of this work may help to deliver a flexible and compact microreactor design that allows upscaling from laboratory to field-scale applications of the CMC with optimized performance.

Nomenclature

A	Total cross-sectional area of the reaction microchannel in a microreactor, m^2
$F_{CH_4,i}$	Inlet molar flow rate of CH_4, mol s^{-1}
$F_{CH_4,o}$	Outlet molar flow rate of CH_4, mol s^{-1}
$F_{CO_x,o}$	Outlet molar flow rate of CO or CO_2, mol s^{-1}
$F_{H_2,o}$	Outlet molar flow rate of H_2, mol s^{-1}
h	Channel height, m
$l_{j,tot}$	Total channel length between bifurcation indices j and j+1, m
$l_{j,1}$	Length of horizontal channel at the index j in the tree-like bifurcated structure, m
Q_{tot}	Total volumetric flow rate, m^3 s^{-1}
r	Ratio of channel width of the downstream to that of the upstream in one bifurcation, -
S	Inner surface area of microchannels subjected to Pt/γ-Al_2O_3 coating, m^2
S_{H_2}	Selectivity of H_2, %
S_{CO_x}	Selectivity of CO or CO_2, %
U	Mean velocity of methane-air mixture in the reaction microchannel, m s^{-1}
V_{tot}	Total microchannel volume for reaction in a microreactor, m^3
W_{cat}	Catalyst mass, g
w_j	Channel width at scale j in the tree-like bifurcated structure, m
X_{CH_4}	CH_4 conversion, %

Greek symbols

τ	Mean residence time, s

Φ	Inlet molar ratio of oxygen to methane, -
φ	Specific catalyst loading, g m^{-2}
μ	Dynamic viscosity, Pa s
ρ	Density, kg m^{-3}

Abbreviation

CMC	Catalytic methane combustion
GC	Gas chromatography
i.d.	Inner diameter
MW	Molecular weight
o.d.	Outer diameter
PVA	Polyvinyl alcohol

5.1. Introduction

Natural gas has been reported to have a largest increment in consumption in the past decade, accounting for nearly half of the increase in global energy demand in year 2018 [1-3]. The combustion of natural gas presents a particular advantage of higher energy content per CO_2 emission (55.7 kJ g^{-1} if fully based on methane as its main component) than coal (39.3 kJ g^{-1}) and petroleum (43.6 kJ g^{-1}), a character which is essential to a low carbon future. In addition to the abundant natural gas reserves proven worldwide, biomethane could be obtained from organic wastes and residues by biomass gasification/digestion [4,5], providing a competitive energy supply towards a more electrified world [3]. As a result, natural gas has been suggested as a substitute for oil and coal as a future leading energy source for the next 20 years [3,6]. According to the International Renewable Energy Agency (IRENA) [6], the utilization of petroleum and coal would decline by 70% and 85%, respectively, by 2050, whereas natural gas would be the largest source by then and achieve peak on its utilization at around 2027 [6]. Thus, a great number of researches have been devoted to the development of energy-efficient natural gas combustion systems in many aspects for their application in the industrial, transport and domestic areas, etc. [7].

However, the gas industry faces some commercial and environmental challenges [5], due to the releasing of pollutant emissions (e.g., NO_x, CO and unburned hydrocarbon) by the conventional flame combustion of methane typically occurring at above 1400 ^{o}C. The harmful impacts of these emissions on the human health and environment have been well recognized [8] and the applicable regulations over EU countries have become more and more stringent in these years [9]. In this context, the catalytic methane combustion (CMC) as a promising alternative has received increasing attention [10]. A lower working temperature (e.g., < 600 °C) is needed for the complete oxidation of methane in the presence of catalyst because of the reduced activation energy (40-80 kJ mol^{-1}) compared to that for conventional combustion (100-200 kJ mol^{-1}). Hence, the exhaust emissions (especially of NO_x) can be remarkably abated [7,10-12]. Abundant literature is available on the CMC, as summarized by recently published review papers [10,13-15]. These existing CMC studies distinguish themselves by focusing on the catalyst development [16-19] and mechanisms [20-24], different types of catalytic reactors [25-29] and (optimized) reaction conditions [30-33], as well as the target applications [29,34,35].

Various types of catalysts have been studied for the CMC including noble metal catalysts and mixed oxides catalysts (perovskites and hexaaluminate) [10,36,37]. Among them, noble metal catalysts (e.g., Pt, Pd, Rh) are the most commonly used and well developed owing to their high

specific surface area, high catalytic activity and low light-off temperature [30,38]. Bimetallic catalysts (e.g., Pd-Pt/Al$_2$O$_3$) often show higher catalytic activity and selectivity than their monometallic counterparts due to the synergistic effect by metal-metal interaction [39,40]. Additionally, different supports and additives (e.g., ZrO$_2$, CeO$_2$ [41,42]) have been introduced to improve the catalytic activity through the acceleration of oxygen exchange. In terms of the catalyst form, washcoated catalysts have undergone rapid development in recent years. The washcoated catalyst is commonly deposited as a thin layer on structured surfaces of monolithic reactors or (multichannel) microreactors, in order to avoid the high pressure drop and large temperature gradient likely existing in conventional fixed/packed bed reactors loaded with catalyst powders or pellets [27]. In this regard, the good adhesion and coverage of the coated catalyst layer on the channel walls are essential for the CMC performance of the reactor. The suspension method [43-46] and sol-gel method [47,48] are most commonly used for washcoating. It has been reported that the preparation method, binder nature, pH value and particle size could be the key factors that have to be adapted to obtain a high thermal stability and a uniform coverage of the coating [46].

Among different types of structured reactors immobilized with coated catalysts for the CMC, microreactors present a great potential [49,50], primarily owing to their high specific surface area that leads to substantially enhanced mass and heat transfer rates [51,52]. These features are especially beneficial for handling the CMC or highly exothermic reactions in general by suppressing the presence of temperature hot spots due to the local accumulation of reaction heat [53-55]. In particular, plate-type microreactors containing a multitude of microchannels arranged in parallel have attracted great interests. In combination with the well-adhered catalyst coating on the wall surface, the plate-type multichannel microreactors offer numerous advantages, including the compact design with relatively high specific surface area, small pressure drop, easy to manufacture and the scaling-up potential to handle a large amount of reactive gas. For instance, the experimental study by O'Connell et al. [27] shows that a 100 % conversion could be obtained in a multichannel microreactor (500 μm width × 250 μm depth, 14 channels in total) washcoated with Pt-W or Pt-Mo/γ-Al$_2$O$_3$ catalyst at 600 ^{o}C and a total gas flow rate of 107 mL min^{-1} (space velocity of 74,000 h^{-1}) and an O$_2$/CH$_4$ molar ratio of 2.2. He et al. [46] experimentally performed the CMC in a multichannel reactor (275 mm length × 1.5 width mm × 1 mm height, 32 channels in total) over the washcoated Pt/γ-Al$_2$O$_3$ catalyst. A 95.75 % methane conversion was obtained at 450 ^{o}C under a total gas flow rate of 110 mL min^{-1} (space velocity: 6,557 h^{-1}) and an O$_2$/CH$_4$ molar ratio of 2. Moreover, the compact and modular feature

of the plate-type multichannel microreactor makes it possible for a better utilization of the reaction heat [56,57]. The development of the so-called autothermal reactor that combines the CMC (exothermic reaction) with another endothermic reaction (e.g., methane steam reforming to produce hydrogen or syngas) within a single device has become a research hotspot over the past decade [58]. Mundhwa et al. [56,57] proposed a stacked autothermal reactor design which was composed of two plates with parallel microchannels (5 cm length × 1 mm width, 15 channels, coated with ca. 20 μm thick Pt/Al_2O_3 catalyst) for the CMC and other two plates of cavity shape (5 cm length × 5 cm width × 100 μm depth, with washcoated Ni/Al_2O_3 catalyst) for the methane steam reforming reaction. Their numerical results show that this compact multiple plate design (especially under the co-current mode between flows) could reduce the required amount of catalyst for the CMC by 70% and maintain a uniform temperature profile for the methane steam reforming [56,57]. The scale-out strategy of microreactor stacks has been investigated numerically for coupling such exothermic and endothermic processes [59]. The results illustrate that a certain number of stacks (e.g., > 15) was needed so that the released reaction heat could compensate for the heat loss and thus drive the reforming reaction effectively [59].

It is noteworthy that most of the plate-type multichannel microreactors tested for the CMC or simulated for its autothermal coupling have a simple configuration like parallel straight channels [27,46,56-60]. In this respect, the influence of the operating parameters and the washcoated catalyst properties (e.g., of the promising noble metal based one) on the CMC performance still needs more systematic investigations, as the current understanding is still far from being sufficient. Moreover, there is still much room for the reactor performance improvement by optimizing the internal microchannel configurations that lead to a better process control (e.g., narrowed residence time distribution and more uniform reactant flow distribution) and catalyst utilization (e.g., high catalyst surface area and improved gas-solid mass transfer) in the CMC. Such microreactor performance optimization is equally important towards obtaining a better usage of the released reaction heat from the CMC in energy applications, such as the small-scale water boiler and the autothermal reaction device.

As a continuation of our previous study [46], this work has firstly presented an experimental investigation into the CMC performance over the microreactor with parallel straight channels coated with $Pt/\gamma-Al_2O_3$ catalyst. The influence of different operation conditions (e.g., temperature, flow rate and oxygen to methane molar ratio), catalyst loading and thickness, reaction microchannel length was studied. Then, the reaction performance of this type of

microreactor was compared with those of other five type of microreactors with different channel configurations. The studied configurations cover some relatively simple channel geometries (cavity and double serpentine channels) and more complicated ones (obstacled channels, meshed circuit and vascular network). The methane conversion between different microreactor designs has been compared and explained based on the internal channel surface area, residence time and the specific catalyst loading. Moreover, the use of tree-like bifurcation structure for fluid distribution or collection in the microreactor was explored towards improved reaction performance. The findings of this work may help to achieve a flexible and compact design of microreactors that allows upscaling from laboratory to field-scale applications of the CMC with optimized performance.

5.2. Experimental

5.2.1. Experimental setup and procedures

The experimental test rig is shown in Fig. 5.1. Two mass flow controllers (MFC, Brooks SLA5850) were used to adjust the flow rates of methane and the synthetic air for the CMC experiment. The total gas flow rate was adjusted from 110 to 500 mL min^{-1} (based on ca. 20 ^{o}C and 1 atm).

For each test, the oven (Nabertherm, LT 9/11/B170) was firstly heated up to the target temperature at a ramp of ca. 15 ^{o}C min^{-1} flowing with air to prevent any reaction happened during heating up process. Once the oven temperature reached the target reaction temperature ranging between 300 ^{o}C and 500 ^{o}C, the methane-air gas mixture (at an O_2/CH_4 molar ratio from 0.5 to 6) first passed through the inlet pre-heating coil (stainless steel; i.d.: 3.7 mm, o.d.: 6 mm, ca. 20 cm in length) in the oven, and was then introduced into the plate-type microreactor where the catalytic reaction happened. The product gas first flew out through a condenser to remove water, and was then analyzed by an online gas chromatography (GC).
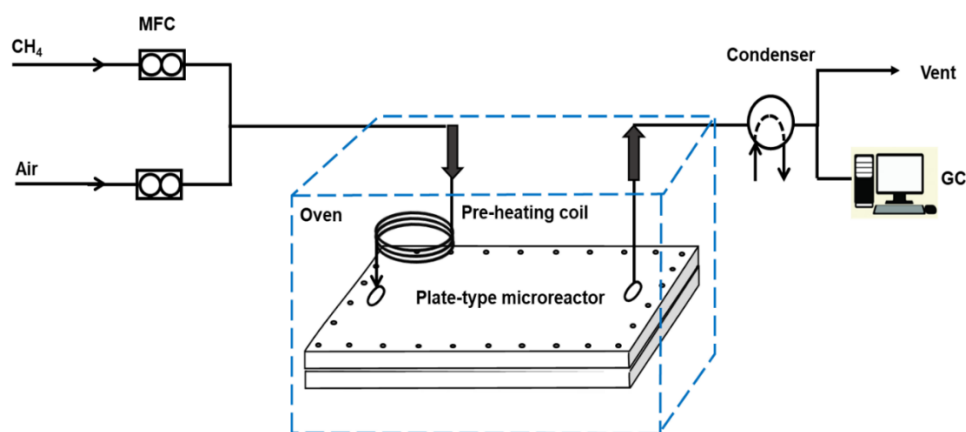
Fig. 5.1. Test rig for the CMC in the plate-type microreactor.

5.2.2. Reactor design and fabrication

The plate-type microreactor has an overall dimension of 190 mm in length, 130 mm in width and 10 mm in height. It was designed as a sandwich shape with a reaction plate (made of FeCrAlloy, i.e., Kanthal A-1, 22 % Cr, 5.8 % Al and Fe for balance) in the middle, enclosed by two additional blind plates (made of stainless steel) as the outside shell (Fig. 5.2). One blind plate has additional inlet and outlet ports in order to interface with the reaction platelet (*vide infra*). A graphite gasket (3 mm in thickness) was installed in between these plates to prevent the gas leakage and bolts were used on the peripherals for further sealing. A liquid leak detector (Snoop) was applied on the assembled microreactor in order to ensure the tightness before each series of the test.

The middle reaction plates have an overall dimension of 112.5 mm (length) × 50 mm (width) × 3 mm (height). Each plate has a single inlet port and outlet port (i.d.: 6.5 mm) aligned with the central line, the distance between their centers being 82.5 mm. Six shapes of the internal flow network have been designed and machined on one side of the plate, all of them having a symmetric geometry, as shown in Fig. 5.2. Each flow network consists of three parts: the inlet distributor, reaction microchannels subjected to the catalyst coating (on two sides and the bottom surface of the microchannel wall) and outlet collector. A detailed description of the six reactors (Reactors #1-6) and its flow network is presented as follows. Note that except for the cavity case (Reactor #2), all the reaction microchannels have a rectangular cross-section of 1.5 mm in width and 1 mm in height.

Reactor #1 (denoted as the straight parallel channel microreactor) has a basic shape of 16 parallelized and straight reaction microchannels of 60 mm in length. The thickness of the separating walls between neighbouring microchannels is 1.5 mm.

Reactor #2 (denoted as the cavity microreactor) has a simple cavity geometry for reaction (dimension: 66.45 mm length × 46.5 mm width × 1.0 mm depth).

Reactor #3 (denoted as the double serpentine channel microreactor) consists of two serpentine reaction microchannels arranged in axial symmetry. For each zigzag unit, the channel length of the horizontal section is 21 mm and that of the vertical section is 4.5 mm, the angle of zigzags being 90 º. The thickness of the separating walls is 1.5 mm. The total length of each serpentine microchannel is 547.02 mm.

Reactor #4 (denoted as the obstacled parallel channel microreactor) differs from the basic straight parallel channel microreactor (Reactor #1) by the presence of solid obstacles (square

shape, 1.5 mm × 1.5 mm) along the flow direction in the reaction microchannels. Each microchannel thus assumes a split-and-recombine shape around successive obstacles (4.5 mm × 4.5 mm, 10 pieces for each, 80 in total). The thickness of walls separating the microchannels is 1.5 mm. The connection unit between repeating split-and-recombine units is 1.5 mm in length and 1.5 mm in width.

Reactor #5 (denoted as the meshed circuit microreactor) presents a meshed flow circuit with channel interlacing, inspired by the land crack architecture in nature [61]. The reaction microchannels are intersected at a crossing angle of 90°. The solid diamond blocks formed between the adjacent microchannels have a dimension of 2.74 mm × 2.74 mm with 143 pieces in total.

Reactor #6 (denoted as the vascular microreactor) has two vascular blocks arranged in axial symmetry. For each vascular block, there are two side vertical microchannels (69 mm length × 1.5 mm width) for gas splitting whereas one central vertical microchannel (66 mm length × 1.5 mm width) for recombining. The side and central vertical microchannels are connected by means of short horizontal microchannel sections (9 mm length × 1.5 mm width, 86 pieces in total) that are arranged in a staggered pattern and separated by rectangular parallelepipeds (9 mm in length and 1.5 mm in width).

The inlet fluid distributor and outlet fluid collector fed with the reaction microchannel(s) also differ to some extent in Reactors #1-6. The combination of a multi-scale bifurcated distributor and a simple rectangular collector was employed for Reactors #1, 2, 4 and 5 (Fig. 5.2). Regarding Reactors #3 and #6, the above structures are not very appropriate due to the geometrical constraints, i.e., the reaction microchannel being either limited in number (only two in Reactor #3) or with a special shape (vascular in Reactor #6). Thus, a simple bilateral divergent or convergent channel network was used as the distributor or collector, respectively. The design, scaling relations and detailed dimensions for these distributors/collectors are found in Appendix 5.A.
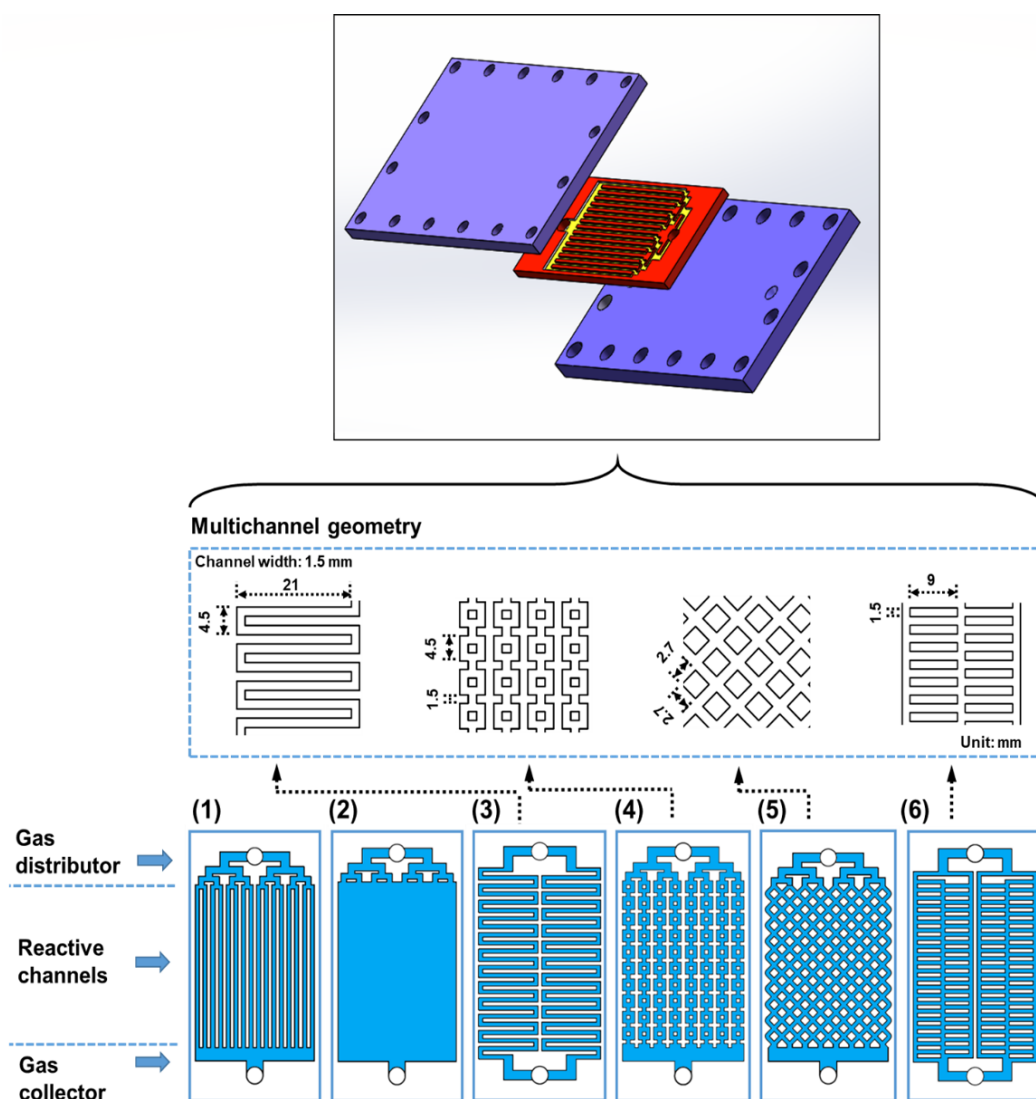
Fig. 5.2. Schematics of various plate-type microreactors. Reactors #1-6 denote, respectively, the straight parallel channel microreactor, cavity microreactor, double serpentine channel microreactor, obstacled parallel channel microreactor, meshed circuit microreactor and vascular microreactor.

5.2.3. Catalyst preparation and coating procedures

The reaction platelets were first immersed with acetone at 45 ^oC for 30 min in the ultrasonic bath (PCE-UC 20) with the frequency being 40 kHz, in order to remove oil, grease and other dirt [62]. Thermal pretreatment was subsequently performed at 900 ^oC (ramp from room temperature: 20 ^oC min^{-1}; 10 h at the final temperature), in order to generate a thin alumina layer over the substrate surface which could be a strong bonding between the Pt/γ-Al$_2$O$_3$ coating layer and the substrate.

The slurry suspension method was applied for the coating deposition in microreactors [63,64].

The materials used for preparing the catalytic coating were as follows: γ-Al_2O_3 (3 μm, 99.97 % on metals basis), PVA (98-99 % hydrolyzed), acetic acid and tetraammineplatinum (II) nitrate ($Pt(NH_3)_4(NO_3)_2$, 99.99 % on metals basis) purchased from Alfa Aesar. The γ-Al_2O_3 slurry was prepared by mixing γ-Al_2O_3 powder, PVA binder and acetic acid [43], based on the optimized composition identified in our previous study [46]: 5 wt% PVA (MW of 146,000 - 186,000), 20 wt% Al_2O_3 (3 μm) and 1 wt% acetic acid. The γ-Al_2O_3 slurry was then heated up to 65 °C for 2 h under 300 rpm stirring and stored at room temperature for at least 2 weeks to remove the bubbles inside the slurry before use.

The prepared slurry as the catalyst support precursor was first deposited on the walls (two sides and bottom) of the reaction microchannels for all Reactors #1 to 6 using syringe injection. The applied slurry weight was adjusted as per the required catalyst specific loading (*vide infra*). The excessive suspension outside the microchannel was immediately removed with a razor blade. The platelets were then dried at room temperature overnight for at least 8 h, subsequently dehydrated at 120 °C for 8 h and finally calcined at 600 °C (ramp from room temperature: 2 °C min^{-1}; 2 h at the final temperature).

The incipient wetness impregnation was performed by manually dropping the $Pt(NH_3)_4(NO_3)_2$ solution with a certain Pt concentration (1.5 wt%, 3.5 wt% or 5 wt%) into the reaction microchannel of the platelet coated with γ-Al_2O_3. The impregnated coating was then dried at room temperature overnight for at least 8 h, and finally calcined at 500 °C (ramp from room temperature: 2 °C min^{-1}; 2 h at the final temperature). The adhesion of the Pt/γ-Al_2O_3 washcoat catalyst prepared following this procedure has been tested in our previous study by the ultrasonic test and no appreciable weight loss has been found [46]. Fig. 5.3 shows the prepared reaction plates with the coated catalyst. Some geometric parameters of these reactors and the involved Pt/γ-Al_2O_3 catalyst coating characteristics are presented in Table 5.1. Note that all the area and volume calculations are based on bare microchannels without considering the coating thickness. Based on SEM images from our previous study [46], the coating thickness range is ca. 18 μm (upper parts at side walls) to ca. 110 μm (corner parts), which is much smaller than the microchannel width/height.
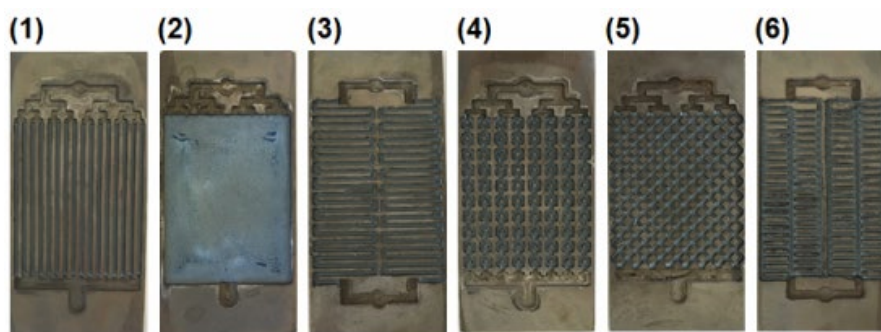
Fig. 5.3. Reaction platelets coated with Pt/γ-Al$_2$O$_3$ catalyst in Reactors #1-6.

Table 5.1

Geometric parameters of the tested microreactors and the involved Pt/γ-Al$_2$O$_3$ catalyst coating characteristics.

Reactor	S (mm^2)			W_{cat}	φ	V_{tot} [c]	τ [d]
	Bottom side [a]	Wall side [b]	Total	(g)	(g m^{-2})	(mm^3)	(s)
#1	1476.00	1998.02	3474.02	0.27 [e]	78.30 [e]	1476.00	5.90
#2	3089.00	202.88	3291.88	0.25	76.40	3089.00	12.36
#3	1650.06	2200.08	3850.14	0.27	70.26	1650.06	6.60
#4	1620.00	1920.00	3540.00	0.24	67.51	1620.00	6.48
#5	1676.45	1815.26	3491.71	0.24	68.45	1676.45	6.71
#6	2166.00	2249.08	4415.08	0.26	58.28	2166.00	8.66

[a] The surface area of the bottom of the reaction microchannel. [b] The surface area of two sides walls of the reaction microchannel; [c] Volume of the reaction microchannel; [d] Residence time in the reaction microchannel, calculated based on a total gas flow rate of 150 mL min^{-1}. [e] Other catalyst weights and specific loadings were also tested. Here only the values for comparison with other type of microreactors are shown.

5.2.4. Analytical procedure

Gas product was analyzed by an online MicroGC (Agilent, R490 OBC) equipped with a thermal conductivity detector. A Molsieve 5Å column (MS5A, length: 20 m) and a pre-column (PPU, length: 10 m) were used. The concentrations of the reference gas used were 5.12 ± 0.1 mol% CH$_4$, 2.015 ± 0.04 mol% C$_3$H$_8$, 2.024 ± 0.061 mol% C$_3$H$_6$, 9.99 ± 0.2 mol% H$_2$, 9.98 ± 0.2 mol% CO, 1.994 ± 0.04 mol% C$_2$H$_2$, 1.999 ± 0.04 mol% n-C$_4$H$_{10}$, 2.017 ± 0.04 mol% C$_2$H$_4$, 9.92 ± 0.02

mol% CO_2, and N_2 for the rest. Argon was used as the carrier gas. The MicroGC oven temperature was heated from 40 °C up to 100 °C (ramp: 20 °C min^{-1}) and maintained for 7.5 min. SOPRANE II software was used for the peak area integration and data analysis.

5.2.5. Definitions

The CH_4 conversion (X_{CH_4}), CO_2 (CO) selectivity (S_{CO_x}) and H_2 selectivity (S_{H_2}) are calculated based on Eqs. (5.1) - (5.3), respectively.

$$X_{CH_4} = \frac{F_{CH_4,i} - F_{CH_4,o}}{F_{CH_4,i}} \times 100\ \% \tag{5.1}$$

$$S_{CO_x} = \frac{F_{CO_x,o}}{F_{CH_4,i} - F_{CH_4,o}} \times 100\ \% \tag{5.2}$$

$$S_{H_2} = \frac{F_{H_2,o}}{F_{CH_4,i} - F_{CH_4,o}} \times 100\ \% \tag{5.3}$$

where F stands for the molar flow rate (based on ca. 20 °C and 1 atm). The subscripts i and o indicate the inlet and outlet of the plate-type microreactor, respectively.

The mean residence time (τ) is defined as the total void volume of the coated microchannel(s) (V_{tot}) divided by the total volumetric flow rate of the gas mixture entering the reactor (Q_{tot}).

$$\tau = \frac{V_{tot}}{Q_{tot}} \tag{5.4}$$

The catalyst specific loading φ (unit: g m^{-2}) of the Pt/γ-Al$_2$O$_3$ washcoat catalyst deposited on the reaction platelet is calculated as the catalyst mass (W_{cat}) gained on the substrate (i.e., after calcination) divided by the total surface area (S) of the reaction microchannel subject to the coating.

$$\varphi = \frac{W_{cat}}{S} \tag{5.5}$$

The mean velocity of the gas mixture in the reaction microchannel is defined as the total volumetric flow rate of the gas mixture divided by the total reaction microchannel cross-sectional area (A).

$$U = \frac{Q_{tot}}{A} \tag{5.6}$$

5.3. Results and discussion

5.3.1. CMC performance of the straight parallel channel microreactor

In our previous study [46], the straight parallel channel microreactor of a larger dimension (317.5 mm length × 50 mm width × 3 mm height) with washcoated Pt/γ-Al$_2$O$_3$ catalyst has been investigated for the CMC. In order to gain a deeper understanding of the influence of among others the catalyst loading, thickness, channel length and fluid distribution/collection structure on the methane conversion, the similar type of microreactor, though with a relative smaller dimension (112.5 mm length × 50 mm width × 3 mm height), has been prepared with Pt/γ-Al$_2$O$_3$ coating in this work and examined under different reaction conditions.

5.3.1.1 Effect of the operating conditions

The methane conversion as a function of the reaction temperature (i.e., the oven temperature) under different flow rates at an inlet oxygen to methane molar ratio (Φ) of 2 is shown in Fig. 5.4. For a given temperature, a higher methane conversion was obtained at a lower flow rate, due to a longer residence time (c.f. Eq. (5.4)). At the beginning when the operating temperature is relatively low (300 - 350 ^{o}C), the methane conversion has no significant difference between different flow rates (150 – 500 mL min^{-1}). Under such circumstances, the reaction rate is slow and (largely) controlled by kinetics (i.e., predominately determined by the reaction temperature and catalyst mass). Thus, the methane conversion is at a very low level (< 3%) and the conversion difference between each flow rate is not very discernible. As the temperature increased, the methane conversion presented a significant increase and the light-off phenonemnon occurred. This indicates that the favorable coverage of the adsorbed methane and oxygen over the catalyst surface facilitated by the temperature rise has been reached. Meanwhile, the significant increase in the intrinsic kinetic rate and the catalytic activity during the light-off is likely attributed to the rapid rise of the local temperature as well given the strongly exothermic reaction of methane combustion. The light-off temperature corresponding to a 50% methane conversion (T_{50} value) relevant to conditions in Fig. 5.4a is shown in Table 5.2. When the operating temperature continued to increase (e.g., > 450 ^{o}C), the reaction tended to be (more) governed by mass transfer, because the kinetic rate rapidly increased (according to the Arrhenius equation), but the gas-catalyst mass transfer rate was hardly to catch up with (given much less comparable increase in the species diffusivity in the gas mixture and coating). It is worth noting that the decrement in the methane conversion rendered a slowdown when comparing 150 mL min^{-1} to 300 mL min^{-1} and 300 mL min^{-1} to 500 mL min^{-1} throughout the

temperature from ca. 400 to 500 ºC. This is in line with T_{50} value difference in Table 5.2.

Fig. 5.4b further compares the methane conversion as a function of the flow rate at a given temperature of 400 or 450 ºC. The methane conversion presented an obvious decrease with the increasing total flow rate, as already revealed in Fig. 5.4a. It is worth noting that the decrease in the methane conversion at a sufficiently high flow rate tends to be insignificant. This could be due to the improved external mass transfer at high flow rates which compensate, to some extent, the conversion decrease (due to the shortened residence time). The conversion trends revealed here are in general similar to those for the straight parallel channel microreactor tested in our previous study [44]. Table 5.3 further lists a performance comparison (in terms of the light-off temperature and the highest methane conversion) between Reactor #1 and the capillary microreactor (tested in Chapter 4) as well as another straight parallel channel microreactor (tested in Chapter 3). A similar performance was found in all systems, albeit the fine details differ a bit due to the different reaction conditions and microreactor dimensions in use. These results confirm that the coating has been successfully applied onto the current microreactor and functioned well in the CMC.

(b)
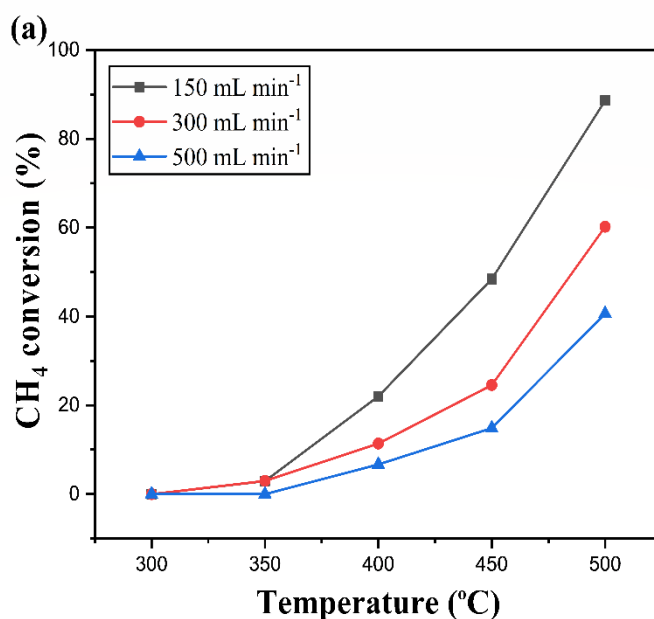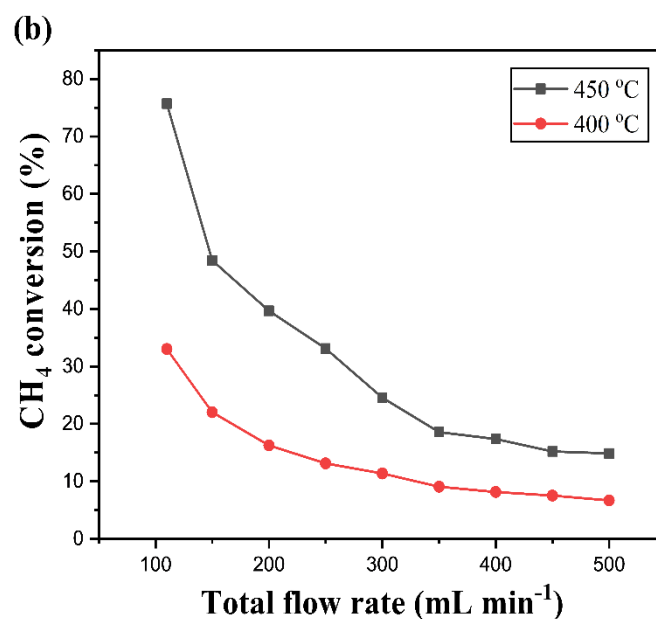
Fig. 5.4. Methane conversion as a function of (a) the temperature and (b) the total gas flow rate over the washcoated 3.5 wt% Pt/γ-Al$_2$O$_3$ catalyst in Reactor #1 (straight parallel channel microreactor). Conditions: T = 300 ºC - 500 ºC, Φ = 2, Q_{tot} = 110 - 500 mL min^{-1}.

Table 5.2

T_{50} value for the CMC experimental data presented in Fig. 5.4a.

Total flow rate	T_{50} [a, b]
(mL min^{-1})	(ºC)
150	451.8
300	487.6
500	516.0

Note: [a] T_{50} indicates the temperature for reaching 50% methane conversion; Conditions are shown in Fig. 5.4a.

[b] Estimated from the polynomial regression line used for fitting the measured conversion curve as a function of the temperature for different flow rates. The polynomial is in the form of $T_{50} = B_0 + B_1 X_{CH_4} + B_2 X_{CH_4}^2$, where B_0, B_1 and B_2 are the fitting constants.

Table 5.3

Comparison of the light-off temperature (T_{50} value) and the highest methane conversion in various microreactors.

Sources	Microreactor	Dimension (mm)	Conditions	T_{50} (°C) [a]	T_x (°C) [b]
Chapter 3	Multichannel; FeCrAlloy	275 (length) × 1.5 (width) × 1.0 (depth); 16 channels in each plate, 32 in total	110 mL min⁻¹, T: 300 - 450 °C; $\Phi = 2$; $\varphi = 80.8$ g m⁻²; $\tau = 7.20$ s; 3.8 wt% Pt/γ-Al₂O₃	402.4	$T_{95.6} = 450$
Chapter 4	Capillary; 316L stainless steel	100 (length) × 4.6 (i.d.) × 6.35 (o.d.)	30 mL min⁻¹; T: 350 - 500 °C; $\Phi = 2$; $\varphi = 56.3$ g m⁻²; $\tau = 3.32$ s; 3.0 wt% Pt/γ-Al₂O₃	397.4	$T_{95.9} = 500$
Chapter 5	Multichannel; FeCrAlloy (Reactor #1)	60 (length) × 1.5 (width) × 1.0 (depth), 16 channels in total	150 mL min⁻¹; T: 350 - 500 °C; $\Phi = 2$; $\varphi = 78.3$ g m⁻²; $\tau = 0.81$ s; 3.5 wt% Pt/γ-Al₂O₃	451.8	$T_{88.6} = 500$

Note: [a] T_{50} value (denotes as the light-off temperature) indicates the temperature for reaching 50% methane conversion;

[b] T_x value indicates the reaction temperature for reaching X% methane conversion;

5.3.1.2. Effect of catalyst loading and coating thickness

The reaction was further performed at various flow rates in Reactor #1 (straight parallel channel microreactor) with different Pt loadings (1.5 wt%, 3.5 wt% and 5.0 wt% Pt/γ-Al$_2$O$_3$) by maintaining almost a constant catalyst weight (W_{cat} = 0.25 ± 0.02 g). In more detail, during the catalyst preparation only the concentration of Pt precursor solution was changed according to the required Pt loading. The obtained results are presented in Fig. 5.5. At the same total gas flow rate, a higher Pt loading (and with that more Pt available in the catalyst) is accompanied by a higher methane conversion. Thus, the overall reaction rate is significantly promoted by the increased kinetic rate at higher Pt loadings. The methane conversion rendered an obvious drop as increasing the total flow rate, due to the reduction of residence time. The extent of such conversion decrease seems more pronounced especially at the highest catalyst loading studied (5.0 wt% Pt/γ-Al$_2$O$_3$), indicating that the influence of the external mass transfer was more pronounced therein given the highest kinetic rate involved.
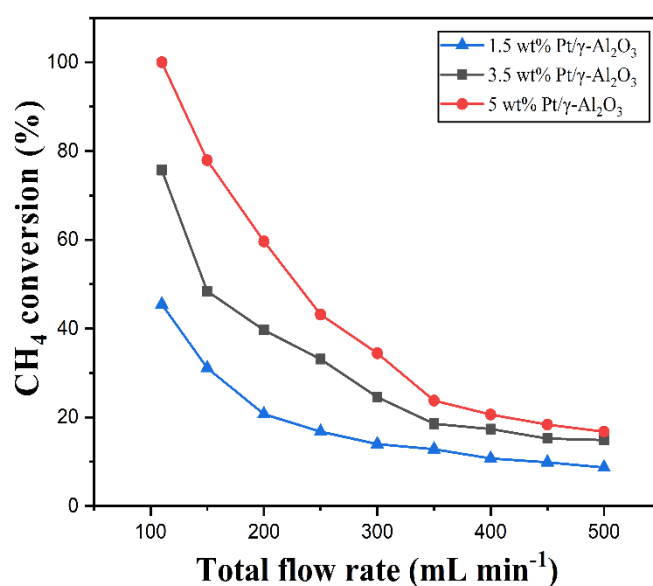
Fig. 5.5. Methane conversion as a function of the total gas flow rate over different Pt loadings in Reactor #1 (straight parallel channel microreactor). Conditions: T = 450 ºC, Φ = 2, Q_{tot} = 110 - 500 mL min^{-1}, W_{cat} = 0.25 ± 0.02 g.

To further investigate the influence of internal diffusion limitation (if present) on the microreactor performance, the coating thickness of 3.5 wt% Pt/γ-Al$_2$O$_3$ catalyst was varied in the experiment by applying different catalyst mass (W_{cat}) onto the reaction microchannel walls in Reactor #1. That is, the higher the W_{cat}, the thicker the coating layer and subsequently the

higher the specific catalyst loading φ (Eq (5.5)). Microreactors with different values of φ varying from 39.45 to 90.39 g m^{-2} in Reactor #1 have been prepared, and the catalyst layer visually presented a uniform and well-dispersed coating throughout the parallelized reaction microchannels. Fig. 5.6 illustrates that the methane conversion presents a maximum at about φ = 57.57 g m^{-2} for a given temperature (more clearly seen at above 350 °C) and total flow rate. This phenomenon is probably due to a more or less optimized match between the internal diffusion rate and the intrinsic kinetic rate at φ = 57.57 g m^{-2}. For lower φ values (e.g., 39.45 g m^{-2}), this might be explained by the fact that although the thinner coating layer herein facilitated the internal diffusion, the accompanied insufficient amount of active sites for the reaction (given the Pt weight decrease in the catalyst) has reduced the methane conversion. For higher φ values (e.g., 78.30 and 90.39 g m^{-2}), the more significant internal diffusion resistance is likely present due to the increased thickness of the catalyst layer, resulting in a lower methane conversion (despite the Pt weight increase in the catalyst). For a more quantitative prediction of the conversion trend as shown in Fig. 5.6, a good knowledge on the reaction kinetics and reactant diffusion within the coating layer (which depends primarily on the pore structure and morphology of the coating) need to be further acquired.
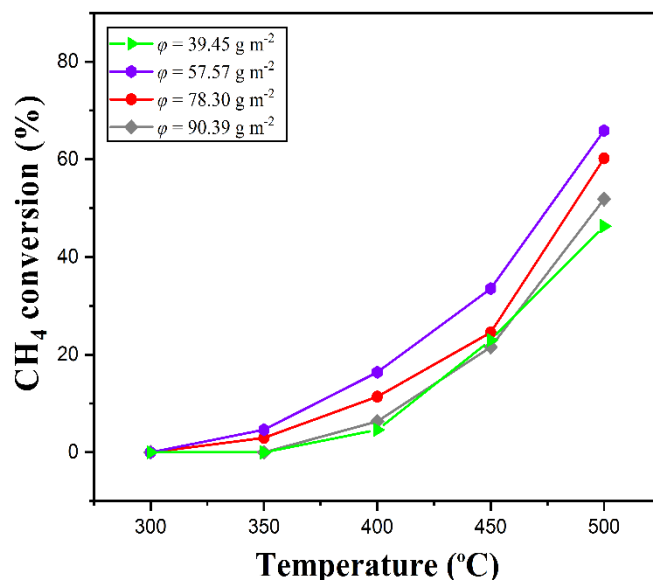
Fig. 5.6. Methane conversion as a function of the reaction temperature under different specific catalyst loading (φ) in Reactor #1 (straight parallel channel microreactor). Conditions: T = 300 - 500 °C, Φ = 2, Q_{tot} = 300 mL min^{-1}, 3.5 wt% Pt/γ-Al$_2$O$_3$ catalyst.

5.3.1.3. Effect of reaction microchannel length

To gain further insights into the influence of external mass transfer on the reaction rate, the methane conversion in experiments with the straight parallel channel microreactors of different reaction microchannel lengths (50-275 mm) is compared in Fig. 5.7, where the microchannel width/height is the same. The specific catalyst loading is kept more or less identical ($\varphi = 82.5 \pm 5$ g m^{-2}). As displayed in Fig. 5.7, the methane conversion increased with increasing microchannel length at 400 °C for a given mean velocity of the methane-air mixture (U; Eq. (5.6)). This is logical given the increased residence time in the longer microchannel. A significant increase in the microchannel length (from 60 to 275 mm) did not result in a conversion increase of similar extent. This shows that the reaction is (at least) limited by the external mass transfer, given that under internal diffusion limitation or kinetic control, the overall reaction rate should increase linearly with the catalyst weight applied on the microchannel wall.
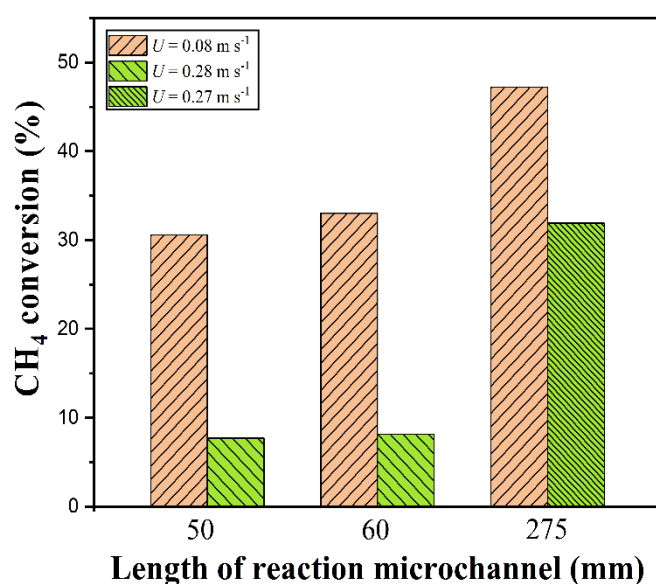
Fig. 5.7. Methane conversion as a function of the reaction microchannel length at different mixture velocities (U). Conditions: $T = 400$ °C, $\Phi = 2$, 3.5 wt% Pt/γ-Al$_2$O$_3$ catalyst, $\varphi = 81.33$, 78.30, and 87.37 g m^{-2} for the microchannel lengths of 50, 60 and 275 mm, respectively, Data for 60 mm microchannel length is based on experiments with Reactor #1 (straight parallel channel microreactor). Data for 50 mm and 275 microchannel lengths are from the respective experiments with another microreactor of otherwise the same geometry and the microreactor used in our previous study [44] (but with different numbers of microchannels of the same

width/height).

As already revealed in Fig. 5.4b, the methane conversion at a given temperature decreased with the increasing flow rate in the microreactor (Reactor #1), which is insignificant at sufficiently high flow rates (e.g., Q_{tot} = 400 mL min^{-1}; corresponding to a U of 0.28 m/s). The results of Fig. 5.7 further suggest that at such high Q_{tot} or U values, the methane conversion can be still improved by increasing the microchannel length (translated into a longer residence time). This also implies that if the reaction is operated at a much higher Q_{tot} (than 400 mL min^{-1}) in Fig. 5.4b, a significant drop in the methane conversion is expected (i.e., the conversion does not level off at such high flow rates).

5.3.1.4. Effect of bifurcated tree-like structure as distributor or collector

The flow distribution behaviour within the reaction microchannel network may have a great impact on the microreactor performance in the CMC. In the experiments performed above in Reactor #1, the bifurcated tree-like structure was used as the inlet fluid distributor a simple rectangular collector at the microchannel outlet (Fig. 5.2). Regarding the multi-scale tree-like component, its relevant position with respect to the reaction microchannel will influence flow distribution properties, as shown in the previous study [65]. In order to experimentally verify the influence of such tree-like component on the catalytic performance, additional experiments were performed with Reactor #1, by switching the microreactor outlet and inlet (i.e., by feeding the gas mixture at the microreactor outlet). Thus, the tree-like structure functioned here as the product collector and the rectangular collector as the fluid distributor.

Fig. 5.8 presents an interesting observation: for Reactor #1, the tree-like structure used as the outlet product collector exhibited a higher methane conversion than that used as the inlet gas distributor. This indicates a somewhat significant difference in the pressure (drop) between the distributor case and collector case [65]. When the tree-like structure was used as the gas collector, the pressure drop in the collector side is higher than the case of using the simple rectangular chamber as the collector, and the pressure drop in the distributor side is lower. This means that in the former case, the local pressures at the inlet and outlet of the reaction microchannel are higher than those in the latter case, which is beneficial for a more uniform fluid distribution and thus a better methane conversion. In other words, the lower pressure drop on the distributor side tends to improve the uniform delivery of fluid into each reaction microchannel, and the higher pressure at the reaction microchannel outlet would make the flow therein less affected by the flow behavior within the outlet collector structure. These are also

in line with the literature report that less vortex was produced and less energy was dissipated when using such tree-like structure as the collector compared with the distributor case [65].

Fig. 5.8 further shows that the conversion improvement in the former case is more pronounced at higher total flow rates. This is possibly because the bifurcated tree-like distributor is shown to be capable of guaranteeing a relatively uniform flow distribution among parallel channels/tubes at small flow rates [66,67]. Nevertheless, the inevitable flow distribution non-uniformity at high flow rates due to the increasing impact of inertial forces is an intrinsic character of such structure [66]. Thus, the tree-like component used as the outlet collector is able to provide a more uniform and stable flow distribution among parallel straight microchannels even under high flow rate conditions. The residence time difference across different reaction microchannels is thereby smaller, leading to a better usage of the catalysts and consequently higher methane conversion.
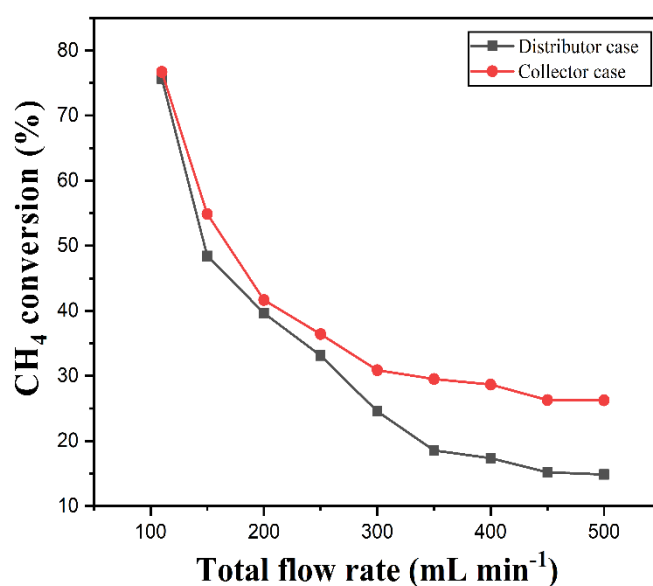
Fig. 5.8. Influence of the location of the tree-like bifurcated component (i.e., used as the inlet gas distributor or outlet product collector) on the methane conversion in Reactor #1 (parallel straight channel microreactor). Conditions: T = 450 °C, Φ = 2, Q_{tot} = 110 - 500 mL min^{-1}, 3.5 wt% Pt/γ-Al$_2$O$_3$.

5.3.2. Comparison of the CMC performance in microreactors with different internal channel configurations

In the following sub-sections, the CMC performance of Reactor #1 (parallel straight channel microreactor) has been compared with other five plate-type microreactors with different

internal channel configurations as shown in Fig. 5.2, with regard to the effect of the operating temperature, total gas flow rate and molar ratio of O_2 to CH_4 (Φ). In all reactors, the washcoated 3.5 wt% $Pt/\gamma\text{-}Al_2O_3$ catalyst has the almost identical weight (0.25 ± 0.02 g; Table 5.1).

5.3.2.1. Effect of temperature on the performance of different microreactors

The methane conversion as a function of the reaction temperature in different microreactors is shown in Fig. 5.9a-c for different total flow rates (150 - 500 mL min^{-1}) and Φ = 2. The same trend as presented in Fig. 5.4a was observed. At the lower temperature of 300 - 350 ^{o}C, the methane conversion in all Reactors #1-6 is very low (< ca. 5%) and has no obvious difference at different flow rates. This is because the reaction is mainly controlled by kinetics and mass transfer is not the main factor determining the reaction rate. As the temperature increased, the methane conversion presented a significant increase (especially at a lower flow rate), and the light-off phenomenon occurred. An obvious difference in the methane conversion was found among the different channel configurations of Reactors #1 - 6 at higher temperatures (> ca. 400 ^{o}C) when the (external) mass transfer gradually became the limiting factor, especially at a relatively low gas flow rate (e.g., 150 mL min^{-1}; Fig. 5.9a). At a relatively high flow rate (e.g., 500 mL min^{-1}; Fig. 5.9c), the gap in the methane conversion between different reactors is narrowed, due to the (largely) improved external mass transfer rate.

(a)

(b)

(c)
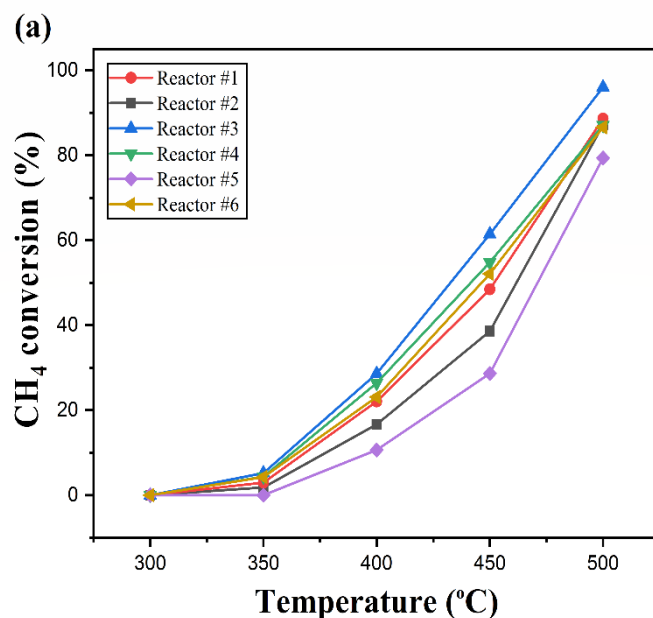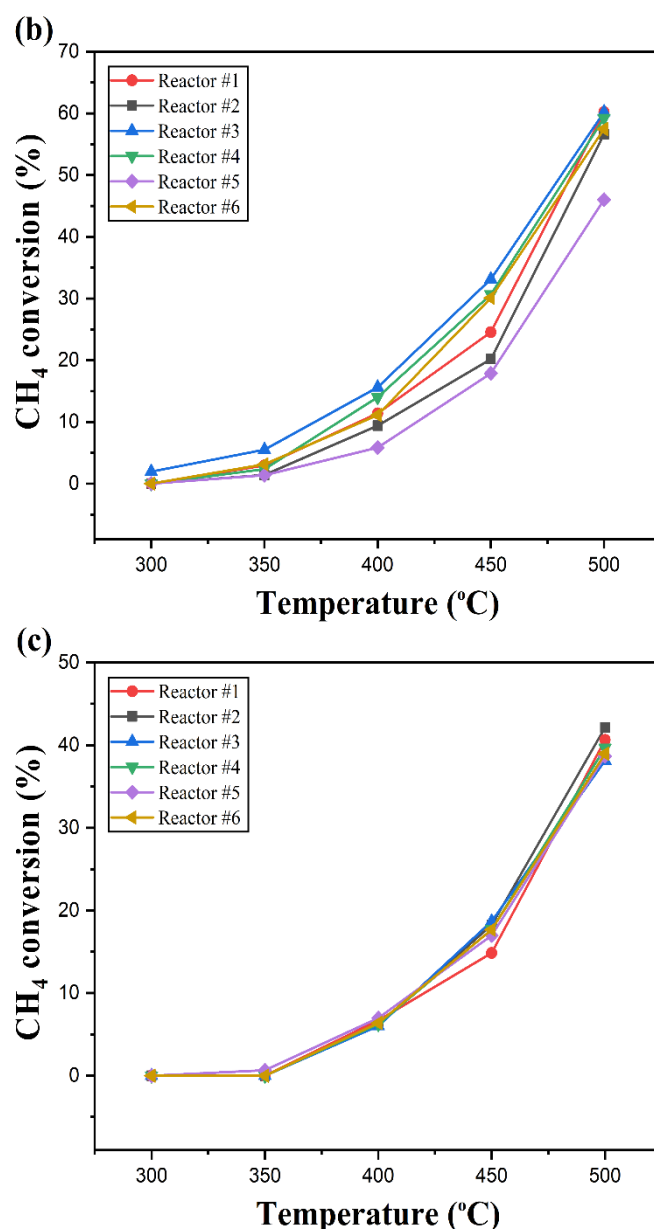
Fig. 5.9. Methane conversion as a function of the reaction temperature at the total flow rate of (a) 150 mL min^{-1}, (b) 300 mL min^{-1} and (c) 500 mL min^{-1} in plate-type microreactors with different channel configurations (Reactors #1 - 6) Conditions: T = 300 ^{o}C - 500 ^{o}C, Φ = 2, 3.5 wt% Pt/γ-Al$_2$O$_3$ catalyst. Other reactor details and catalyst properties are shown in Table 5.1.

With regard to the different channel configurations in microreactors, the methane conversion ranked with the following order: double serpentine channels (Reactor #3) > obstacled straight channels (Reactor #4) > vascular network (Reactor #6) > straight parallel channels (Reactor #1) > cavity (Reactor #2) > meshed circuit (Reactor #5). This trend is more pronounced at a lower total flow rate (e.g., 150 mL min^{-1}; Fig. 5.9a) and becomes insignificant at higher flow rate (e.g., 500 mL min^{-1}; Fig. 5.9c). The straight parallel channel microreactor (Reactor #1)

presented a higher methane conversion than the cavity microreactor (Reactor #2). The relatively lower methane conversion in Reactor #2 might be due to the negative effect of the non-uniform velocity profile of the gas since only 1 flat cavity was involved (Fig. 5.2), even though it has the longest mean residence time (c.f. Table 5.1). In other words, the catalyst coating around the cavity experienced different contact times with the reactant mixture, leading to an overall conversion decrease. In contrast, the gas flow distribution should be (much) improved in Reactor #1, given the flow was distributed into 16 parallel straight microchannels contributing to a more uniform contact time between the reactants and catalyst. The obstacle reactor (Reactor #4) is actually an improved version of Reactor #1, with a slightly higher coating surface area and longer mean residence time (c.f. Table 5.1). Besides, the structure of successive obstacles with the split-and-recombine shape enabled to improve the gas mixing and further enhance the external mass transfer compared to Reactor #1, especially at the mass transfer limited regime (at relatively higher temperatures or low flow rates). It thus offered a slight increase in the methane conversion under the same working conditions compared with Reactor #1. Among all the tested reactors, the highest methane conversion has been achieved by using the double serpentine channel microreactor (Reactor #3). This could be attributed primarily to a relatively higher coating surface area (than all the others except Reactors #6) and relatively longer residence time (than Reactors #1 and 4). In addition, the double serpentine structure could effectively promote the gaseous mixing due to the formation of secondary flow on the channel cross-section [68], thus improving their transfer to the coating external surface and contributing to a better conversion. The vascular reactor (Reactor #6) has the highest coating surface area as well as a longer residence time than the other reactors except Reactor #2 (Table 5.1). Despite these advantages, it presented a methane conversion level in between those of Reactors #4 and 1 (Figs. 9a and b). This is likely due to the non-uniform fluid distribution among the horizontal microchannel sections and thus an insufficient utilization of the coated catalyst. Some microchannels could be overloaded with gas mixture in the vascular network while others were underloaded, which might be related to the vascular structure causing a less uniform distribution of gas mixture. An improved design by carefully adjusting the resistance in the vertical diverging/converging channels may help solve this problem, based on the study of Tondeur et al. [61]. The lowest methane conversion was found in the meshed circuit microreactor (Reactor #5) under the same tested conditions. It has been reported that the flow pattern in the meshed circuit was similar to a continuous stirred tank reactor, and likely tended to be the divergent flow pattern even at low Reynolds numbers [69]. This indicates that the gas

has the chance to flow towards different directions due to divergent flow appeared in the meshed circuit. This probably resulted in the non-uniform flow distribution and/or somewhat broad residence time distribution, and thus a lowest methane conversion.

In summary, guidelines regarding the optimal channel configurations in plate-type microreactors for the CMC should comprehensively consider the coating surface area, residence time (distribution), fluid distribution uniformity, and the efficient use of catalyst in order to achieve a desirable methane conversion. Further detailed investigation on the local flow and temperature distribution characteristics by using simulation or optical visualization techniques would help give a clearer view and better understanding in this aspect.

Fig. 5.10 depicts the methane conversion as a function of the operating temperature at $\Phi = 6$ and a total flow rate of 150 mL min^{-1} in Reactors #1 - 6. Similar conversion trends and the same microreactor performance ranking were observed as compared to the case of $\Phi = 2$ (Fig. 5.9a). A lower methane conversion was obtained at $\Phi = 6$ than $\Phi = 2$. A comparison of T_{50} values at $\Phi = 2$ and 6 for different channel configurations is also given in Table 5.4. It is found that the T_{50} value at $\Phi = 2$ is slightly lower than that at $\Phi = 6$ for each channel configuration tested. In other words, the methane conversion decreased a bit when Φ increased from 2 (stoichiometric ratio) to 6 (oxygen-rich). The competitive adsorption between methane and oxygen over the catalyst surface could be one of the main reasons, given the methane adsorption energy is higher than that of oxygen [70]. The adsorbed oxygen is likely to inhibit the weakly adsorbed methane in these light-off experiments, leaving less chances for methane being further oxidized [71]. Thus, the favorable fractional coverage of adsorbed reactants over the active sites is essential for achieving the desired methane conversion. However, caution must be taken when interpreting the trend because the difference in the T_{50} value under $\Phi = 2$ and $\Phi = 6$ is only several degree Celsius (c.f. Table 5.4). An opposite trend may be observed when the operating procedures change as will be further discussed in the following sub-section.
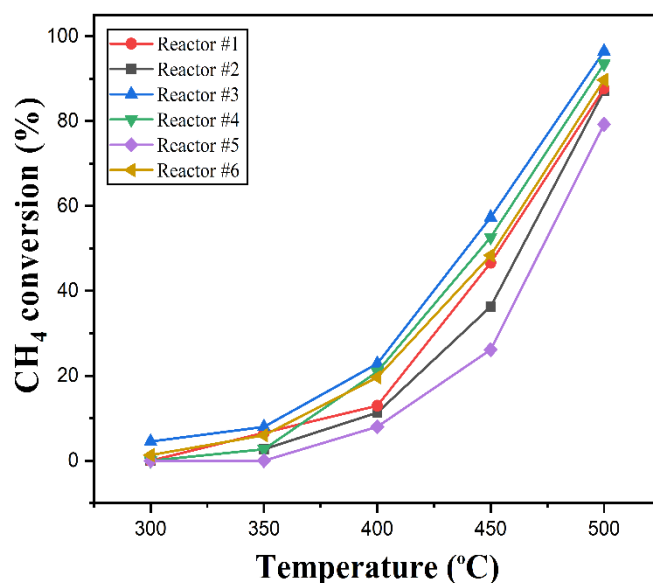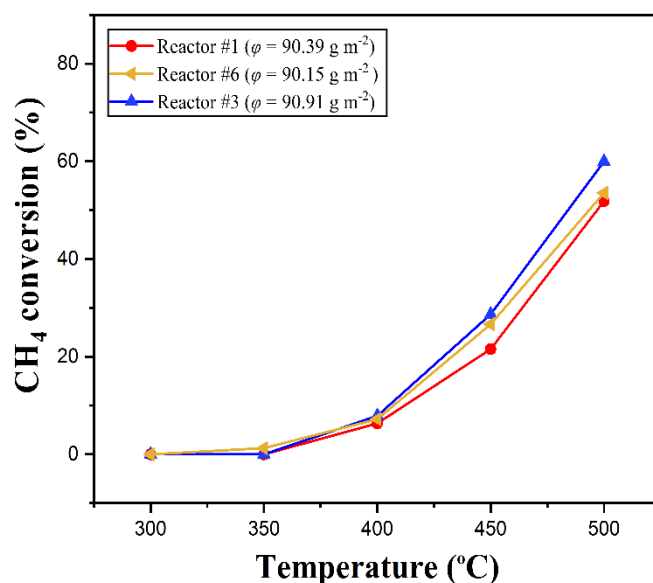
Fig. 5.10. Methane conversion as a function of the temperature in plate-type microreactors with different channel configurations (Reactors #1 - 6). Conditions: T = 300 - 500 ℃, Φ = 6, Q_{tot} = 150 mL min^{-1}, 3.5 wt% Pt/γ-Al$_2$O$_3$ catalyst. Other reactor parameters and catalyst properties are shown in Table 5.1.

Table 5.4

T_{50} value for the CMC experimental data presented in Figs. 9a and 10.

Reactor	T_{50} (℃) [a, b]	
	Φ = 2	Φ = 6
#1	460.0	462.8
#2	451.8	456.4
#3	437.5	443.5
#4	446.0	448.4
#5	470.6	472.2
#6	449.8	452.2

[a] T_{50} indicates the temperature for reaching 50% methane conversion; Conditions are shown in Figs. 9a and 10.

[b] Estimated from the polynomial regression line (cf. other details in Table 5.2).

The results of Fig. 5.9 were obtained in Reactors #1 - 6 with almost identical catalyst mass. Due to the surface area difference, the specific catalyst loading (φ) differs to some extent per reactor (Table 5.1). This implies a coating thickness difference, which could lead to a different influence of internal diffusion on the overall reaction rate in each microreactor. To further shed light on this, some additional experiments were conducted in Reactors #1, 3 and 6, but now with almost the same specific catalyst loading (φ = 90.5 ± 0.5 g m^{-2}) by adjusting the coated catalyst mass accordingly. As shown in Fig. 5.11, the same conversion trend as a function of the temperature (at a total flow rate of 300 mL min^{-1} and Φ = 2) was observed in Reactors #1, #3, #6 as presented in Fig. 5.9b. Also, the methane conversion decrease follows the same order of Reactor #3 > Reactor #6 > Reactor #1, especially at relative higher temperatures (e.g., > 400 ^{o}C). Since in these reactors the coating thickness can be considered identical, the difference of methane conversion between each reactor is attributed to different channel geometries resulting in the different coating surface area, fluid mixing behaviour and residence time property therein.

Fig. 5.11. Methane conversion as a function of the temperature in plate-type microreactors with different channel configurations (Reactor #1, 3 and 6). Conditions: T = 300 - 500 ^{o}C, Φ = 2, Q_{tot} = 300 mL min^{-1}, 3.5 wt% Pt/γ-Al$_2$O$_3$ catalyst, φ = 90.5 ± 0.5 g m^{-2} (realized by adjusting the coated catalyst mass). Other reactor parameters and catalyst properties are shown in Table 5.1.

5.3.2.2. Effect of molar ratio of O$_2$ to CH$_4$

To investigate the effect of the inlet molar ratio of O$_2$ to CH$_4$ (Φ), the CMC experiments were further conducted in Reactors #1 – 6 at 450 ^{o}C and 150 mL min^{-1}. The results of different tested

reactors are shown in Fig. 5.12. which reveal the same trend in terms of the microreactor performance rank as that shown in Fig. 5.9a. As Φ was increased from 0.5 up to 1.5, the methane conversion was improved gradually in each microreactor, which is due to the (severely) insufficient supply of oxygen limiting the adsorbed methane to be further converted. The highest methane conversion was found at ca. $\Phi = 1.5$ (instead of 2 as the stoichiometric ratio for the methane combustion) for each tested channel configuration. It could be thus due to firstly at $\Phi = 1.5$, there is an increased oxygen supply together with the consumption of methane in not only the combustion reaction, but also side reactions (such as methane partial oxidation and steam reforming) that require less amount of oxygen [72]. Moreover, a higher light-off temperature is required for the above-mentioned side reactions than for the methane combustion [73], thus such side reactions are more favoured to occur at higher temperature levels (e.g., at 450 ^{o}C relevant to Fig. 5.12). The existence of a variety of complex reactions under oxygen-lean conditions can be confirmed by the selectivities of CO_2, CO and H_2 as displayed in Fig. 5.13. For $\Phi \geq 2$, only CO_2 could be found as product ($S_{CO_2} = 100$ %) while no CO or H_2 was detected in the product gas. For $\Phi < 2$, more amounts of CO and H_2 were produced, i.e., the selectivity of CO is ca. 2% - 4% and H_2 ca. 4% - 16% while the rest product is CO_2. Moreover, it seems that a balance between the adsorbed oxygen and methane has been achieved on the catalyst surface at ca. $\Phi = 1.5$ for the best methane conversion, which largely explains the significant conversion drop at $\Phi = 2$ or above. A way to further increase the methane conversion (e.g., to above 90%) at this stoichiometric ratio is by raising the reaction temperature (e.g., see Fig. 5.9a). With Φ increasing from 2 to 6, the hysteresis effect plays an important role in determining the reaction conversion. The hysteresis phenomenon has been demonstrated via switching the molar ratio of O_2 to CH_4, where a higher conversion could be maintained when changing back to the low conversion conditions [74,75]. That is, a (relatively) high conversion state has been previously obtained at $\Phi = 0.5$ - 1.5 and could be maintained to some extent when further increasing the Φ value afterwards. Under such circumstances, the catalyst surface was primarily dominated by the adsorbed oxygen over the catalyst surface, and the oxygen concentration on the catalyst could be considered as constant in the present molar ratio experiment due to high conversion state. Given the less methane present in the feed and competing for a constant number of active sites, relatively more methane had the possibility to be adsorbed and converted, leading to a slight conversion increase at $\Phi > 2$.

To further elucidate the observed conversion trend especially at $\Phi > 2$, Table 5.5 compares the methane conversion in the molar ratio experiment here (Fig. 5.12) and that in the light-off

experiment (Figs. 9a and 10) under the same working conditions. The methane conversion turned out to be consistently higher in the molar ratio experiment. This can be explained by the hysteresis phenomenon present in the molar ratio experiment (procedurally related), but absent in the light-off experiment.
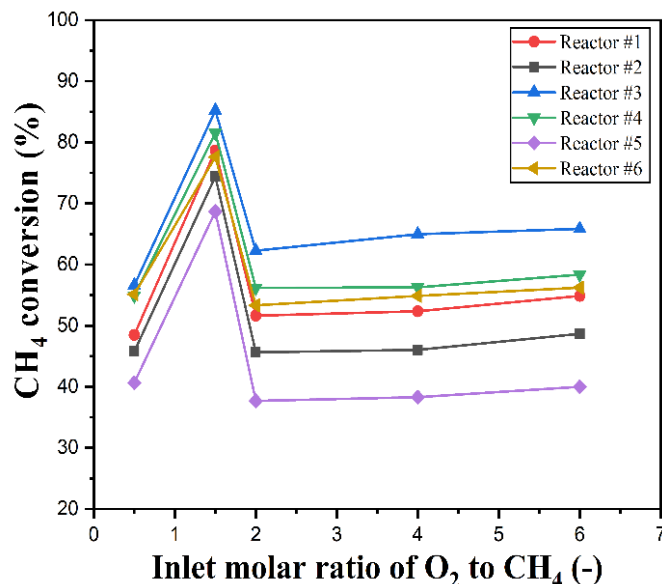

Fig. 5.12. Methane conversion as a function of Φ in in various plate-type microreactors. Conditions: T = 450 °C, Φ = 0.5 - 6 (sequentially changed from small to large values in the experiments), Q_{tot} =150 mL min^{-1}. 3.5 wt% Pt/γ-Al$_2$O$_3$, Other reactor parameters and catalyst properties are shown in Table 5.1.
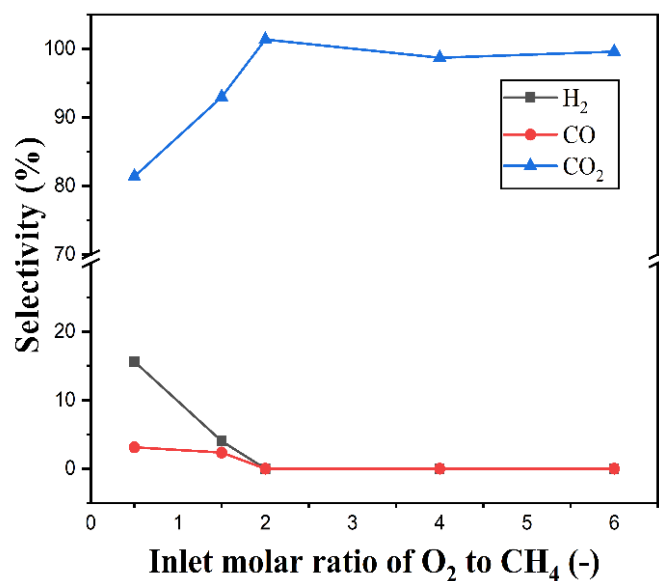
Fig. 5.13. Selectivities of H$_2$, CO, CO$_2$ as a function of Φ in the straight parallel channel microreactor (Reactor #1). Other conditions are the same as in Fig. 5.12.

Table 5.5

Comparison of the methane conversion in different reactors between the light-off experiment and the molar ratio experiment.

Reactor	X_{CH_4} in light-off experiment [a]		X_{CH_4} in molar ratio experiment [b]	
	$\Phi = 2$	$\Phi = 6$	$\Phi = 2$	$\Phi = 6$
#1	38.6	36.3	45.6	48.7
#2	48.4	46.6	51.6	54.9
#3	60.4	57.3	62.3	65.8
#4	54.8	52.6	56.2	58.4
#5	28.6	26.2	37.7	40.0
#6	52.1	48.4	53.3	56.2

[a] Conditions are shown in Figs. 5.9a and 5.10, $T = 450$ °C;

[b] Conditions are shown in Fig. 5.12.

5.3.2.3. Effect of total flow rate

The methane conversion as a function of the total flow rate in various plate-type microreactors (Reactors #1 - 6) is further displayed in Fig. 5.13. Generally, the methane conversion remarkably decreased when the total flow rate increased, mainly due to the decreased mean residence time (τ; cf. Eq. (5.4)) in every tested reactor. With the increased flow rate, the methane conversion decrease tended to slow down and became insignificant especially at sufficiently high flow rates (ca. 300 mL min^{-1} for Reactors #1 and 5; ca. 450 mL min^{-1} for Reactors #2 - 4 and 6). This could be due to the (much) improved external mass transfer at such high flow rates that contributed positively to the methane conversion. To improve the conversion at such high flow rates, the catalyst loading/mass and/or the operating temperature should be increased, so that the kinetic rate increases and contributes more to the overall reaction rate.
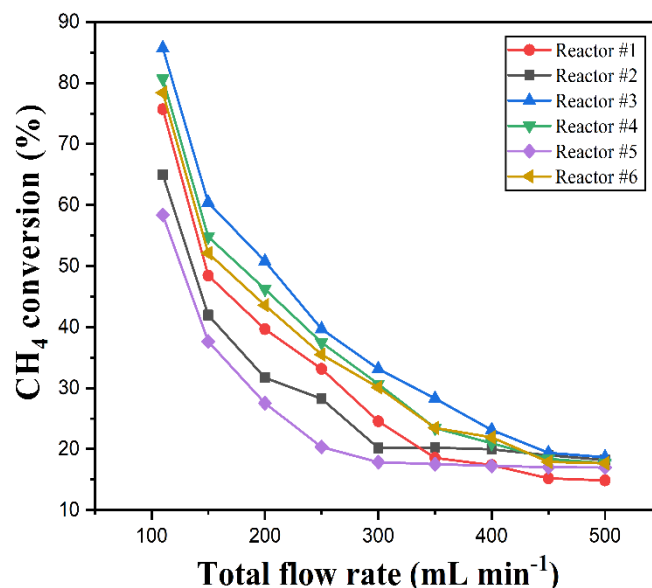
Fig. 5.14. Methane conversion as a function of the total gas flow rate in various plate-type microreactors. Conditions: T = 450 °C, Φ = 2, 3.5 wt% Pt/γ-Al$_2$O$_3$. Other reactor parameters and catalyst properties are shown in Table 5.1.

5.4. Conclusions and prospects

An experimental investigation has been firstly performed for the CMC in the straight parallel channel microreactor (made of FeCrAlloy) with washcoated Pt/γ-Al$_2$O$_3$ catalyst. At increasing operating temperature, a remarkable increase in the methane conversion was observed. An obvious decrease in the methane conversion was found upon increasing the total flow rate due to the reduction of the residence time, and such conversion decrease is insignificant at sufficiently high flow rates due to the improved external mass transfer. The existence of an optimal catalyst specific loading (φ = 57.6 g m^{-2}) rendering the highest methane conversion has been observed. A higher specific loading (e.g., φ = 90.39 g m^{-2}) hinders the mass transfer due to a more significant internal diffusion limitation in the thicker coating layer, whereas a lower specific loading (e.g., φ = 39.45 g m^{-2}) could not provide sufficient active sites, both leading to a lower methane conversion. In this type of microreactor, the bifurcated tree-like structural component placed at the outlet as the gas collector has presented a higher methane conversion than that using it as the inlet gas distributor. This could be attributed to the presence of a more uniform gas distribution in the former case.

Other five type of microreactors with different channel configurations (comprising cavity, double serpentine microchannels, obstacled microchannels, meshed circuit and vascular

network) have also been tested. Their performance in the CMC has been compared with that of the straight parallel channel microreactor, with regard to the influence of various factors including the reaction temperature, inlet molar ratio of O_2 to CH_4 and total flow rate. The results suggest that the double serpentine channel microreactor exhibited the highest methane conversion, whereas the meshed circuit microreactor showed the lowest conversion. The effective usage of the coating surface area, a more uniform flow distribution and the sufficient residence time are essential factors that contribute to the higher methane conversion. A higher methane conversion was obtained in the molar ratio experiment than that in the light-off experiment under otherwise identical conditions, mainly due to the hysteresis phenomenon. The highest methane conversion can be achieved in each microreactor at $\Phi = 1.5$, because of the additional involvement of other complex side reactions under oxygen-lean conditions. Moreover, the methane conversion for each tested reactor has appeared to decrease with the total gas flow rate increase due to the reduced residence time, despite the gradually improved external mass transfer.

This study is expected to provide useful guidelines regarding the optimal channel configurations in plate-type microreactors for the CMC, in view of future scaling-up in practice. A close investigation into the fluid distribution and temperature characteristics in different channel configurations of the plate-type microreactor using CFD simulation or optical visualization techniques could be the next research step to further elucidate the reaction performance. Moreover, the heat and mass transfer behaviour, reaction mechanism and kinetics need to be further investigated and addressed for a better design and operation of these microreactors.

Appendix 5.A

Design and sizing of the inlet fluid distributor and outlet fluid collector structures

The design of tree-like bifurcated structure is based on the literature [76,77], and the detailed configuration is presented in Fig. 5.A.1a. The gas mixture flows through the cascade bifurcations, allowing a (uniform) splitting into the downstream channels. The sharp fillet structures were designed, but it tends to be the concentric fillet structure in actual plate-type multichannel reactors due to the manufacture limitation. It is reported that flow separation and recirculation could occur in the sharp fillet structure, and the concentric fillet structure without backflow is recommended [78]. The detailed geometric parameters of the tree-like bifurcation are presented in Table 5.A.1. The design of channel width at the index j (w_j) is based on the following

equation:

$$w_j = w_n/r^{n-j} \qquad (5.A.1)$$

where r is equal to 0.77 and w_n (width of the channel at the last index n) is equal to 1.50 mm [77]). The calculation of $l_{j,tot}$ (channel length between indices j and $j+1$) is based on the equation of

$$l_{j,tot}/w_j = 0.05 Re_j \qquad (5.A.2)$$

where Re_j is the Reynolds number at each index j and calculated as

$$Re_j = \frac{\rho \times \frac{Q_{tot}/2^j}{w_j h} \times \frac{2 h w_j}{(h+w_j)}}{\mu} \qquad (5.A.3)$$

Thus, there is

$$Re_{j+1}/Re_j = \frac{1}{2} \frac{h + w_n/r^{n-j}}{(h + w_n/r^{n-j-1})} \qquad (5.A.4)$$

In order to save more space for the reaction microchannel, a simple rectangular structure was utilized as the gas collector for Reactors #1, 2, 4 and 5, with its dimensions presented in Fig. 5.A.1c. Simple bilateral divergent/convergent channels (Fig. 5.A.1b) were used for both the inlet and outlet structures of Reactors #3 and 6.
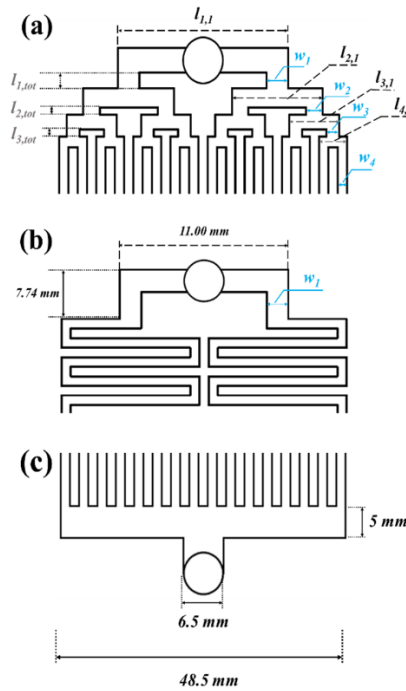
Fig. 5.A.1. Geometry and dimensions of the inlet/outlet structures: (a) the inlet distributor for Reactors #1, 2, 4, 5; (b) the inlet distributor and outlet collector for Reactors #3 and 6; (c) the outlet collector for Reactors #1, 2, 4 and 5.

Table 5.A.1

Geometric parameters of tree-like bifurcated structure.

Index number j	w_j	$l_{j,tot}$	w_j/w_{j-1}	$l_{j,tot}/w_j$	$l_{j,1}$	Re_j [a]
	(mm)	(mm)	(-)	(-)	(mm)	(-)
Index 1	3.48	3.25	0.77	0.93	27.48	18.64
Index 2	2.68	1.52	0.77	0.57	14.68	11.35
Index 3	2.06	0.70	0.77	0.34	8.06	6.82
Index 4	1.50	0.30	0.73	0.20	4.50	4.03

Note: [a] Re_j value is based on a total flow rate of 300 mL min^{-1}.

References

[1]   C. Zou, Q. Zhao, G. Zhang, B. Xiong, Energy revolution: from a fossil energy era to a new energy era, Nat. Gas Ind. B. 3 (2016) 1-11. https://doi.org/10.1016/j.ngib.2016.02.001.

[2]   G. Karavalakis, T.D. Durbin, M. Villela, J.W. Miller, Air pollutant emissions of light-duty vehicles operating on various natural gas compositions, J Nat. Gas Sci. Eng,. 4 (2012) 8-16. https://doi.org/10.1016/j.jngse.2011.08.005.

[3]   International Energy Agency (IEA). Natural Gas Information. https://www.iea.org/reports/natural-gas-information-2019. [Acessed 20 April 2020].

[4]   M. Mehrpooya, M. Khalili, M.M.M. Sharifzadeh, Model development and energy and exergy analysis of the biomass gasification process (Based on the various biomass sources), Renew Sust Energ Rev. 91 (2018) 869-887. https://doi.org/10.1016/j.rser.2018.04.076.

[5]   F. Ahmad, E.L. Silva, M.B.A. Varesche, Hydrothermal processing of biomass for anaerobic digestion-A review, Renew Sust Energ Rev. 98 (2018) 108-124. https://doi.org/10.1016/j.rser.2018.09.008.

[6]   D. Gielen, Global energy transformation - a roadmap to 2050, International Renewable Energy Agency (IRENA), 2018.

[7]   A.W. Petrov, D. Ferri, F. Krumeich, M. Nachtegaal, J.A. van Bokhoven, O. Kröcher, Stable complete methane oxidation over palladium based zeolite catalysts, Nat. Commun. 9 (2018) 2545-2553. http://dx.doi.org/10.1038/s41467-018-04748-x.

[8]   I. Manisalidis, E. Stavropoulou, A. Stavropoulos, E. Bezirtzoglou, Environmental and Health Impacts of Air Pollution: A Review, Frontiers in Public Health. 8 (2020).

[9]   Official Journal of the European Union. Commision regulation (EU) No. 813/2013, http://data.europa.eu/eli/reg/2013/813/oj; [Accessed 2 August 2013].

[10]   J. Chen, H. Arandiyan, X. Gao, J. Li, Recent advances in catalysts for methane combustion, Catal. Surv. Asia. 19 (2015) 140-171. https://doi.org/10.1007/s10563-015-9191-5.

[11]   J.H. Lee, D.L. Trimm, Catalytic combustion of methane, Fuel Process. Technol. 42 (1995) 339-359. http://doi.org/10.1016/0378-3820(94)00091-7.

[12]   R.J. Farrauto, Low-temperature oxidation of methane, Science. 337 (2012) 659-660. https://doi.org/10.1126/science.1226310.

[13]   J. Yang, Y. Guo, Nanostructured perovskite oxides as promising substitutes of noble metals catalysts for catalytic combustion of methane, Chin. Chem. Lett. 29 (2018) 252-260. https://doi.org/10.1016/j.cclet.2017.09.013.

[14]   A. Cruellas, T. Melchiori, F. Gallucci, M. van Sint Annaland, Advanced reactor concepts for oxidative coupling of methane, Catal. Rev. 59 (2017) 234-294. https://doi.org/10.1080/01614940.2017.1348085.

[15]   L. He, Y. Fan, J. Bellettre, J. Yue, L. Luo, A review on catalytic methane combustion at low temperatures: Catalysts, mechanisms, reaction conditions and reactor designs, Renew Sust Energ Rev. (2019) 109589.

[16]   R.J. Farrauto, M. Hobson, T. Kennelly, E. Waterman, Catalytic chemistry of supported palladium for combustion of methane, Appl. Catal. A. 81 (1992) 227-237. https://doi.org/10.1016/0926-860X(92)80095-T.

[17]   D. Wang, J. Gong, J. Luo, J. Li, K. Kamasamudram, N. Currier, A. Yezerets, Distinct reaction pathways of methane oxidation on different oxidation states over Pd-based three-way catalyst (TWC), Appl. Catal. A. 572 (2019) 44-50. https://doi.org/10.1016/j.apcata.2018.12.022.

[18]   I.E. Beck, V.I. Bukhtiyarov, I.Y. Pakharukov, V.I. Zaikovsky, V.V. Kriventsov, V.N. Parmon, Platinum nanoparticles on Al_2O_3: Correlation between the particle size and activity in total methane oxidation, J. Catal. 268 (2009) 60-67. https://doi.org/10.1016/j.jcat.2009.09.001.

[19]   C.-P. Hwang, C.-T. Yeh, Platinum-Oxide Species Formed on Progressive Oxidation of Platinum Crystallites Supported on Silica and Silica–Alumina, J. Catal. 182 (1999) 48-55. http://dx.doi.org/10.1006/jcat.1998.2304.

[20]   E. Garbowski, C. Feumi-Jantou, N. Mouaddib, M. Primet, Catalytic combustion of methane over palladium supported on alumina catalysts: Evidence for reconstruction of particles, Appl. Catal. A. 109 (1994) 277-291. https://doi.org/10.1016/0926-860X(94)80124-X.

[21]   C.A. Müller, M. Maciejewski, R.A. Koeppel, A. Baiker, Combustion of methane over palladium/zirconia: effect of Pd-particle size and role of lattice oxygen, Catal. Today. 47 (1999) 245-252. https://doi.org/10.1016/S0920-5861(98)00305-8.

[22]   D. Ciuparu, E. Altman, L. Pfefferle, Contributions of lattice oxygen in methane combustion over PdO-Based catalysts, J. Catal. 203 (2001) 64-74. http://doi.org/10.1006/jcat.2001.3331.

[23]   C.A. Müller, M. Maciejewski, R.A. Koeppel, R. Tschan, A. Baiker, Role of lattice oxygen in the combustion of methane over PdO/ZrO_2: combined pulse TG/DTA and MS study with ^{18}O-labeled catalyst, The Journal of Physical Chemistry. 100 (1996) 20006-20014. https://doi.org/10.1021/jp961903a.

[24]   S. Seimanides, M. Stoukides, Catalytic oxidation of methane on polycrystalline palladium supported on stabilized zirconia, J. Catal. 98 (1986) 540-549. https://doi.org/10.1016/0021-9517(86)90342-8.

[25]   P. Jodłowski, R. Jędrzejczyk, D. Chlebda, A. Dziedzicka, Ł. Kuterasiński, A. Gancarczyk, M. Sitarz, Non-noble

metal oxide catalysts for methane catalytic combustion: sonochemical synthesis and characterisation, Nanomaterials. 7 (2017) 174. https://doi.org/10.3390/nano7070174.

[26]   Y.S. Seo, S.P. Yu, S.J. Cho, K.S. Song, The catalytic heat exchanger using catalytic fin tubes, Chem. Eng. Sci. 58 (2003) 43-53. http://dx.doi.org/10.1016/S0009-2509(02)00475-X.

[27]   M. O'Connell, G. Kolb, R. Zapf, Y. Men, V. Hessel, Bimetallic catalysts for the catalytic combustion of methane using microreactor technology, Catal. Today. 144 (2009) 306-311. https://doi.org/10.1016/j.cattod.2008.10.053.

[28]   Q. Dong, S. Zhang, Z. Duan, Q. Zhou, An energy analysis of the catalytic combustion burner, Heat. Technol. Energy Eff. (2006). http://hdl.handle.net/1969.1/5530.

[29]   D. X.Chun, Applied studies on methane catalytic combustion development of a natural gas premixed catalytic burner and boiler for household applications. 2005; Sichuan University. Thesis in chinese.

[30]   R. Burch, P.K. Loader, Investigation of Pt/Al_2O_3 and Pd/Al_2O_3 catalysts for the combustion of methane at low concentrations, Appl. Catal., B. 5 (1994) 149-164. http://dx.doi.org/10.1016/0926-3373(94)00037-9.

[31]   M. Lyubovsky, L.L. Smith, M. Castaldi, H. Karim, B. Nentwick, S. Etemad, R. LaPierre, W.C. Pfefferle, Catalytic combustion over platinum group catalysts: fuel-lean versus fuel-rich operation, Catal. Today. 83 (2003) 71-84. http://dx.doi.org/10.1016/s0920-5861(03)00217-7.

[32]   Z. Wang, J. Deng, Y. Liu, H. Yang, S. Xie, Z. Wu, H. Dai, Three-dimensionally ordered macroporous $CoCr_2O_4$-supported Au-Pd alloy nanoparticles: Highly active catalysts for methane combustion, Catal. Today. 281, Part 3 (2017) 467-476. https://doi.org/10.1016/j.cattod.2016.05.035.

[33]   M. Halabi, M. De Croon, J. Van Der Schaaf, P. Cobden, J. Schouten, Intrinsic kinetics of low temperature catalytic methane-steam reforming and water-gas shift over $Rh/Ce_\alpha Zr_{1-\alpha}O_2$ catalyst, Appl. Catal. A. 389 (2010) 80-91. https://doi.org/10.1016/j.apcata.2010.09.005.

[34]   H. Hao, Z. Liu, F. Zhao, W. Li, Natural gas as vehicle fuel in China: A review, Renew Sust Energ Rev. 62 (2016) 521-533. https://doi.org/10.1016/j.rser.2016.05.015.

[35]   S. Su, X. Yu, A 25 kWe low concentration methane catalytic combustion gas turbine prototype unit, Energy. 79 (2015) 428-438. http://dx.doi.org/10.1016/j.energy.2014.11.031.

[36]   M. Bhagiyalakshmi, R. Anuradha, S.D. Park, T.S. Park, W.S. Cha, H.T. Jang, Effect of bimetallic Pt-Rh and trimetallic Pt-Pd-Rh catalysts for low temperature catalytic combustion of methane, Bull. Korean Chem. Soc. 31 (2010) 120-124. https://doi.org/10.5012/bkcs.2010.31.01.120.

[37]   P. Gélin, M. Primet, Complete oxidation of methane at low temperature over noble metal based catalysts: a review, Appl. Catal., B. 39 (2002) 1-37. http://dx.doi.org/10.1016/S0926-3373(02)00076-0.

[38]   S.B. T.V. Choudhary, V.R. Choudhary, Catalysts for combustion of methane and lower alkanes review, Appl. Catal. A. 234 (2002) 1-23. https://doi.org/10.1016/S0926-860X(02)00231-4.

[39]   K. Persson, K. Jansson, S. Jaras, Characterisation and microstructure of Pd and bimetallic Pd-Pt catalysts during methane oxidation, J. Catal. 245 (2007) 401-414. https://doi.org/10.1016/j.jcat.2006.10.029.

[40]   K. Persson, A. Ersson, A.M. Carrera, J. Jayasuriya, R. Fakhrai, T. Fransson, S. Järås, Supported palladium-platinum catalyst for methane combustion at high pressure, Catal. Today. 100 (2005) 479-483. https://doi.org/10.1016/j.cattod.2004.08.018.

[41]   G. Pecchi, P. Reyes, T. López, R. Gómez, $Pd-CeO_2$ and $Pd-La_2O_3$/alumina-supported catalysts: their effect on the catalytic combustion of methane, J. Non-Cryst. Solids. 345 (2004) 624-627. https://doi.org/10.1016/j.jnoncrysol.2004.08.110.

[42]   S. Specchia, E. Finocchio, G. Busca, G. Saracco, V. Specchia, Effect of S-compounds on Pd over $LaMnO_3 \cdot 2ZrO_2$ and $CeO_2 \cdot 2ZrO_2$ catalysts for CH_4 combustion, Catal. Today. 143 (2009) 86-93. https://doi.org/10.1016/j.cattod.2008.10.035.

[43]   R. Zapf, C. Becker-Willinger, K. Berresheim, H. Bolz, H. Gnaser, V. Hessel, G. Kolb, P.Löb, A.K. Pannwitt, A. Ziogas, Detailed characterization of various porous alumina-based catalyst coatings within microchannels and their testing for methanol steam reforming, Chem. Eng. Res. Des. 81 (2003) 721-729. https://doi.org/10.1205/026387603322302887.

[44]   N.R. Peela, A. Mubayi, D. Kunzru, Washcoating of γ-alumina on stainless steel microchannels, Catal. Today. 147 (2009) S17-S23. https://doi.org/10.1016/j.cattod.2009.07.026.

[45]   M. Liauw, M. Baerns, R. Broucek, O. Buyevskaya, J. Commenge, J. Corriou, L. Falk, K. Gebauer, H. Hefter, O. Langer, Microreaction Technology: Industrial Prospects. Springer, 2000, pp. 224-234.

[46]   L. He, Y. Fan, L. Luo, J. Bellettre, J. Yue, Preparation of $Pt/\gamma-Al_2O_3$ catalyst coating in microreactors for catalytic methane combustion, Chem. Eng. J. 380 (2020) 122424. https://doi.org/10.1016/j.cej.2019.122424.

[47]   X. Xu, H. Vonk, A. Cybulski, J.A. Moulijn, Alumina washcoating and metal deposition of ceramic monoliths, Stud. Surf. Sci. Catal., Elsevier, 1995, pp. 1069-1078.

[48]   K. Haas-Santo, M. Fichtner, K. Schubert, Preparation of microstructure compatible porous supports by sol-gel synthesis for catalyst coatings, Appl. Catal. A. 220 (2001) 79-92. https://doi.org/10.1016/S0926-860X(01)00714-1.

[49]   B. Schmidt, M. Liauw, Mass transfer limitations in microchannel reactors, Catal. Today. 110 (2005) 15-25.

https://doi.org/10.1016/j.cattod.2005.09.019.

[50]   P.L. Mills, D.J. Quiram, J.F. Ryley, Microreactor technology and process miniaturization for catalytic reactions-A perspective on recent developments and emerging technologies, Chem. Eng. Sci. 62 (2007) 6992-7010. https://doi.org/10.1016/j.ces.2007.09.021.

[51]   J. Ganley, K. Riechmann, E.G. Seebauer, R. Masel, Porous anodic alumina optimized as a catalyst support for microreactors, J. Catal. 227 (2004) 26-32. https://doi.org/10.1016/j.jcat.2004.06.016.

[52]   J.C. Ganley, E.G. Seebauer, R.I. Masel, Porous anodic alumina microreactors for production of hydrogen from ammonia, AlChE J. 50 (2004) 829-834. https://doi.org/10.1002/aic.10078.

[53]   C.M. Miesse, R.I. Masel, C.D. Jensen, M.A. Shannon, M. Short, Submillimeter-scale combustion, AlChE J. 50 (2004) 3206-3214. https://doi.org/10.1002/aic.10271.

[54]   K.F. Jensen, Microreaction engineering-is small better?, Chem. Eng. Sci. 56 (2001) 293-303. https://doi.org/10.1016/S0009-2509(00)00230-X.

[55]   M.H. Exchangers, Microreactors: new technology for modern chemistry, Weinheim: Wiley/VCH, 2000.

[56]   M. Mundhwa, R.D. Parmar, C.P. Thurgood, A comparative parametric study of a catalytic plate methane reformer coated with segmented and continuous layers of combustion catalyst for hydrogen production, J. Power Sources. 344 (2017) 85-102. http://dx.doi.org/10.1016/j.jpowsour.2017.01.082.

[57]   M. Mundhwa, C.P. Thurgood, Numerical study of methane steam reforming and methane combustion over the segmented and continuously coated layers of catalysts in a plate reactor, Fuel Process. Technol. 158 (2017) 57-72. http://doi.org/10.1016/j.fuproc.2016.12.002.

[58]   R.C. Ramaswamy, P.A. Ramachandran, M.P. Duduković, Coupling exothermic and endothermic reactions in adiabatic reactors, Chem. Eng. Sci. 63 (2008) 1654-1667. http://dx.doi.org/10.1016/j.ces.2007.11.010.

[59]   M.S. Mettler, G.D. Stefanidis, D.G. Vlachos, Scale-out of microreactor stacks for portable and distributed processing: coupling of exothermic and endothermic processes for syngas production, Ind. Eng. Chem. Res. 49 (2010) 10942-10955. https://doi.org/10.1021/ie100459b.

[60]   H. Mei, C. Li, S. Ji, H. Liu, Modeling of a metal monolith catalytic reactor for methane steam reforming-combustion coupling, Chem. Eng. Sci. 62 (2007) 4294-4303. http://dx.doi.org/10.1016/j.ces.2007.05.011.

[61]   D. Tondeur, Y. Fan, J.-M. Commenge, L. Luo, Uniform flows in rectangular lattice networks, Chem. Eng. Sci. 66 (2011) 5301-5312. https://doi.org/10.1016/j.ces.2011.07.027.

[62]   V. Meille, S. Pallier, G. Santacruzbustamante, M. Roumanie, J. Reymond, Deposition of γ-Al$_2$O$_3$ layers on structured supports for the design of new catalytic reactors, Appl. Catal. A. 286 (2005) 232-238. https://doi.org/10.1016/j.apcata.2005.03.028.

[63]   L. Giani, C. Cristiani, G. Groppi, E. Tronconi, Washcoating method for Pd/γ-Al$_2$O$_3$ deposition on metallic foams, Appl. Catal., B. 62 (2006) 121-131. https://doi.org/10.1016/j.apcatb.2005.07.003.

[64]   P.A.R. Cebollada, E. Garcia Bordejé, Optimisation of physical properties of γ-alumina coating microreactors used for the growth of a carbon nanofiber layer, Chem. Eng. J. 149 (2009) 447-454. https://doi.org/10.1016/j.cej.2009.02.016.

[65]   Y. Fan, R. Boichot, T. Goldin, L. Luo, Flow distribution property of the constructal distributor and heat transfer intensification in a mini heat exchanger, AlChE J. 54 (2008) 2796-2808. https://doi.org/10.1002/aic.11597.

[66]   P. Zhou, D. Tarlet, Y. Fan, X. Hu, L. Luo, Water-in-oil emulsification in a bifurcated tree-like network: Flow distribution properties and their impact on the emulsion polydispersity, Chem. Eng. Res. Des. 134 (2018) 420-433. https://doi.org/10.1016/j.cherd.2018.04.031.

[67]   X. Guo, Y. Fan, L. Luo, Multi-channel heat exchanger-reactor using arborescent distributors: A characterization study of fluid distribution, heat exchange performance and exothermic reaction, Energy. 69 (2014) 728-741. https://doi.org/10.1016/j.energy.2014.03.069.

[68]   R.H. Liu, M.A. Stremler, K.V. Sharp, M.G. Olsen, J.G. Santiago, R.J. Adrian, H. Aref, D.J. Beebe, Passive mixing in a three-dimensional serpentine microchannel, Journal of microelectromechanical systems. 9 (2000) 190-197. https://doi.org/10.1109/84.846699.

[69]   Z. Ni, E. Seebauer, R.I. Masel, Effects of microreactor geometry on performance: differences between posted reactors and channel reactors, Ind. Eng. Chem. Res. 44 (2005) 4267-4271. https://doi.org/10.1021/ie048956w.

[70]   O. Deutschmann, R. Schmidt, F. Behrendt, J. Warnat, Numerical modeling of catalytic ignition, Symposium (International) on Combustion. 26 (1996) 1747-1754. http://dx.doi.org/10.1016/S0082-0784(96)80400-0.

[71]   S. Oh, P. Mitchell, R. Siewert, Methane oxidation over noble metal catalysts as related to controlling natural gas vehicle exhaust emissions, Catalytic control of air pollution. ACS Publication, Washington, DC, 1992.

[72]   G.S. Bugosh, V.G. Easterling, I.A. Rusakova, M.P. Harold, Anomalous steady-state and spatio-temporal features of methane oxidation on Pt/Pd/Al$_2$O$_3$ monolith spanning lean and rich conditions, Appl. Catal., B. 165 (2015) 68-78. https://doi.org/10.1016/j.apcatb.2014.09.058.

[73]   K.H. Delgado, L. Maier, S. Tischer, A. Zellner, H. Stotz, O. Deutschmann, Surface reaction kinetics of steam- and CO$_2$-reforming as well as oxidation of methane over nickel-based catalysts, Catalysts. 5 (2015) 871-904. https://doi.org/10.3390/catal5020871.

[74]   A. Amin, A. Abedi, R. Hayes, M. Votsmeier, W. Epling, Methane oxidation hysteresis over Pt/Al$_2$O$_3$, Appl. Catal. A. 478 (2014) 91-97. https://doi.org/10.1016/j.apcata.2014.03.032.

[75]   I.Y. Pakharukov, A.Y. Stakheev, I.E. Beck, Y.V. Zubavichus, V.Y. Murzin, V.N. Parmon, V.I. Bukhtiyarov, Concentration hysteresis in the oxidation of methane over Pt/γ-Al$_2$O$_3$: X-ray absorption spectroscopy and kinetic study, ACS Catal. 5 (2015) 2795-2804. https://doi.org/10.1021/cs501964z.

[76]   P. Li, D. Coopamah, N. Dhar. Analysis and optimization of flow distribution channels for uniform flow in fuel cells. in ASME 2008 Fluids Engineering Division Summer Meeting collocated with the Heat Transfer, Energy Sustainability, and 3rd Energy Nanotechnology Conferences. 2008. American Society of Mechanical Engineers Digital Collection.

[77]   H. Liu, P. Li, Even distribution/dividing of single-phase fluids by symmetric bifurcation of flow channels, Int. J. Heat Fluid Flow. 40 (2013) 165-179. https://doi.org/10.1016/j.ijheatfluidflow.2013.01.011.

[78]   H. Liu, P. Li, K. Wang, The flow downstream of a bifurcation of a flow channel for uniform flow distribution via cascade flow channel bifurcations, Appl. Therm. Eng. 81 (2015) 114-127. http://dx.doi.org/10.1016/j.applthermaleng.2015.02.028.

Chapter 6

Catalytic methane combustion: conclusions, challenges and

future prospects

In this chapter, the main findings of this thesis have been firstly summarized. Then, the challenges and future prospects have been proposed for the catalytic methane combustion (CMC) in microreactors.

6.1. Summary of the current thesis

The main conclusions in this work are summarized as follows.

In Chapter 2, a comprehensive literature review of CMC has been presented, including the different catalyst types, reaction mechanisms and kinetics, reaction conditions (e.g., the effect of temperature, space velocity, oxygen to methane molar ratio, natural gas composition, operating pressure) and various applied reactors (e.g., fix-bed, wall-coated, membrane, fluidized bed), which offers a comprehensive reference for the follow-up research in this field.

In Chapter 3, the stability and adhesion of washcoated $Pt/\gamma-Al_2O_3$ catalyst has been examined in a multichannel microreactor. A best adhesion of $\gamma-Al_2O_3$ layer could be obtained by choosing the suitable binder (e.g., PVA with 3 - 5 wt% and MW of 57,000 - 186,000), initial $\gamma-Al_2O_3$ particle size (3 μm) and pH value (pH ≈ 3.5), in order to form the sufficient hydrogen bridges with the well-dispersed alumina. Furthermore, the FeCrAlloy used as the microreactor substrate presented a better adhesion both for rectangular and round channels than 316L stainless steel. The washcoated $Pt/\gamma-Al_2O_3$ catalyst was further realized in the parallelized multichannel microreactor for CMC tests following the above identified optimized coating procedure. It has been found that the operating temperature has the greater influence on the methane conversion compared with those of the gas flow rate and O_2/CH_4 molar ratio. The favourable coverage of the adsorbed methane and oxygen over the catalyst surface is essential to obtain a desired methane conversion. Moreover, more reaction heat was released from the reaction at a higher flow rate, causing an obvious temperature increase along the microreactor. Similarly, the microreactor temperature was increased with increasing O_2/CH_4 molar ratio. The temperature profile along the multi-channel microreactor is in line with the methane conversion obtained therein.

In Chapter 4, the CMC was performed in the single-layer and multi-layer washcoated $Pt/\gamma-Al_2O_3$ catalysts deposited inside the capillary microreactors. Two different cases were tested in the multi-layer system. In case 1, the total weight of Pt in the catalyst in the multi-layer system was maintained theoretically the same as that the single-layer system. In case 2, the theoretical Pt loading in the multi-layer system was kept identical to the respective single layer system. The coating thickness in both cases could be assumed to increase proportionally with the number

of layers. The influences of operating conditions (e.g., the reaction temperature, molar ratio of oxygen to methane and total flow rate) as well as the Pt weight and loading were examined. In the single-layer catalyst system, a best methane conversion of 95.17% could be obtained under 500 °C at a total flow rate of 30 mL min^{-1} and an oxygen to methane molar ratio (Φ) = 2. The methane conversion exhibited a remarkable increase with the increasing Pt loading or mass, and the light-off phenomenon started to occur at above 400 °C. The difference in the increment of the methane conversion tended to slow down with the Pt loading increase, possibly caused by the more significant internal diffusion limitation in the coating given the increased intrinsic kinetic rate. A lower methane conversion was obtained at Φ = 5 than that at Φ = 2 in the light-off experiment due to the competitive adsorption of the reactants. The decrease in the methane conversion tend to slow down at sufficiently high flow rates, which could be attributed to the improved external mass transfer that compensated the decreased conversion therein. In the multi-layer system in case 1, the double-layer catalyst system yielded a lower methane conversion at Φ =2 and 5 than that of the corresponding single-layer system at otherwise identical working conditions. This is possibly caused by the more significant internal diffusion resistance in thicker coating layers. When it comes to case 2, the double- and triple-layer catalyst systems generally yielded a higher methane conversion at Φ =2 and 5 than that of the respective single-layer system, indicating the (active) participation of all coating layers (instead of the top layer alone) in the reaction. Another implication is that in case 2, the reaction rate tended to be more limited by the catalyst amount than the internal diffusion. However, the methane conversion is nearly identical between the single-layer and the double- and triple-layer (case 2) systems at Φ = 1 throughout the studied temperature range (350 - 500 °C), because the reaction rate is mainly limited by the insufficient oxygen supply.

In Chapter 5, the straight parallel channel microreactor (Reactor #1) deposited with Pt/γ-Al$_2$O$_3$ catalyst was firstly examined for the CMC. The optimized specific catalyst loading of 57.6 g m^{-2} presented a best methane conversion. An obvious decrease in the methane conversion with higher or lower specific catalyst loadings could be explained by the increased internal diffusion resistance in thicker coatings or and the absence of sufficient active sites in thinner coatings, respectively. A higher methane conversion could be obtained when using the tree-like structure as the outlet product collector rather than as the inlet fluid distributor, especially at high flow rates. This could be explained by the higher local at the inlet and outlet of the reaction microchannel, which is beneficial for a more uniform fluid distribution therein. Subsequently, the CMC has been performed in other plate-type microreactors with various internal channel

configurations coated with Pt/γ-Al$_2$O$_3$ catalyst, including cavity microreactor (Reactor #2), double serpentine channel microreactor (Reactor #3), obstacled straight channel microreactor (Reactor #4), meshed circuit microreactor (Reactor #5) and vascular microreactor (Reactor #6). The double serpentine channel microreactor has shown the highest methane conversion, which could be due to the proper coverage of the coating surface area and a relatively long residence time. Moreover, an improved gaseous mixing in the serpentine microchannels could resulted in an improved external mass transfer and thus contributed to a higher methane conversion. On the contrary, the meshed circuit microreactor presented the lowest methane conversion, probably due to the divergent flow presented in the flow circuit. This probably resulted in a non-uniform flow distribution and/or somewhat broader residence time distribution, and thus the lowest methane conversion. The results regarding the influence of the reaction temperature, molar ratio of O$_2$:CH$_4$ and total flow rate in these microreactors are generally in line with those observed in Chapter 4.

6.2. Short-term research work as a continuation of the current thesis

Although a substantial research effort has been elaborated in this thesis, the investigations are still far from being over, especially on the improved catalyst activity, the understanding of the catalytic behaviour between active sites and the adsorbed reactants, the reaction pathways, and ways to suppresses the catalyst deactivation. Possible extensions of the current thesis are briefly summarized as follows.

6.2.1. Noble metal catalyst

In the current thesis, the monometallic Pt/γ-Al$_2$O$_3$ catalyst has been used for the CMC. The improvement of catalyst activity (e.g., using different active species and supports) has not been addressed. In this regard, the bimetallic catalysts (e.g., Pt-Pd [1,2], Pd-Ce [3,4], Pt-Co [5]) could be selected as a priority for the following research work. Bimetallic catalysts present many advantages over monometallic catalysts [6-8], because of the presence of a better synergetic effect between the metal-metal interactions [9,10]. Moreover, the introduction of Pt into Pd-based catalyst is beneficial to increase the dispersion of active sites [11], thermostability [12] and the oxygen exchange [13]. The increased cost is their main disadvantage. More efforts should be paid on combining non-noble or transitional metals (e.g., Fe, Ni, Mg, Co) with noble metal catalysts (e.g., Pt, Pd), which could ensure the high catalytic activity at a reasonable cost of catalysts.

In addition to the active species mentioned above, the catalyst support also plays an important

role. In our thesis, γ-Al$_2$O$_3$ has been used exclusively as the support, due to its high chemical stability and mechanical resistance. However, surface properties of γ-Al$_2$O$_3$ might be changed at the high temperature levels, which could result in the reduced specific surface area and thereby lower catalyst activity. ZrO$_2$, CeO$_2$, MgO, SiO$_2$, zeolites and other non-noble metal oxides with improved thermal stability may be considered as the support for the next stage. It is reported that the introduction of CeO$_2$ as support effectively promoted the oxygen species exchange between the active composition and support [14,15]. The addition of ZrO$_2$ in PdO/Al$_2$O$_3$ catalyst exhibited a better active site reformation, resulting in a higher methane conversion [16]. Moreover, the support properties (e.g., basicity/acidity, electrophilic/electrophobic properties) could directly affect the oxidation state of the active species, which in turn determines the catalytic activity. Yoshida et al. [17] reported that Pd/MgO and Pd/ZrO$_2$ catalyst with lower acidity presented a decrease in the methane conversion despite the higher Pd oxidation state on MgO and ZrO$_2$. The highest methane conversion can be found for Pd/Al$_2$O$_3$ and Pd/SiO$_2$ catalyst due to the use of higher acidic supports. When the acidity continued to increase, SiO$_2$-ZrO$_2$, SiO$_2$-Al$_2$O$_3$ catalysts rendered a decrease in the methane conversion as a result of lower Pd oxidation state from the strong acidic support [17]. Additionally, the binary oxide could be formed between the support and the active species (e.g., PdO-MgO) so as to stabilize the cluster anion by electrooptic cations.

Based on the discussion above, more promising attempts could include (but is not limited to) Pt-Mg, Pt-Ni, Pt-Fe as active species, and ZrO$_2$, CeO$_2$, SiO$_2$, TiO$_2$ as support. Other substituted additives (e.g., La, Mn, V, Ba, etc.) may also be considered to further adjust the catalyst acid/base strength, the interaction strength between active species and support, and the increase of oxygen vacancies.

6.2.2. Coating preparation

In current thesis, Pt/γ-Al$_2$O$_3$ catalyst has been successfully coated onto the microreactor wall by using the suspension method (i.e., the slurry coating technique). This method needs to be experimentally adjusted once varying active species and supports, i.e., for various bimetallic catalysts (e.g., Pt-Mg, Pt-Ni, Pt-Fe as active species, and ZrO$_2$, CeO$_2$, SiO$_2$, TiO$_2$ as support). Other preparation methods need to be attempted in order to ensure the adaptability for certain washcoat catalysts, as referred to elsewhere (e.g., a dip-coating [18], sol-gel [19,20], chemical vapor deposition [21,22], physical vapor deposition [23,24]).

In the thesis, Pt/γ-Al$_2$O$_3$ coating catalyst has been studied in round tube made of stainless steel.

The adhesion properties have been found to still have space for improvement (Chapter 2). The introduction of Fe_2O_3, NiO, Cr_2O_3 into $Pt/\gamma-Al_2O_3$ coating catalyst may help, owing to the possible formation of chemical bonding between catalyst and stainless steel. The main composition of stainless steel (e.g., Fe, Ni, Cr) might have more affinity with the catalyst containing those species, and thus further verification is needed. Meanwhile, it is strongly suggested to test the recycling of washcoat catalyst in the stainless steel microreactor, and to compare the fresh and the re-used washcoat catalyst regarding the catalytic performance in future studies.

Additionally, as for the bimetallic catalyst preparation, it is worth noting that different structures (e.g., core-shell [25,26], alloy [27], heterostructure [28]) could be adjusted by employing different preparation methods, resulting in the significant difference on the catalyst activity [29]. Among different structures, Pt-Pd alloy can be easily formed during the calcination step by traditional impregnation methods [30], leading to the improved catalytic activity [30,31]. However, other studies illustrated that the formation of Pt-Pd alloy structure presented a negative influence on the methane conversion [32,33]. This different point of view might be due to different procedures during the catalyst preparation, or the different reaction conditions triggered [34]. The property of single Pt and Pd particles might be deprived after the formation of Pt-Pd alloy. Therefore, the development of bimetallic catalysts with a precise control of the target structure is still a challenge by far.

6.2.3. Catalyst deactivation

In Chapters 3 and 4, the catalyst life of $Pt/\gamma-Al_2O_3$ has been examined in the fixed-bed reactor or microreactor for up to 100 h, and the catalyst activity presented an obvious decrease at increasing reaction time in our experiment. Herein, the catalyst deactivation is another important issue to be addressed to prolong the catalyst life for its wider application in practice [35]. By overviewing catalyst deactivation causes and mechanisms [36,37], three fundamental reasons can be generally summarized: poisoning, coking or fouling, and ageing. The coke deposition is carried out by blocking active sites, whereas catalyst aging is commonly caused by sintering that refers to the reduction of specific surface area, and eventually result in the structure modification and catalyst deactivation. Meanwhile, the catalyst poisoning could be also caused by the strong chemisorption on the active sites from the impurities (e.g., sulfur, chlorine) included in the reactant gases, resulting in the alteration of active sites and irreversible deactivation of catalyst [37].

More attempts thereby are proposed to deal with the catalyst deactivation in the future research.

(1) As for Pd-based catalysts, at least both the dispersed and crystalline PdO phases are commonly considered as active sites existing on Al_2O_3 support, as reported by Farrauto et al. [16]. Owing to the highly exothermic reaction, the actual temperature inside the catalyst could be extremely high (adiabatic temperature rise is equal to ca. 2000 ^{o}C at Φ = 2). It results in the growth of Pt particles and the formation of less active PtO_2 [38,39], which will possibly accelerate the catalyst deactivation [40]. The addition of promoters (rare earth oxides) into the catalysts could be alternative solutions to resist deactivation by increasing the thermal decomposition temperature[16]. Additionally, the use of bi-/triple-metallic catalysts may also dramatically prevent the catalyst deactivation [41].

(2) The reversible deactivation of catalyst caused by water vapor and CO_2 could be attribute to the formation of hydroxyl group over the catalyst surface, hindering the exchange of oxygen species [42,43]. Further experimental work on preparing new supports and/or additives to suppress the formation of hydroxide is highly recommended in order to enhance the oxygen mobility.

(3) One of the highly challenging issues is to develop catalyst with the excellent resistance to the sulfur poisoning. The noble-metal catalyst could be easily poisoned when exposed to the natural gas containing sulfur compounds (e.g. SO_2/H_2S) [44,45]. The mechanism of Pd-based catalyst deactivation by sulphur poisoning has been established by many researchers [35,44,45]. The formation of the inactive stable sulphate species ($PdSO_3/PdSO_4$) results in the irreversible deactivation of the catalyst, and the capacity of SO_2 adsorption plays an important role in the sulfur resistance [46]. Thus, it is essential to develop the noble metal-based catalysts with high resistance to sulphur species which are able to dramatically decrease the stability of Pd sulphate species over the catalyst surface.

(4) The catalyst regeneration is an essential strategy to effectively reuse catalysts after deactivation. It has been reported that sulfur-poisoned Pd-based could be regenerated under H_2 or He atmosphere, somehow removing the sulfur species from the catalyst surface [47]. Overall, the comprehensive understanding of the regeneration mechanism and kinetics is not much reported. More effective procedures and methods for the catalyst regeneration are still needed by far.

As for this thesis, the recycling of washcoat catalyst needs further investigation on the stainless steel microreactor. It would be interesting to characterize the catalyst recovery efficiency and

the catalyst activity after certain rounds of recycling experiment.

(5) Possible pretreatment on desulfurization of natural gas still needs to be improved in order to better satisfy the downstream reactions. Concerning the pollutant regulations, more investigation should be invested on biomethane in the future, which is a green alternative path with low emission compared with convention fuel resources.

6.2.4. Kinetics and mechanisms

In the thesis, the kinetics and mechanisms have not been investigated. There are some conflicts between the proposed different mechanisms by far, where the main difference between Langmuir-Hinshelwood and Eley-Rideal mechanisms is whether both methane and oxygen adsorb on the catalyst surface or only the adsorbed oxygen reacts with gaseous methane. And the reaction rate for these two mechanisms is relevant to the partial pressure of methane and oxygen. The Mars-van-Krevelen mechanism, widely accepted in the open literature, believes that oxygen vacancies over the surface of PdO_x crystallites play an important role due to the formation of Pd-O bonds. It is reported that reaction order of oxygen over the Pd/Al_2O_3 catalyst is equal to 0.04, whereas methane reaction order is 0.62. The reaction order of oxygen increased to 0.23 in the $Pd-Co/Al_2O_3$ catalyst and the methane reaction order decreased to 0.59, which might be due to that Co^{2+} activated more active oxygen species over the catalyst surface [48]. This suggested that the reaction followed the Langmuir-Hinshelwood mechanism over these two catalysts. However, as for Pd-Co-DEG (diethylene glycol)/Al_2O_3 catalyst, the reaction followed the Mars-van-Krevelen mechanism because the Pd-O bond formed via reacting with the adsorbed methane, and the partial pressure of oxygen presented a little influence on the reaction rate. Future investigations on the kinetic parameters and mechanisms over various catalysts, especially on the bimetallic catalysts (e.g., Pt-Ni, Pt-Fe, etc.), are still required.

6.2.5. Mass transfer characterization

In the current thesis, the mass transfer characteristics have been briefly discussed on both the capillary and plate-type microreactors. Future investigations on the mass transfer could be focused on: (1) the internal diffusion as a function of the Pt/ γ-Al_2O_3 coating properties (e.g., thickness, pore structure, Pt particle size) subject to different coating preparation methods, and their quantitative influence on the CMC reaction. (2) the gas-solid mass transfer models to be built up for different reaction microchannel configurations, which requires a good understanding in the flow behaviour of the reactant mixture as well. (3) The simulation studies on the flow and temperature profiles over various geometries of micro reactors under different

reaction conditions (e.g., flow rate, O_2:CH_4 molar ratio) , and their influence on mass transfer and reaction in order to compare with the experimental work presented in Chapter 5.

6.2.6. Partial methane oxidation

The partial methane oxidation under molar ratios of O_2:CH_4 < 2 has been briefly mentioned in the PhD thesis (Chapters 4 and 5), over the same Pt/γ-Al_2O_3 catalyst. The proportion of CO_2 in the product is too high in our experiments, which results in the undesirable synthesis gas ratio of H_2/CO. It might be due to the unfavorable reactant ratio and unsuitable catalyst that result in the overoxidation of products. Many interesting works remain to be performed in this respect in order to generate the syngas. Effect of the reactant ratio, pressure, temperature and mechanisms on the product selectivity has been evaluated in many earlier studies [49-51]. The carbon deposition over the catalyst mainly due to thermal decomposition of CH_4 and CO at high temperatures will easily result in the catalyst deactivation. Moreover, special attention is needed on the influence of different CH_4/O_2 ratios on the product selectivity distribution, and an H_2/CO ratio of 2 is ideal for downsteam processes for methanol synthesis.

6.3. Future prospects for long term research

6.3.1. Catalysts

The mixed oxide catalysts have not been involved in this PhD thesis despite that they play an important role in this field. Regarding the hexaaluminate, a great effort has been made on improving the specific surface area and catalyst activity, but many more efforts are still required in future studies so as to improve the catalyst activity. It could be summarized as follows. (1) The highly dispersed noble nanoparticles supported on hexaaluminates with the high specific surface area is expected to develop further in details. The high dispersion of active centres after reduction could be formed via the high-dispersion noble nanoparticles in the structure of hexaaluminates, which significantly improves the catalyst activity. (2) Co-substituted metal alloys could be formed via bi-/triple-noble nanoparticles supported on hexaaluminates, and the structure of hexaaluminate catalyst might be modified, which probably improves the catalyst activity towards the targeted reactions. The fundamental understanding and investigations on the surface structure of hexaaluminates with substituted metals are still lacking, especially on the coherent relationship between the noble-metal substitution, oxygen vacancies, active oxygen species and catalyst activity. Moreover, the interaction between active sites and reactants (or intermediates) is still not clear. (3) The improvement of the specific surface area could be achieved by preventing the particle growth during the crystallization. It has been

reported that the calcination procedure could be operated under inert atmosphere for the crystallization process before removing the template, which may effectively suppress the growth and agglomeration of particles [52]. More studies on the preparation methods are still required, especially on how to increase the specific surface area.

Regarding the perovskite catalyst, a significant progress has been reached for the CMC. Some promising directions for perovskite catalysts may be summarized as follows for the potential industrial applications. (1) The three-dimensional perovskite with hierarchically porous structure exhibited a superior catalytic activity, which could be attributed to the maximized exposure of active sites over the catalyst surface with abundant internal space to accommodate the reactants. Given this unique structure and desirable specific surface area, the well-defined porous structures with layered three-dimensional perovskites could be a very attractive direction for the next generation of high-activity catalysts. (2) Various morphologies of perovskite catalysts with regard to their influence of the catalytic activity are interesting to be investigated, such as nanowire structure, layered nanostructure. However, the structure collapse induced by the reduced activity of nanostructured perovskite catalysts might hinder further applications, which is also a challenging barrier to be overcome. (3) The principal influence of foreign-cation substitution on oxygen mobility and redox property is still unknown. The investigation needs to be performed on the intercontact between oxygen vacancies, lattice oxygen mobility and surface adsorbed oxygen. This is crucial for the catalyst activity because it could offer an in-depth understanding of the reaction mechanism. Moreover, the development of the new substitution systems with inexpensive material is also needed in order to improve the catalyst activity and reduce the cost.

6.3.2. Catalytic methane combustion coupling with endothermic reactions

In this section, the representative (micro)reactors coupling the CMC with different endothermic reactions are discussed, which could be considered as one of the most promising applications in the future [53].

6.3.2.1. Different reactors

The principle of coupling reactions is to maintain the system energetically self-sustaining by employing the heat generated from an exothermic reaction to drive an endothermic reaction. The reactor design, the energy conservation, the boundary conditions, etc., are main factors to cope with. In this section, the representative type of reactors and endothermic reactions are typically addressed.

As for regenerative coupling reactor, the exothermic and endothermic reactions alternatively happen in the same catalytic reactor. Temperature distribution along the reactor becomes more complex due to the continuous switching between the exothermic and endothermic reactions as well as the (significant) heat losses. Meanwhile, such frequent switching in the heating and cooling process easily results in the rapid damage of catalyst activity.

As for the direct coupling reactor, the exothermic and endothermic reaction take place at same time in the same catalytic reactor but without a separating wall between the reactions [54]. The reduction of heat losses between exothermic and endothermic reactions due to the direct heat exchange is one of main advantages of this type reactor [55]. The applied catalysts with bifunctions are one of the major concerns herein because the catalysts have to favor both exothermic and endothermic reactions.

As for the recuperative coupling reactor, both the exothermic and endothermic reactions take place in the same reactor but the conductive walls are applied between two reactions to transfer the released heat [53,54]. The process of heat exchange in the reactor can be performed in the different flow modes (e.g., co-current, counter-current), offering the respective advantages (and disadvantages). The outlet gases in the exothermic and endothermic reactions are able to be separated in this type of reactor, which is beneficial for the energy recovery and gas collection (e.g., H_2, synthesis gas from methane steam reforming). Therefore, more studies could be carried out on the following aspects:

(1) As for the direct coupling reactor, due to the reactant mixing, the products from the outlet stream collect from both reactions. Commonly the membrane reactor could be introduced at the end of reactor in order to collect and separate the hydrogen as the desire product (methane steam reforming as the endothermic reaction). As for the recuperative coupling in the microreactor, studies are mainly focused on the numerical simulations in order to investigate an optimized flow direction mode for the favourable energy supply. In order to obtained the higher yield, the multiple stacked microchannel reactors by coupling the methane combustion with the endothermic reaction are recommended, but rarely tested experimentally so far.

(2) The experiment results reported by Yin et al. [56] exhibited that it might be unable to accomplish the coupling of CMC with methane reforming (with CO_2) without additional heat supply. Thus, the extra heat source has to be introduced in order to maintain the whole energy balance of the system. Attention should also be paid to the selection of reactor material. The stainless steel with the relatively good heat conductivity enables to limit the formation of

hotspots, but on the other hand the heat losses could be greatly increased [57,58]. Thus, the reduction of surface to volume ratio, the utilization of the high insulation and high reflectance materials [59,60], the vacuum operation [61,62], etc., could be the possible solutions to reduce the thermal losses.

(3) The flow direction is another important parameter to be considered in the recuperative reactor, which could significantly influence the conversion of reactants. With respect to the co-current mode, the higher average temperature and reaction rate could be reached than the counter-current mode [63-65], and the hot spots and cold spots might be more easily to be formed under counter-current conditions. The alternative solutions could be the optimization of the catalyst location, the thickness (e.g., single/multi-layer systems) in the autothermal (micro)reactor. Meanwhile, the less amount of catalysts may be placed in the potential hotspots, and vice versa, in order to balance the temperature profile along the reactors.

(4) The actual temperature inside the catalysts/channel might be significantly different from the measured temperature by thermocouples on the catalysts/channel surface (in microreactors). Thus, the simulation results being predicted based on the experimental temperature could be different from the actual conversion values. One of the possible approaches is to employ the infrared camera mapping the actual temperature during the reaction. Thus, at least one side of reactor walls must be composed of a transparent material (e.g., quartz) to allow the optical visibility. While carrying out the experiment in the optically accessible reactor, the temperature profile could be clearly observed by the infrared temperature measurement on the catalyst surface [66]. In this way, a great number of mapping points at different positions of reactors could be collected, offering a more accurate reference to discriminate between the different mass/heat transfer models and preventing the errors in the fitted kinetic parameters.

(5) The experiment investigations would be very attractive for plate-type microreactors with alternate stacks (i.e., one above another) by combining the catalytic methane combustion with endothermic reactions. The modelling studies have been performed by e.g., Mundhwa et al. [65,67]. However, more experiment work needs to be carried out to verify the modelling results published in the literature. Typically, the actual heat and mass transfer models could be built up based on the experiment data under different conditions. This could provide a useful guideline for the scale-up of such microreactor systems aiming at industrial applications of the CMC in the future.

6.3.2.2. Representative endothermic reactions

Some representative endothermic reactions are commonly used for coupling with the CMC, such as the methane steam reforming, methane reforming with CO_2, dehydrogenation of propane to propylene, etc. One of the main applications of methane autothermal reforming is to produce the synthesis gas with high H_2/CO ratio by utilizing the energy from the CMC. A selective membrane is commonly used to remove some of the undesired product gases, so as to obtain highly-purity hydrogen from the endothermic reaction. The applied catalysts in the recuperative coupling reactor could be designed independently for exothermic and endothermic reactions. Commonly, Pt-Ni pair is one of the most frequent combinations. However, on the endothermic side, the coke formation of the catalyst is still a main challenge for methane steam/CO_2 reforming reaction [68,69]. It has been reported that the addition of Rh to Ni-/Mg-based catalysts is able to prevent the coke formation [68,69], and the bifunctional catalysts is still need to be well developed in the future.

References

[1] K. Persson, K. Jansson, S. Jaras, Characterisation and microstructure of Pd and bimetallic Pd-Pt catalysts during methane oxidation, J. Catal. 245 (2007) 401-414. https://doi.org/10.1016/j.jcat.2006.10.029.

[2] K. Persson, A. Ersson, A.M. Carrera, J. Jayasuriya, R. Fakhrai, T. Fransson, S. Järås, Supported palladium-platinum catalyst for methane combustion at high pressure, Catal. Today. 100 (2005) 479-483. https://doi.org/10.1016/j.cattod.2004.08.018.

[3] C. Shi, L. Yang, J. Cai, Cerium promoted Pd/HZSM-5 catalyst for methane combustion, Fuel. 86 (2007) 106-112. https://doi.org/10.1016/j.fuel.2006.05.029.

[4] L.H. Xiao, K.P. Sun, X.L. Xu, X.N. Li, Low-temperature catalytic combustion of methane over Pd/CeO_2 prepared by deposition-precipitation method, Catal. Commun. 6 (2005) 796-801. https://doi.org/10.1016/j.catcom.2005.07.015.

[5] Y. Mahara, T. Tojo, K. Murata, J. Ohyama, A. Satsuma, Methane combustion over $Pd/CoAl_2O_4/Al_2O_3$ catalysts prepared by galvanic deposition, RSC Advances. 7 (2017) 34530-34537. https://doi.org/10.1039/c7ra06150a.

[6] J.A. Rodriguez, D.W. Goodman, The nature of the metal-metal bond in bimetallic surfaces, Science. 257 (1992) 897-903. https://doi.org/10.1126/science.257.5072.897.

[7] P. Qu, S. Wang, W. Hu, Y. Wu, J. Chen, G. Zhang, P. Shen, Y. Chen, L. Zhong, A novel strategy to design PtPd bimetallic catalysts for efficient methane combustion, Catal. Commun. 135 (2020) 105900. https://doi.org/10.1016/j.catcom.2019.105900.

[8] K. Persson, A. Ersson, K. Jansson, N. Iverlund, S. Jaras, Influence of co-metals on bimetallic palladium catalysts for methane combustion, J. Catal. 231 (2005) 139-150. https://doi.org/10.1016/j.jcat.2005.01.001.

[9] K. Gschneidner, A. Russell, A. Pecharsky, J. Morris, Z. Zhang, T. Lograsso, D. Hsu, C.C. Lo, Y. Ye, A. Slager, A family of ductile intermetallic compounds, Nat. Mater. 2 (2003) 587-591. https://doi.org/10.1038/nmat958.

[10] T. Krenke, E. Duman, M. Acet, E.F. Wassermann, X. Moya, L. Mañosa, A. Planes, Inverse magnetocaloric effect in ferromagnetic Ni-Mn-Sn alloys, Nat. Mater. 4 (2005) 450-454. https://doi.org/10.1038/nmat1395.

[11] E.D. Goodman, S. Dai, A.-C. Yang, C.J. Wrasman, A. Gallo, S.R. Bare, A.S. Hoffman, T.F. Jaramillo, G.W. Graham, X. Pan, Uniform Pt/Pd bimetallic nanocrystals demonstrate platinum effect on palladium methane combustion activity and stability, ACS Catal. 7 (2017) 4372-4380. https://doi.org/10.1021/acscatal.7b00393.

[12] H. Nassiri, R.E. Hayes, N. Semagina, Stability of Pd-Pt catalysts in low-temperature wet methane combustion: Metal ratio and particle reconstruction, Chem. Eng. Sci. 186 (2018) 44-51. https://doi.org/10.1016/j.ces.2018.04.028.

[13] A. Maione, F. André, P. Ruiz, Structured bimetallic Pd-Pt/γ-Al_2O_3 catalysts on FeCrAlloy fibers for total combustion of methane, Appl. Catal., B. 75 (2007) 59-70. https://doi.org/10.1016/j.apcatb.2007.03.011.

[14] G. Pecchi, P. Reyes, T. López, R. Gómez, Pd-CeO_2 and Pd-La_2O_3/alumina-supported catalysts: their effect on the catalytic combustion of methane, J. Non-Cryst. Solids. 345 (2004) 624-627. https://doi.org/10.1016/j.jnoncrysol.2004.08.110.

[15] R.J. Farrauto, J.K. Lampert, M.C. Hobson, E.M. Waterman, Thermal decomposition and reformation of PdO catalysts; support effects, Appl. Catal., B. 6 (1995) 263-270. https://doi.org/10.1016/0926-3373(95)00015-1.

[16] R.J. Farrauto, M. Hobson, T. Kennelly, E. Waterman, Catalytic chemistry of supported palladium for combustion of methane, Appl. Catal. A. 81 (1992) 227-237. https://doi.org/10.1016/0926-860X(92)80095-T.

[17] H. Yoshida, T. Nakajima, Y. Yazawa, T. Hattori, Support effect on methane combustion over palladium catalysts, Appl. Catal., B. 71 (2007) 70-79. https://doi.org/10.1016/j.apcatb.2006.08.010.

[18] V. Meille, Review on methods to deposit catalysts on structured surfaces, Appl. Catal. A. 315 (2006) 1-17. https://doi.org/10.1016/j.apcata.2006.08.031.

[19] X. Xu, H. Vonk, A. Cybulski, J.A. Moulijn, Alumina washcoating and metal deposition of ceramic monoliths, Stud. Surf. Sci. Catal., Elsevier, 1995, pp. 1069-1078.

[20] K. Haas-Santo, M. Fichtner, K. Schubert, Preparation of microstructure compatible porous supports by sol-gel synthesis for catalyst coatings, Appl. Catal. A. 220 (2001) 79-92. https://doi.org/10.1016/S0926-860X(01)00714-1.

[21] M. Karches, M. Morstein, P. Rudolf von Rohr, R.L. Pozzo, J.L. Giombi, M.A. Baltanás, Plasma-CVD-coated glass beads as photocatalyst for water decontamination, Catal. Today. 72 (2002) 267-279. https://doi.org/10.1016/S0920-5861(01)00505-3.

[22] T. Aaltonen, M. Ritala, T. Sajavaara, J. Keinonen, M. Leskelä, Atomic layer deposition of platinum thin films, Chem. Mater. 15 (2003) 1924-1928. https://doi.org/10.1021/cm021333t.

[23] L.L. Pranevicius, P. Valatkevicius, V. Valincius, C. Montassier, Catalytic behavior of plasma-sprayed Al-Al_2O_3 coatings doped with metal oxides, Surf. Coat. Technol. 125 (2000) 392-395. https://doi.org/10.1016/S0257-8972(99)00584-8.

[24] L. Pranevicius, L.L. Pranevicius, P. Valatkevicius, V. Valincius, Plasma spray deposition of Al-Al_2O_3 coatings doped with metal oxides: catalytic applications, Surf. Coat. Technol. 123 (2000) 122-128. https://doi.org/10.1016/S0257-8972(99)00520-4.

[25] M. Cargnello, J.D. Jaén, J.H. Garrido, K. Bakhmutsky, T. Montini, J.C. Gámez, R. Gorte, P. Fornasiero, Exceptional activity for methane combustion over modular Pd@CeO_2 subunits on functionalized Al_2O_3, Science. 337 (2012) 713-717. https://doi.org/10.1126/science.1222887.

[26] M. Danielis, S. Colussi, C. de Leitenburg, L. Soler, J. Llorca, A. Trovarelli, Outstanding methane oxidation performance of Palladium-embedded ceria catalysts prepared by a one-step dry ball-milling method, Angew. Chem. 130 (2018) 10369-10373. https://doi.org/10.1002/anie.201805929.

[27] K. Persson, L.D. Pfefferle, W. Schwartz, A. Ersson, S.G. Järås, Stability of palladium-based catalysts during catalytic combustion of methane: The influence of water, Appl. Catal., B. 74 (2007) 242-250. https://doi.org/10.1016/j.apcatb.2007.02.015.

[28] D. Wang, Y. Li, Bimetallic nanocrystals: liquid-phase synthesis and catalytic applications, Adv. Mater. 23 (2011) 1044-1060. https://doi.org/10.1002/adma.201003695.

[29] X. Zou, Z. Rui, H. Ji, Core-shell NiO@PdO nanoparticles supported on alumina as an advanced catalyst for methane oxidation, ACS Catal. 7 (2017) 1615-1625. https://doi.org/10.1021/acscatal.6b03105.

[30] C. Carrillo, T.R. Johns, H. Xiong, A. DeLaRiva, S.R. Challa, R.S. Goeke, K. Artyushkova, W. Li, C.H. Kim, A.K. Datye, Trapping of mobile Pt species by PdO nanoparticles under oxidizing conditions, The journal of physical chemistry letters. 5 (2014) 2089-2093. https://doi.org/10.1021/jz5009483.

[31] H. Nie, J.Y. Howe, P.T. Lachkov, Y.-H.C. Chin, Chemical and structural dynamics of nanostructures in bimetallic Pt-Pd catalysts, their inhomogeneity, and their roles in methane oxidation, ACS Catal. 9 (2019) 5445-5461. https://doi.org/10.1021/acscatal.9b00485.

[32] K. Persson, K. Jansson, S.G. Järås, Characterisation and microstructure of Pd and bimetallic Pd-Pt catalysts during methane oxidation, J. Catal. 245 (2007) 401-414. https://doi.org/10.1016/j.jcat.2006.10.029.

[33] H. Nassiri, K.E. Lee, Y. Hu, R.E. Hayes, R.W. Scott, N. Semagina, Platinum inhibits low-temperature dry lean methane combustion through palladium reduction in Pd-Pt/Al_2O_3: An in situ X-ray absorption study, ChemPhysChem. 18 (2017) 238-244. https://doi.org/10.1002/cphc.201600993.

[34] L. Liotta, G. Di Carlo, G. Pantaleo, G. Deganello, Catalytic performance of Co_3O_4/CeO_2 and Co_3O_4/CeO_2-ZrO_2 composite oxides for methane combustion: Influence of catalyst pretreatment temperature and oxygen concentration in the reaction mixture, Appl. Catal., B. 70 (2007) 314-322. https://doi.org/10.1016/j.apcatb.2005.12.023.

[35] P. Gélin, L. Urfels, M. Primet, E. Tena, Complete oxidation of methane at low temperature over Pt and Pd catalysts for the abatement of lean-burn natural gas fuelled vehicles emissions: influence of water and sulphur containing compounds, Catal. Today. 83 (2003) 45-57. http://dx.doi.org/10.1016/s0920-5861(03)00215-3.

[36] C.H. Bartholomew, Mechanisms of catalyst deactivation, Appl. Catal. A. 212 (2001) 17-60. https://doi.org/10.1016/S0926-860X(00)00843-7.

[37] P. Forzatti, L. Lietti, Catalyst deactivation, Catal. Today. 52 (1999) 165-181. https://doi-org.proxy-ub.rug.nl/10.1007/978-3-662-05981-4_14.

[38] K. Murata, Y. Mahara, J. Ohyama, Y. Yamamoto, S. Arai, A. Satsuma, The metal-support interaction concerning the particle size effect of Pd/Al_2O_3 on methane combustion, Angew. Chem. Int. Ed. 56 (2017) 15993-15997. https://doi.org/10.1002/anie.201709124.

[39] K. Narui, H. Yata, K. Furuta, A. Nishida, Y. Kohtoku, T. Matsuzaki, Effects of addition of Pt to PdO/Al_2O_3 catalyst on catalytic activity for methane combustion and TEM observations of supported particles, Appl. Catal. A. 179 (1999) 165-173. https://doi.org/10.1016/S0926-860X(98)00306-8.

[40] M. Reinke, J. Mantzaras, R. Bombach, S. Schenker, A. Inauen, Gas phase chemistry in catalytic combustion of methane/air mixtures over platinum at pressures of 1 to 16 bar, Combust. Flame. 141 (2005) 448-468. https://doi.org/10.1016/j.combustflame.2005.01.016.

[41] M. Bhagiyalakshmi, R. Anuradha, S.D. Park, T.S. Park, W.S. Cha, H.T. Jang, Effect of bimetallic Pt-Rh and trimetallic Pt-Pd-Rh catalysts for low temperature catalytic combustion of methane, Bull. Korean Chem. Soc. 31 (2010) 120-124. https://doi.org/10.5012/bkcs.2010.31.01.120.

[42] H. Geng, Z. Yang, L. Zhang, J. Ran, Y. Chen, Experimental and kinetic study of methane combustion with water over copper catalyst at low-temperature, Energy Convers. Manage. 103 (2015) 244-250. https://doi.org/10.1016/j.enconman.2015.06.076.

[43] W.R. Schwartz, D. Ciuparu, L.D. Pfefferle, Combustion of Methane over Palladium-Based Catalysts: Catalytic Deactivation and Role of the Support, The Journal of Physical Chemistry C. 116 (2012) 8587-8593. https://doi.org/10.1021/jp212236e.

[44] Z. Yang, J. Liu, L. Zhang, S. Zheng, M. Guo, Y. Yan, Catalytic combustion of low-concentration coal bed methane over $CuO/\gamma-Al_2O_3$ catalyst: effect of SO_2, RSC Advances. 4 (2014) 39394-39399. https://doi.org/10.1039/C4RA05334F.

[45] D.L. Mowery, R.L. McCormick, Deactivation of alumina supported and unsupported PdO methane oxidation catalyst: the effect of water on sulfate poisoning, Appl. Catal., B. 34 (2001) 287-297. http://doi.org/10.1016/S0926-3373(01)00222-3.

[46] J. Chen, H. Arandiyan, X. Gao, J. Li, Recent advances in catalysts for methane combustion, Catal. Surv. Asia. 19 (2015) 140-171. https://doi.org/10.1007/s10563-015-9191-5.

[47] V.H. Nissinen, N.M. Kinnunen, M. Suvanto, Regeneration of a sulfur-poisoned methane combustion catalyst: Structural evidence of Pd_4S formation, Appl. Catal., B. 237 (2018) 110-115. https://doi.org/10.1016/j.apcatb.2018.05.057.

[48] J. Lin, Y. Chen, X. Liu, X. Chen, Y. Zheng, F. Huang, Y. Xiao, Y. Zheng, L. Jiang, Microstructural property regulation and performance in methane combustion reaction of ordered mesoporous alumina supported palladium-cobalt bimetallic catalysts, Appl. Catal., B. 263 (2020) 118269. https://doi.org/10.1016/j.apcatb.2019.118269.

[49] A.P. York, T. Xiao, M.L. Green, Brief overview of the partial oxidation of methane to synthesis gas, Top. Catal. 22 (2003) 345-358. https://doi.org/10.1023/A:1023552709642.

[50] C. Diehm, O. Deutschmann, Hydrogen production by catalytic partial oxidation of methane over staged Pd/Rh coated monoliths: Spatially resolved concentration and temperature profiles, Int. J. Hydrogen Energy. 39 (2014) 17998-18004. https://doi.org/10.1016/j.ijhydene.2014.06.094.

[51] R. Schwiedernoch, S. Tischer, C. Correa, O. Deutschmann, Experimental and numerical study on the transient behavior of partial oxidation of methane in a catalytic monolith, Chem. Eng. Sci. 58 (2003) 633-642. https://doi.org/10.1016/S0009-2509(02)00589-4.

[52] J. Gao, C. Jia, M. Zhang, F. Gu, G. Xu, Z. Zhong, F. Su, Template preparation of high-surface-area barium hexaaluminate as nickel catalyst support for improved CO methanation, RSC advances. 3 (2013) 18156-18163. https://doi.org/10.1039/C3RA41660G.

[53] M. Rahimpour, M. Dehnavi, F. Allahgholipour, D. Iranshahi, S. Jokar, Assessment and comparison of different catalytic coupling exothermic and endothermic reactions: a review, Appl. Energy. 99 (2012) 496-512. https://doi.org/10.1016/j.apenergy.2012.04.003.

[54] V. Salvatore, M. Luca, Catalytic combustion for supplying energy for endothermic reaction, J Adv Chem Eng. 4 (2014) 107. https://doi.org/10.4172/2090-4568.1000107.

[55] F. Dautzenberg, M. Mukherjee, Process intensification using multifunctional reactors, Chem. Eng. Sci. 56 (2001) 251-267. https://doi.org/10.1016/S0009-2509(00)00228-1.

[56] F. Yin, S. Ji, H. Mei, Z. Zhou, C. Li, Coupling of highly exothermic and endothermic reactions in a metallic monolith catalyst reactor: A preliminary experimental study, Chem. Eng. J. 155 (2009) 285-291. http://dx.doi.org/10.1016/j.cej.2009.03.029.

[57] P.D. Ronney, Analysis of non-adiabatic heat-recirculating combustors, Combust. Flame. 135 (2003) 421-439. https://doi.org/10.1016/j.combustflame.2003.07.003.

[58] J. Frauhammer, G. Eigenberger, L.v. Hippel, D. Arntz, A new reactor concept for endothermic high-temperature reactions, Chem. Eng. Sci. 54 (1999) 3661-3670. http://dx.doi.org/10.1016/S0009-2509(98)00454-0.

[59] S. Vaccaro, L. Malangone, P. Ciambelli, Micro-scale catalytic reactor for syngas production, Ind. Eng. Chem. Res. 49 (2010) 10924-10933. https://doi.org/10.1021/ie100464b.

[60] D.S.A. Simakov, M. Sheintuch, Demonstration of a scaled-down autothermal membrane methane reformer for hydrogen generation, Int. J. Hydrogen Energy. 34 (2009) 8866-8876. http://dx.doi.org/10.1016/j.ijhydene.2009.08.037.

[61] T. Terazaki, M. Nomura, K. Takeyama, O. Nakamura, T. Yamamoto, Development of multi-layered microreactor with methanol reformer for small PEMFC, J. Power Sources. 145 (2005) 691-696. http://dx.doi.org/10.1016/j.jpowsour.2005.02.065.

[62] L.R. Arana, S.B. Schaevitz, A.J. Franz, M.A. Schmidt, K.F. Jensen, A microfabricated suspended-tube chemical reactor for thermally efficient fuel processing, Journal of Microelectromechanical Systems. 12 (2003) 600-612. http://dx.doi.org/10.1109/JMEMS.2003.817897.

[63] S. Vaccaro, L. Malangone, P. Ciambelli, Modelling of a catalytic micro-reactor coupling endothermic methane reforming and combustion, Int. J. Chem. React. Eng. 8 (2010). https://doi.org/10.2202/1542-6580.2121.

[64]   M. Rahimpour, E. Pourazadi, A comparison of hydrogen and methanol production in a thermally coupled membrane reactor for co-current and counter-current flows, Int. J. Energy Res. 35 (2011) 863-882. http://dx.doi.org/10.1002/er.1744.

[65]   M. Mundhwa, R.D. Parmar, C.P. Thurgood, A comparative parametric study of a catalytic plate methane reformer coated with segmented and continuous layers of combustion catalyst for hydrogen production, J. Power Sources. 344 (2017) 85-102. http://dx.doi.org/10.1016/j.jpowsour.2017.01.082.

[66]   M. Bosco, F. Vogel, Optically accessible channel reactor for the kinetic investigation of hydrocarbon reforming reactions, Catal. Today. 116 (2006) 348-353. https://doi.org/10.1016/j.cattod.2006.05.064.

[67]   M. Mundhwa, C.P. Thurgood, Numerical study of methane steam reforming and methane combustion over the segmented and continuously coated layers of catalysts in a plate reactor, Fuel Process. Technol. 158 (2017) 57-72. http://doi.org/10.1016/j.fuproc.2016.12.002.

[68]   Y. Wang, Y.H. Chin, R.T. Rozmiarek, B.R. Johnson, Y. Gao, J. Watson, A.Y.L. Tonkovich, D.P. Vander Wiel, Highly active and stable $Rh/MgOAl_2O_3$ catalysts for methane steam reforming, Catal. Today. 98 (2004) 575-581. http://doi.org/10.1016/j.cattod.2004.09.011.

[69]   Z. Hou, T. Yashima, Small amounts of Rh-promoted Ni catalysts for methane reforming with CO_2, Catal. Lett. 89 (2003) 193-197. https://doi.org/10.1023/A:1025746211314.

Samenvatting

De belangrijkste conclusies in dit werk worden als volgt samengevat.

In Hoofdstuk 2 is een uitgebreid literatuuroverzicht van CMC gepresenteerd, inclusief de verschillende katalysatortypes, reactiemechanismen en kinetiek, reactiecondities (bijv. Het effect van temperatuur, ruimtesnelheid, molaire verhouding zuurstof tot methaan, aardgassamenstelling, bedrijfsdruk) en verschillende toegepaste reactoren (bv. fix-bed, wall-coated, membraan, wervelbed), wat een uitgebreide referentie biedt voor het vervolgonderzoek op dit gebied.

In Hoofdstuk 3 zijn de stabiliteit en adhesie van washcoated Pt / γ-Al$_2$O$_3$ katalysator onderzocht in een multikanaals microreactor. Een beste hechting van de γ-Al$_2$O$_3$-laag kan worden verkregen door het geschikte bindmiddel te kiezen (bijv. PVA met 3-5 gew.% En MW van 57.000 - 186.000), initiële γ-Al$_2$O$_3$ deeltjesgrootte (3 μm) en pH-waarde (pH=3.5), om voldoende waterstofbruggen te vormen met het goed gedispergeerde aluminiumoxide. Bovendien vertoonde de FeCrAlloy die als microreactor-substraat werd gebruikt een betere hechting voor zowel rechthoekige als ronde kanalen dan 316L roestvrij staal. De washcoated Pt / γ-Al$_2$O$_3$-katalysator werd verder gerealiseerd in de parallelle multikanaals microreactor voor CMC-tests volgens de hierboven geïdentificeerde geoptimaliseerde coatingprocedure. Gebleken is dat de werktemperatuur de grotere invloed heeft op de methaanomzetting vergeleken met die van het gasdebiet en de O$_2$/CH$_4$ molaire verhouding. De gunstige dekking van het geadsorbeerde methaan en zuurstof over het katalysatoroppervlak is essentieel om een gewenste methaanomzetting te verkrijgen. Bovendien kwam er meer reactiewarmte vrij uit de reactie bij een hoger debiet, waardoor een duidelijke temperatuurstijging langs de microreactor ontstond. Evenzo werd de microreactortemperatuur verhoogd met toenemende O$_2$/CH$_4$ molaire verhouding. Het temperatuurprofiel langs de meerkanaals microreactor is in lijn met de daarin verkregen methaanomzetting.

In Hoofdstuk 4 werd de CMC uitgevoerd in de enkellaagse en meerlagige washcoated Pt/γ-Al$_2$O$_3$-katalysatoren afgezet in de capillaire microreactoren. In het meerlagensysteem zijn twee verschillende gevallen getest. In geval 1 werd het totale gewicht van Pt in de catalsyt in het meerlagensysteem theoretisch hetzelfde gehouden als dat van het enkellaagssysteem. In geval 2 werd de theoretische Pt-belasting in het meerlaags systeem identiek gehouden aan het respectievelijke enkellaags systeem. Aangenomen mag worden dat de laagdikte in beide

gevallen evenredig toeneemt met het aantal lagen. De invloeden van de bedrijfsomstandigheden (bijv. De reactietemperatuur, molaire verhouding van zuurstof tot methaan en totale stroomsnelheid) evenals het Pt-gewicht en de belasting werden onderzocht. In het enkellaagse katalysatorsysteem kon een beste methaanomzetting van 95,17% worden verkregen onder 500 ^{o}C bij een totale stroomsnelheid van 30 ml min-1 en een molaire verhouding van zuurstof tot methaan (Φ) = 2. De methaanomzetting vertoonde een opmerkelijke toename met de toenemende Pt-belasting of -massa, en het light-off-fenomeen begon op te treden boven 400 ^{o}C. Het verschil in de toename van de methaanomzetting had de neiging te vertragen met de toename van de Pt-belasting, mogelijk veroorzaakt door de meer significante interne diffusielimiet in de coating gezien de verhoogde intrinsieke kinetische snelheid. Een lagere methaanomzetting werd verkregen bij Φ = 5 dan bij Φ = 2 in het light-off-experiment vanwege de competitieve adsorptie van de reactanten. De afname van de methaanomzetting heeft de neiging te vertragen bij voldoende hoge stroomsnelheden, wat zou kunnen worden toegeschreven aan de verbeterde externe massaoverdracht die de verminderde omzetting daarin compenseerde. In het meerlaags systeem in geval 1 leverde het dubbellaagse katalysatorsysteem een lagere methaanomzetting op bij Φ = 2 en 5 dan die van het overeenkomstige enkellaags systeem bij verder identieke werkomstandigheden. Dit wordt mogelijk veroorzaakt door de grotere interne diffusieweerstand in dikkere coatinglagen. Als het gaat om case 2, leverden de dubbellaagse en drielaagse katalysatorsystemen over het algemeen een hogere methaanconversie op bij Φ = 2 en 5 dan die van het respectievelijke enkellaags systeem, wat de (actieve) deelname van alle coatinglagen aangeeft (in plaats daarvan van de bovenste laag alleen) in de reactie. Een andere implicatie is dat in geval 2 de reactiesnelheid meer beperkt werd door de hoeveelheid katalysator dan door de interne diffusie. De methaanomzetting is echter vrijwel identiek tussen de enkellaagse en dubbellaagse en dubbellaagse (geval 2) systemen bij the = 1 in het gehele temperatuurbereik (350 - 500 ^{o}C), omdat de reactiesnelheid voornamelijk wordt beperkt door de onvoldoende zuurstoftoevoer.

In Hoofdstuk 5 werd de rechte microreactor met parallelle kanalen (Reactor # 1) afgezet met Pt/γ-Al$_2$O$_3$-katalysator eerst onderzocht op de CMC. De geoptimaliseerde specifieke katalysatorbelading van 57,6 g m^{-2} leverde een beste methaanomzetting op. Een duidelijke afname in de methaanomzetting met hogere of lagere specifieke katalysatorbeladingen zou kunnen worden verklaard door respectievelijk de verhoogde interne diffusieweerstand in dikkere coatings of en het ontbreken van voldoende actieve plaatsen in dunnere coatings. Een hogere methaanomzetting zou kunnen worden verkregen door de boomachtige structuur te

gebruiken als de afvoerproductcollector in plaats van als de inlaatvloeistofverdeler, vooral bij hoge stroomsnelheden. Dit zou kunnen worden verklaard door de hogere locale bij de inlaat en uitlaat van het reactie-microkanaal, wat gunstig is voor een meer uniforme vloeistofverdeling daarin. Vervolgens is de CMC uitgevoerd in andere plaatvormige microreactoren met verschillende interne kanaalconfiguraties gecoat met Pt/γ-Al$_2$O$_3$-katalysator, inclusief holtemicroreactor (Reactor # 2), dubbele serpentinekanaal-microreactor (Reactor # 3), belemmerde rechte kanaal-microreactor (Reactor # 4), microreactor met mazen (Reactor # 5) en vasculaire microreactor (Reactor # 6). De microreactor met dubbel serpentinekanaal heeft de hoogste methaanconversie laten zien, wat te wijten zou kunnen zijn aan de juiste dekking van het coatingoppervlak en een relatief lange verblijftijd. Bovendien zou een verbeterde gasmenging in de serpentine microkanalen kunnen resulteren in een verbeterde externe massaoverdracht en dus kunnen bijdragen aan een hogere methaanomzetting. Integendeel, de microreactor met mazen vertoonde de laagste methaanomzetting, waarschijnlijk als gevolg van de divergerende stroming in het stroomcircuit. Dit heeft waarschijnlijk geresulteerd in een niet-uniforme stroomverdeling en / of iets bredere verblijftijdverdeling en daarmee de laagste methaanomzetting. De resultaten met betrekking tot de invloed van de reactietemperatuur, molaire verhouding van O$_2$: CH$_4$ en totale stroomsnelheid in deze microreactoren komen over het algemeen overeen met die waargenomen in Hoofdstuk 4.

Résumé

Les principales conclusions de ce travail sont résumées comme suit.

Dans le chapitre 2, une revue complète de la littérature sur la CMC a été présentée, y compris les différents types de catalyseurs, les mécanismes de réaction et la cinétique, les conditions de réaction (par exemple, l'effet de la température, la vitesse, le rapport molaire oxygène / méthane, la composition du gaz naturel, la pression de fonctionnement) et divers réacteurs appliqués (par exemple, à lit fixe, à revêtement mural, à membrane, à lit fluidisé), qui offre une référence complète pour les recherches dans ce domaine.

Au chapitre 3, la stabilité et l'adhérence du catalyseur Pt/γ-Al$_2$O$_3$ enduit de lavage ont été examinées dans un microréacteur multicanal. Une meilleure adhérence de la couche de γ-Al$_2$O$_3$ pourrait être obtenue en choisissant le liant approprié (par exemple, PVA avec 3 à 5% en masse et PM de 57 000 à 186 000), la taille initiale des particules γ -Al$_2$O$_3$ (3 µm) et la valeur du pH (pH $\approx$ 3.5), afin de former les ponts hydrogène suffisants avec l'alumine bien dispersée. De plus, le FeCrAlloy utilisé comme matière du microréacteur a présenté une meilleure adhérence pour les canaux rectangulaires et ronds que l'acier inoxydable 316L. Le catalyseur Pt/γ-Al$_2$O$_3$ enduit a en outre été réalisé dans le microréacteur multicanal parallèles pour les tests CMC suivant une procédure de revêtement optimisée. On a constaté que la température de fonctionnement a la plus grande influence sur la conversion du méthane par rapport à celles du débit de gaz et du rapport molaire O$_2$/CH$_4$. La bonne couverture du méthane et de l'oxygène adsorbés sur la surface du catalyseur est essentielle pour obtenir une conversion de méthane souhaitée. De plus, une plus grande quantité de chaleur est libérée par la réaction quand le débit est élevé, provoquant ainsi une augmentation significative de la température le long du microréacteur. De même, la température du microréacteur augmente avec l'augmentation du rapport molaire O$_2$/CH$_4$. Le profil de température le long du microréacteur multicanal est en lien avec la conversion de méthane qui y est obtenue.

Au chapitre 4, la CMC a été réalisée dans les catalyseurs Pt/γ-Al$_2$O$_3$ monocouches et multicouches à revêtement lavé déposés à l'intérieur des microréacteurs capillaires. Deux cas différents ont été testés dans le système multicouche. Dans le cas 1, le poids total de Pt dans le catalyseur dans le système multicouche a été maintenu théoriquement le même que celui du système monocouche. Dans le cas 2, la charge théorique de Pt dans le système multicouche a été maintenue identique à celle du système monocouche respectif. L'épaisseur du revêtement

dans les deux cas peut être supposée augmenter proportionnellement avec le nombre de couches. Les influences des conditions de fonctionnement (par exemple, la température de réaction, le rapport molaire de l'oxygène au méthane et le débit total) ainsi que le poids et la charge de Pt ont été examinés. Dans le système de catalyseur monocouche, une meilleure conversion de méthane de 95,17% pourrait être obtenue sous 500 °C à un débit total de 30 mL min-1 et un rapport molaire oxygène / méthane (Φ) = 2. La conversion de méthane a montré une augmentation remarquable avec l'augmentation de la charge ou de la masse de Pt, et le phénomène d'allumage a commencé à se produire au-dessus de 400 °C. La différence dans l'incrément de la conversion du méthane avait tendance à ralentir avec l'augmentation de la charge de Pt, probablement causée par la limitation de diffusion interne plus importante dans le revêtement étant donné la vitesse cinétique intrinsèque accrue. Une conversion de méthane plus faible a été obtenue à Φ = 5 qu'à Φ = 2 dans l'expérience d'allumage en raison de l'adsorption compétitive des réactifs. La diminution de la conversion du méthane a tendance à ralentir à des débits suffisamment élevés, ce qui pourrait être attribué au transfert de masse externe amélioré qui compensait la conversion diminuée dans celui-ci. Dans le système multicouche du cas 1, le système catalytique à double couche a donné une conversion de méthane inférieure à Φ = 2 et 5 à celle du système monocouche correspondant dans des conditions de travail par ailleurs identiques. Ceci est probablement dû à la résistance à la diffusion interne plus importante dans les couches de revêtement plus épaisses. Dans le cas 2, les systèmes catalytiques à double et triple couche ont généralement donné une conversion de méthane plus élevée à Φ = 2 et 5 que celle du système monocouche respectif, indiquant la participation (active) de toutes les couches de revêtement (à la place de la couche supérieure seule) dans la réaction. Une autre implication est que dans le cas 2, la vitesse de réaction avait tendance à être plus limitée par la quantité de catalyseur que par la diffusion interne. Cependant, la conversion du méthane est presque identique entre les systèmes monocouche et double et triple couche (cas 2) à Φ = 1 dans toute la plage de température étudiée (350-500 °C), car la vitesse de réaction est principalement limitée par l'approvisionnement insuffisant en oxygène.

Au chapitre 5, le microréacteur à canal parallèle droit (réacteur # 1) déposé avec un catalyseur Pt/γ-Al$_2$O$_3$ a d'abord été examiné pour la CMC. La charge de catalyseur spécifique optimisée de 57,6 g m^{-2} a présenté une meilleure conversion de méthane. Une diminution significative de la conversion du méthane avec des charges de catalyseur spécifiques supérieures ou inférieures pourrait être expliquée par la résistance à la diffusion interne accrue dans les revêtements plus épais ou et par l'absence de sites actifs suffisants dans les revêtements plus minces,

respectivement. Une conversion de méthane plus élevée pourrait être obtenue en utilisant la structure en forme d'arbre comme collecteur de produit en sortie plutôt que comme distributeur de fluide d'entrée, en particulier à des débits élevés. Ceci pourrait être expliqué par une distribution de fluide plus uniforme à l'intérieur du réacteur dans ce dernier cas. Par la suite, la CMC a été réalisée dans d'autres microréacteurs de type plaque avec diverses configurations de canaux internes revêtus de catalyseur $Pt/\gamma-Al_2O_3$, y compris un microréacteur à cavité (réacteur # 2), un microréacteur à double canal serpentin (réacteur # 3), un microréacteur à canal droit obstrué (Réacteur # 4), microréacteur à circuit maillé (réacteur # 5) et microréacteur vasculaire (réacteur # 6). Le microréacteur à double canal serpentin a montré la conversion de méthane la plus élevée, ce qui pourrait être dû à la couverture appropriée de la surface de revêtement et à un temps de séjour relativement long. De plus, un mélange gazeux amélioré dans les micro canaux serpentins pourrait aboutir à un transfert de masse externe amélioré et contribuer ainsi à une conversion plus élevée du méthane. Au contraire, le microréacteur à circuit maillé présentait la conversion de méthane la plus faible, probablement en raison du débit divergent présenté dans le circuit d'écoulement. Cela a probablement abouti à une distribution de débit non uniforme et / ou une distribution du temps de séjour quelque peu plus large, et donc la conversion de méthane la plus faible. Les résultats concernant l'influence de la température de réaction, du rapport molaire O_2: CH_4 et du débit total dans ces microréacteurs sont globalement en cohérence avec ceux observés au chapitre 4.

Acknowledgements

PhD has been coming to the end after around four years and taken a long journey to achieve this point. I would like to take the opportunity to express my sincere gratitude to all those people who always support and help me when I experienced all these ups and downs during this special journey.

First of all, I would like to express my sincere thanks to all my supervisors: Prof. Jun Yue and Prof. Hero Jan Heeres from the University of Groningen, and Prof. Lingai Luo, Prof. Jérôme Bellettre, Prof. Yilin Fan from Université de Nantes. I would like to express my special thanks to Jun even at the very beginning for giving me the opportunity to have an interview with you on August 13th, 2015. Then, my PhD journey started on February 1st, 2016 in Groningen. Your professional guidance and support always encouraged me to think critically in searching for explanations. Our progress meetings were very instrumental, which always led me to obtain a deeper understanding and new conclusions of the obtained results. I have learnt a lot from you! You gave me numerous comments and questions on my thesis and paper manuscript, which has surely improved the quality of my research. I also would like to thank Prof. Heeres for the great support and guidance during my PhD study in Groningen. Although we did not have many meetings, you have surely inspired me to do a better research during our discussion. I am very grateful to Prof. Lingai Luo. We had quite some discussion. The encouragement and advice you gave me are certainly very constructive, and you are a very nice person in life and also rigorous in the scientific point of view. Also, I would like to thank you very much, Yilin Fan, for your shared knowledge, responsibility and patience that helped me make every success of this project, and thank you a lot for your time and great effort you have made on my experiment. Without your helpful and thoughtful corrections and input, my papers can't be published smoothly for sure. Particularly, I would like to thank you so much, Jérôme Bellettre, for all the time and effort you have put into my project. It was so lucky that my office was just next to yours. My problems and questions were always solved effectively, you were always there when I needed help no matter what, and you were always very instructive to help me analyse the reason behind it. Thanks a lot! Because all of you, each single research day has become smooth and meaningful!

L, Fatim'zahra Boujdad, Walid Hemaya. For many other people I do not mention here, your support in the past years is for sure highly appreciated.

Finally, I would like to express my deepest love to my parents, my mother Yingguang Li and my father Jiamo He. I would never be here without you both. Love you both to the moon and back is not enough, for such a great unconditional support and understanding, always! 谢谢爷爷奶奶姥姥姥爷叔叔阿姨舅舅伯伯, 大明哥, 李琼姐和弟弟妹妹们. 最最感谢世界上最最最棒的爸爸妈妈, 感激一路以来有你们, 感谢无条件的理解和支持, 千言万语不足够, 只希望你们健康快乐, 你们陪我长大, 我陪你们到老, 永远爱你们!

Li He

August 2020, Nantes

List of publications

(1) L. He, Y. Fan, J. Bellettre, J. Yue, L. Luo. A review on methane catalytic combustion at low temperatures: catalysts, reaction conditions and reactor designs. Renewable & Sustainable Energy Reviews. 2019, 109589.

(2) L. He, Y. Fan, L. Luo, J. Bellettre, J. Yue. Preparation of Pt/γ-Al$_2$O$_3$ catalyst coating in microreactors for catalytic methane combustion. Chemical Engineering Journal. 2020 (380) 122424.

(3) L. He, D. Vreugdenhil, Y. Fan, J. Bellettre, L. Luo, J. Yue. Capillary microreactors with single- and multi-layer Pt/γ-Al$_2$O$_3$ catalyst coatings for catalytic methane combustion. (to be submitted to Chemical Engineering Journal).

(4) L. He, Y. Fan, J. Bellettre, Yue J., L. Luo. Catalytic methane combustion in plate-type microreactors with different channel configurations: an experimental study. (to be submitted to Chemical Engineering Science)

List of attended conferences

(1) Li He, Yilin Fan, Lingai Luo, Hero J. Heeres, Jun Yue, Jérôme Bellettre. Catalytic methane combustion in a multi-channel micro reactor over washcoated Pt/γ-Al$_2$O$_3$ catalyst. 14th GLS International Congress, Guilin, China, June 2019.

(2) Li He, Yilin Fan, Lingai Luo, Jun Yue, and Jérôme Bellettre. Catalytic methane combustion in a multi-channel microreactor. 27th Congrés Français de Thermique, Nantes, France, June 2019.

(3) Li He, Yilin Fan, Lingai Luo, Jérôme Bellettre, Hero J. Heeres, Jun Yue. A study of γ-Al$_2$O$_3$ washcoated on microchannel platelet. CHAINS, Veldhoven, the Netherlands, December 2018.

(4) Li He, Yilin Fan, Lingai Luo, Jérôme Bellettre, Hero J. Heeres, Jun Yue. Catalytic methane combustion over a washcoated Pt/γ-Al$_2$O$_3$ catalyst in a multi-channel microreactor. ENTEG Autumn Meeting, Haren, the Netherlands, November 2018.